A Probabilistic Corrosion Model for Copper-Coated Used Nuclear Fuel Containers

by

Allan Konrad Järvine

A thesis
presented to the University of Waterloo
in fulfillment of the
thesis requirement for the degree of
Doctor of Philosophy
in
Civil Engineering

Waterloo, Ontario, Canada, 2022

Examining Committee Membership

The following served on the Examining Committee for this thesis. The decision of the Examining Committee is by majority vote.

External Examiner:	Rehan Sadiq Professor, Dept. of Civil Engineering, University of British Columbia
Supervisor(s):	Mahesh D. Pandey Professor, Dept. of Civil and Environmental Engineering, University of Waterloo
Internal Member:	Adil Al-Mayah Professor, Dept. of Civil and Environmental Engineering, University of Waterloo
Internal Member:	Robert Gracie Professor, Dept. of Civil and Environmental Engineering, University of Waterloo
Internal Member:	Stefano Normani Research Assistant Professor, Dept. of Civil and Environmental Engineering, University of Waterloo
Internal-External Member:	Gordon Savage Professor, Dept. of System Design Engineering, University of Waterloo

Author's Declaration

This thesis consists of material all of which I authored or co-authored: see Statement of Contributions included in the thesis. This is a true copy of the thesis, including any required final revisions, as accepted by my examiners.

I understand that my thesis may be made electronically available to the public.

Statement of Contributions

Allan Konrad Järvine is the sole author of Chapters 1, 2, 5, 6, and all appendices. Exception to sole authorship of material are as follows:

Research presented in Chapters 3 and 4

The contents of Chapters 3 and 4 were published in *Nuclear Engineering and Design* (Järvine et al., 2019) and *Nuclear Technology* (Järvine et al., 2020), respectively. Allan Konrad Järvine wrote the draft manuscripts, on which all co-authors contributed intellectual input. Specifically, the co-authors were Mr Alan G Murchison and Dr Peter G Keech, both of the Nuclear Waste Management Organization (NWMO), and Prof Mahesh D Pandey, supervisor. Mr Murchison provided the necessary support and access to relevant data and technical reports to conduct this work, and reviewed and edited the manuscripts. Dr Peter Keech also provided access to reports and reviewed and edited the corrosion-related contents of the manuscripts.

Citations:

Chapter 3: Järvine, A. K., Murchison, A. G., Keech, P. G., and Pandey, M. D. (2019). A probabilistic model for estimating life expectancy of used nuclear fuel containers in a canadian geological repository: Baseline model. *Nuclear Engineering and Design*, 352:110202.

Chapter 4: Jävine, A. K., Murchison, A. G., Keech, P. G., and Pandey, M. D. (2020). A probabilistic model for estimating life expectancy of used nuclear fuel containers in a canadian geological repository: Effects of latent defects and repository temperature. *Nuclear Technology*, 206(7):1036–1058.

Abstract

Lifetime predictions of used nuclear fuel containers destined for permanent storage in Deep Geological Repositories (DGRs) are challenged by the uncertainty surrounding the environment and the performance of both containers and engineered barriers over repository timescales. Much of the work to characterise the response of engineered barriers to postulated evolving environmental conditions and degradation mechanisms is limited to very short-term laboratory tests or at best in-situ large-scale experiments spanning less than a few decades. While much is learned from these test programmes, the fact remains that long-term performance of many tens of thousands of Used Fuel Containers (UFCs) across a timescale of 100,000 years or more cannot be estimated with a significant degree of confidence by extrapolating single point results of short-term experiments. This is particularly true when there is a desire to understand the progression of container failures and the timing of contaminants subsequently released into the geosphere. Used Fuel Container (UFC) lifetime predictions require a probabilistic approach to address uncertainty. Accordingly, this thesis addresses three objectives. The first is to develop a probabilistic model to estimate the time to penetrate through the copper coating of a UFC, assuming sulphide-induced corrosion is the primary degradation mechanism of concern. Within this model, also develop a framework to account for the design of the Engineered Barrier System (EBS) and proposed repository layout. The second is to enhance the probabilistic corrosion model by integrating the potential effects of latent copper coating defects and the single temperature transient predicted for the repository. The third is to develop a stochastic process model for pitting corrosion, integrate the same into the sulphide-induced corrosion model, and estimate the time to penetrate through the copper coating based on both degradation mechanisms. To satisfy the first two objectives, this work presents a unique Monte Carlo probabilistic framework. With respect to the third objective, modelling pitting corrosion in copper under postulated repository environments poses a significant challenge since there is no relevant data and the likelihood of this mechanism remains a much debated topic. To overcome this challenge and facilitate demonstration of the approach to modelling pit growth, surrogate data is utilised. In addition to detailing various options for modelling pit growth, this work presents a novel and more transparent, self-contained approach to the estimation of the underlying process intensity when pit growth is modelled via a non-homogeneous Markov process. Finally, the combined effect of pitting and sulphide-induced corrosion on UFC copper-coating lifetimes is demonstrated. The modelling results are for the purpose of illustrating a potential methodology only.

Acknowledgements

I would like to begin by thanking my supervisor, Prof Mahesh Pandey, who provided the initial vision to see the events occurring in a repository as "random" outcomes. Significant support was received throughout the course of this work by the staff at NWMO, particularly Mr Alan Murchison, Dr Peter Keech, Dr Scott Briggs, and Mr Chris Hatton, who faithfully supported the development of the UFC lifetime model and provided access to key personnel and reports in a very timely manner. The author is very grateful for their support. I'm particularly indebted to the assistance received by Dr Scott Briggs who graciously provided data files for the three-dimensional (3-D) diffusion calculations and kindly generated various UFC mesh models to support the one-dimensional (1-D) modelling framework developed herein.

Dedication

To Monika, Adina, Caleb, and Emily, for whom I chose to embark on this journey.

Table of Contents

List of Figures

List of Tables

List of Abbreviations

LR Likelihood Ratio 191

1-D one-dimensional xi, xl, 24, 26, 27, 40, 62, 131

2-D two-dimensional 40, 45, 49

3-D three-dimensional xi, 24, 26–28, 55

CANDU® CANada Deuterium Uranium 1, 9

CDF Cumulative Distribution Function 157, 170–172

CI Confidence Interval 188

CTMC Continuous-Time Markov Chain 5, 89, 112–119, 121, 126–128, 130, 132, 155, 160

CTMCs Continuous-Time Markov Chains 113

DEPS-EA DEPS Evolutionary Algorithm 187

DGR Deep Geological Repository xxi, xxvii, xxxiii, xli, 1, 4, 5, 12, 17, 18, 22, 24, 37, 40, 49, 50, 57, 62, 63, 68, 73–75, 78, 81, 83, 85, 131–133, 172, 224

DGRs Deep Geological Repositories ix

EBS Engineered Barrier System ix, 6, 55

ECDF Empirical Cumulative Distribution Function 33, 53, 213, 214

EDZ excavation damage zone 20, 133

EVA Extreme Value Analysis 5, 126, 158, 169, 173

FOD Foreign Object Damage 67, 83

GEV Generalised Extreme Value xxiv, xxviii, 98, 101, 126–128, 130, 158, 169–173, 175–181, 183–188, 190–193, 195–200, 203–205, 207–209, 214, 216–218, 220, 221, 224, 227, 228, 230, 233

GL Generalised Likelihood 182

GML Generalised Maximum Likelihood 182, 184, 185

GMLE Generalised Maximum Likelihood Estimator 182, 184

GPD Generalised Pareto Distribution 5, 85, 96–98, 101, 117, 126–128, 159, 169, 188, 195, 196, 207–211, 213, 218, 220, 224, 225, 227, 230, 233

GRG Generalized Reduced Gradient for Nonlinear Programming 187

HPP Homogeneous Poisson Process 90, 92, 93, 118

iid independent and identically distributed 38, 44, 49, 57, 66, 158, 169, 193, 231

L-BFGS-B Limited Broyden-Fletcher-Goldfarb-Shanno 187

LHS Latin Hypercube Sampling 40, 45, 49, 68, 79

LM L-Moments 175

MCMC Markov Chain Monte Carlo 182–184

MIC Microbiologically Influenced Corrosion 1, 11, 12

ML Maximum Likelihood 175–177, 180–182, 184–186, 188

MLE Maximum Likelihood Estimator 169, 178–182, 186, 220

MRL Mean Residual Life 208–210, 214–216

NDE Non-destructive Examination 64, 83

NHMP Non-homogeneous Markov Process 5, 85, 89, 112, 118, 119, 122, 126, 128, 196

NHPP Non-homogeneous Poisson Process xxxix, xlii, 5, 85, 89, 90, 93–97, 101, 112, 118, 119, 121, 130, 132, 196, 227–231

NHPPP Non-homogeneous Poisson Point Process 209, 215, 220, 228, 230, 232, 233

NWMO Nuclear Waste Management Organization 1, 12, 27, 62, 66

OLS Ordinary Least Squares 122

PDF Probability Density Function 39, 45, 171, 172

PMF Probability Mass Function 64, 66

POT Peaks-Over-Threshold 5, 85, 96–98, 117, 126, 207, 218, 230

PWM Probability-Weighted Moments 175, 181, 182

Q-Q Quantile-Quantile 189, 191, 193, 194, 211

RH relative humidity 18, 20

RMSE Root Mean Square Error 182, 184, 185

RV random variable xxxvi, xxxvii, xxxix, xlii, xliii, 17, 38–40, 44, 49, 56, 57, 63, 64, 66, 68, 70, 77–79, 92, 95, 96, 101, 116, 117, 127, 157, 163, 170, 171, 178, 179, 194, 207, 212, 215, 233

RVs random variables 38–40, 44, 45, 49, 57, 68, 78, 91, 127, 160, 169, 170, 177, 190

SE standard error 188

SKB Swedish Nuclear Fuel and Waste Management Company 12, 13, 23, 44

SLSQP Sequential Least Squares Programming 187, 233

SRB Sulphate-reducing Bacteria 1, 12, 22, 57, 133

UFC Used Fuel Container ix, xi, xvi, xx, xxi, xxiii, xxiv, xxvii, xxxiii–xxxvii, xxxix–xlii, 1–7, 15, 17–20, 22–24, 26, 27, 36–41, 44–46, 49, 53, 54, 56, 57, 62–68, 70, 72–74, 76–79, 81–83, 85, 89, 90, 96, 112, 125–133, 176, 185, 201–204, 224, 235

UFCs Used Fuel Containers ix, xxxv, xli, 3, 6, 15, 17, 18, 20, 24, 26, 36, 39, 40, 44, 45, 63, 64, 68, 70, 73, 74, 78, 85, 132

WAPDEG WAste Package DEGradation 14, 15

List of Symbols

$A^i_{\mathbf{Corr}}$ Area: area of the ith node/panel on the discretised surface of a UFC where corrosion takes place, units of length squared 36

$A_{\mathbf{Corr}}$ Area: specified area on the UFC where corrosion takes place, units of length squared 23

C^k_0 Concentration: sulphide ion concentration (M; mol/litre, at times also stated as ppm or ppb) at the boundary of the kth emplacement room 37

C^{max}_0 Concentration: maximum sulphide ion concentration (M; mol/litre, at times also stated as ppm or ppb) assumed for a postulated crystalline rock DGR 54

C_0 Concentration: sulphide ion concentration (M; mol/litre, at times also stated as ppm or ppb) at the boundary of the emplacement room 24

C Concentration: sulphide ion concentration (M; mol/litre, at times also stated as ppm or ppb) at the surface of a UFC 24

$D^j_{\mathbf{HS}}$ Diffusion coefficient: the effective diffusion coefficient for HS^- associated with the jth buffer box, equivalently applicable to the jth UFC, area per unit time 37

$D^{max}_{\mathbf{HS}}$ Diffusion coefficient: the assumed maximum effective diffusion coefficient for HS^- in compacted bentonite, area per unit time 54

$D_{\mathbf{HS}}$ Diffusion coefficient: the effective diffusion coefficient for HS^- in compacted bentonite, area per unit time 24

$D_{\mathbf{T}_i}, D_{\mathbf{T}_j}$ Diffusion coefficients: the assumed maximum effective diffusion coefficient for HS^- in compacted bentonite, associated with repository temperatures at time periods i, j, area per unit time 76

F_{ϵ_i} Cumulative distribution function: empirical cumulative distribution function associated with the ith Cox-Snell residual ϵ_i 213

F Cumulative distribution function: arbirtrary cumulative distribution function 169

$H(t)$ Cumulative hazard function: the cumulative hazard function defined by the negative natural logarithm of the survival function $S(t)$, $-\ln(S(t))$, for an arbitrary random variable T 212

$H(z)$ Cumulative distribution function: the limiting cumulative distribution function for normalised maximum random variable as the number of random variables approaches infinity, also referred to as the Generalised Extreme Value distribution 170

H_0 Null hypothesis: the null hypothesis used in goodness-of-fit tests 213

$\mathbf{H}$ Matrix: the Hessian matrix, comprising the matrix of second partial derivatives of the log-likekihood function 179

$\mathbf{I_O}$ Matrix: the Observed Information matrix, comprising the negative of the matrix of second partial derivatives of the log-likekihood function 180

$\mathbf{I}$ Matrix: the Fisher Information matrix, comprising the negative expectation of the matrix of second partial derivatives of the log-likekihood function; also used to represent a square identity matrix, with diagonals equal to 1 and all other entries equal to zero 179

$J_{\mathbf{HS}}$ Mass flux: the flux of sulphide ions arriving at the surface of a UFC, moles per area per unit time 24

K Constant: represents the quotient of the copper density and the product of the stochiometric coefficient for the copper-sulphide reaction and molar mass of copper 37

L Function: the likelihood function associated with random variable observations 178

$M_{\mathbf{Cu}}$ Molar mass: the molar mass of copper, g/mol 23

M_n Maximum of a sequence of random variables: the maximum of a sequence of random variables representing pit depths 169

M Ratio: the ratio of the UFC surface area to the corrosion coupon area, referred to as "size effect" 201

$N(t)$ Random variable: a random variable, representing the cumulative count from a counting process, associated with an underlying stochastic process 93

$N^i_{\mathbf{HS}}$ Quantity: the amount of sulphide ions in moles reacting at the ith node/panel of the discretised surface of a UFC 36

$N_{\mathbf{HS}}$ Quantity: the amount of sulphide ions in moles reacting at the copper surface 23

$\mathbf{N}$ Collection of numbers: a counting process, consisting of a collection or set of numbers, indexed in time, associated with an underlying stochastic process 93

$\mathbb{N}_0$ Naturals: set of natural numbers starting with 0 112

N Number: the number of UFCs in a repository 10

$\mathbf{P}(s,t)$ Matrix: the matrix of probability transition functions, representing the probability of transitioning from state j at time s to state k by time t, $t > s$, for all j, k in the state space of the Markov chain 113

$R(t)$ Reliability function: the reliability function (also referred to as the survival function $S(t)$) defined by one minus the cumulative distribution function $F(t)$, $(1 - F(t))$, for an arbitrary random variable T 212

$\mathbb{R}_+$ Positive reals: the real number line from zero and greater (i.e., $[0, \inf)$ 92

$\mathbb{R}$ Reals: the real numbers or real number line 228

$S(t)$ Survival function: the survival function (also referred to as the reliability function $R(t)$) defined by one minus the cumulative distribution function $F(t)$, $(1 - F(t))$, for an arbitrary random variable T 212

$\mathbf{S}$ Vector: the score vector or partial derivative of the log-likelihood function; also represents the state space for random variable $X(t)$ associated with a stochastic process 179

$TTF^i_{\mathbf{Corr}}$ Random variable: the time for the ith node/panel on the discretised surface of a UFC to sustain first full penetration of the copper coating 36

$TTF_{\mathbf{Corr}}$ Random variable: UFC first time-to-failure 55

TTF_{min} Random variable: the minimum of the UFC first times-to-failure derived from a bounding point estimate 54

$\mathbf{T}$ Set: the set of times whereby a random variable $X(t)$ is indexed, associated with a stochastic process 92

T_i, T_j Temperatures: repository temperatures at time periods i, j 76

$\mathbf{\Theta}$ Collection of parameter vectors: parameter space, consisting of all possible values for $\mu, \alpha, \kappa,$ and b of the Generalised Extreme Value distribution 178

$X(t)$ Random variable: the random variable associated with a stochastic process, indexed in time t and taking on values in state space $\mathbf{S}$ 91

$X_1, X_2, \ldots, X_n$ Sequence of random variables: sequence of random variables associated with pit depths 169

X_1 Random variable: the random variable associated with the minimum of the set of random variables, consisting of the product of copper coating thickness and the effective diffusion length at the ith node/panel on the discretised surface of a UFC, for all i 38

X_2 Random variable: the random variable associated with the minimum of the set consisting of the random variable associated with the quotient of the random variable (RV) X_1 and the random variable associated with the effective diffusion coefficient for HS^- for the jth buffer box, for all j 44

X_3 Random variable: the random variable associated with the minimum of the set consisting of the random variable associated with the quotient of the RV X_2 and the random variable associated with the sulphide ion concentration at the boundary of the kth emplacement room, for all k 49

$X^k_{C_0}$ Random variable: the random variable associated with the sulphide ion concentration at the boundary of the kth emplacement room 49

$X^j_{D_{\mathbf{HS}}}$ Random variable: the random variable associated with the effective diffusion coefficient for HS^- for the jth buffer box 44

$X^{max}_{d_{\mathbf{Corr}}}$ Random variable: maximum corrosion rate sustained by a UFC 77

$X_{\mathbf{def}}$ Random variable: Bernoullli random variable associated with a defective UFC 64

$X^{max}_{\mathbf{depth},r}$ random variable: the random variable associated with the maximum corrosion rate sustained during the rth time step of the cooldown period 78

$X^{max}_{\mathbf{depth,total}}$ Random variable: total maximum corrosion depth sustained by a UFC by the end of a cooling period 79

$X^{i}_{\mathbf{dia}}$ Random variable: the random variable associated with a defect diameter assigned to a UFC 66

$X_{i,j}$ Random variable: the random variable associated with maximum corrosion pit of the ith coupon of the jth exposure period 177

$X^{i}_{t_{\mathbf{Cu}}}$ Random variable: the random variable associated with the copper coating thickness at the ith node/panel on the discretised surface of a UFC 38

$X^{\mathbf{net}}_{t_{\mathbf{Cu}}}$ Random variable: the random variable associated with the net copper coating thickness (coating thickness minus defect diameter) at the ith node/panel on the discretised surface of a UFC, after taking into account the potential for a defect 68

$\mathbf{X}_1$ Collection of random variables: the set consisting of the random variables associated with the minimum of the set of random variables, consisting of the product of copper coating thickness and the effective diffusion length at the ith node/panel on the discretised surface of a UFC, for all i, determined from a specified number of realisations 40

$\mathbf{X}_2$ Collection of random variables: the set consisting of the random variable associated with the minimum of the set consisting of the random variable associated with the quotient of the RV X_1 and the random variable associated with the effective diffusion coefficient for HS^- for the jth buffer box, for all j 47

$\mathbf{X}_3$ Collection of random variables: the set consisting of the random variable associated with the minimum of the set consisting of the random variable associated with the quotient of the RV X_2 and the random variable associated with the sulphide ion concentration at the boundary of the kth emplacement room, for all k 50

$\mathbf{X}_{C_0}$ Collection of random variables: the set consisting of the random variable associated with the sulphide ion concentration at the boundary of the kth emplacement room, for all k 49

$\mathbf{X}_{D_{\mathbf{HS}}}$ Collection of random variables: the set consisting of the random variable associated with the effective diffusion coefficient for HS^- for the jth buffer box, for all j 44

$\mathbf{X}_{t_{\mathbf{Cu}}}$ Collection of random variables: the set consisting of the random variable associated with the copper coating thickness at the ith node/panel on the discretised surface of a UFC, for all i 38

$\mathbf{X}$ Collection of random variables: the set—defining a stochastic process—consisting of the random variables $X(t)$, indexed in time t and taking on values in state space $\mathbf{S}$ 91

Y_2^r Random variable: the random variable associated with the maximum of the set representing the product of the temperature factor for the rth step and the random variable associated with the effective diffusion coefficient for HS^- for the jth buffer box divided by the minimum effective diffusion length 78

Y_3^r Random variable: the random variable associated with the maximum of the set representing the product of the random variable Y_2^r, the random variable associated with the HS^- concentration for the kth emplacement room, and a constant 79

a_n Normalising constant: the normalising constant applied to M_n and typically referred to as the scale 170

α^* Scale parameter: modified scale parameter for the Generalised Pareto distribution in a Peaks-Over-Threshold framework 207

α_M Time-dependent parameter: Generalised Extreme Value distribution scale time-dependent and size-effect parameter, representing the scale parameter defined as a function of time raised to a power plus the effect of size 201

α_t Time-dependent parameter: Generalised Extreme Value distribution scale time-dependent parameter, representing the scale parameter defined as a function of time raised to a power 175

α Scale parameter: scale parameter for the Generalised Extreme Value distribution 171

b_n Normalising constant: the normalising constant applied to M_n and typically referred to as the location 170

β_r Correction factor: temperature correction factor associated with the rth time step approximating the repository cooling curve 78

b Exponential term: the power to which time is raised to represent the time dependence of the location and scale parameters of the Generalised Extreme Value distribution 175

$d^i_{\mathbf{Corr}}$ Corrosion rate: corrosion depth per unit time at the ith node/panel for a mass-transport-limited process associated with sulphide-induced corrosion 36

$d_{\mathbf{Corr}}$ Corrosion rate: corrosion depth per unit time for a mass-transport-limited process associated with sulphide-induced corrosion 23

$\Delta l_x, \Delta l_y, \Delta l_z$ Lengths: mutually perpendicular infinitesimally small length increments 24

∇C Concentration gradient: sulphide ion concentration gradient established from the outer surface of a bentonite buffer box to the surface of UFC 24

$\epsilon_{i,j}$ Residual: Cox-Snell residual associated with ith maximum corrosion pit depth observed at exposure period j; also simply labelled ϵ 194

η_i, η_j Viscosity: viscosity of water at repository time periods i, j 76

f_{C_0} Probability density function: the probability density function assigned to the sulphide concentration in the boundary of the emplacement room 50

$f_{D_{\mathbf{HS}}}$ Probability density function: the probability density function assigned to the effective diffusion coefficient for HS^- 47

$f_{\mathbf{HS}}$ Stoichiometric coefficient: the stoichiometric coefficient for the reaction of copper with sulphide 23

$f_{Markov}(x, t)$ Probability mass function: the distribution of probabilities across damage states for a Markov chain at some time t 125

$f_{\mathbf{N}}(\rho)$ Density: sample-function or joint density, obtained in the limit as the increment in ith time interval goes to zero from the right, for the occurence of event rho for the Non-homogeneous Poisson Process (NHPP) $\mathbf{N}$ 95

f_{X_1} Probability density function: the estimated sampling distribution for the RV X_1 47

f_{X_2} Probability density function: the estimated sampling distribution for the RV X_2 50

$f_{t_{\mathbf{Cu}}}$ Probability density function: the probability density function assigned to the copper coating thickness 43

$g_{\boldsymbol{\theta}}(x, t)$ Probability density function: an arbitrary probability density function with parameter vector $\boldsymbol{\theta}$ 177

γ Radioactive decay radiation: gamma rays, electromagnetic radiation greater than keV 11

κ Shape parameter: shape parameter for the Generalised Extreme Value distribution 171

$l^{i}_{\mathbf{eff}}$ Length: the effective 1-D diffusion path length for sulphide ions, from the boundary of the buffer box to the surface of UFC, for the ith node/panel on the discretised surface of a UFC 36

$l^{min}_{\mathbf{eff}}$ Length: the minimum effective 1-D diffusion path length for sulphide ions from the boundary of the buffer box to the surface of UFC, derived for a particular discretised UFC mesh size 54

$l_{\mathbf{eff}}$ Length: the effective 1-D diffusion path length for sulphide ions from the boundary of the buffer box to the surface of UFC 26

λ Parameter: rate parameter for the Exponential distribution 212

l Function: the log-likelihood function associated with random variable observations 178

$\mu_0, \alpha_0, \kappa_0,$ **and** b_0 Time-dependent parameters: initial values used for the numerical minimisation of the likelihood or log-likelihood function for the Generalised Extreme Value distribution 187

μ_M Time-dependent parameter: Generalised Extreme Value distribution location time-dependent and size-effect parameter, representing the location parameter defined as a function of time raised to a power plus the effect of size 201

μ_t Time-dependent parameter: Generalised Extreme Value distribution location time-dependent parameter, representing the location parameter defined as a function of time raised to a power 175

μ Location parameter: location parameter for the Generalised Extreme Value distribution 171

m Block size: the number of sequences of random variables from which a maximum is determined, equivalent to the number of corrosion coupons from which a maximum pit depth is measured 171

$n_j^{\mathbf{UFC}}$ Number: the number of pit depth exceedances associated with a specific threshold u_j assigned to the quarter hemispherical end-cap of a UFC 224

n_j Number: the number of pit depth exceedances associated with a specific threshold u_j 224

n Number: the number of nodes/panels formed when the UFC surface is discretised using a particular mesh size 38

$p_{j,k}(s,t)$ Probability transition function: the probability transition function, representing the probability of transitioning from state j at time s to state k by time t, $t > s$, in a Markov chain 112

$\pi(\cdot)$ Distribution: prior distribution associated with a parameter, used in the context of a Bayesian formulation 182

p Probability parameter: the probability of an undetected UFC defect for the early titanium UFCs, and for defects in the copper coating of the latest UFCs 10

$q_j(t)$ Function: infinitesimal transition function, also called intensity of passage, representing the rate at which the process leaves or transitions out of state j 113

$q_{j,k}(t)$ Function: infinitesimal transition function, also called intensity of transition, representing the rate at which the process leaves or transitions out of state j to state k, given that at time t it is in state j 113

$\rho_{\mathbf{Cu}}$ Density: density of copper, g/m^3 24

ρ Event: the event of observing a sample path of a non-homogeneous Poisson process 94

$t^i_{\mathbf{Cu}}$ Thickness: the thickness of the copper coating at the ith node/panel on the discretised surface of a UFC 36

$t^{min}_{\mathbf{Cu}}$ Thickness: the minimum copper coating thickness associated with the baseline (manufacturing-based) distribution assumed for the production of UFCs 54

$t_{\mathbf{Cu}}$ Thickness: the thickness of the copper coating associated with the baseline (manufacturing-based) distribution assumed for the production of UFCs 39

t_{min}, t_{max} Times: the minimum and maximum timescales anticipated for the DGR during the dry, oxic period 125, 204

$\boldsymbol{\theta_1}$ Parameter vector: parameter vector, consisting of μ, α, κ, and b of the Generalised Extreme Value distribution, where the subscript 1 differentiates the parameter vector from those derived for the Generalised Pareto distribution, the non-homogeneous Point process, etc. 186

$\hat{\boldsymbol{\theta}}$ Parameter vector: parameter vector, consisting of estimates for μ, α, κ, and b of the Generalised Extreme Value distribution, that maximise the likelihood function (also depicted as $\hat{\boldsymbol{\theta}}_{\mathbf{1}}$); and also $\hat{\boldsymbol{\theta}}_{\mathbf{2}}$ and $\hat{\boldsymbol{\theta}}_{\mathbf{3}}$, representing the estimated parameter vector for the Generalised Pareto distribution and the non-homogeneous Point process, respectively 178

$\boldsymbol{\theta}$ Parameter vector: parameter vector, consisting of $\mu, \alpha, \kappa,$ and b of the Generalised Extreme Value distribution 177

t_r Time: the length of time associated with the rth step approximation of the cooldown period in the repository 78

u_0 Threshold: arbitrary threshold pit depth used in the Peaks-Over-Threshold framework 209

u Threshold: threshold pit depth used in the Peaks-Over-Threshold framework 207

$v(x)$ Intensity density: the partial derivative with respect to x of the intensity measure $\Lambda(x)$, otherwise known as the intensity density or instantaneous rate of occurrence of events for an arbitrary NHPP 228

$x_1, x_2, \ldots, x_n$ Sequence of observations: sequence of observed pit depths associated with the sequence of random variables $X_1, X_2, \ldots, X_n$ 170

x_+ Upper endpoint: the upper endpoint of the Generalised Extreme Value distribution 175

$x_{i,j}$ Observed pit depth: the observed maximum pit depth of the ith coupon of the jth exposure period 177

x^i Random variable: the random variable associated with the product of copper coating thickness and the effective diffusion length at the ith node/panel on the discretised surface of a UFC 38

x_p Quantile: the quantile pit depth, corresponding to the non-exceedance probability p of the Generalised Extreme Value distribution 172

$\mathbf{x}$ Collection of random variables: the set consisting of the random variable associated with the product of copper coating thickness and the effective diffusion length at the ith node/panel on the discretised surface of a UFC, for all i 38

$y_{i,j}$ Variable: the variable associated with the natural logarithm of the argument of the likelihood function for the Generalised Extreme Value distribution with maximum pit depth observation i at exposure period j 187

y^j Random variable: the random variable associated with the quotient of the RV X_1 and the random variable associated with the effective diffusion coefficient for HS^- for the jth buffer box 44

$\mathbf{y}$ Collection of random variables: the set consisting of the random variable associated with the quotient of the RV X_1 and the random variable associated with the effective diffusion coefficient for HS^- for the jth buffer box, for all j 44

z^k Random variable: the random variable associated with the quotient of the RV X_2 and the random variable associated with the sulphide ion concentration at the boundary of the kth emplacement room 49

$\mathbf{z}$ Collection of random variables: the set consisting of the random variable associated with the quotient of the RV X_2 and the random variable associated with the sulphide ion concentration at the boundary of the kth emplacement room, for all k 49

z Random variable: the random variable associated with a pit depth, used in the context of the maximum of a sequence of random variables 170

Chapter 1

Introduction

For a Canadian DGR, the two primary engineered barriers employed to provide containment and isolation are the UFC and highly compacted bentonite clay (Hall and Keech 2017). Figures 1.1 through 1.3 provide an illustration of a conceptual DGR, a UFC, and a section of an emplacement room with a UFC inside a bentonite clay buffer box surrounded by gap fill, respectively. The present design of the Canadian UFC consists of a carbon steel structure, comprising a 47-mm thick cylindrical shell with 30 mm thick hemispherical ends, Figure 1.2. For corrosion protection, a nominally 3-mm-thick copper layer is electrodeposited onto the external surfaces of the container and head prior to encapsulation. Forty-eight CANada Deuterium Uranium (CANDU®) used nuclear fuel bundles will be encapsulated within each UFC, which will be welded shut, after which a cold spray process will be used to complete the copper coating. Each UFC is to be contained within a buffer box, which consists of bentonite clay buffer compacted to a specified dry density. Once the buffer boxes are placed into emplacement rooms, gaps formed between the buffer boxes and the emplacement room walls will be filled with compacted bentonite pellets, Figure 1.3.

Microbiologically Influenced Corrosion (MIC) due to sulphides from Sulphate-reducing Bacteria (SRB) is presently identified as the most consequential of potential environmental degradation mechanisms to which the UFC copper coating is susceptible over the timescale of the DGR (King et al., 2017). Accordingly, a 1.3 mm corrosion allowance is presently defined for the UFC for 106 years (Kwong, 2011). Validating the present configuration of the UFC with respect to evolving conditions in a DGR, particularly those that may compromise the currently proposed corrosion allowance, has been the focus of programmes at the Nuclear Waste Management Organization (NWMO) and for the international waste management community targeting the use of copper for nuclear waste containers. As a result, to date significant research has been performed to better understand the corrosion of

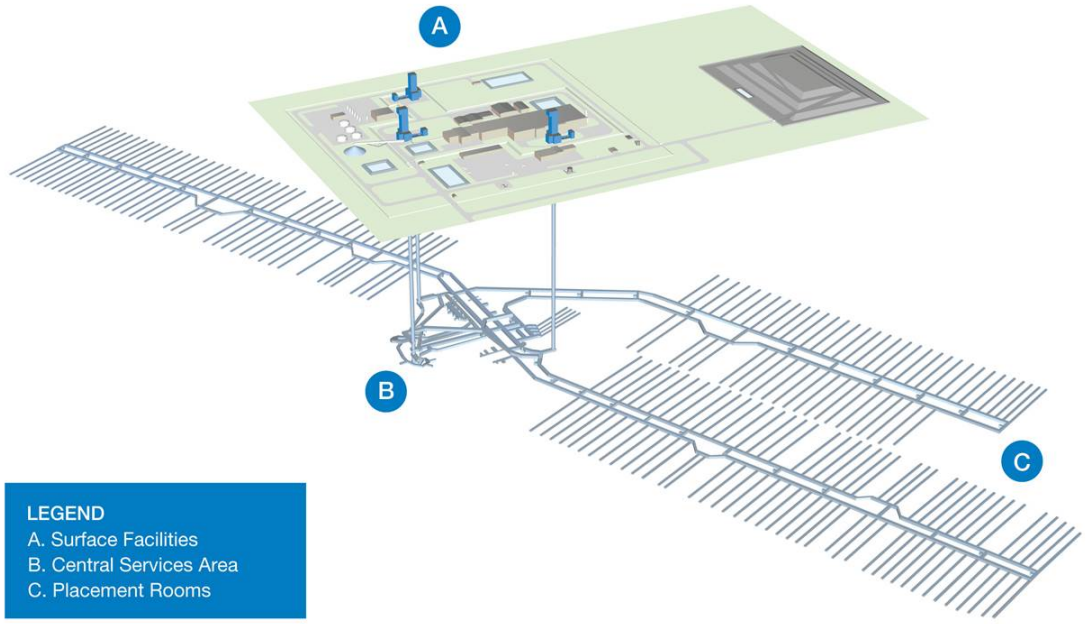

Figure 1.1: Illustration of a Deep Geological Repository, DGR (courtesy of NWMO)

copper under repository conditions (Chen et al., 2010, 2011, 2014, 2017a,b, 2018; Martino et al., 2014, 2017). While this body of research has provided a high degree of confidence with respect to understanding the fundamental mechanisms of copper corrosion—a requirement critical to the underpinning of mechanistic-based models, most of this research is focused on short-term experiments with a limited number of variables under consideration. Deterministic, single-point estimates of the time to fully penetrate UFC copper coatings, which are derived by extrapolating experimental results, are necessary for the evaluation of proposed corrosion allowance but are of limited utility to safety assessments interested in forecasting both the fraction and uncertainty in the timing of failed UFCs over the timescales of interest. Consequently, UFC lifetime predictions require a probabilistic approach.

Numerous container lifetime models have been developed in support of safety (performance) assessments for a range of container reference materials (Bullen, 1996; Hansen et al., 2014; Johnson et al., 1996; Pensado and Pabalan, 2008; Qin and Shoesmith, 2008;

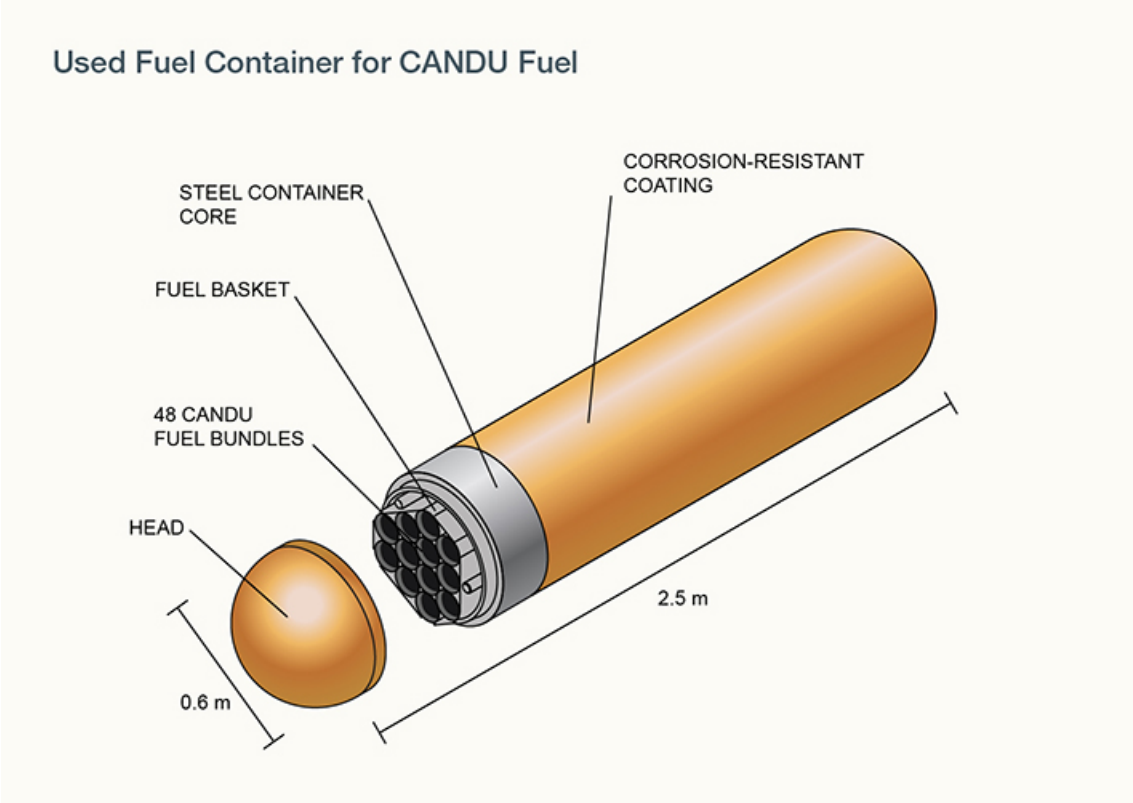

Figure 1.2: Artistic rendering of a Used Fuel Container (courtesy of NWMO)

Rechard et al., 2014a,b; Shoesmith et al., 1995, 1997; SKB, 2011). While some of these models are probabilistic in framework, to the best of this author's knowledge, and at the time two papers from this work were published, a fully probabilistic lifetime model did not appear to exist for copper-coated UFCs. The first part of this work has filled this gap by presenting a fully probabilistic UFC lifetime model, using a simple Monte Carlo approach and based solely on sulphide-induced corrosion.

Although overwhelming evidence to date points to sulphide-induced corrosion as the dominant degradation mechanism affecting the UFC copper-coated surface, there has been an on-going interest to consider the plausibility for pitting corrosion to occur during the early, oxic phase or—more importantly—the latter, long-term anoxic period in a repository. Historically, as summarised in King and Lilja (2014), pitting corrosion in copper canisters was first treated empirically using a pitting factor derived from long-term burial tests and archaeological artefacts. A pitting factor is the ratio of the maximum to the mean pit

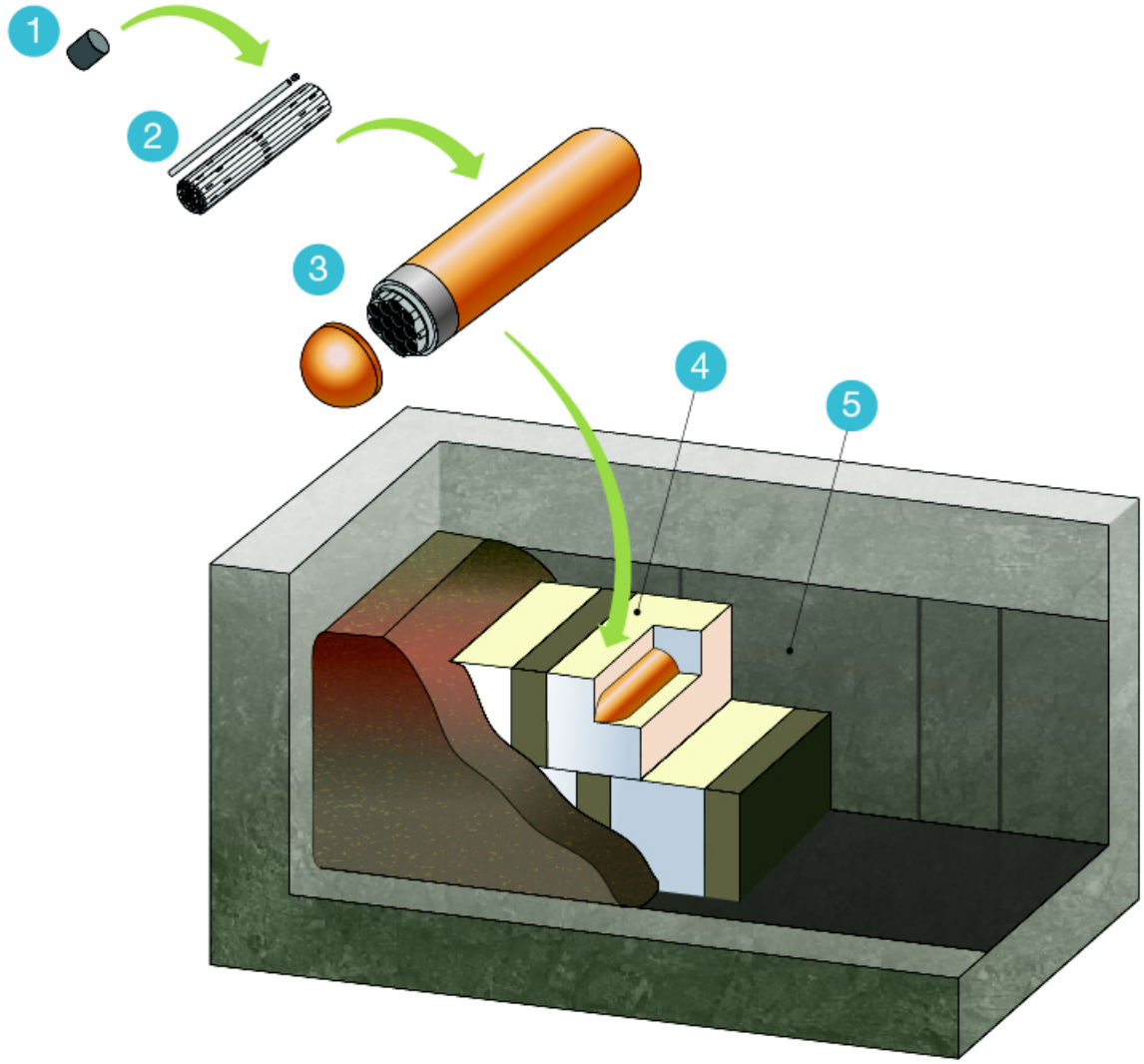

Figure 1.3: Artistic rendering of an emplacement room, showing a sequential view of a fuel pellet (1), a fuel bundle and pencil (2), a UFC (3), a bentonite buffer box (4), and emplacement room walls (5) (courtesy of NWMO).

depths. With time, as more relevant test data became available, pitting corrosion was seen to manifest as surface roughening (King and Lilja, 2013, 2014). This remains the prevailing view (e.g., see Hall et al., 2021). Additionally, within the context of a Canadian DGR, it was shown experimentally by Li et al. (2019) that postulated environmental conditions adjacent to a UFC copper surface are unfavourable to the formation of a passive state,

which is a necessary pre-condition for pitting corrosion to occur. This conclusion holds true for both the oxic and anoxic periods postulated for a DGR.

Notwithstanding, at least two probabilistic approaches have been applied to modelling pitting corrosion in copper canisters destined for geological repositories. The first appears to be by King and LeNeveu (1991), who applied Extreme Value Analysis (EVA) to account for pitting corrosion damage in 25-mm thick copper shell containers. The second, and more recent, is by Briggs et al. (2021), who developed a deterministic pitting corrosion model (with distributed parameters) for copper canisters planned for deposition into a Swedish DGR. While the Briggs et al. (2021) model is not a lifetime model, it is noteworthy because of the novel approach employed to predict the likelihood of pitting in the face of limiting data. Independent of and occurring concurrently with the work by Briggs et al. (2021), this author developed a stochastic process approach for estimating the extent of pitting corrosion in a UFC during the short oxic period of a DGR. As will be discussed in Chapter 5, the stochastic process approach is developed using surrogate data from short-term pitting corrosion experiments and is easily integrated into the UFC lifetime model presented in the preceding chapters. Implied in this perspective is the eventual availability of short-term, relevant copper pitting corrosion data, which may be generated during in-situ studies planned for the Underground Demonstration Facility of a DGR (pg. 58 Noronha, 2016). But unlike a simple regression model that may be fitted to short-term pitting corrosion data and used subsequently to predict pit depths outside the model time domain, the stochastic model presented here first formulates an expression for the underlying intensity of the pitting process by approximating the occurrence of extreme pit depths as a NHPP, with pit depth magnitudes modelled by a time-variant Generalised Pareto Distribution (GPD) within a Peaks-Over-Threshold (POT) framework. Subsequently, the stochastic model uses this intensity in a Non-homogeneous Markov Process (NHMP), specifically a Continuous-Time Markov Chain (CTMC), to propagate an initial distribution of pitting damage to a future time. The incorporation of a well-defined, stochastic process intensity into the Markov model is novel. Moreover, to maximise the utility of available data, pit depth exceedances—rather than pit depth maxima—are propagated through the Markov chain.

Consequently, this thesis presents a single probabilistic UFC copper-coating lifetime model that integrates a Monte Carlo methodology, which accounts for sulphide-induced corrosion over the entire timescale of a DGR, with a stochastic process approach for estimating the extent of pitting corrosion during the oxic period of a DGR. No such model appears to exist. The results of this model are for the purpose of illustrating a potential methodology to assess the life of copper coatings within a proposed repository environment.

1.1 Objectives

The objectives of this thesis are as follows:

1. With sulphide-induced corrosion as the single degradation mechanism, develop a probabilistic framework to estimate the copper coating life of UFCs. Within this framework, to the extent possible given the present knowledge, aim to account for the physical constraints imposed by the EBS; that is, formulate a model that is realistic in capturing the restrictions presented by the repository layout and EBS.

2. Extend this model to account for the effect of both latent defects in the UFC corrosion barrier and variation in repository temperature on predicted UFC copper coating lifetimes.

3. Review stochastic models for pitting corrosion, develop a stochastic model that readily integrates into the above framework, and subsequently demonstrate the ability to estimate the copper coating lifetimes of UFCs under the combined effect of general sulphide-induced and pitting corrosion.

1.2 Organisation

Chapter 2 provides a historical overview of UFC models, focusing particularly on the evolution of models developed for the Canadian scenario. Models developed by various other international jurisdictions are also discussed to a limited extent, where relevant.

Chapter 3 presents a detailed formulation of a baseline probabilistic model to predict UFC lifetimes. The chapter introduces the concept of a physics-of-failure model, within which several important model constructs are introduced. One is the effective diffusion length parameter; a parameter critical to transforming an otherwise 3-D problem to one that is 1-D and fully amenable to simple Monte Carlo simulation methods. A second important construct is the identification of a random outcome viewed from the perspective of the proposed physics-of-failure model and a hypothetical repository. Together these two constructs form the underpinning of the baseline model. The contents of this chapter were accepted for publication on July 8, 2019 in Nuclear Engineering and Design (Järvine et al., 2019).

Chapter 4 extends the formulation of the baseline model by incorporating additional life-limiting factors, such as latent defects postulated to occur in the UFC external cop-

per coating and repository temperature. The contents of this chapter were accepted for publication on December 1, 2019 in Nuclear Technology (Järvine et al., 2020).

Chapter 5 details the two-part stochastic model, comprising a non-homogeneous Poisson process approximation for the pitting corrosion intensity and a pure-birth, linear-growth-rate Markov process (non-homogeneous in rate) for modelling the evolution of pit depths exceeding a time-variant threshold level. This chapter concludes with an estimate of the combined effect of sulphide-induced and pitting corrosion on UFC lifetimes for an oxic period of arbitrary length.

Lastly, overall conclusions and proposed future work are summarised in Chapter 6.

Chapter 2

Brief Historical Review of Used Fuel Container Models

This chapter provides a historical review of lifetime models developed internationally for used nuclear fuel waste containers, with particular focus on the Canadian experience. Section 2.1 reviews the early Canadian experience with modelling lifetimes for titanium containers. Section 2.2 details the subsequent Canadian work on predicting container lifetimes with copper as the reference material. Section 2.3 highlights the approach undertaken in Sweden for copper shell waste containers. Section 2.4 brings attention to the complementary modelling work carried out in the United States for a two-layered waste container, whose outer layer is constructed from a corrosion resistant nickel-based alloy. The probabilistic framework exemplified by the United States experience is especially pertinent to the approach adopted in this work. Lastly, section 2.5 summarises the chapter.

2.1 Canadian Experience—Titanium Used Fuel Container Life Prediction

With respect to the Canadian context for container life prediction modelling, the seminal work of Doubt (1984) provided a rigorous assessment of the type and sources of defects likely to affect the longevity of containers on the basis of lessons learned from inspection of components (e.g., pressure vessels) for power generation applications and CANDU® reactor components such as fuel bundles and fuel channel calandria/pressure tubes. Using a geometric mean of the combined data, Doubt estimated that approximately 1 in 5000

containers placed in a repository would contain a significant partial through wall or entirely through wall defect sufficient to initiate early failure. The estimate was later revised to 1 in 10^3 to 1 in 10^4 containers would contain a life-limiting defect (Johnson et al., 1994).

By the 1990s, results of experimental testing allowed life prediction methodologies to develop suitably, resulting in a first-generation repository post closure model based on corrosion-resistant Grade-2 titanium (Ti-2) as the reference container material, with placement of containers into vertical bore holes the emplacement strategy (Shoesmith et al., 1995, 1997). Crevice corrosion and hydrogen-induced cracking were the two degradation mechanisms modelled for Ti-2, and early failures arising from undetected defects were also incorporated into the model. With respect to the latter, a Binomial distribution consisting of N trials, where N represented the number of containers in a repository sector, and probability, p, where p represented the probability of any container having a significant undetected defect, was sampled to determine how many containers per repository sector would possess a significant defect and fail very early in life. The probability p was treated as a random variable with a Lognormal distribution, having a geometric mean equal to 2×10^{-4} container failures per year (i.e., 1 in 5000 containers). Left tail of the Lognormal distribution was truncated at 10^{-4} container failures per year (i.e., 1 in 10000 containers), while the right tail was truncated at 10^{-3} container failures per year (i.e., 1 in 1000 containers), to reflect the results of Doubt (1984). The model assumed that within 50 years post closure, all containers with undetected defects would fail.

Crevice corrosion was assumed to initiate immediately following closure and modelled as a temperature dependent mechanism. Three temperature zones (hot, cold, and cool) were assigned to the repository to represent the temperature of the containers based on their location (i.e., in the centre versus the extremities of the repository, and somewhere in between). Three distinct temperature profiles as a function of time were created to reflect the expected yet variable evolution of temperatures in the repository within each of the zones.

This first-generation model predicted that approximately 97% of Ti-2 containers would fail by crevice corrosion, with only 0.1% failing by crevice corrosion before 1,000 years. Within 6,000 years, all Ti-2 containers were predicted to fail. The model generated a cumulative distribution, which provided the fraction of failed Ti-2 containers as a function of post closure time.

2.2 Canadian Experience—Copper Used Fuel Container Life Prediction

A shift away from the bore-hole emplaced Ti-2 containers to the in-room emplaced copper shell containers was introduced formally in the post-closure long-term vault (repository) safety assessment by Johnson et al. (1996). Unlike the modelling for Ti-2 containers (Johnson et al. (1994); Shoesmith et al. (1995, 1997)), where two significant degradation mechanisms were postulated to cause eventual failures of containers within 6,000 years post closure, long-term assessment of copper shell containers, of which two designs were under consideration, would not identify a single corrosion degradation mechanism capable of causing failure of the copper shell within 10^6 years post closure (Johnson et al., 1996). Failure in the copper shell container scenario was defined as either full penetration of the 25-mm thick copper shell by a combination of pitting and uniform corrosion (King and LeNeveu, 1991), where pitting and uniform corrosion were both limited to the aerobic period in the evolution of the repository, or if the copper shell sustained 16 mm of uniform corrosion, thereby inducing structural failure from buckling. Uniform corrosion was predicted to result in a maximum wall penetration of 11 μm. After all the O_2 in the repository was consumed, however, uniform corrosion of the copper shell would stop. Pitting was treated outside the corrosion model using an extreme-value analysis of pit depth data from the literature. Again, pitting was limited to the aerobic period in the repository, and the maximum pit depth over a period of 10^6 years was predicted to be less than 6 mm. Since both pitting and uniform corrosion were not predicted to occur in the anoxic period of the repository, the onset of which was estimated to occur 670 years after repository closure (Kolar and King, 1995), the maximum pit depths estimated by extreme-value analysis for a 10^6-year timescale would never be realised and, therefore, failure of containers could not occur either by uniform corrosion, pitting, or both within 10^6 years following closure.

In addition to uniform corrosion and pitting, the long-term assessment of the copper shell containers also considered the potential contribution from atmospheric corrosion, stress corrosion cracking, radiolysis by γ-radiation, crevice corrosion, and MIC. All these were summarily evaluated and determined to either have negligible effect or to be very unlikely due to the absence of factors necessary for the respective mechanisms to be active. The exception was MIC.

Microbiologically influenced corrosion arising from the formation of biofilms on the container surface was ruled out due to the predicted relatively dry and "sterile" conditions prevailing immediately following placement. Relatively dry conditions were expected because at the beginning and sometime after the placement rooms are sealed, the placement

rooms are both unsaturated due to low flow of groundwater into the placement room and hot as a result of decay heat from used fuel bundles. As well, the initially partially saturated clay buffer material immediately adjacent to the container surfaces was predicted to undergo desiccation. Moreover, γ-radiation effects on microbial colonies in the clay buffer material immediately adjacent to the container surfaces would cause bacterial populations to die out or become dormant, thereby leading to"sterile" conditions. But MIC from the by-products of active anaerobic bacteria in remote areas of the repository during the anoxic period was understood to be very likely.

From the results of corrosion tests on Cu/compacted bentonite clay electrodes in de-aerated saline solution with Na_2S added as an analogue to sulphide produced from reduction of sulphate by anaerobic bacteria (e.g., SRB), King and Stroes-Gascoyne (1995) demonstrated a lowering of the corrosion potential due to diffusion of inorganic sulphide through the bentonite clay. Extending this belief forward and incorporating the mass-balance approach of Werme et al. (1992) to estimate depth of corrosion, King and Stroes-Gascoyne (1995) calculated a corrosion rate of 0.4 nm/yr for a copper container assuming, among other things, steady-state diffusion and a constant remote-area sulphide concentration of 1 ppm (3×10^{-5} mol/L). Remote areas in the repository were defined as the interface between the host rock and the bentonite clay backfill. At a rate of 0.4 nm/yr, total depth of corrosion in 10^6 years post closure was estimated at 0.4 mm. In the Johnson et al. (1996) safety assessment, however, an equivalent corrosion depth of approximately 1 mm was calculated over the same timescale and under similar assumptions but using instead 3 ppm (9×10^{-5} mol/L) for the remote-area sulphide concentration. Apparently, the 3 ppm (9×10^{-5} mol/L) sulphide concentration represented the maximum concentration observed from unpublished MIC experiments at the time (Johnson et al., 1996), which were designed to replicate the experiments by King and Stroes-Gascoyne (1995) but with biotically produced sulphide.

Although sulphides are not found in crystalline and sedimentary groundwaters anticipated for a Canadian DGR (McMurry, 2004), a remote-area sulphide concentration of 3 ppm has been considered as a carried-forward estimate for the corrosion allowance from MIC over a 10^6-year assessment period of interest (Kwong, 2011). The same level of conservatism is integral to the implicit assumption for no container failure by corrosion in the Base Scenario employed in all subsequent published reference case studies (Garisto (2012, 2013); Gierszewski et al. (2004); NWMO (2012)). Within ongoing site investigation work by the NWMO, sulphide concentrations are being assessed.

As indicated in Chapter 1, Briggs et al. (2021) have very recently developed a probabilistic model that provides a novel means to account for pitting corrosion in the Swedish Nuclear Fuel and Waste Management Company (SKB) copper containers. The point to

raise here from the perspective of probabilistic models is that this model employs an empirical relationship, with distributed parameters, to characterise the growth of pits, allowing for a simple Monte Carlo scheme to account for uncertainty. The Monte Carlo scheme is not the novel component of the Briggs et al. (2021) model, however.

2.3 SKB Copper Container Safety Assessment

For the long-term safety assessment of copper spent fuel canisters at Forsmark Sweden (SKB, 2011), corrosion calculations were performed conservatively using a constant sulphide concentration derived from analysis of groundwater samples. In particular, for the intact clay buffer scenario, a sulphide concentration of 10^{-5} mol/L was chosen, representing the 90% upper bound of a modified cumulative distribution of groundwater samples (SKB, 2010b). For a partially eroded buffer scenario, the mean of the modified distribution of groundwater samples, 5×10^{-6} mol/L, was assigned to each canister borehole in the corrosion calculations. As in the Canadian experience, the SKB long term safety assessments and supporting corrosion calculations incorporate a deterministic—yet conservative—approach to corrosion of copper by sulphide. Although cumulative distributions of corrosion rates are also generated in the SKB assessments, the distributions arise primarily from sampling of flow distributions associated with site-specific hydrogeological Discrete Fracture Network modelling SKB (2010b, 2011) and not, rather, by also sampling the distribution of groundwater sulphide concentrations. Notwithstanding, the approach taken by SKB for incorporating the groundwater sulphide concentration data into long-term safety assessment has been deemed reasonable by an independent review Bath (2014).

2.4 U.S. Yucca Mountain Performance Assessment Experience

In the U.S., spent nuclear fuel and high-level nuclear waste were planned for disposal in waste containers to be placed in an underground repository located potentially in Yucca Mountain, Nevada (DOE (U.S. Department of Energy), 2008). A two-barrier system, consisting of a corrosion resistant outer layer (Alloy 22) and a structural support inner layer (Type 316 stainless steel), defines the waste container design (DOE (U.S. Department of Energy), 2002). Depending on the configuration, some containers would incorporate an overhead drip shield made of titanium to protect from drips from the repository ceiling

and falling rock. A container configured with a drip shield is referred to as a waste package. As part of performance assessment, waste package degradation is simulated using a stochastic model named WAste Package DEGradation (WAPDEG), which incorporates a set of empirically and semi-empirically derived degradation models to account for various waste package outer layer degradation mechanisms postulated to be active over the evolving conditions in the repository (Hansen et al., 2014; Pensado and Pabalan, 2008; Rechard et al., 2014a,b).

While both the alloy systems employed in the proposed U.S. waste containers and the postulated Yucca Mountain repository environment do not share strong similarities with their counterparts in the current Canadian reference cases, the stochastic approach to materials degradation adopted by the WAPDEG model is of significant interest to this work. In fact, a review of the available literature of life expectancy models developed by various international entities for used fuel (and/or high-level waste) containers (or canisters) has not identified a more comprehensive and detailed model than WAPDEG. The WAPDEG model calculates rates of degradation based on user-specified waste container exposure histories that consist of temperature and relative humidity time histories arranged in a look-up table format. Exposure histories allow for spatial and temporal variation in waste container environment and when coupled with environment-dependent degradation models a stochastic approach to waste container life expectancy is facilitated.

Eighteen different probability distributions are implemented in WAPDEG. These give the user considerable flexibility in modelling variability. One very pertinent example is WAPDEG's ability to account for parameter uncertainty by sampling from various degradation model parameter distributions. The WAPDEG model also enables the variance of a probability distribution to be shared among the three levels defined by the waste container (first level), a patch on a waste container surface (second level), and sites on the patch for localised corrosion degradation (third level). Further, spatial variability within a container and from container to container is also one of the most relevant uses of the probability distributions. Patches arise from the discretization of the container surface into sub-areas (i.e., patches), each with assumed homogenous corrosion properties. The extent of variability from patch to patch within a single container can be also user defined.

Besides modelling general corrosion and localised corrosion (from various mechanisms), WAPDEG also permits the incorporation of manufacturing defects into a waste container to account for their effect on life expectancy. The process includes user-defined inputs such as the probability that a barrier (e.g., outer layer) of a waste container has manufacturing defects, the distribution of the number of manufacturing defects per barrier, and the distribution of defect size. Once degradation of a container outer layer has begun, WAPDEG randomly samples a number from the interval 0 to 1 and compares the randomly selected

number to the probability that a container has manufacturing defects. If the random number selected is greater than the probability of container defects, then WAPDEG samples from the number of manufacturing defects per barrier distribution and assigns the number of defects selected to the container barrier by distributing randomly the number of manufacturing defects across all patches.

Of the many available outputs (e.g., average number of patch failures, average number of pit failures, etc.), WAPDEG also provides a cumulative distribution of waste container failure times over the analysis time defined by the user.

It's important to recognise that other waste package models incorporating a probabilistic framework were also developed for the Yucca Mountain albeit to a smaller and less comprehensive scale, targeting specific degradation processes (e.g., Bullen, 1996; Qin and Shoesmith, 2008). In general, however, the WAPDEG model is the most comprehensive.

2.5 Review Summary

The foregoing historical perspective is by no means exhaustive, but it is sufficient to provide an understanding of the various approaches pursued by international groups to estimate life expectancy of UFCs. One recent UFC lifetime prediction review (King, 2014) has highlighted the importance of being able to justify long-term used-fuel container lifetime predictions from degradation models based on empirical results derived over very short experimental timelines (relative to repository timescales). A crucial and necessary requirement is, therefore, the ability to underpin predictions by coupling empirically derived models to a strong understanding of degradation mechanisms. In this respect, the work to date on the corrosion of copper has gone a long way towards providing a measure of confidence in the ensuing estimates of UFC lifetimes. However, greater confidence in UFC lifetime estimation is achieved when uncertainty in degradation model inputs is treated from a probabilistic perspective.

Chapter 3

Baseline Model

This chapter summarises the evolution of the DGR environment (Section 3.1), within which the two degradation mechanisms addressed in the UFC lifetime model (Section 3.2) are placed in time. Following this, Section 3.3 formulates sulphide-induced corrosion as a mass-balance, mass-transport phenomenon. Section 3.4 introduces the effective diffusion length, a model construct critical to the employment of a Monte Carlo methodology and arising from the discretisation of the UFC surface. With the ground work laid, Section 3.5 develops the probabilistic framework for the baseline UFC lifetime model. Limitations of the model are discussed in Section 3.6. A brief summary of the chapter is provided in Section 3.7.

In a very generic sense, the problem statement addressed by this chapter may be defined as the solution for the time to failure t in the failure condition expressed by $h - X(t) \leqslant 0$. Here, $X(t)$ is a RV representing total degradation sustained on the surface of a UFC by time t at a rate of degradation R, and h is the copper coating thickness. This generic representation of the problem statement is given to aid the understanding but is not used explicitly in the model formulation. The precise problem statement addressed by this chapter is to characterise the distribution of first times to failure for UFCs placed in a crystalline rock DGR. Failure is defined as full penetration of the copper coating.

3.1 Long-term Evolution of a Conceptual DGR

The present understanding of the long-term evolution of a conceptual DGR has been recently summarised by King et al. (2017). The major highlights are as follows.

The DGR is predicted to sustain a single temperature transient lasting approximately 10^5 years following closure. For a conceptual DGR in crystalline rock (for example), the transient is due to decay heat generated by the placement of approximately 108000 UFCs (Noronha, 2016). The actual shape of the temperature transient profile will depend on various factors, not least of which are site-specific variables such as: the times to re-saturate emplacement rooms (i.e., rate of in-flux of groundwater); the degree to which re-saturation occurs homogeneously (i.e., spatial, time variant distribution of re-saturation); and the impact of a 30-year placement period (Noronha, 2016), which leads to a staggered input of heat as rooms and panels are sequentially sealed off. Notwithstanding the preceding uncertainties, numerical models developed to date to simulate heat transport in crystalline rock in the Canadian Shield (Guo, 2015, 2016, 2017) are consistent with other crystalline rock repository thermal transient simulations (Ikonen and Raiko, 2015) and can be employed with a measure of confidence to predict the temperature profile. As shown in Figure 3.1, the most recent model results estimate a peak UFCs surface temperature of less than 90°C within the first 100 years post-closure.

During the thermal transient period, the repository (or more precisely the near-field) is also predicted to undergo several transient stages before long-term, stable conditions set in, Standish et al. (2016); King et al. (2017); Ibrahim et al. (2018). As will be discussed shortly, the (sum) total estimated duration of the early stages is expected to be short relative to the final (long-term) stage. This implies that degradation mechanisms operative during the early stages will have finite timespans in which to be of consequence to the life expectancy of a UFC. In the ensuing discussion, the stages advanced by King et al. (2017) are introduced and viewed from the perspective of the near-field. The near-field environment comprises the UFC, the buffer, and the portion of the geosphere significantly altered by the presence of the repository.

Stage 1, which is identified as the immediate post-placement period, lasting days to months depending on various factors, is characterised as a period where the near-field environment will be aerobic due to trapped oxygen in the sealed emplacement rooms and humid, with relative humidity (RH) ranging from approximately 80% at the start to slightly above 40% towards the end of the stage. Additionally, the dose rate from gamma radiation as a result of mostly fission product decay in the spent fuel will be at its highest during this stage. Some estimates put the dose rate at the external surface of the UFC—at

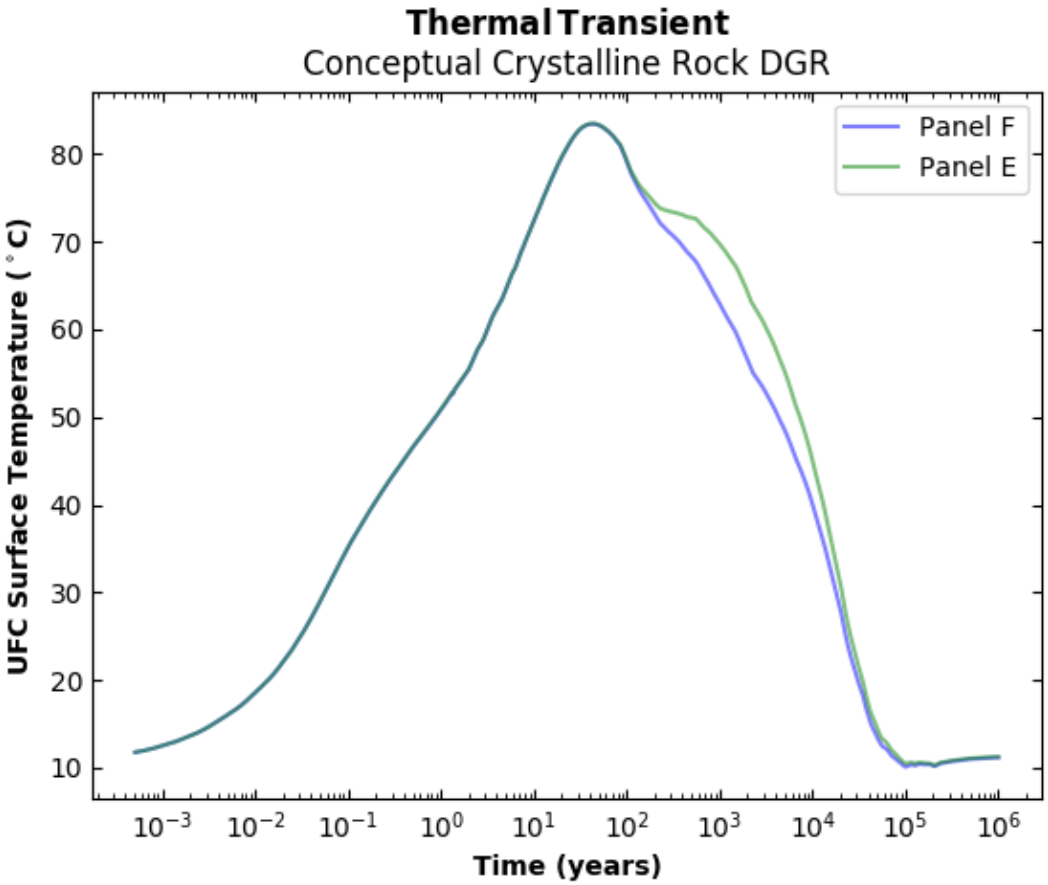

Figure 3.1: UFC surface temperature profile per Guo (2017).

placement—at approximately 1.1 Gy/hr (corresponding to 30 years post-reactor removal), decaying approximately exponentially thereafter to levels approaching 10^{-5} Gy/hr within the first 500 years (Morco et al., 2017). Of significance to the UFC life expectancy is the potential for aqueous corrosion to occur during Stage 1 due to high humidity and oxic conditions.

Stage 2 is characterised as the dry-out period. As the near-field transitions from Stage 1 to Stage 2, higher temperatures due to continuing decay heat from the spent fuel bundles will drive moisture from a volume of bentonite buffer material immediately adjacent to the surface of the UFC towards the host rock. Experimentally, large-scale mock-up (Fernández and Villar, 2010) and real-scale in-situ (Chijimatsu et al., 2001; Rutqvist et al., 2001; Salas

et al., 2014; Samper et al., 2018; Zheng et al., 2011) tests have confirmed that water content in the bentonite buffer material adjacent to simulated containers (with constant or variable heat sources) is reduced and driven to the extremities of the experimental set-up (e.g., host rock or large-scale container). In the latter region (i.e., at the buffer/host rock interface), water vapour condenses and is absorbed by the bentonite interfacing with the host rock, causing localised swelling (swelling of the bentonite from groundwater in-flux can also occur at the same interface during this period but is dependent on local hydrogeologic conditions). The preceding references record that migration of the vapour phase away from the heat source is quite rapid and dependent on both the temperature of the container and the porosity of the bentonite barrier (i.e., dry density). Consequently, it is anticipated that for the first group of UFCs emplaced in any given emplacement room, the onset of Stage 2 may occur before or soon after the same emplacement room is sealed off. Simplistically, Stage 2 ends when the advancing saturation front originating from the host rock begins to raise the relative humidity of the near-field above its minimum. Thus, the duration of Stage 2 is governed by the thermal conductivity and vapour phase permeability of the buffer material and the rate and spatial and time-variant distribution of groundwater in-flux. Of significance to the UFC life expectancy is the implication that aqueous corrosion is very unlikely during Stage 2.

Stage 3 refers to the gradual saturation of the bentonite buffer and the eventual re-wetting of the UFC. Stage 3 is a transition period, characterised by a change from low RH (e.g., approximately 40%) to full (i.e., 100%) bentonite buffer saturation. According to King et al. (2017), the near-field is expected to reach a fully saturated state within approximately 50 years. There are, however, many factors that determine the time to reach full saturation. For low permeability crystalline rock, the assumption of a homogeneous in-flux of groundwater acting over the interface of the bentonite buffer and host rock is challenged by the occurrence of hydraulically active fractures in the excavation damage zone (EDZ). As shown by Dessirier et al. (2016, 2017), saturation in bentonite can be localised to hydraulic fracture sites intersecting the emplacement room, with surrounding regions of the bentonite buffer remaining relatively unsaturated. Consequently, the duration of Stage 3 is highly dependent on the hydrogeological characteristics of the host site and the nature of the EDZ. Of significance to the UFC life expectancy is the potential for aqueous corrosion to occur during Stage 3 as a result of increasingly humid conditions (particularly at $> 75\%$ RH), subsequent absorption of moisture by deliquescent salt deposits previously formed during the desiccation of the bentonite in immediate contact with the UFC (Stage 2), and the presence of oxidants either from residual oxygen and/or radiolysis.

Stage 4 is the final stage and represents a state in which the near-field is fully saturated with anoxic bentonite pore water. However, the early part of Stage 4 denotes a gradual

cool down of the near-field to ambient, long-term repository temperatures, along with a gradual change of the pore water chemistry from partially to fully anoxic, depending on the levels of radiolytic oxidant production at this stage. Of significance to the UFC life expectancy is the potential for aqueous corrosion to occur indefinitely in Stage 4. The four stages are summarised pictorially in Figure 3.2.

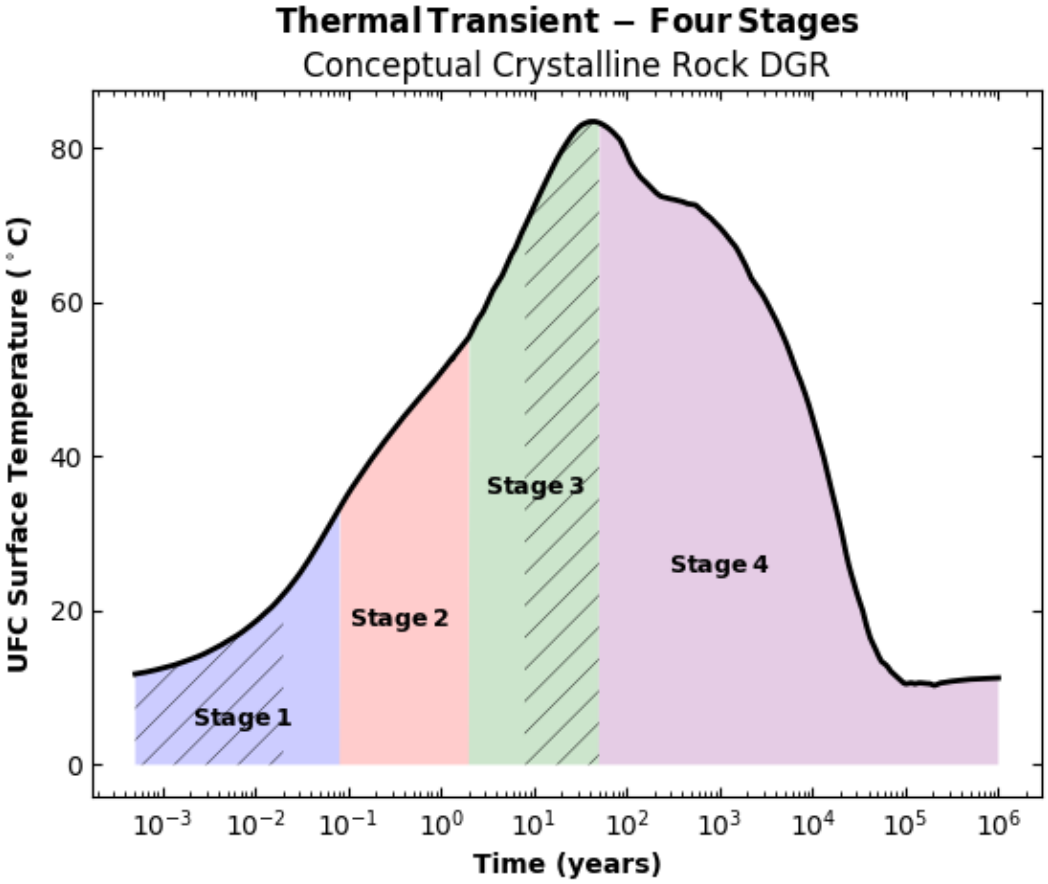

Figure 3.2: Four stages predicted during the thermal transient in a conceptual crystalline rock DGR. Temperature profile represents repository Panel E after Guo (2017), and the stage durations after King et al. (2017). Hatched regions represent periods during which RH is predicted to be greater than 75%.

3.2 Degradation Mechanisms of Concern

For the purposes of this work, two degradation mechanisms are of concern. The first and primary is sulphide-induced corrosion, which is predicted to be operative during Stage 4. The second is localised or pitting corrosion, which is considered plausible but unlikely during the oxic period characterising Stage 1 and to a much lesser extent Stage 2. Other copper-related degradation mechanisms are discussed in Hall et al. (2021) but are not modelled herein because they are not presently considered of significant impact to UFC life expectancy.

Sulphide-induced Corrosion—Anoxic Period

The onset of Stage 4 is defined by the realisation of 100% saturation of the near-field under fully anoxic conditions. Used fuel container surface temperatures are expected to be slightly below peak temperatures (e.g., $< 90°C$) at the start of Stage 4, and with time near-field pore-water chemistries will normalise towards an equilibrium with groundwater chemistries and be pH neutral. It is also anticipated that with diminishing gamma fields, the near-field environment will become predominantly reducing. Consequently, under these conditions the UFC copper surfaces will be thermodynamically stable but only in the absence of HS^- (Bojinov et al., 2004; Bojinov and Makela, 2003; Smith, 2007). The introduction of sulphide anions (HS^-) will de-stabilise and anodically dissolve copper via a two-step process (pg 133 Smith, 2007) that leads to the growth of a cuprous sulphide (Cu_2S) film (Smith et al., 2007):

$$Cu + HS^- \rightleftharpoons Cu(HS)_{ads} + e^-, \tag{3.1}$$

$$Cu(HS)_{ads} + Cu + HS^- \rightleftharpoons Cu_2S + e^-. \tag{3.2}$$

For a Canadian DGR, the dominant source[1] of aqueous sulphides is from microbial activity occurring at the host rock/buffer interface due to SRB (King et al., 2017). However, sulphide concentrations arising from SRB activity are predicted to be quite low ($< 10^{-4}$ M). For such low concentrations, it is argued that the interfacial anodic reaction (i.e., at the copper/bentonite interface) will be governed by HS^- mass transport (King et al., 2017). This is a slow diffusion process controlled by the diffusivity of HS^- in saturated bentonite.

[1]While there are other potential reactions that lead to the release of hydrogen sulphide ions, such as chemical dissolution of sulphide-containing minerals (e.g., pyrite) from the bentonite buffer, hydrogen sulphide produced from anaerobic microbial activity in the near- and far-field is expected to be the dominant source for corrosion of the copper coating.

Consequently, sulphide-induced corrosion is modelled as a mass-balance, mass-transport phenomenon.

Localised (Pitting) Corrosion—Oxic Period

Lasting anywhere from 6 months to 1.5 years (Fig 2(d) King et al., 2017), the oxic period may result in localised corrosion of the UFC surface due to the reaction of copper with some of the trapped oxygen in an emplacement room. Oxygen (along with chloride) concentration determines the corrosion potential (an electrochemical measure of the tendency for corrosion to occur). When the corrosion potential is greater than the oxide-film breakdown potential, pit initiation occurs. Subsequent pit growth happens while the corrosion potential is greater than the repassivation potential, the potential at which a passive oxide film is formed and pit growth is arrested. Together, these make up the underlying criteria for localised corrosion. In this work, the theoretical formulation for the electrochemical processes governing pit initiation, growth, and arrest are ignored. Instead, the occurrence of extreme pit depths during the oxic period is approximated phenomenologically by a non-homogeneous Poisson process, specifically a counting process, with pit depth evolution modelled as a non-homogenenous Markov process. Both to be discussed in Chapter 5.

3.3 Sulphide-induced Corrosion Formulation

Equation 3.3 describes the overall sulphide-induced copper corrosion reaction:

$$2\,\mathrm{Cu} + \mathrm{H_2O} + \mathrm{HS^-} \rightleftharpoons \mathrm{Cu_2S} + \mathrm{H_2} + \mathrm{OH^-}. \tag{3.3}$$

Under a mass-transport-limited corrosion process, corrosion depth per unit time d_{Corr}, which is equivalent to corrosion rate, may be calculated simplistically using the mass-balance approach adopted by SKB (SKB, 2010a):

$$d_{\mathrm{Corr}} := \frac{N_{\mathrm{HS}} f_{\mathrm{HS}} M_{\mathrm{Cu}}}{A_{\mathrm{Corr}} \rho_{\mathrm{Cu}}}, \tag{3.4}$$

where N_{HS} is the amount of sulphide reacting at the copper surface, which is directly related to the flux of $\mathrm{HS^-}$ at a specified area of the UFC per unit time; f_{HS} is the stoichiometric coefficient for the reaction shown in Equation 3.3, which is 2, for 2 moles of copper react with 1 mole of $\mathrm{HS^-}$; M_{Cu} is the molar mass of copper; A_{Corr} is the specified area on the

surface of the UFC where corrosion takes place; and ρ_{Cu} is the density of copper. For N_{HS} Fick's First Law of diffusion is employed (excludes any reaction/sink terms) to conveniently describe the diffusion of HS^-, denoted J_{HS}, through the groundwater-saturated bentonite barriers under steady-state conditions:

$$J_{HS} = -D_{HS}\nabla C. \tag{3.5}$$

The diffusion of HS^- to a discrete point on the surface of the UFC is inherently a 3-D problem, where the concentration gradient, ∇C, is a function both of diffusion distance, defined as a 3-D path $(\Delta l_x, \Delta l_y, \Delta l_z)$, and initial and final HS^- concentrations (C_0,C) present on a boundary characterised by irregularly shaped surfaces (e.g., corner of buffer box). As written, Equation 3.5 implies the HS^- effective diffusion coefficient (D_{HS})—associated with mass transport through the bentonite clay barriers—is isotropic and constant throughout the volume of material. Invoking the assumption that D_{HS} is isotropic and constant throughout, the amount of HS^-, N_{HS}, reacting at a specified area, A_{Corr}, on the surface of copper-coated UFC can be determined as per Equation 3.6:

$$N_{HS} = -D_{HS}\nabla C A_{Corr}. \tag{3.6}$$

Due to the 3-D geometry of both the emplacement room and the rectangular buffer boxes encapsulating the UFCs, a numerical approach is typically required to solve the HS^- diffusion problem represented by Equation 3.6, . Such calculations were performed recently by Briggs et al. (2017) and hereafter referred to as the Briggs model. Within the Briggs model, which is built on COMSOL Multiphysics®, the sulphide diffusion problem is handled under two scenarios: (1) a constant external boundary sulphide concentration for a single UFC within a buffer box, and (2) a constant external boundary sulphide concentration for a representative set of UFCs within an emplacement room. Their results for a single UFC within a buffer box, Figure 3.3, showed that sulphide flux is greatest at the hemispherical ends of the UFC and lowest in areas on the cylindrical portion of the UFC located directly opposite the corners of the buffer box. These results underscore the need to assess the mass-transport problem from a 3-D perspective, or at minimum incorporate the 3-D effects into 1-D analyses.

To facilitate the use of Equations 3.4 through 3.6, the following assumptions are formally employed: the sulphide-induced copper corrosion process is mass-transport-limited, D_{HS} is isotropic and constant throughout, and a steady-state diffusion condition exits from start of analysis. The latter is a conservative assumption within the Briggs model. For simplicity, the present model treats the base level defining the lifetimes of UFCs in a hypothetical DGR as a HS^- diffusion problem for a single UFC placed inside a buffer box,

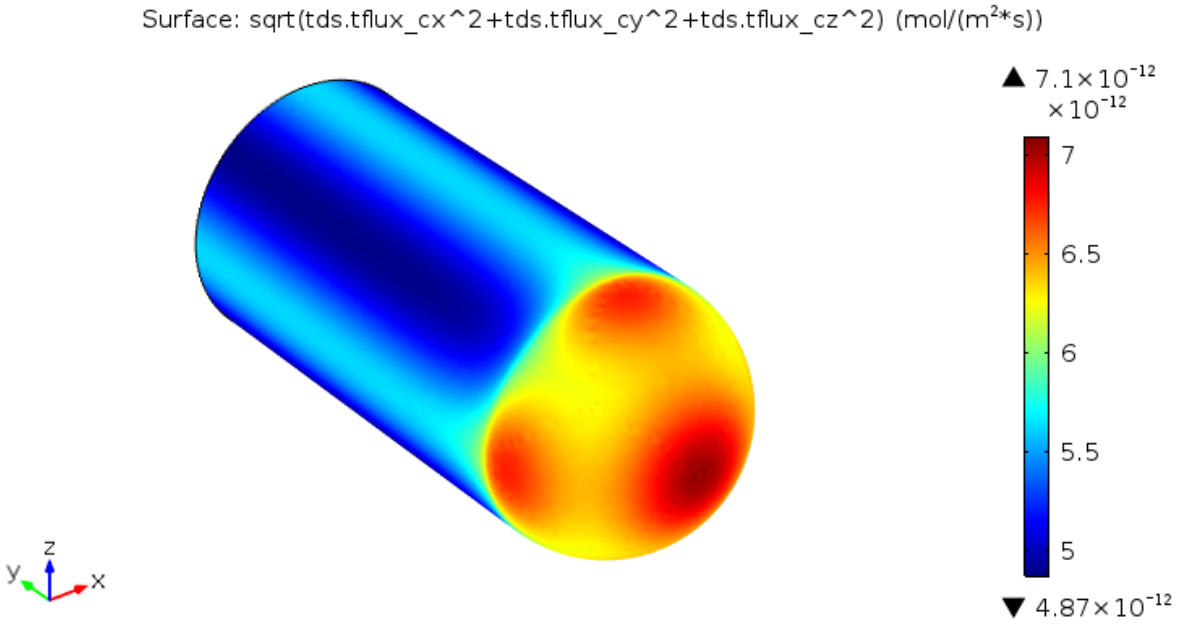

Figure 3.3: Flux distribution shown for one half of a UFC, $C_0 = 9.07 \times 10^{-5}$ M (3 ppm), Briggs et al. (2017), with permission.

with the external surfaces of the buffer box defining the initial HS^- concentration boundary. Essentially, the additional diffusion path afforded by the bentonite pellet backfill is ignored in this model, and all HS^- produced at the rock/backfill interface is conservatively assumed to be transferred to the external surfaces of the buffer box. Further, saturation is assumed to occur uniformly within an emplacement room such that, over time as steady state is approached, the HS^- concentration normalises to a constant value throughout the emplacement room. This assumption implies that $[HS^-]$ is time-invariant once steady state is reached—an assumption that may not necessarily be conservative. These assumptions are summarised below:

- Saturation of the emplacement rooms (and buffer boxes) by the in-flow of groundwater occurs homogenously.
- At saturation, the $[HS^-]$ at the gap-fill/rock interface normalizes to a constant value throughout the entire emplacement room.
- The boundary for the diffusion problem is transferred from the walls of the emplace-

ment room (i.e., gap-fill/rock interface) to the external surface of each buffer box, effectively eliminating the gap-fill diffusion path.

- The boundary condition at the buffer box external surface is defined by a constant [HS^-], which is time-invariant once the emplacement room reaches 100% saturation.
- The effective diffusion coefficient for the bentonite buffer is isotropic and constant throughout a buffer box.
- Steady state condition exists at the start of analysis (i.e., time for [HS^-] to normalize at the gap-fill/rock interface and time for establishment of steady state diffusion is ignored).
- The sulphide-induced copper corrosion process is mass-transport-limited.

3.4 Discretisation of UFC Surface

The approach adopted is to transform an inherently 3-D sulphide diffusion problem for the corrosion of the copper-coated UFCs into one that is 1-D in formulation, analytical (i.e., closed form), amenable to Monte Carlo methods, and relatively true to the conditions of the original problem.

3.4.1 Effective Diffusion Length

To achieve the above objectives under assumed steady-state conditions, Equation 3.5 is re-written in one-dimensional form and re-arranged, as shown in Equation 3.7, by introducing the term "effective" diffusion length, l_{eff}. The formulation in Equation 3.7 assumes the concentration gradient across the buffer box is linear, and that conservatively all HS^- arriving at the UFC surface is immediately used up to form the cuprous sulphide film (i.e., $C = 0$). For very dilute concentrations of HS^-, where interfacial reaction rates are higher than HS^- mass transport rates, this assumption is reasonable.

$$l_{\text{eff}} = -D_{\text{HS}} \frac{C - C_0}{J_{\text{HS}}}. \tag{3.7}$$

The effective diffusion length represents the equivalent diffusive path taken by all HS^- reaching an arbitrary, small area on the surface of the UFC from a specified external boundary of known constant HS^- concentration, C_0. This is somewhat analogous to an

equivalent point load derived from a uniformly distributed load or from hydrostatic pressure acting over a small area. The results of the Briggs model revealed that, for a constant C_0, points on the UFC directly opposite the corner regions of the buffer box exhibited the lowest fluxes. Intuitively, this is reasonable given that corners of the buffer box are further away from the opposite surfaces of the UFC than other locations on the buffer box. But a straight one-to-one correlation does not exist between flux and diffusion path as indicated by Equation 3.7. Simply transforming the 3-D problem into one dimension by equating the diffusion path taken as the absolute distance separating a point on the corner of the buffer box from a directly opposite point on the cylindrical surface of the UFC, for example, does not correspond with the flux determined by the 3-D numerical diffusion calculations performed in the Briggs model. The reason for this is the contribution from adjacent regions in the corner of the buffer box, which gives rise to a 3-D flux profile. The effective diffusion length, therefore, is a convenient means of transforming the 3-D problem into one that is 1-D, provided the surface of a UFC is divided into reasonably small contiguous areas and a means exists to estimate l_{eff}. While the computation of l_{eff} is based on the results of a numerical model (i.e., Briggs model) where the boundary condition defined at the outer surface of the buffer box (and by implication at the host rock) assigns a constant HS^- concentration, this does not pose a limitation to the proposed model framework. The effective diffusion length is dependent on geometry (i.e., buffer box and UFC) and not on boundary conditions associated with chemical species concentration. Consequently, a heterogeneous [HS^-] may be assigned to the buffer box boundary by simply defining C_0 as a function of node position. This then is a flexibility and not a limitation.

3.4.2 UFC Surface Mesh Models

To support computation of l_{eff}, a UFC surface was discretised using COMSOL Multiphysics® into a series of seven meshes consisting of triangular elements. Discretisation was carried out by Dr Briggs at the NWMO and subsequently supplied to this author in support of the modelling framework. Average characteristic lengths[2] for the triangular elements were chosen as 0.02 m, 0.03 m, 0.04 m, 0.06 m, 0.08 m, 0.10 m, and 0.12 m to assess mesh-size sensitivity and identify a computationally optimal mesh size without significantly compromising agreement with the Briggs model. Figure 3.4 and Figure 3.5 illustrate the smallest and largest of these. Owing to the symmetry of the UFC geometry, and because the work in the Briggs model showed that maximum fluxes occur at the hemispherical ends, the model developed hereafter considers only one quarter of one hemisphere.

[2]Characteristic length of a triangular mesh element in COMSOL Multiphysics® refers to the longest edge length.

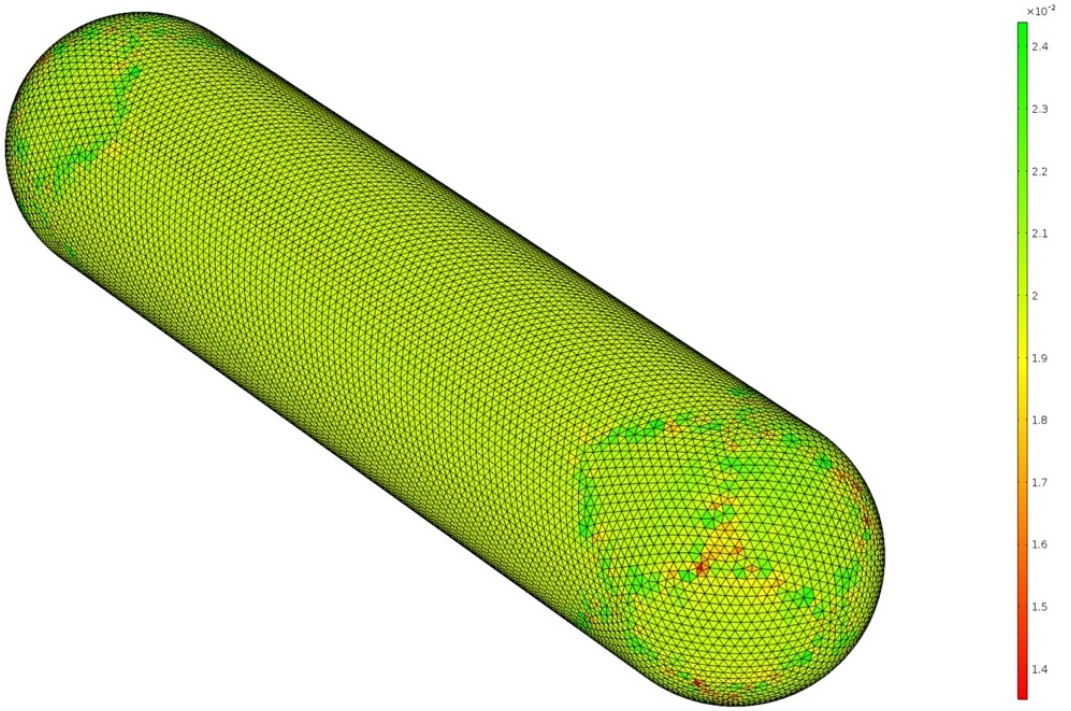

Figure 3.4: Discretisation of UFC surface shown with triangular elements and an average characteristic length of 0.02 m. The colour scale represents the element size.

For each mesh model, flux values (J_{HS}) obtained from the numerical results of the Briggs model were assigned to each node of the triangular elements. Assignment of flux values was achieved by recognising that each node of the triangular-element mesh represents a coordinate point in 3-D space, or equivalently a vector. Consequently, the mesh design employed by the Briggs model was vectorised such that all nodes were assigned corresponding vector and flux values. The vectorised results from the Briggs model were subsequently compared with the vector representation of each mesh model and closest matching vectors were assigned a corresponding flux value from the Briggs model. Once flux values were assigned to each node in each mesh model, Equation 3.7 was used to calculate l_{eff} for each node by using the values for C_0 and D_{HS} employed in the Briggs model. Histograms of l_{eff} for the 0.02 m and 0.12 m mesh models, along with the Briggs model, are shown in Figure 3.6, Figure 3.7, and Figure 3.8, respectively.

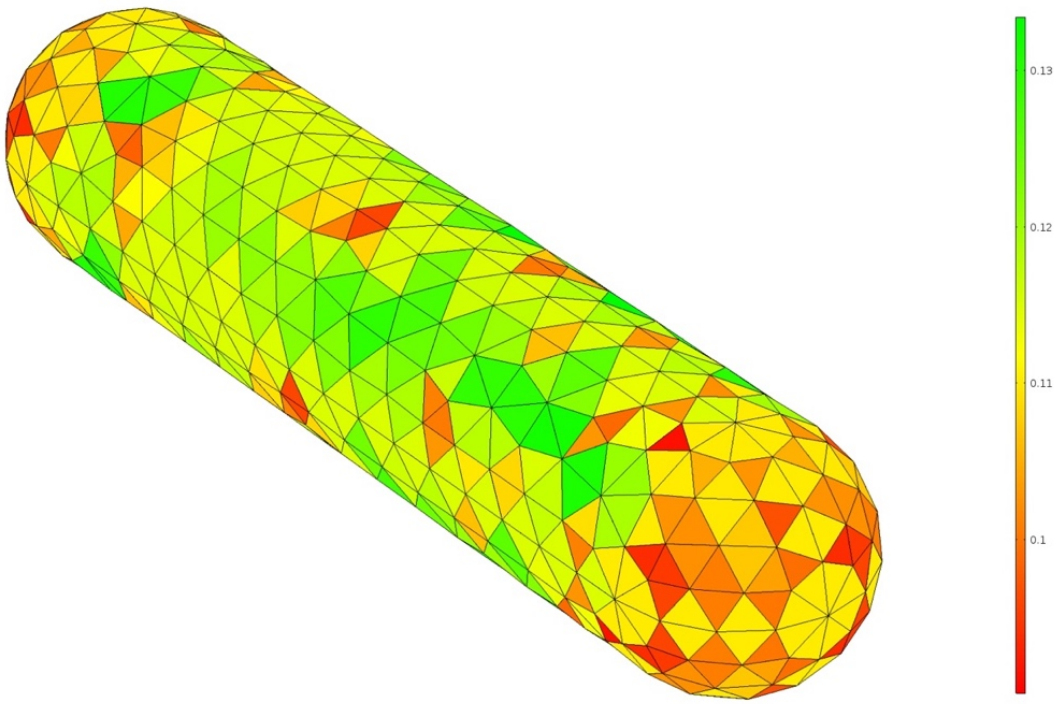

Figure 3.5: Discretisation of UFC surface shown with triangular elements and an average characteristic length of 0.12 m. The colour scale represents the element size.

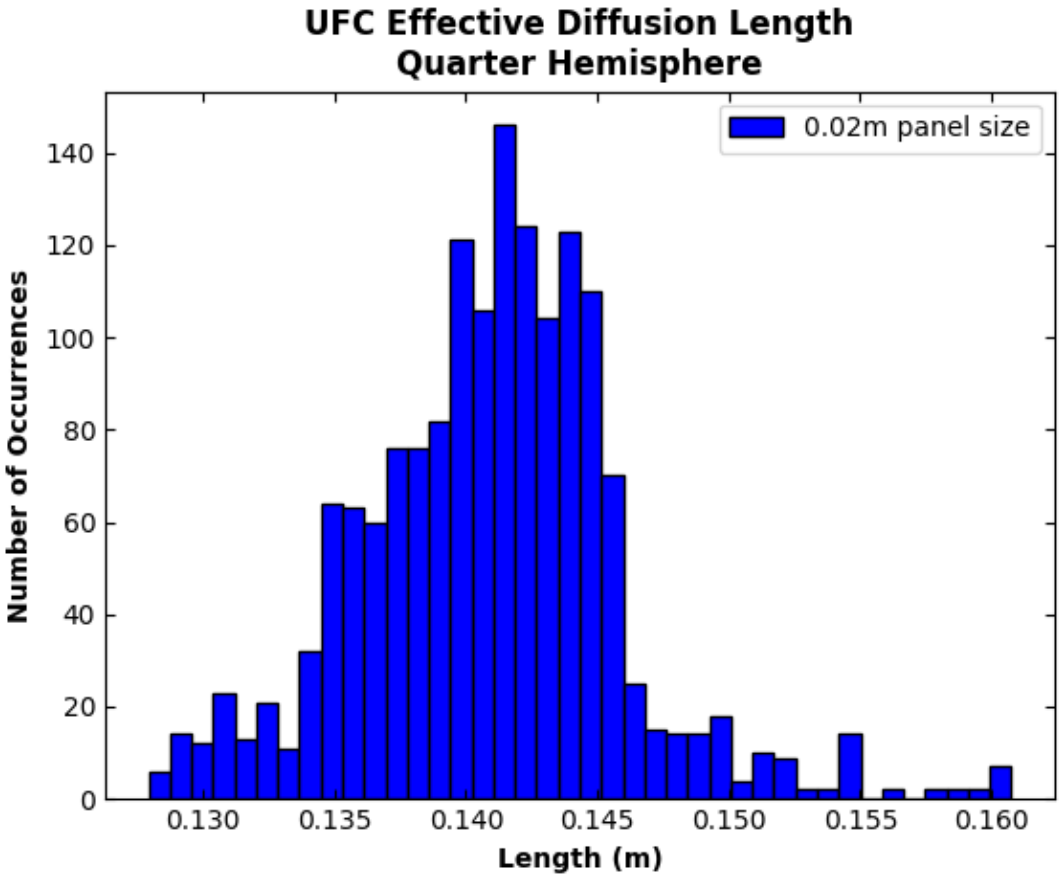

Figure 3.6: Histogram of effective diffusion lengths for the 0.02 m UFC mesh model.

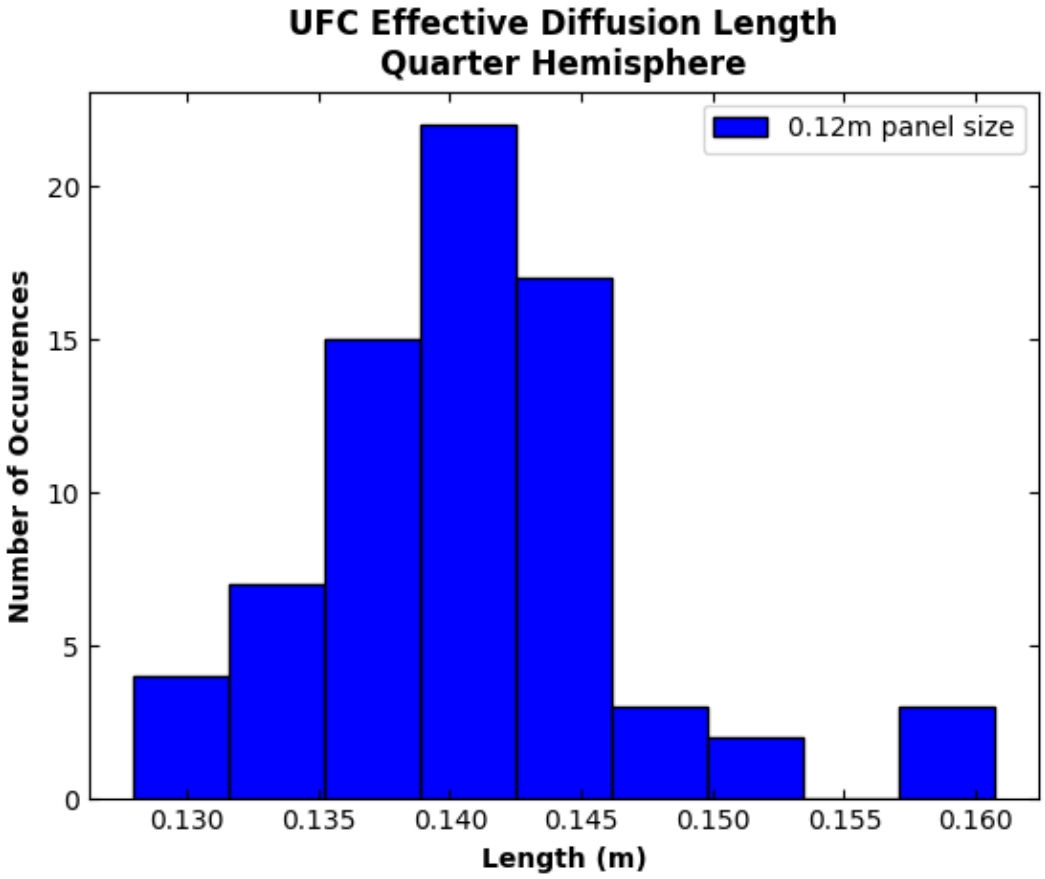

Figure 3.7: Histogram of effective diffusion lengths for the 0.12 m UFC mesh model.

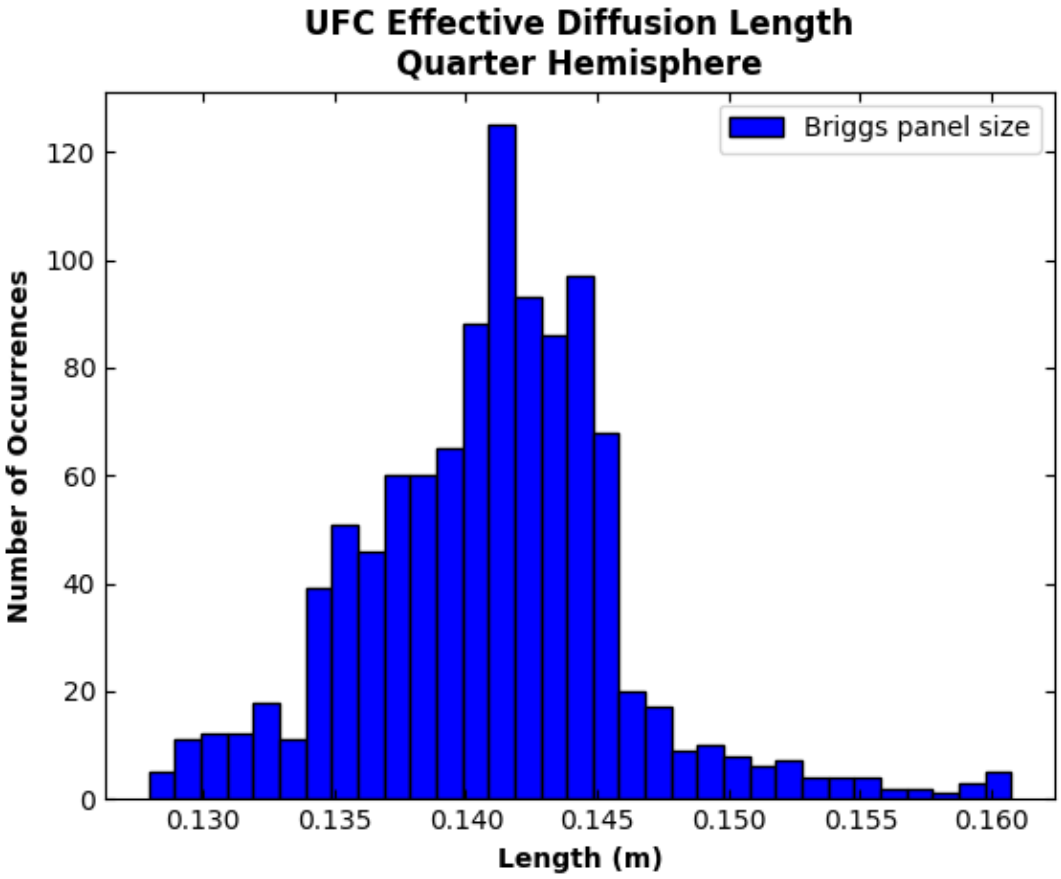

Figure 3.8: Histogram of effective diffusion lengths for the Briggs model.

For comparison, the Empirical Cumulative Distribution Function (ECDF)s associated with the flux values derived from the above discretisation scheme are compared with the Briggs model (Figure 3.9 through Figure 3.11). These results indicate that the 0.02 m mesh model is a very good approximation of the Briggs model, but the coarser discretisation models are not significantly different. The triangular elements are also referred to as "panels", a term which will be used later in this thesis.

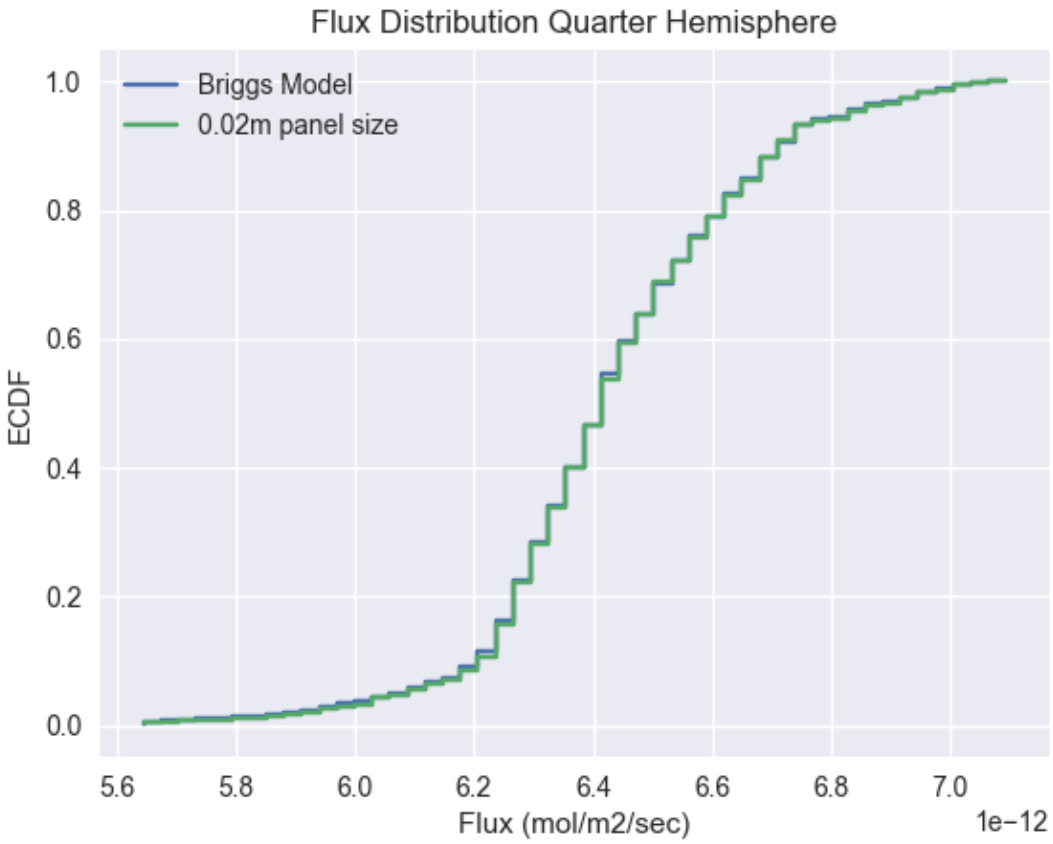

Figure 3.9: Comparison of ECDF flux values for the 0.02 m mesh model and the Briggs model (Briggs et al., 2017).

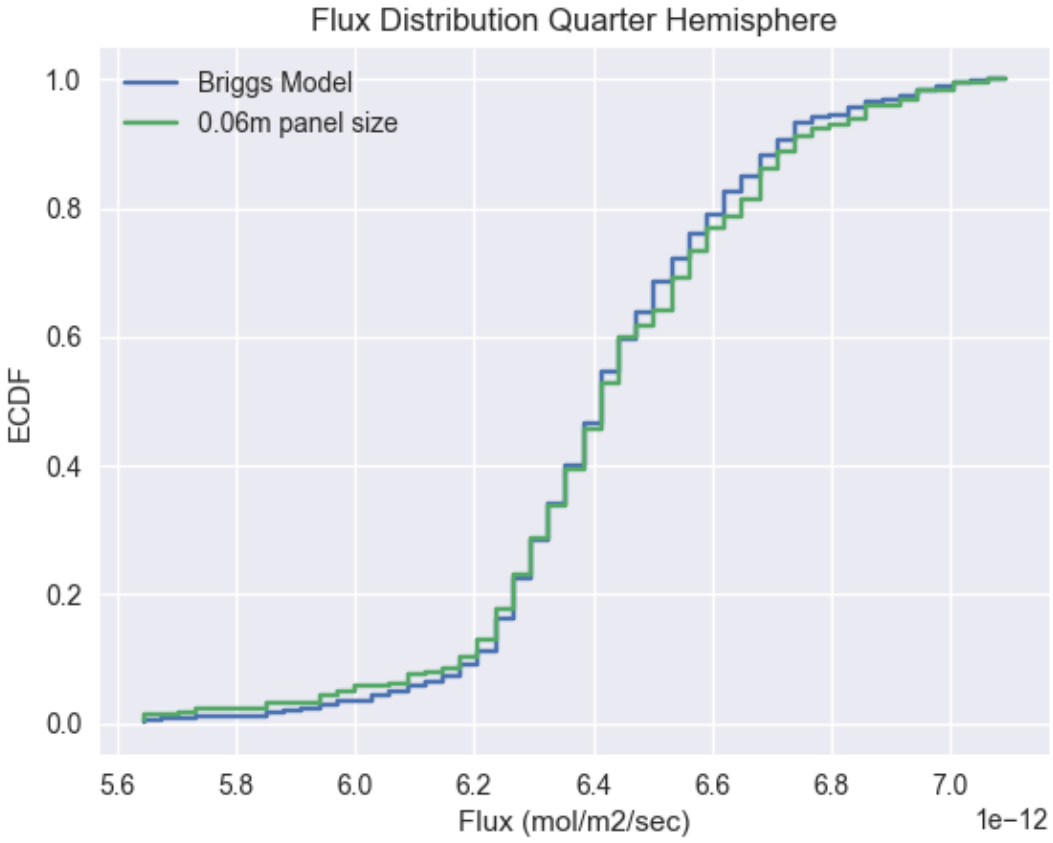

Figure 3.10: Comparison of ECDF flux values for the 0.06 m mesh model and the Briggs model (Briggs et al., 2017).

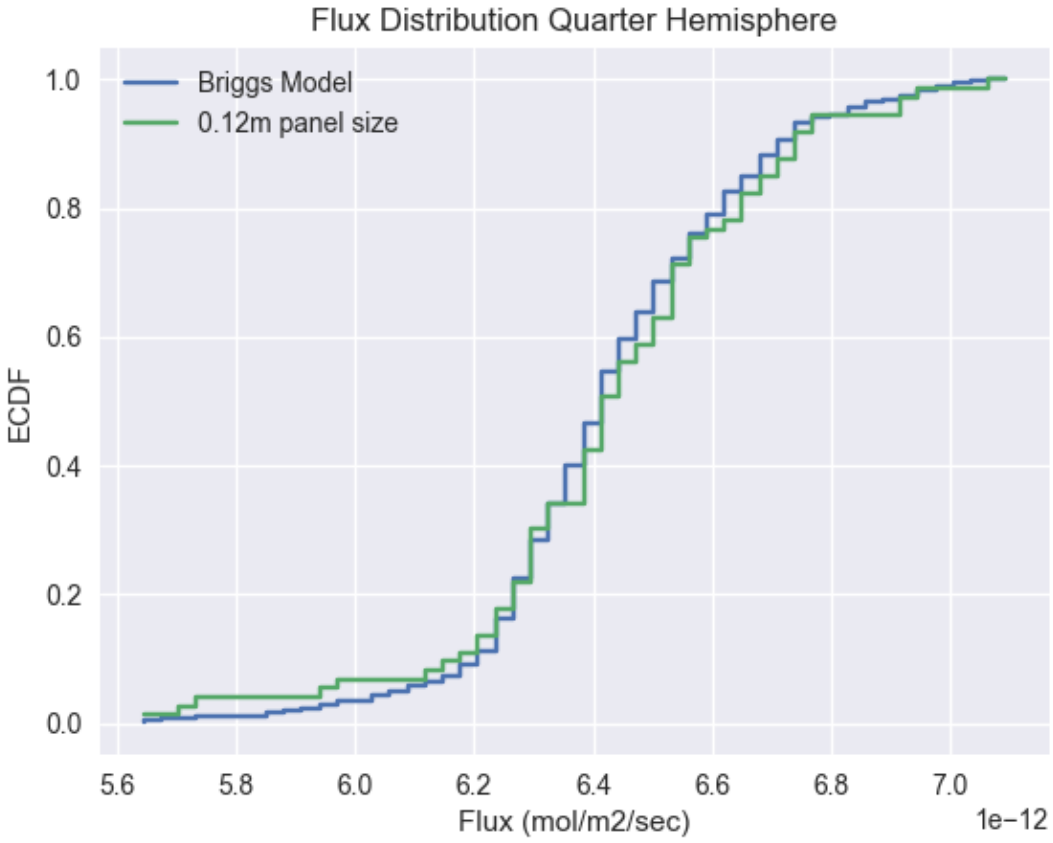

Figure 3.11: Comparison of ECDF flux values for the 0.12 m mesh model and the Briggs model (Briggs et al., 2017).

3.5 Probabilistic Framework

3.5.1 Time-to-Failure Formulation

Based on the above, the amount of HS^- arriving at the ith node of the discretised UFC model per unit time, designated as N^i_{HS}, is

$$N^i_{\text{HS}} \coloneqq \frac{D_{\text{HS}} C_0}{l^i_{\text{eff}}} A^i_{\text{Corr}}, \tag{3.8}$$

where A^i_{Corr} and l^i_{eff} represent the unit area and the effective diffusion length assigned to the ith node, respectively. Moreover, from Equation 3.4 corrosion depth per unit time for the ith node d^i_{Corr}, which is equivalent to corrosion rate, is

$$d^i_{\text{Corr}} \coloneqq \frac{N^i_{\text{HS}} f_{\text{HS}} M_{\text{Cu}}}{A^i_{\text{Corr}} \rho_{\text{Cu}}}. \tag{3.9}$$

Substituting Equation 3.8 into Equation 3.9 leads to a final expression for the corrosion rate of the ith node

$$d^i_{\text{Corr}} \coloneqq \frac{D_{\text{HS}} C_0 f_{\text{HS}} M_{\text{Cu}}}{l^i_{\text{eff}} \rho_{\text{Cu}}}. \tag{3.10}$$

It follows that the time TTF^i_{Corr} to fully penetrate, or breach the full thickness, of the copper coating at the ith node, as a result of sulphide-induced corrosion, can be calculated by dividing the node-specific copper coating thickness t^i_{Cu} by the node-specific corrosion rate d^i_{Corr}:

$$TTF^i_{\text{Corr}} \coloneqq \frac{t^i_{\text{Cu}} l^i_{\text{eff}} \rho_{\text{Cu}}}{D_{\text{HS}} C_0 f_{\text{HS}} M_{\text{Cu}}}. \tag{3.11}$$

Simply put, TTF^i_{Corr} represents the ith node time-to-failure. The objective of the baseline UFC model is to characterise the distribution of TTF^i_{Corr}, specifically the distribution of the minimum of TTF^i_{Corr}. This is equivalent to characterising the distribution of UFCs first times to failure.

3.5.2 Multi-level Model Formulation

Inspection of Equation 3.11 informs the reader that in an arbitrary emplacement room, across the surface of a given UFC, node times to failure are directly proportional to the products comprising copper coating thickness t^i_{Cu}, effective diffusion length l^i_{eff}, and a constant defined as $\rho_{\text{Cu}}/D_{\text{HS}} C_0 f_{\text{HS}} M_{\text{Cu}}$. That the expression $\rho_{\text{Cu}}/D_{\text{HS}} C_0 f_{\text{HS}} M_{\text{Cu}}$ represents a

fixed value for a randomly selected UFC, located inside an arbitrary emplacement room, stems from the assumptions employed in Section 3.3, and is exploited subsequently to structure a model with multiple levels representative of the proposed DGR configuration in crystalline rock.

To bring the multi-level framework into sharper focus, consider that for a conceptual crystalline rock DGR, there are presently 375 buffer boxes assigned per emplacement room (Noronha, 2016). Based on the assumption that the effective HS^- diffusion coefficient D_{HS} varies from buffer box to buffer box, one can define the jth effective diffusion coefficient D^j_{HS} ($j = 1, 2, \ldots, 375$) to represent the effective HS^- diffusion coefficient assigned to the buffer box surrounding the jth UFC under evaluation. Similarly, by invoking the assumption that $[HS^-]$ normalises with time as steady state diffusion is approached, the argument is made that at steady state $[HS^-]$ is constant for any given emplacement room—but different from room to room. This is one interpretation of homogeneous (uniform) saturation. Additionally, for a conceptual crystalline rock DGR, there are presently 36 emplacement rooms assigned per repository panel (Noronha, 2016). As a result, one can speak of the kth ($k = 1, 2, \ldots, 36$) emplacement room in a repository panel where $[HS^-]$ has attained a steady state, constant value designated by the symbol C^k_0. Lastly, out of convenience the quotient $\rho_{Cu}/(f_{HS}M_{Cu})$ is replaced by a single symbol K to inform the reader that it is a constant. Within this framework, Equation 3.11 can be re-written more succinctly as

$$TTF^i_{Corr} \coloneqq \frac{t^i_{Cu} l^i_{eff}}{D^j_{HS} C^k_0} K. \tag{3.12}$$

Equation 3.12 provides a means to estimate the time to failure of the ith node of the jth UFC, in the kth emplacement room, in an arbitrarily selected repository panel. This framework could be extended to support differentiation of the lth repository panel, but presently there are only two types of panels (four of each type, eight total), suggesting limited value in further extending the multi-level framework (though this decision could easily be revisited). Consequently, for the proposed framework expressed by Equation 3.12, three levels are in view, Table 3.1.

Level 1—UFC/Buffer Box

Equation 3.12 shows that at Level 1 t^i_{Cu} and l^i_{eff} are the only model parameters subject to variation. While l^i_{eff} varies across the UFC surface from node to node, it is not a random variable: it is predetermined by the UFC and buffer box geometries, which—for the purpose of this model—remain (sufficiently) constant throughout the repository timescales of interest. In contrast, t^i_{Cu} is considered to vary randomly across the surface of a UFC. On

Table 3.1: Multi-level framework for the UFC lifetime model

Level	Description	Index
1	UFC Node	i
2	UFC/Buffer Box	j
3	Emplacement Room	k

this basis, one can define $\mathbf{X}_{t_{\text{Cu}}}$ as the set of all independent and identically distributed (iid) random variables (RVs) $X^i_{t_{\text{Cu}}}$ $\forall i; i = 1, 2, \ldots, n$, where $X^i_{t_{\text{Cu}}}$ represents the copper coating thickness assigned to the ith node from the baseline distribution characterising the expected thickness tolerance in the coppper coating manufacturing process. For convenience, the symbol t^i_{Cu} was used earlier to facilitate development of Equation 3.12. Now, it is clearer if differentiation is made between the baseline distribution for t_{Cu}—associated with the manufacturing process—and the RV $X^i_{t_{\text{Cu}}}$, which takes on a value from the baseline t_{Cu} distribution. Also, this differentiation emphasises that each UFC will possess a collection $\mathbf{X}_{t_{\text{Cu}}}$ of RVs $X^i_{t_{\text{Cu}}}$, such that

$$\mathbf{X}_{t_{\text{Cu}}} \coloneqq \left\{ X^i_{t_{\text{Cu}}} \right\} \quad \forall i; i = 1, 2, \ldots, n,$$

with n equal to the number of nodes (equivalently the number of panels) associated with a particular mesh size. Continuing with Equation 3.12, a new iid RV $\mathbf{x}$ may be defined as the set of all n elements that represent the product $X^i_{t_{\text{Cu}}} \times l^i_{\text{eff}}$:

$$\mathbf{x} \coloneqq \left\{ x^i : x^i = X^i_{t_{\text{Cu}}} l^i_{\text{eff}} \right\} \quad \forall i; i = 1, 2, \ldots, n.$$

The RV x^i represents the product of the node-specific copper coating thickness and the node-specific effective diffusion length. From a time-to-failure perspective, the interest lies in finding the inputs to Equation 3.12 for which TTF^i_{Corr} attains its minimum over the set of all candidate $X^i_{t_{\text{Cu}}}$ and l^i_{eff} (i.e., $argmin_{X^i_{t_{\text{Cu}}}, l^i_{\text{eff}}} \{TTF^i_{\text{Corr}}\}$), for a given UFC, in an arbitrary emplacement room. Consequently, define for Level 1 the RV X_1 to represent the minimum of the set of all x^i for an arbitrary UFC; that is,

$$X_1 \coloneqq min(\mathbf{x}) = min \left\{ X^i_{t_{\text{Cu}}} l^i_{\text{eff}} \right\} \quad \forall i; i = 1, 2, \ldots, n. \tag{3.13}$$

Strictly speaking, the RV X_1 should contain the superscript j to demonstrate that it is assigned to the jth UFC. For reasons to be discussed below, however, the superscript is not included in the formulation. Also, the unit of X_1 is m^2 (i.e., area), but area has no immediate significance.

Across an emplacement room X_1 will vary randomly. While X_1 is certainly a model construct, defined to transfer knowledge of Level 1—in the form of a pertinent RV—to the remaining levels of the modelling framework, it also offers some insight into the factors that contribute to TTF^i_{Corr}. For example, X_1 may be viewed as a variable that points to where failure on the surface of an arbitrary UFC will occur first, or where x^i is at a minimum across a quarter of a hemispherical end-cap. While not immediately useful in this work, interest in future modelling may lie in locating the point of first release (i.e., leak) of radioactive species from a UFC.

Currently, the UFC copper coating processes are electrochemical deposition for the entire surface and cold spray technology only at the closure welds. A thickness equal to 3.0 mm + 1.0/0.0 mm is specified for the UFCs. For modelling purposes, the baseline distribution for t_{Cu}—associated with the preceding manufacturing processes—is assumed arbitrarily to be adequately described by a Lognormal[3] function, truncated at the minimum and maximum values given in Table 3.2. Practically speaking, this is equivalent to stating that each node on an arbitrary UFC takes on a value from this distribution. Alternatively, this means that $X^i_{t_{\text{Cu}}}$ is ∼Lognormal, and that for every UFC there exists a collection $\mathbf{X}_{t_{\text{Cu}}}$ representing the set of n RVs sampled from the Lognormal Probability Density Function (PDF) shown in Figure 3.12.

Table 3.2: Assumed values for the UFC copper coating thickness

Description	Value (m)
Geometric Mean	3.55×10^{-3}
Minimum	3.00×10^{-3}
Maximum	4.00×10^{-3}
90th Percentile	3.80×10^{-3}

The computation of X_1 requires the vector or array associated with the set of l^i_{eff}, whose values (along with the magnitude of n) are mesh size dependent. In this work, the optimal mesh size was determined by examining the mean, minimum, and maximum value of 1000 X_1 random samples drawn for each mesh size (i.e., 0.02 m, 0.03 m, 0.04 m, 0.06 m, 0.08 m,

[3]In the early days of formulating the UFC lifetime model, the expected variation in the as-manufactured copper coating thickness was better explained by the Lognormal function versus, say, the Normal distribution. As time progressed, the expected copper coating thickness variation changed, suggesting that the Normal distribution would adequately express this variation. However, since all the code had been developed with the Lognormal distribution in mind, the decision was made to stay with the Lognormal.

0.10 m, and 0.12 m). The results showed that a reasonable compromise between accuracy (i.e., statistics similar to those of the smaller mesh sizes) and computational efficiency (i.e., lowest number of nodes reasonably possible) was achieved for a 0.06-m mesh size. Consequently, a mesh size of 0.06 m, resulting in $n = 255$, was adopted for all ensuing simulations.

To examine the variation in X_1, one could restrict attention to a single emplacement room, but this would yield a sample of size 375 (for 375 UFCs per emplacement room), which arguably could be subject to sampling distribution variability arising from differences in $\mathbf{X}_{t_{\mathrm{Cu}}}$ from UFC to UFC. Alternatively, across a single panel in the proposed crystalline rock DGR there are $36 \times 375 = 13000$ planned UFCs, which represents a more statistically valid sample size. Note, one can extend this to include the eight panels planned for the DGR in crystalline rock (Noronha, 2016), resulting in a total of $8 \times 36 \times 375 = 108000$ UFCs. While this number offers very robust sampling distribution statistics (i.e., sampling distribution of $min(\mathbf{x})$), it is considered unnecessarily excessive for the purposes of this work. To reduce the computational burden while securing a reasonable level of statistical robustness in the proposed modelling framework, a repository "panel" was chosen as the representative statistical unit for this model, with a chosen sample size of 10000 UFCs (instead of 13000) to streamline calculations and maintain a level of independence[4] from realised UFC emplacement numbers. Consequently, a sample size of 10000 UFCs was chosen to assess the distribution of X_1.

In practical terms, n random samples were drawn using a 1-D Latin Hypercube Sampling (LHS) scheme[5] (discussed later in this chapter) from the distribution shown in Figure 3.12. Each draw represented the RV $X^i_{t_{\mathrm{Cu}}}$, which was assigned to one of the n nodes on the discretised surface of an arbitrary UFC—1 of 10000 arbitrary UFCs. The resultant collection $\mathbf{X}_{t_{\mathrm{Cu}}}$, consisting of n RVs $X^i_{t_{\mathrm{Cu}}}$, was multiplied element-wise by the (constant) vector comprising n unique elements $l^i_{\mathrm{eff}}, \forall i$. The element-wise product constituted the set $\mathbf{x}$. Moreover, the minimum of $\mathbf{x}$, Equation 3.13, represented a single realisation from the postulated X_1 distribution (conversely, the distribution of X_1 represents the sampling distribution of $min(\mathbf{x})$). Repeating this for another 9999 realisations and combining the results offered an estimate of the X_1 distribution, which is depicted in Figure 3.13. Algorithm 1 provides a basic summary of the process, with $\mathbf{X}_1 := \{X_1\}$. Gains in computation

[4]By independence it is meant that the achieved UFC emplacement numbers will vary due to geological factors encountered during exacavation of the emplacement rooms. Consequently, the number 10000 is independent of geological factors constraining the number of UFCs and is as equally valid as 13000.

[5]Sampling of the Lognormal distribution shown in Figure 3.12 did not necessitate a 1-D LHS scheme. But because it was necessary to do so for subsequent sampling within the proposed multi-level modelling framework, a decision was made early on in the writing of the computer code to standardise to a LHS sampling scheme, making slight modifications as required from 1-D to two-dimensional (2-D).

efficiency were achieved by transforming the "for-loop" structure into matrix operations and by parallel processing. All scripts were written in Python 3.6.9.

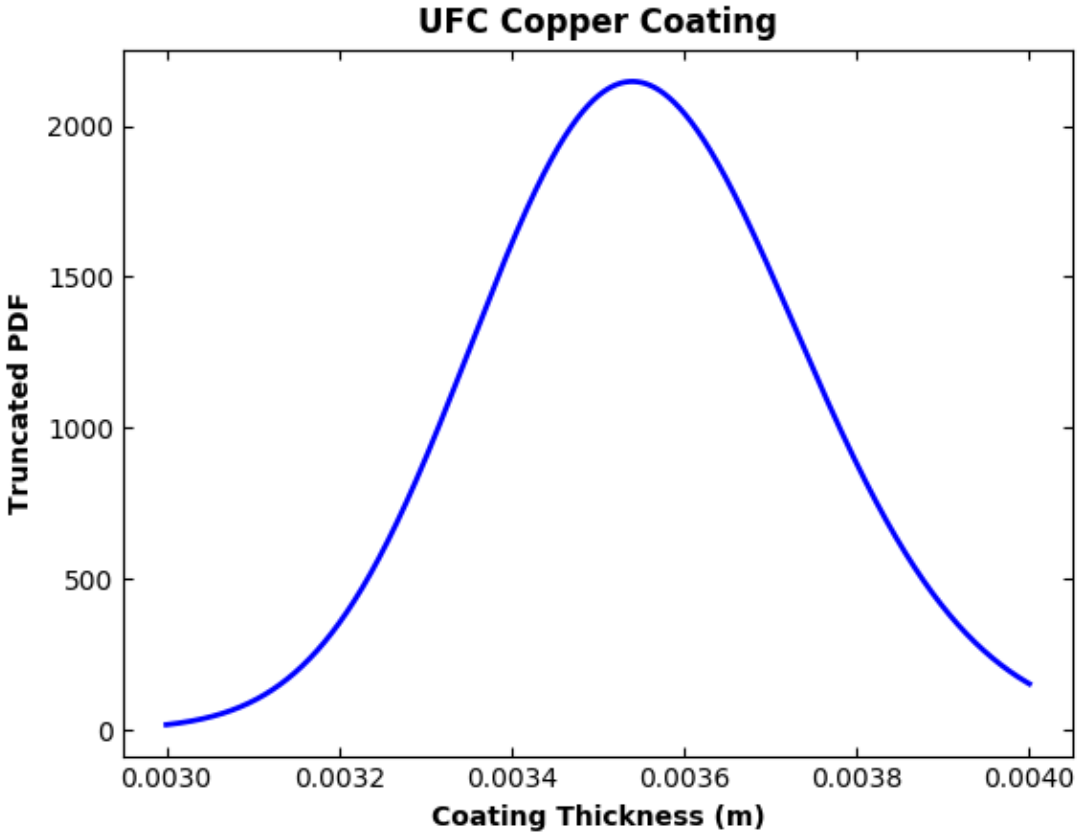

Figure 3.12: Postulated copper coating thickness distribution. An arbitrary node/panel of an arbitrary UFC takes on a value from this distribution. The distribution is Lognormal, truncated at 3 mm and 4 mm, having the parameters listed in Table 3.2.

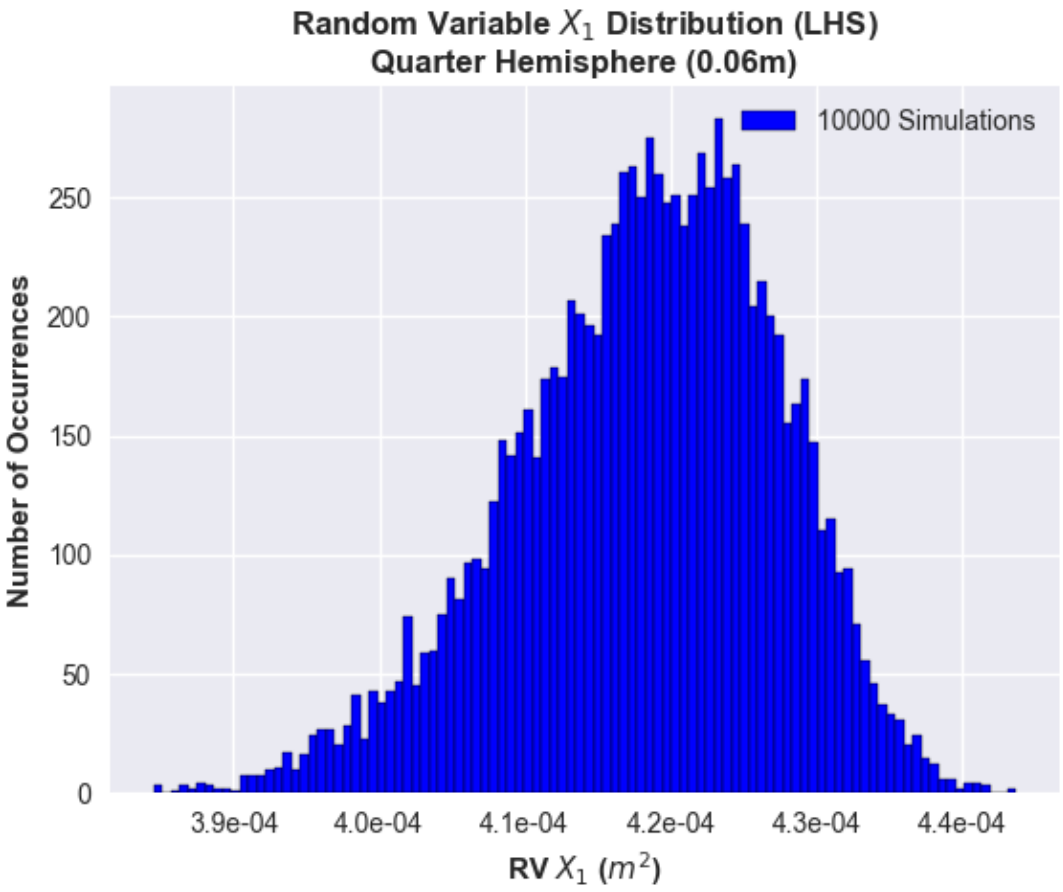

Figure 3.13: Estimated distribution for RV X_1, based on a 0.06-m mesh size.

Algorithm 1 Generation of postulated X_1 distribution

Require: $f_{t_{\mathrm{Cu}}} \sim Lognorm, \{l^i_{\mathrm{eff}}\}\, \forall i; i = 1, 2, \ldots, n$

Initialise variables, arrays: $\mathbf{x}, \mathbf{X}_1 = \mathbf{0}, \mathbf{0}$
for r in range(10000) **do**
    for i in range(n) **do**
        $X^i_{t_{\mathrm{Cu}}} \leftarrow$ sample $f_{t_{\mathrm{Cu}}}$
        $l^i_{\mathrm{eff}} \leftarrow$ sample $\{l^i_{\mathrm{eff}}\}$
        $x^i \leftarrow X^i_{t_{\mathrm{Cu}}} \times l^i_{\mathrm{eff}}$
        $\mathbf{x}$.append(x^i)
    $X_1 \leftarrow min(\mathbf{x})$
    $\mathbf{X}_1$.append(X_1)
plot $\mathbf{X}_1$

Level 2—Buffer Box/Emplacement Room

From the perspective of an arbitrary emplacement room, Equation 3.12 communicates that UFC time-to-failure is inversely proportional to the effective diffusion coefficient exhibited by the manufactured buffer boxes. More specifically, for any given buffer box, surrounding an arbitrarily chosen UFC, in any arbitrarily chosen emplacement room, a unique value for the HS^- effective diffusion coefficient D^j_{HS} in compacted bentonite is assumed. Here, the superscript j denotes the jth arbitrarily selected buffer box (or equivalently the jth UFC). In fact, when expressed in terms of X_1, Equation 3.14, the message conveyed is that from the perspective of an arbitrary emplacement room (i.e., the perspective understands C^k_0 and K are constant) the first UFC to fail (to sustain a 100% through-coating penetration by sulphide-induced corrosion) occurs when the quotient X_1/D^j_{HS} is at a minimum.

$$TTF^i_{\text{Corr}} \coloneqq \frac{X_1}{D^j_{\text{HS}} C^k_0} K. \tag{3.14}$$

In keeping with the formulation introduced in Level 1, one can thus define $\mathbf{X}_{D_{\text{HS}}}$ as the set of all iid RVs $X^j_{D_{\text{HS}}}$ $\forall j; j = 1, 2, \ldots, m$, where $X^j_{D_{\text{HS}}}$ represents the effective HS^- diffusion coefficient assigned to the jth buffer box (equivalently the jth UFC), in the kth emplacement room, from the baseline distribution characterising the expected manufacturing variation in D_{HS}. Similarly, a new iid RV $\mathbf{y}$ is defined as the set of all m elements that represent the quotient $X_1/X^j_{D_{\text{HS}}}$; that is,

$$\mathbf{y} \coloneqq \left\{ y^j : y^j = X_1/X^j_{D_{\text{HS}}} \right\} \quad \forall j; j = 1, 2, \ldots, m.$$

Of the $m = 375$ UFCs located in an arbitrarily selected emplacement room, the first UFC failure will occur at $min\left\{y^1, y^2, \ldots, y^m\right\}$. Consequently, define for Level 2 the RV X_2 to represent the minimum of the set of all y^j for an arbitrary emplacement room:

$$X_2 \coloneqq min(\mathbf{y}) = min\left\{X_1/X^j_{D_{\text{HS}}}\right\} \quad \forall j; j = 1, 2, \ldots, m. \tag{3.15}$$

While the unit of X_2 is time, it does not represent time to failure. Instead, X_2 indicates where across an arbitrarily selected emplacement room first failure will occur, or which UFC fails first. Again, this may become advantageous in future modelling where there may be interest in locating the region of first radioactive release.

The RV $X^j_{D_{\text{HS}}}$ takes on values from the baseline distribution that will be governed by many factors, least of which is the large-scale manufacturing route chosen for the production of compacted bentonite. For this work, for dry densities in excess of 1500 kg/m^3, D_{HS} is sourced from SKB's SR-Site safety assessment data report (SKB, 2010b) and is assumed

for ambient repository temperatures (i.e., 11°C, Guo, 2017)—actual ambient repository temperature will be site- and depth-specific. A truncated distribution is assigned for D_{HS} by fitting arbitrarily a Lognormal function to the data in Table 3.3. The postulated Lognormal PDF for D_{HS} is shown in Figure 3.14. As a result, $X^j_{D_{\mathrm{HS}}} \sim$ Lognormal, and for every emplacement room there exists a collection $\mathbf{X}_{D_{\mathrm{HS}}}$ representing the set of m RVs sampled from the Lognormal distribution shown in Figure 3.14.

Table 3.3: Assumed values for the effective HS^- diffusion coefficient D_{HS} in compacted bentonite

Description	Value (m^2/yr)
Geometric Mean	3.15×10^{-4}
Minimum	3.15×10^{-5}
Maximum	1.89×10^{-3}
90th Percentile	1.00×10^{-3}

It is important to pause for a moment and understand the subtle but important difference in using X_1 in lieu of X^j_1 in Equation 3.14. The use of X^j_1 restricts the scale of the problem to 375, 13500, or 108000 UFCs and would unnecessarily add complexity to the modelling framework (i.e., the tracking on a per UFC basis of the quotient $X^j_1/X^j_{D_{\mathrm{HS}}}$) without accompanying statistical gains. Restricting the scale of the problem to 10000 UFCs offers a generic, independent approach (i.e., the sampling of the X_1 distribution) without loss of statistical robustness.

Estimating the distribution of X_2 requires additional consideration, particularly since X_2 is a model construct whose validity rests on the imposed constraint that C^k_0 is constant across the kth emplacement room. From this perspective, the sampling unit is a single emplacement room, but to ensure robust sampling distribution statistics (i.e., $min(\mathbf{y})$) the number of samples is set to 10000—a generic scale restriction. Application wise, this translates to calculating y^j by assigning at random an effective diffusion coefficient to $X^j_{D_{\mathrm{HS}}}$ from the distribution for D_{HS}, Figure 3.14, while also drawing a single sample from the X_1 distribution. The collection $\mathbf{y}$ represents the set of all y^j for a single emplacement room. Computing $X_2 \coloneqq min(\mathbf{y})$ subsequently amounts to drawing a single sample or one realisation from the distribution for X_2. Alternatively, this is viewed as one simulation of an arbitrary emplacement room. Additionally, to improve the performance of the basic Monte Carlo sampling technique when sampling from the X_1 and D_{HS} distributions, respectively, a 2-D LHS technique was employed (Groen et al., 2014; McKay et al., 1979). The basic

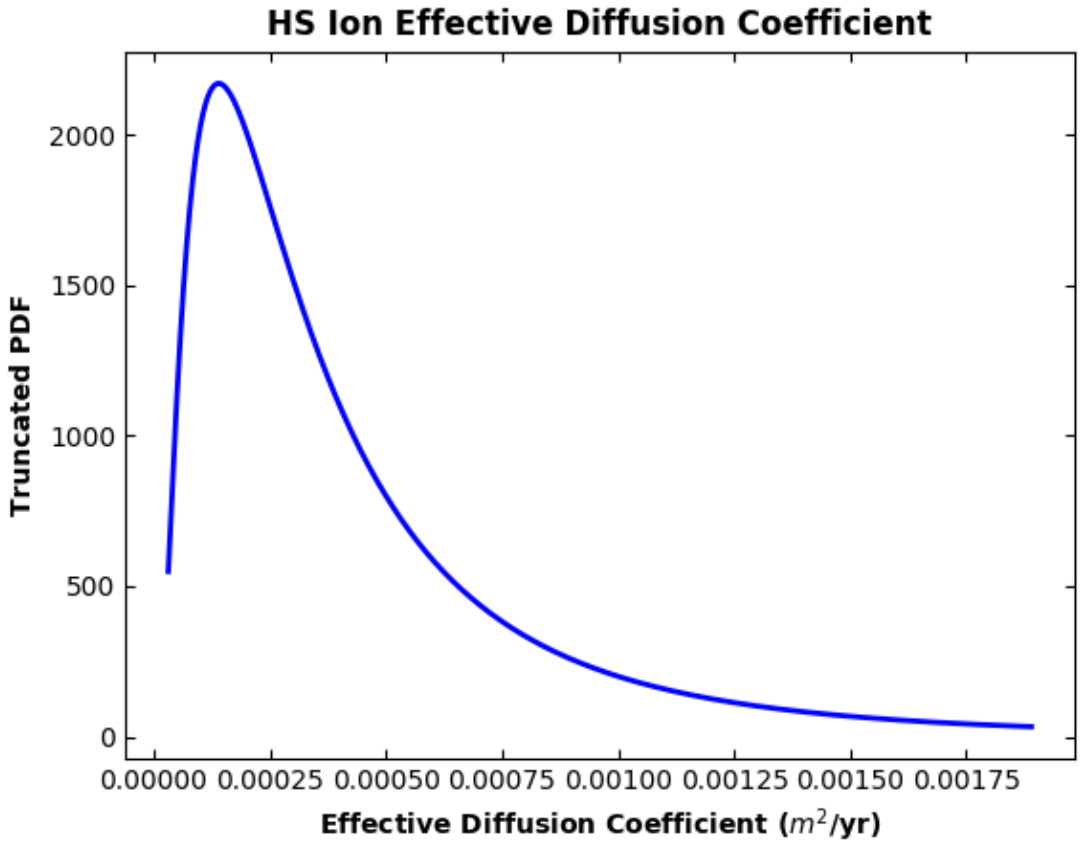

Figure 3.14: Postulated distribution for the effective HS^- diffusion coefficient D_{HS} in compacted bentonite. As part of the Level 2 modelling framework, an arbitrary buffer box (or UFC) located in an arbitrary emplacement room takes on a single value from this distribution. The distribution is Lognormal, truncated at the lower and upper limits defined in Table 3.3.

process is described in Algorithm 2. Consequently, after 10000 realisations, the resultant distribution for X_2 was estimated, as illustrated in Figure 3.15.

Algorithm 2 Generation of postulated X_2 distribution

Require: $f_{D_{\mathrm{HS}}} \sim Lognorm$, f_{X_1}, m

Initialise variables, arrays: $\mathbf{y}, \mathbf{X}_2 = \mathbf{0}, \mathbf{0}$
for r in range(10000) **do**
    for j in range(m) **do**
        $X^j_{D_{\mathrm{HS}}} \leftarrow$ sample $f_{D_{\mathrm{HS}}}$
        $X_1 \leftarrow$ sample f_{X_1}
        $y^j \leftarrow X_1 \div X^j_{D_{\mathrm{HS}}}$
        $\mathbf{y}$.append(y^j)
    $X_2 \leftarrow min(\mathbf{y})$
    $\mathbf{X}_2$.append(X_2)
plot $\mathbf{X}_2$

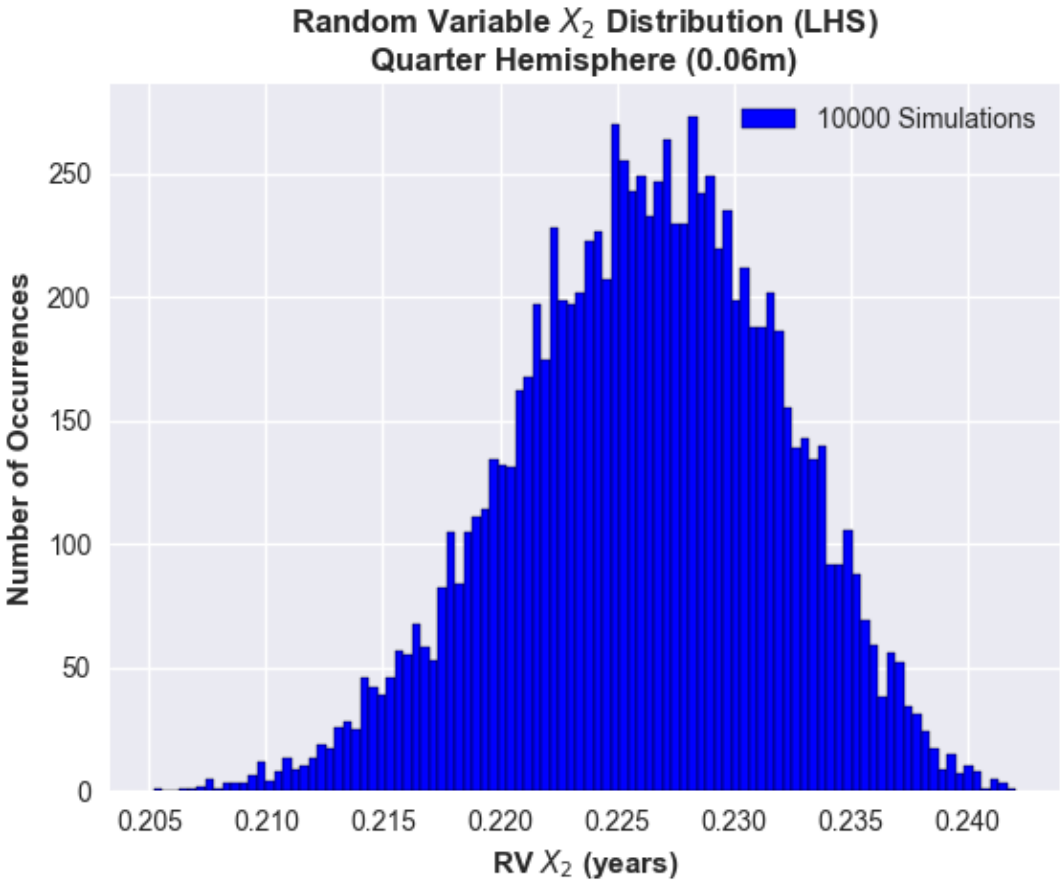

Figure 3.15: Estimated distribution for RV X_2, based on a 0.06-m mesh size.

Level 3—Emplacement Room/Panel

For any given emplacement room, within an arbitrarily chosen panel, a unique value for C_0^k (i.e., [HS^-] at the buffer box/gap-fill/host rock interface) is assumed. The superscript k denotes the kth arbitrarily selected emplacement room, of which there are 36 in one panel, and for which each will with time sustain a first failure of a UFC. Rewriting Equation 3.14 in terms of the RV X_2 leads to the expression

$$TTF^i_{\text{Corr}} \coloneqq \frac{X_2}{C_0^k} K, \tag{3.16}$$

which tells that the first UFC failure occurs when the quotient X_2/C_0^k is at a minimum. Consequently, following the probabilistic framework defined for the previous two levels, one can define for Level 3 $\mathbf{X}_{C_0}$ to be the set of all iid RVs $X^k_{C_0}\, \forall k : k = 1, 2, \ldots, q$, where $X^k_{C_0}$ represents the steady state, constant [HS^-] assigned to the kth emplacement room from the assumed baseline distribution of C_0 in crystalline rock. Accordingly, let $\mathbf{z}$ be defined as a new iid RV, representing the set of all z^k elements expressed by the quotient $X_2/X^k_{C_0}$:

$$\mathbf{z} \coloneqq \left\{ z^k : z^k = X_2/X^k_{C_0} \right\} \quad \forall k; k = 1, 2, \ldots, q.$$

For $q = 36$ emplacement rooms, the first UFC failure occurs at $min(\mathbf{z})$. Then, as with the previous levels, let X_3 be a new RV defined for Level 3 such that

$$X_3 \coloneqq min(\mathbf{z}) \times K = min\left\{ X_2/X^k_{C_0} \right\} \times K \quad \forall k; k = 1, 2, \ldots, q. \tag{3.17}$$

The unit of X_3 is time, and it represents the time of the first UFC failure among 36 emplacement rooms, or time to first failure TTF^i_{Corr}. Knowledge of the first emplacement room to sustain a radioactive leak is ascertained if one tracks which k of 36 emplacement rooms leads to X_3. This would be of particular use if C_0 was also spatially distributed within the crystalline rock DGR. In such a case, the formulation may be adjusted to include differences between repository panel regions (e.g., assuming simplistically that different mean [HS^-] apply to each panel). The current guidance from the NWMO (NWMO, 2017) is that the concentration of HS^- within a repository will vary from 0.15 μM (5 ppb) to 2.72 μM (90 ppb), with further specifics provided in Table 3.4. In the present work, a truncated distribution was assigned to C_0 by fitting a Lognormal function to the specifications provided in Table 3.4. The resultant distribution is shown Figure 3.16.

The distribution of X_3 represents the variation in the minimum UFC times to failure and was estimated by employing a 2-D LHS scheme to draw 10000 simultaneous samples from the X_2 and $X^k_{C_0}$ distributions, respectively. Algorithm 3 describes the general sampling process. The resultant distribution is depicted in Figure 3.17.

Table 3.4: Assumed values for [HS^-] in a crystalline rock DGR (NWMO, 2017)

Description	Value (μM (ppb))
Median	0.60 (20)
Minimum	0.15 (5)
Maximum	2.72 (90)
90th Percentile	1.28 (42)

Algorithm 3 Generation of postulated X_3 distribution

Require: $f_{C_0} \sim$ *Lognorm*, f_{X_2}, q

Initialise variables, arrays: $\mathbf{z}, \mathbf{X}_3 = \mathbf{0}, \mathbf{0}$
for r in range(10000) **do**
    for k in range(q) **do**
        $X_{C_0}^k \leftarrow$ sample f_{C_0}
        $X_2 \leftarrow$ sample f_{X_2}
        $z^k \leftarrow X_2 \div X_{C_0}^k$
        $\mathbf{z}$.append(z^k)
    $X_3 \leftarrow min(\mathbf{z}) \times K$
    $\mathbf{X}_3$.append(X_3)
plot $\mathbf{X}_3$

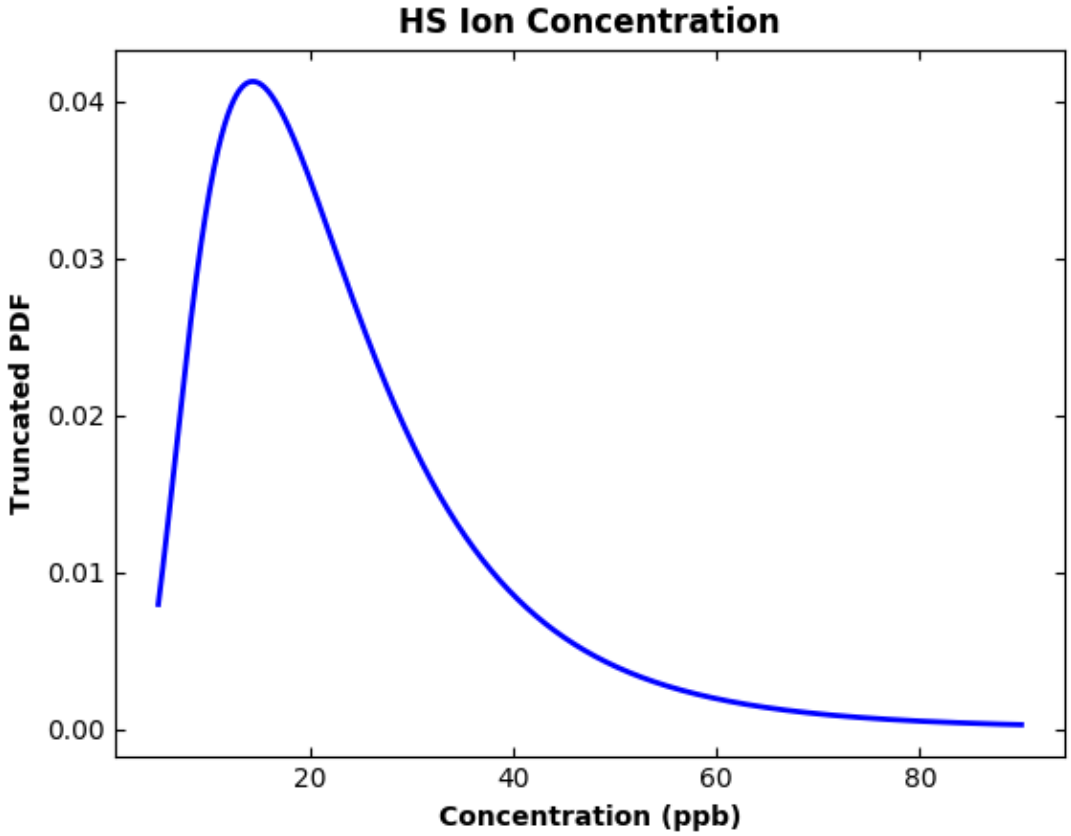

Figure 3.16: Postulated distribution for the concentration of HS^- found in a crystalline rock DGR. As part of the Level 3 modelling framework, an arbitrary emplacement room takes on a single value from this distribution. The distribution is Lognormal, truncated at the lower and upper limits defined in Table 3.4.

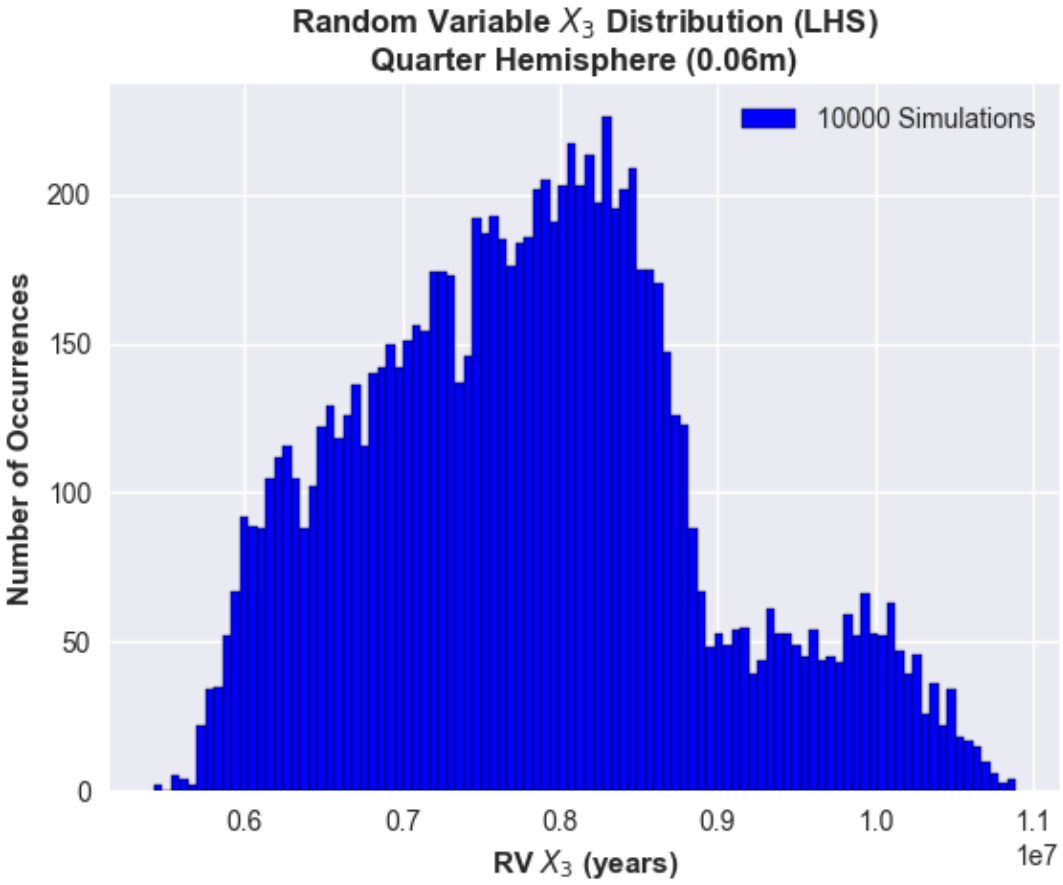

Figure 3.17: Estimated distribution for UFC first times to failure (i.e., RV X_3), based on a 0.06-m mesh size.

3.5.3 Time-to-Failure Predictions

The ECDF for the first or minimum UFC times to failure is presented in Figure 3.18. Corresponding general statistics for the times to first failures are provided in Table 3.5. From these results, half of the first UFC failures are estimated to occur by 8×10^6 years following repository closure, which is approximately equal to the mean time to first failure. The first UFC failure is predicted to occur between 5.42×10^6 to 10.9×10^6 years—a range of $\approx 5.5 \times 10^6$ years—after repository closure.

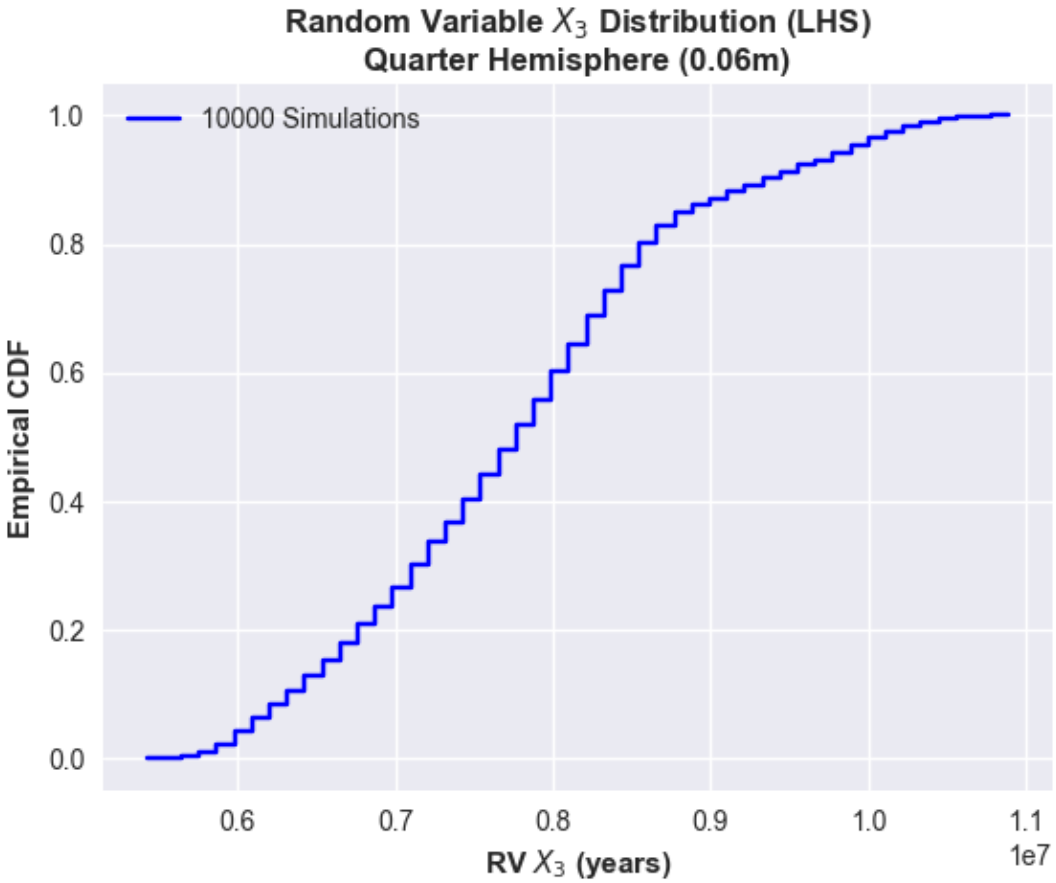

Figure 3.18: Empirical CDF for UFC first times to failure (i.e., RV X_3), based on a 0.06-m mesh size.

Table 3.5: Summary statistics for times to first UFC failures (Baseline Model)

Statistic	Time (10^6 years)
Mean	7.84
Median	7.82
Standard Deviation	1.10
Minimum	5.42
Maximum	10.9

3.5.4 Bounding Point Estimate Comparison

A bounding point estimate was calculated using the appropriate extremes of the model input variables shown in Table 3.6. The bounding point estimate (lower bound) for the first UFC failure time TTF_{min} is 5.23×10^6 years, which is in very good agreement with the minimum first time to failure, 5.42×10^6 years, predicted by the current model, Table 3.5. Increasing the number of realisations from 10000 to 100000, for example, would likely reduce the observed difference.

Table 3.6: Bounding point estimate verification summary (Baseline Model)

Parameter		Units
t_{Cu}^{min}	0.003	m
l_{eff}^{min}	0.1279221	m
D_{HS}^{max}	1.89×10^{-3}	m^2/yr
C_0^{max}	2.72	μM
f_{HS}	2	
M_{Cu}	63.55	g/mole
ρ_{Cu}	8.92×10^6	$\mathrm{g/m}^3$
TTF_{min}	5.23×10^6	yrs
Equivalent Corrosion Rate	5.73×10^{-10}	m/yr

3.5.5 Uncertainty and Sensitivity Analysis

In terms of uncertainty, one can only speak of the predicted mean minimum time-to-failure (7.84×10^6 years) and the associated variance ($(1.10 \times 10^6)^2$ years^2). Anything more is not very meaningful in the context of the present lack of site- and EBS-specific data for the input parameters associated with a Canadian repository. In terms of aleatory (i.e., random) and epistemic (i.e., lack of knowledge) uncertainties, in the present modelling framework all three input parameters ($t_{\text{Cu}}, D_{\text{HS}}, C_0$) have been treated essentially as random variables with aleatory uncertainty. There is epistemic uncertainty surrounding both the distributions chosen for each parameter (model form uncertainty) and the distribution parameters (second order uncertainty). However, due to lack of site- and EBS-specific data and limited expert elicitation, epistemic uncertainty concerning the model input parameters was not given further attention in this work.

The objective of a sensitivity analysis is to decompose the uncertainty (e.g., variance in TTF_{Corr}, $(1.10 \times 10^6)^2$ years^2) into its corresponding parts, which are directly associated with input parameter (e.g., $t_{\text{Cu}}, D_{\text{HS}}, C_0$) uncertainties. In simple words, and in the present context, sensitivity analysis aims to determine what percent of the uncertainty defined by $(1.10 \times 10^6)^2$ years^2 is attributable to each of $t_{\text{Cu}}, D_{\text{HS}}, C_0$. Typically, for deterministic models—where the same output is obtained for a given set of inputs—one can apply variance decomposition to examine the influence of input variability on the output variance. Variance decomposition methods designed to achieve this objective are discussed in Saltelli et al. (2004, 2008). For the present model, however, the model constructs $X_1, X_2,$ and X_3 were developed having in mind $argmin_{(.)}(TTF_{\text{Corr}})$ at each level. This confounds the influence of $t_{\text{Cu}}, D_{\text{HS}}, C_0$ on the variance of TTF_{Corr}. Instead, an ad hoc approach is adopted here to understand how the input parameters under the present multi-level model structure influence the variability in TTF_{Corr}. A more detailed analysis is not warranted since the uncertainties associated with $t_{\text{Cu}}, D_{\text{HS}}, C_0$ were, to a great extent, chosen arbitrarily to facilitate model development and may bear no strong resemblance to final as-manufactured or EBS-related results.

In view of the level-specific $argmin_{(.)}(TTF_{\text{Corr}})$ approach employed in the curent model, it was anticipated that the influential region of the input space (i.e., the region that ultimately impacts TTF_{Corr}), defined by the 3-D hyperspace, whose axes represent respectively the domains of $t_{\text{Cu}}, D_{\text{HS}}, C_0$, would be smaller—perhaps significantly so—than the available input space. To assess this assertion, the values for $X^i_{t_{\text{Cu}}}, X^j_{D_{\text{HS}}},$ and $X^k_{C_0}$, which resulted in the corresponding values for $X_1, X_2,$ and X_3 and which are effectively a sampling from the baseline distributions for $t_{\text{Cu}}, D_{\text{HS}}, C_0$ (equivalently, a trajectory from the input space), were traced throughout the multi-level realisations in the model. For expediency, the num-

ber of realisations per level in this exercise was limited to 1000 and the mesh size to 0.012 m ($n = 73$). The resultant distributions for the traced values for $X^i_{t_{\text{Cu}}}, X^j_{D_{\text{HS}}}$, and $X^k_{C_0}$, which contributed to TTF_{Corr}, were computed and compared against the starting baseline distributions for $t_{\text{Cu}}, D_{\text{HS}}, C_0$. Additionally, for this exercise only, the effective diffusion length l_{eff} was treated as a RV and traced throughout the realisations at each level. A further comparison was made against times to failure determined using a "naive" approach, where the explicit multi-level formulation expressed by Equation 3.12 was replaced by

$$TTF_{\text{Corr}} \coloneqq min \left\{ \frac{t_{\text{Cu}} l_{\text{eff}}}{D_{\text{HS}} C_0} K \right\}, \tag{3.18}$$

with all variables treated as distributed parameters, and the distribution for TTF_{Corr} obtained by simple Monte Carlo sampling of the parameters. More specifically, a sample of size $n = 73$ was drawn from each of the baseline distributions for $t_{\text{Cu}}, D_{\text{HS}}, C_0$ to compute a single value (representing a single realisation) for TTF_{Corr} based on Equation 3.18. This was repeated until 1000 samples were generated and a distribution constructed.

Figure 3.19 summarises the results in four plots, comprising three distributions for each of the input parameters $t_{\text{Cu}}, l_{\text{eff}}, D_{\text{HS}}, C_0$. Note that Figure 3.19 uses the following nomenclature for the preceding variables: tCu, Leff, DiffCoef, and HSConc. In Figure 3.19, the distribution defined by the variable with the suffix "_min" represents the resultant sampling distribution for the variable in question as it is traced through the sampling of X_1, X_2, and X_3 used in the multi-level "Baseline" model presented thus far. The distribution for the variable with the suffix "_no_level" represents the resultant sampling distribution of the variable of interest as it is traced through the determination of first UFC times-to-failure calculated as per Equation 3.18. Lastly, the distribution for the variable with the suffix "_baseline" represents the initial baseline distributions (i.e., assumed manufacturing-based distributions) used in the formulation of the multi-level baseline model (e.g., Figure 3.12, Figure 3.14, and Figure 3.16). The results confirm the initial assertion that the influential input space is significantly smaller than the available space. But the results also show that this is true only for the input parameters $t_{\text{Cu}}, D_{\text{HS}}$, which sustain a significant reduction in variance, but not for the resultant C_0 distribution. This observation was corroborated by a simple linear regression of TTF_{Corr} on the traced values for $t_{\text{Cu}}, l_{\text{eff}}, D_{\text{HS}}, C_0$ associated with X_1, X_2, and X_3. The regression (results not shown) showed that a significant portion of the variance in TTF_{Corr} could be explained by the resultant values for C_0. This is not too difficult to accept since the computation of X_3 (Equation 3.17) is the only instance in which the baseline distribution for C_0 is sampled. In contrast, the computation of X_2 and X_3 in effect leads to a re-sampling of the traced values for $X^i_{t_{\text{Cu}}}$, and $X^j_{D_{\text{HS}}}$. Therefore, a consequence of the sequential level-specific

$argmin_{(\cdot)}(TTF_{\text{Corr}})$ approach adopted in the present modelling framework is a TTF_{Corr} variability that is influenced predominantly by the input parameter C_0, which is the last input parameter to be directly sampled at the last structural level of the model. This bias, which links a significant portion of the variance in TTF_{Corr} to C_0 occurs at the expense of the narrowing of the influential regions of the respective distributions for t_{Cu} and D_{HS} (as well as l_{eff} when treated temporarily as RV in this exercise).

3.6 Limitations

The obvious limitation of the present model is the assumption that local environmental conditions affecting the characteristic distributions of the input parameters D_{HS} and C_0, including potentially l_{eff}, are time invariant (with the manufacturing distribution for t_{Cu} assumed to be constant over the 30-year DGR emplacement period). While the stability and predictability of the geosphere is one of the major reasons for placing used nuclear fuels in a DGR, to assume absolute time-invariance over the timescales of interest may be found—by some—to be simply too difficult to fully justify. The assumption that the characteristics/integrity of the copper coating, compact bentonite buffer, and geosphere lead to time-invariant distributions for $t_{\text{Cu}}, D_{\text{HS}}, C_0,$ including l_{eff}, is an idealisation that enables the present model to be structured as shown, but may not be fully compatible with reality. Unfortunately, formulating expressions that capture sufficiently the stochastic nature of the input parameters is a challenge that possesses its own set of limitations and questions.

A more subtle limitation associated with the use of the proposed probabilistic framework is the assumption concerning iid RVs, which is not likely to be correct in all cases. Factors that may invalidate the assumption of iid include spatial and time-dependent variation of temperature across an emplacement room, potential localised effects from discrete fracture networks in the geosphere, which may influence saturation times and flow of nutrients that support SRB growth, and other localised factors that may be susceptible to time-variant effects (e.g., characteristics of bentonite buffers) because of the +30-year operation life of the DGR (Noronha, 2016). Copper coating thickness may also be correlated with specific regions of the UFC where geometrical factors during electrodeposition lead to certain biases (autocorrelations) in the coating thickness. Consequently, spatial variations in copper coating thickness may need to be modelled more specifically. As more data becomes available, the impact of the iid assumption can be better assessed.

Notwithstanding, the proposed model offers the user a considerable degree of flexbility to experiment with competing understandings of how the input parameters are distributed

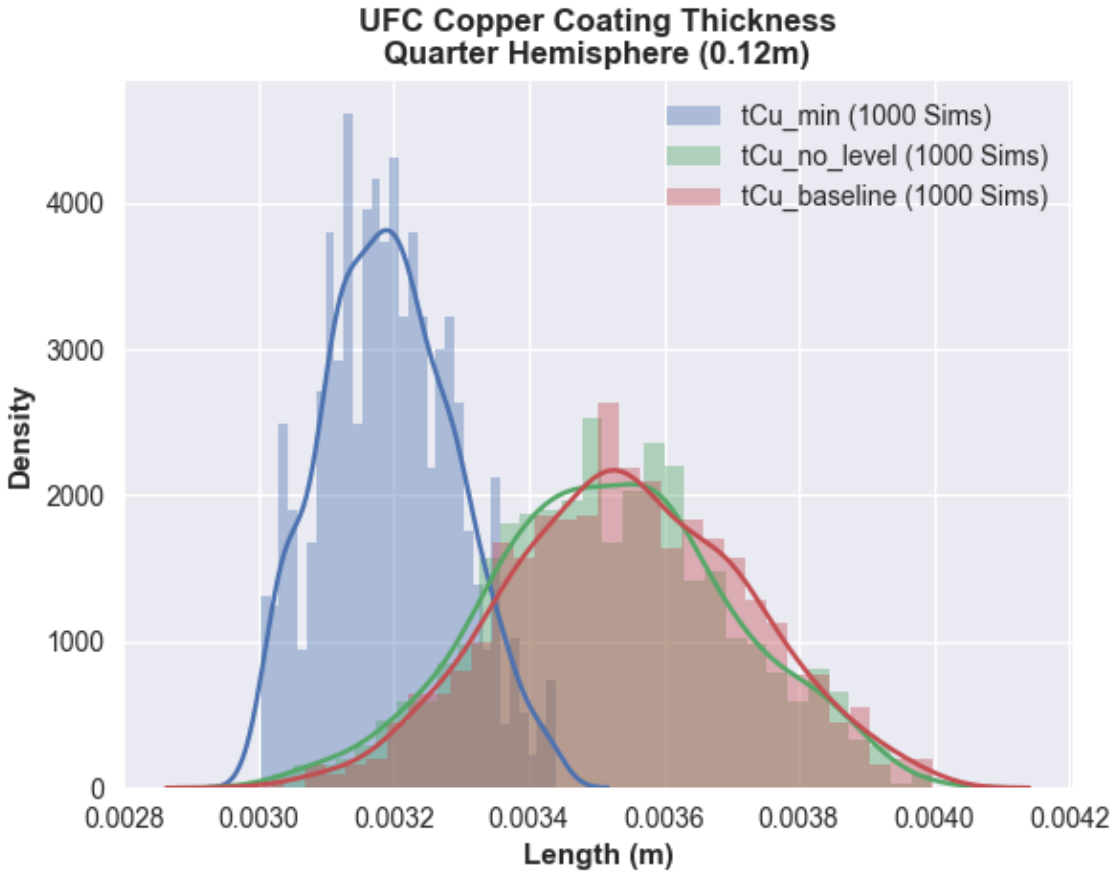

(a)

Figure 3.19: (a) Sampling distributions for tCu_min, tCu_no_level, and tCu_baseline

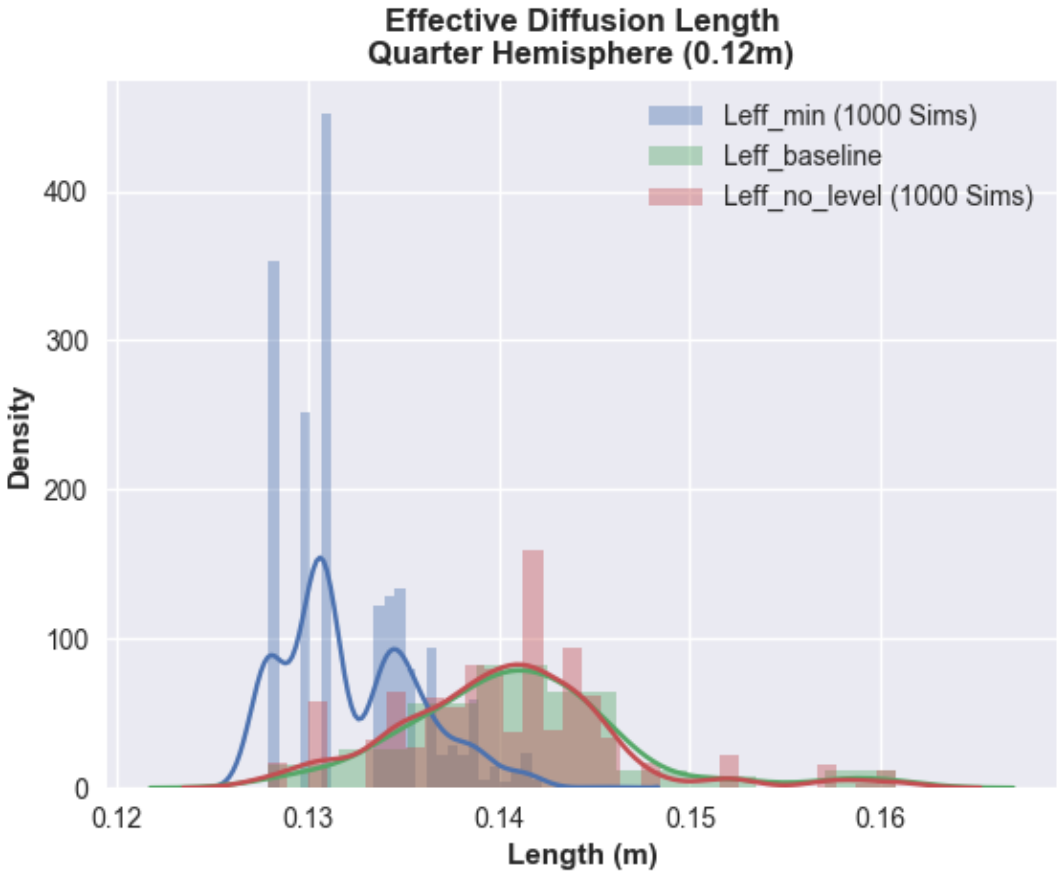

(b)

Figure 3.19: (b) Sampling distributions for Leff_min, Leff_no_level, and Leff_baseline

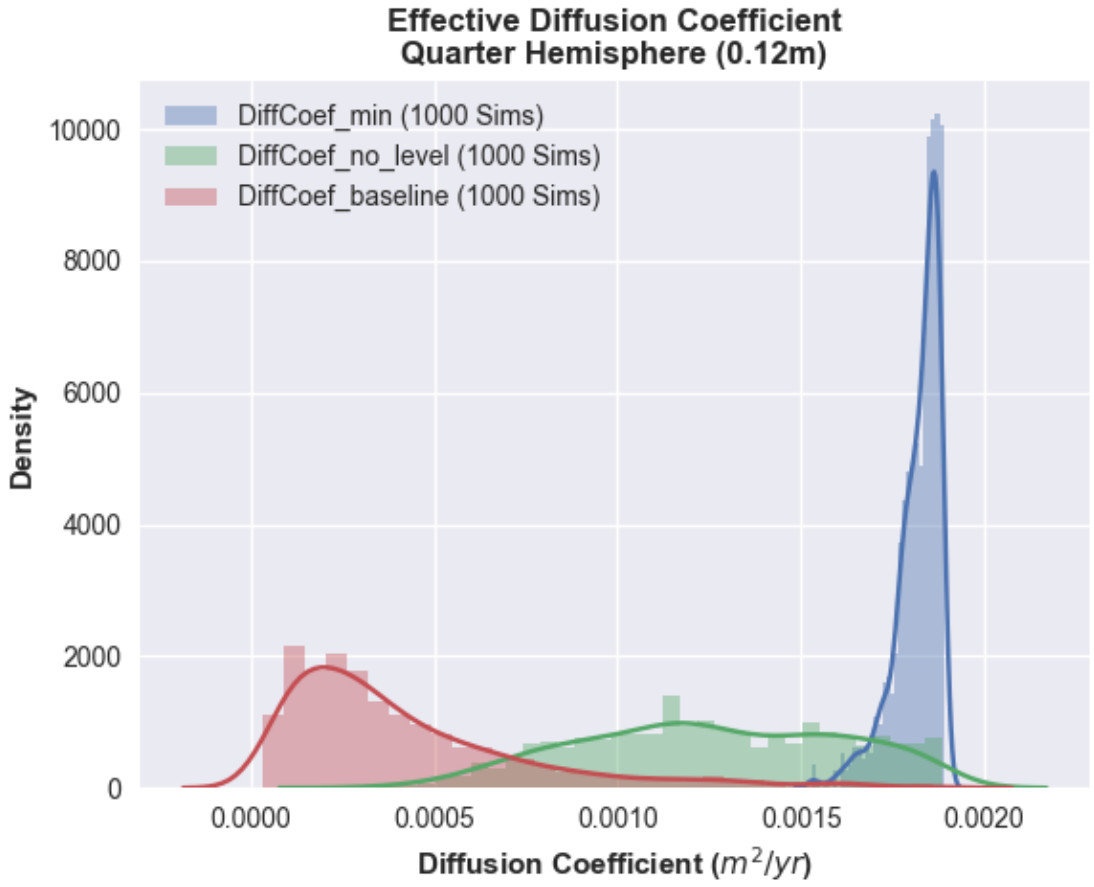

(c)

Figure 3.19: (c) Sampling distributions forDiffCoef_min, DiffCoef_no_level, and DiffCoef_baseline

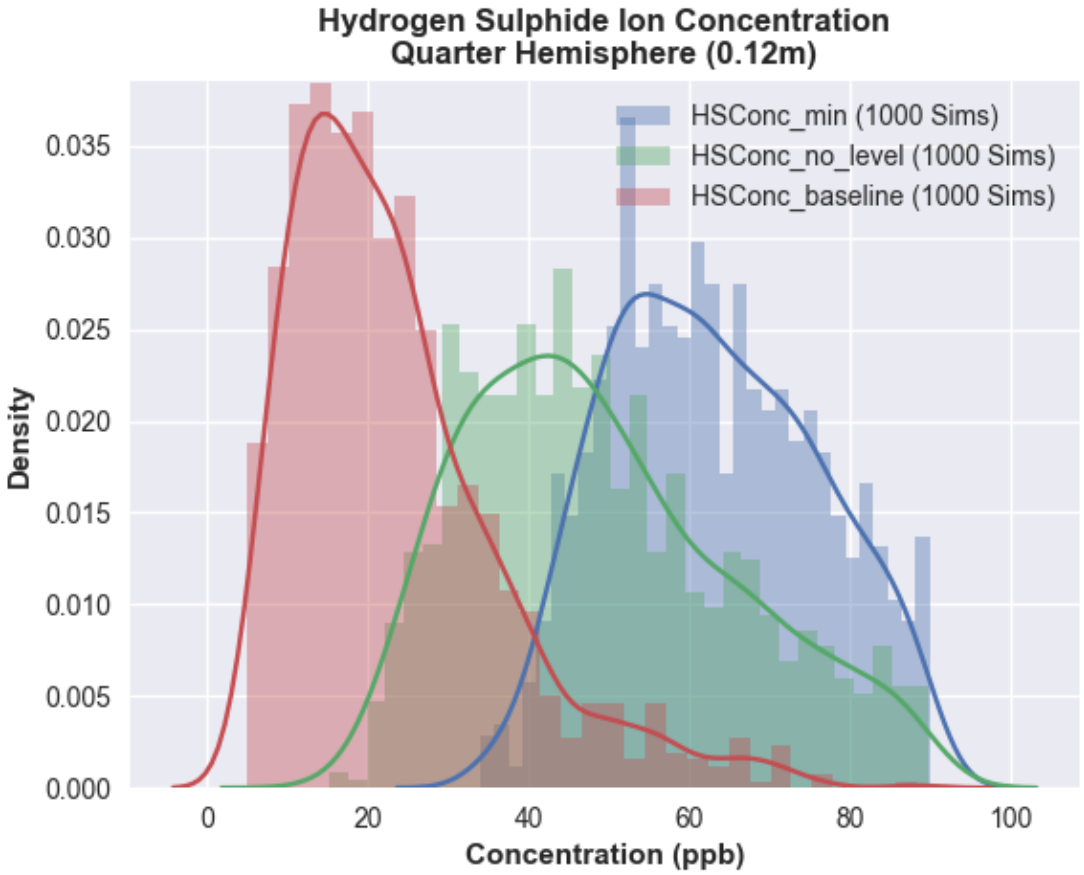

(d)

Figure 3.19: (d) Sampling distributions for HSConc_min, HSConc_no_level, and HSConc_baseline

locally and spatially, DGR layout, etc. With additional effort, the model can also be used to simulate random initiation of radioactive leaks both in time and space across a DGR.

3.7 Summary

A UFC lifetime model has been developed to represent the current understanding that sulphide-induced corrosion of a copper-coated UFC in a conceptual DGR will be mass-transport-limited, with corrosion depth predicted simply by mass balance. A probabilistic framework was constructed to utilise Monte Carlo methods within a 1-D, multi-level representation of the sulphide-induced corrosion mechanism postulated for the proposed crystalline rock DGR. Within the model construct and associated assumptions, the model predicts that 50% of UFC first failures will occur by approximately 8×10^6 years after placement[6], with all first failures occurring by roughly 11×10^6 years after placement.

[6]The statements "following repository closure" and "after emplacement" are, for the purposes of this work, synonymous. While the NWMO presently targets an operational life of approximately 30 years for the repository (Noronha, 2016), in the context of the timescales of a DGR the time from individual UFC placement in an emplacement room to final repository closure is interpreted to be insignificant by this author.

Chapter 4

Effect of Latent Defects and Repository Temperature

This chapter extends the baseline model developed in Chapter 3 by examining the effect on UFC lifetimes of both latent defects in the UFC copper coating and potentially higher than baseline corrosion rates during the temperature transient postulated for the DGR. Section 4.1 details the probabilistic approach applied to latent copper-coating defects, concluding with a simple sensitivity analysis to compare the effect on UFC first times to failure. Section 4.2 describes the higher corrosion rate formulation and compares the combined effect of latent defects and high corrosion rates on UFC lifetimes against baseline results. The chapter concludes with a summary, Section 4.3.

Continuing with the generic problem statement introduced in Chapter 3, this chapter seeks to solve for the time to failure t in the following two generic failure conditions: $[h - X_{dia} - X(t + t_T)|X_{def} = 1] \leqslant 0$ and $[h - X(t + t_T)|X_{def} = 0] \leqslant 0$, whichever is applicable, with $X(t + t_T) = R \times t + R_T \times t_T$. Here, X_{dia} represents the diameter of a latent defect, X_{def} represents a RV that takes on values 1 or 0, signifying the presence or not of a copper coating defect, R_T is the elevated degradation rate during the postulated temperature transient, and t_T is the transient duration during which the degradation rate is elevated above baseline. As before, the generic problem statement helps to understand the objective of this chapter. Actual implementation is more complicated because the ensuing formulation must integrate with the probabilistic framework developed in the preceding chapter.

The precise problem statement addressed by this chapter is to characterise the distribution of first times to failure for UFCs placed in a crystalline rock DGR when provision

is made to account for potential copper coating defects and high corrosion rates due to higher than baselines temperatures sustained by the UFC during the postulated temperature transient.

4.1 Latent Defects Model Formulation

To account for the potential for subsurface defects within the UFC copper coating, the approach taken in the present modelling framework is to treat each UFC as a Bernoulli RV, designated as X_{def}, where "def" denotes a coating defect. Two outcomes are possible:

$$X_{\text{def}} \sim \text{Bern}(p) \coloneqq \begin{cases} 1, & \text{if UFC is defective,} \\ 0, & \text{if UFC is not defective,} \end{cases} \tag{4.1}$$

where p is the probability of defect, or equivalently that a single UFC contains at least one copper coating defect (synonymous with stating that a UFC is defective). For the Bernoulli RV X_{def}, the Probability Mass Function (PMF) is the special case of the Binomial distribution with $k = 0, 1; N = 1$, $\text{Bin}(N, p)$

$$P(X_{\text{def}} = k) \coloneqq \binom{N}{k} p^k (1-p)^{N-k} = \begin{cases} p, & \text{if } k = 1, \\ 1-p, & \text{if } k = 0. \end{cases} \tag{4.2}$$

The probability of a defective UFC (i.e., defect-bearing UFC coating) is handled in a manner similar to Doubt (1984) and Johnson et al. (1994), where the probability of a defect, p, is also treated as a RV. In the present work, a Lognormal distribution is assumed for p, with the distribution truncated at the minimum (1 in 10000) and maximum (1 in 1000) probabilities as per the guidance offered in Doubt (1984) and Johnson et al. (1994). Additionally, for the present model, the general shape of the Lognormal distribution was chosen to coincide with a pre-selected geometric mean and 90th percentile. In the absence of more recent (or relevant) inspection data for electrodeposited copper coatings on large-scale structures, the approach adopted herein was to choose the geometric mean to reflect the belief that Non-destructive Examination (NDE) techniques will lead to a lower likelihood of subsurface-defect-bearing UFCs (i.e., closer to 10^{-4}), with higher probabilities of defective coatings (i.e., at 10^{-3}) observed at much lower frequencies. This belief, which is entirely arbitrary, is expressed in Table 4.1. The resultant distribution for p is shown in Figure 4.1.

Table 4.1: Postulated distribution parameters for p, the probability of a defective UFC

Description	Value
Geometric Mean	1.5×10^{-4}
Minimum	1.0×10^{-4}
Maximum	1.5×10^{-3}
90th Percentile	5.0×10^{-4}

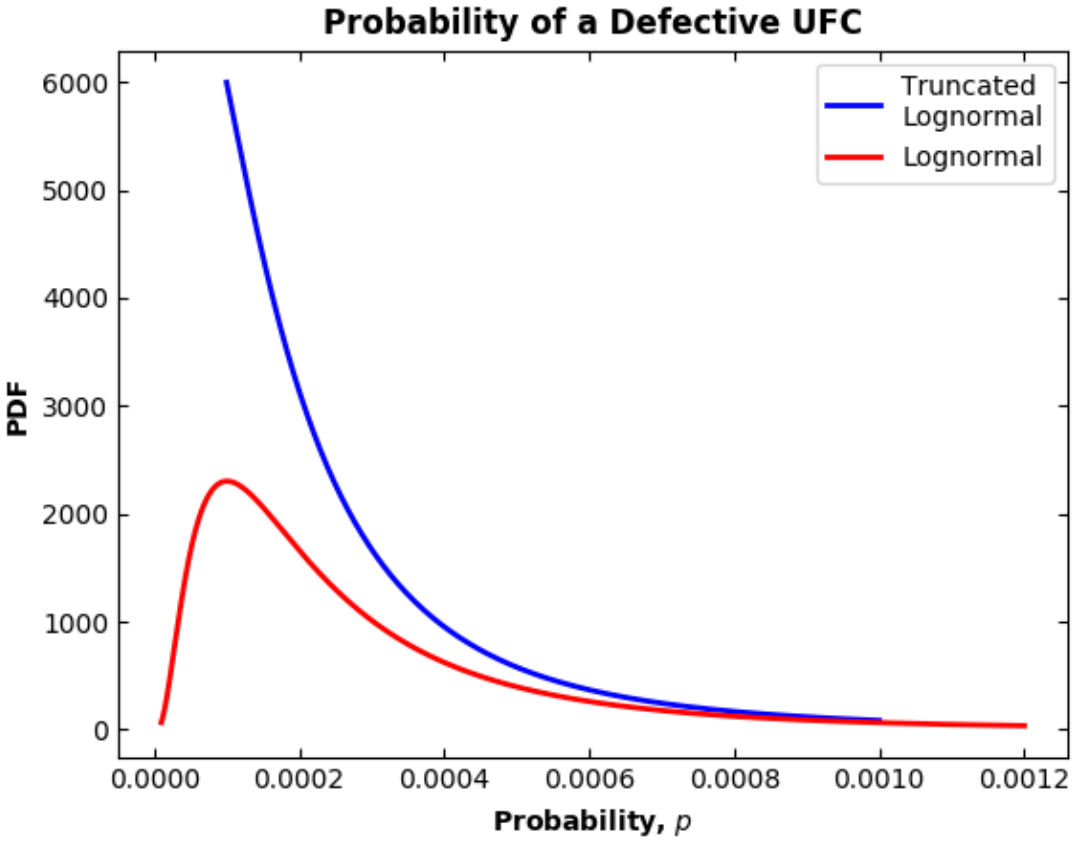

Figure 4.1: Postulated distribution for the probability p of a defective UFC.

As of the time this part of the UFC lifetime model was in development, there was no data available for the distribution of defects expected in the nominally 3-mm thick electrodeposited copper coating. However, the NWMO position at the time (Kremer, 2017) indicated that, while work was ongoing, the maximum diameter of a latent subsurface defect was not expected to exceed 0.8 mm, with 100% detection anticipated for both surface-breaking defects and defect diameters greater than 0.8 mm. For the purpose of this model, a right-tailed Lognormal distribution for defect diameters is assumed, having a geometric mean located near the lower end of the range of diameters to reflect observations for some engineering materials where grain sizes and porosity typically follow a right-tailed, distribution (sometimes Lognormal). The foregoing implies that most of the subsurface coating defects are postulated to be at the low end of the distribution range, with larger defects (i.e., 0.8 mm) seldom observed. Accordingly, the geometric mean and the 90th percentile were chosen to be 0.15 mm and 0.35 mm, respectively, Table 4.2. The corresponding truncated Lognormal distribution is shown in Figure 4.2.

Table 4.2: Postulated UFC copper coating subsurface defect diameters

Description	Size (m)
Geometric Mean	0.15×10^{-3}
Maximum	0.8×10^{-3}
90th Percentile	0.35×10^{-3}

With the aforementioned distributions defined, it is possible to frame the problem of the effect of defects in a probabilistic framework. Following the approach from the previous chapter, a subsurface defect diameter is subsequently defined as an iid RV, designated X^i_{dia}, and randomly assigned to the ith node on a UFC if the Bernoulli RV X_{def} is equal to 1. This is accomplished by sampling from the corresponding PMF, Equation 4.2, with p randomly sampled from its parent distribution, Figure 4.1. More succinctly, when $X_{\text{def}} = 1$ the net copper coating thickness is equal to $X^i_{t_{\text{Cu}}} - X^i_{\text{dia}}$, with $X^i_{t_{\text{Cu}}}$ sampled as per section 3.5.2 and X^i_{dia} from its parent distribution, Figure 4.2. Consequently, the net copper coating thickness, $X^i_{t_{\text{Cu}}} - X^i_{\text{dia}}$, replaces $X^i_{t_{\text{Cu}}}$ in Equation 3.13. Otherwise, if $X_{\text{def}} = 0$, $X^i_{\text{dia}} = 0$.

The foregoing procedure randomly assigns a subsurface defect diameter to all nodes on a UFC if $X_{\text{def}} = 1$. Such a methodology does not differentiate between latent defects with varying propensity to occur at any node (or at all nodes) on a discretised UFC surface. Instead, the approach adopted here is to conservatively assume that a defective

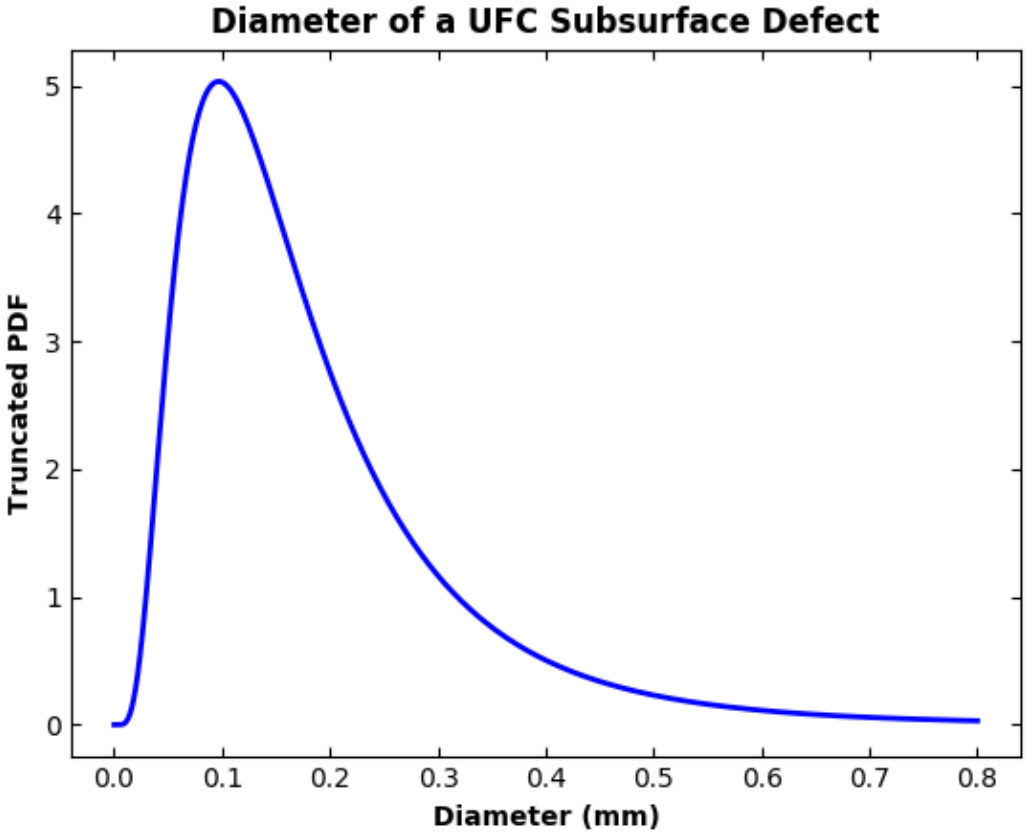

Figure 4.2: Postulated distribution for subsurface defect diameters for a defective UFC.

UFC implies defects present throughout the copper coating. However, since the proposed defect sizes are relatively small and perhaps more representative of inherent porosity in coatings, the position taken in the present modelling framework is that latent defects can be approximated in a manner akin to simulating widespread porosity. For latent defects that result from external or Foreign Object Damage (FOD), the arbitrary assignment across the entire surface is not likely to be very representative of reality. Damage arising from FOD—if it were to occur—is anticipated to arise at vulnerable areas of the UFC, such as contact points during loading/unloading and extremities of the UFC subject to inadvertent contact during transport to the emplacement rooms. Further, FOD would likely require a different distribution and a different interpretation of size, depth, and spatial coverage. But a similar framework may be developed to allow for its incorporation into the present

model.

As a result of the above, to account for the effect of subsurface coating defects, which results in a net copper coating thickness at the ith node $X^{\text{net}}_{t_{\text{Cu}}}$, the earlier formulation for RV X_1 becomes

$$X_1 \coloneqq min(\mathbf{x}) = min\left\{X^{\text{net}}_{t_{\text{Cu}}} l^i_{\text{eff}}\right\} \quad \forall i; i = 1, 2, \ldots, n, \tag{4.3}$$

where

$$X^{\text{net}}_{t_{\text{Cu}}} \coloneqq X^i_{t_{\text{Cu}}} - X^i_{\text{dia}} \quad \forall i; i = 1, 2, \ldots, n. \tag{4.4}$$

When a UFC is not defective, $X^{\text{net}}_{t_{\text{Cu}}}$ is simply $X^i_{t_{\text{Cu}}}$.

Figure 4.3 shows the resultant distribution of X_1 when defects are assigned to a UFC with probability p. When compared with Figure 3.13, the resultant plot demonstrates that at 10000 realisations (simulations in the figure) and with the assumed distribution for p, a limited number of observations occur to the left of the distribution. Increasing the number of realisations to 100000, or greater, would result in more observations to the left of the distribution and would be more relevant for safety assessments since presently 96000 UFCs are estimated for permanent storage within a Canadian DGR[1]. For the purpose of showing the utility of the present model, however, the current number of realisations is deemed adequate. To derive distributions for RVs X_2 and X_3 for the baseline model, the same methodology described in section 3.5.2 is followed. The only exception is that due to the sparseness of the left tail of the X_1 distribution, the sampling scheme to estimate X_2 (and subsequently X_3) was changed from LHS to stratified random sampling with Neyman allocation (pg 24 Kalton, 1983).

[1]Nominally, 108000 UFCs are slated based on the number of panels, but a fraction of the panels will not have 100% space utilization due to a potential need to seal hydraulically conductive fractures.

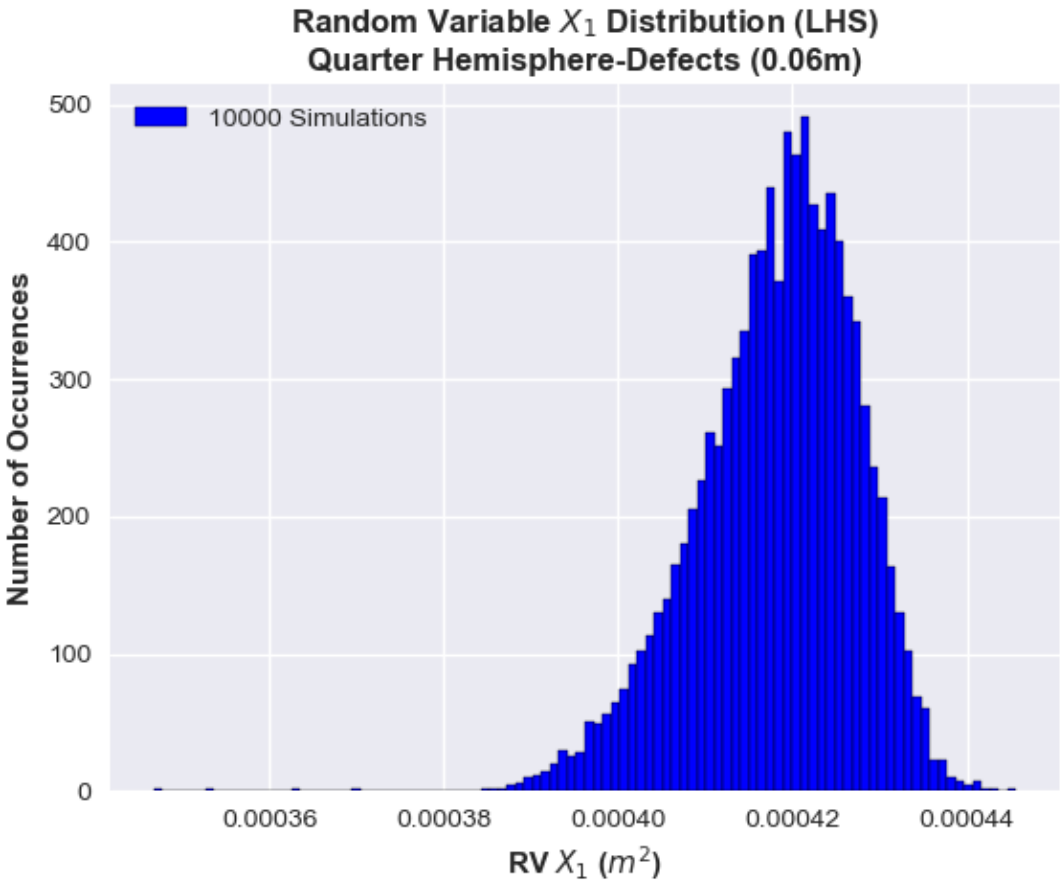

Figure 4.3: Estimated distribution for RV X_1, based on a 0.06-m mesh size and with probability p of subsurface defects modelled by a right-tail Lognormal distribution.

4.1.1 Time-to-Failure Predictions

Figure 4.4 illustrates the distribution of first times to failure (i.e., RV X_3) for UFCs with finite probabilities of subsurface defects. Accompanying summary statistics are included in Table 4.3. When compared with the results for no defects (Table 3.5, Figure 3.17), subsurface defects less than 0.8 mm in diameter, which exhibit a right-tail Lognormal distribution, have a noticeable but not significant effect—relative to repository timescales—in reducing the first times to failure. More specifically, the mean (7.84×10^6 years) and standard deviation (1.08×10^6 years) are—at two significant digits to the right of the decimal—unchanged, but the minimum time to first failure (5.00×10^6 years), when compared with the baseline model, is reduced on average by approximately 8% or 420000 years, at two significant digits to the right of the decimal. The observed reduction in minimum first times to failure is considered a real, "on average" effect as the random seed used in the computer simulations was kept constant throughout all evolutions of the model.

Table 4.3: Summary statistics for times to first UFC failures (Defect Model)

Statistic	Time (10^6 years)
Mean	7.84
Median	7.82
Standard Deviation	1.08
Minimum	5.00
Maximum	10.96

4.1.2 Bounding Point Estimate Comparison

A bounding point estimate was calculated using the appropriate extremes of the model input variables shown in Table 4.4, including the smallest copper thickness t_{Cu}^{min}, after accounting for the largest defect diameter 0.8 mm, the minimum effective diffusion length l_{eff}^{min}, the maximum effective diffusion coefficient for HS^-, D_{HS}^{max}, and the maximum $[HS^-]$, C_0^{max}. The bounding point estimate (lower bound) for the first times to failure TTF_{min} is 3.84×10^6 years, which while noticeably less is still the same order of magnitude (5.23×10^6 years) predicted by the baseline model, Table 3.6. From an equivalent corrosion rate perspective, the difference is again noticeable but of the same order of magnitude, 7.81×10^{-10} m/yr with probabilised defects versus 5.73×10^{-10} m/yr without.

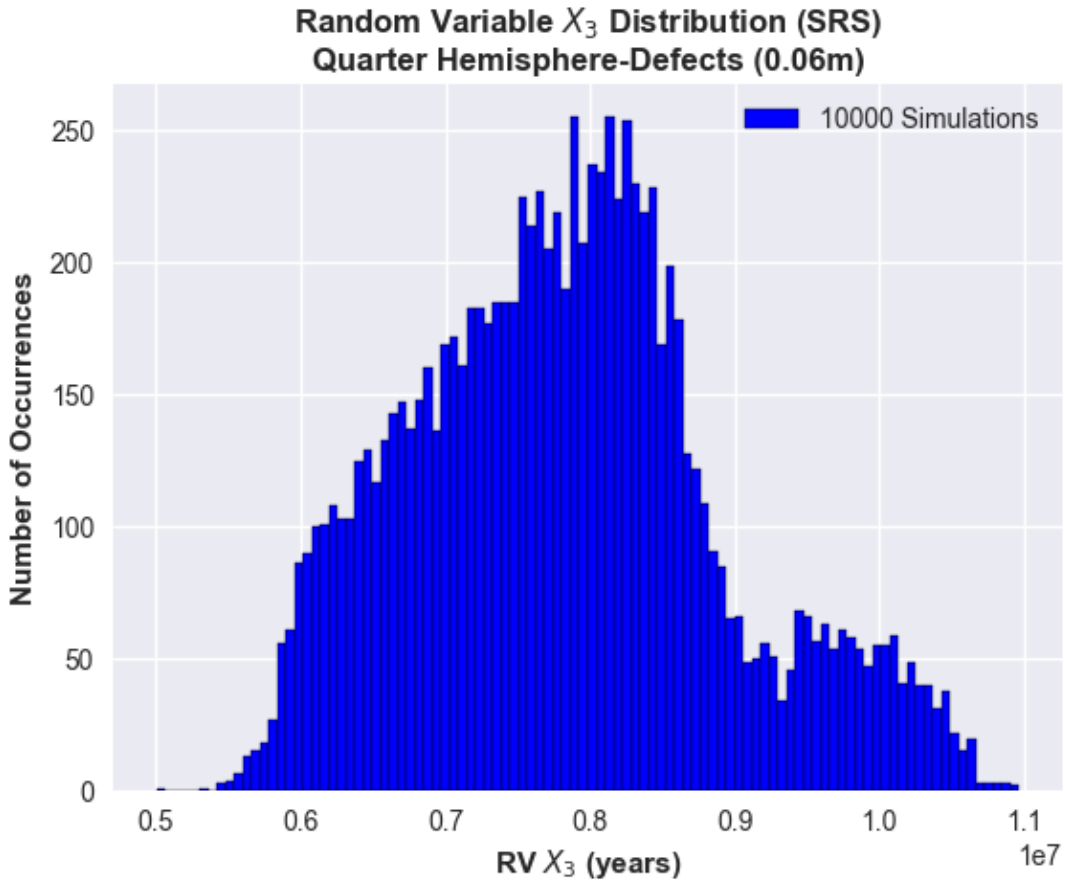

Figure 4.4: Estimated distribution for RV X_3, based on a 0.06-m mesh size and with probability p of subsurface defects modelled by a right-tail Lognormal distribution.

4.1.3 Uncertainty and Sensitivity Analysis

Subsurface defects are expected to fall under aleatory uncertainty, with the form of the distribution and corresponding parameters exhibiting epistemic uncertainty. The shape of distribution in the present model (i.e., right-tail Lognormal) was entirely subjective but loosely based on the author's personal experience with other metallurgical processes. Changing the distribution form and parameters may lead to very different results. To explore this, a two-parameter Weibull function was selected for the defect diameter distribution, with a median and 90th percentile equal to 0.6 mm and 0.7 mm, respectively. The shape of the distribution essentially clusters the defect diameters towards the higher end

Table 4.4: Bounding point estimate verification summary (Defect Model)

Parameter		Units
t_{Cu}^{min}	0.0022	m
l_{eff}^{min}	0.1279221	m
D_{HS}^{max}	1.89×10^{-3}	m^2/yr
C_0^{max}	2.72	μM
f_{HS}	2	
M_{Cu}	63.55	g/mole
ρ_{Cu}	8.92×10^6	g/m^3
TTF_{min}	3.84×10^6	yrs
Equivalent Corrosion Rate	7.81×10^{-10}	m/yr

of the assumed range, Figure 4.5, which is opposite to the right-tail Lognormal distribution of defect diameters assumed for the present defect model. Using the left-tail Weibull distribution, a revised distribution for RV X_3 was computed with 10000 realisations, Figure 4.6. Corresponding summary statistics are included in Table 4.5. An 8% reduction on average in the minimum first times to failure, which is equal to approximately 400000 years, is observed when compared with the results derived from the right-tail Lognormal distribution for defect diameters.

Table 4.5: Summary statistics for times to first UFC failures (Weibull Defect Model)

Statistic	Time (10^6 years)
Mean	7.79
Median	7.79
Standard Deviation	1.10
Minimum	4.60
Maximum	10.82

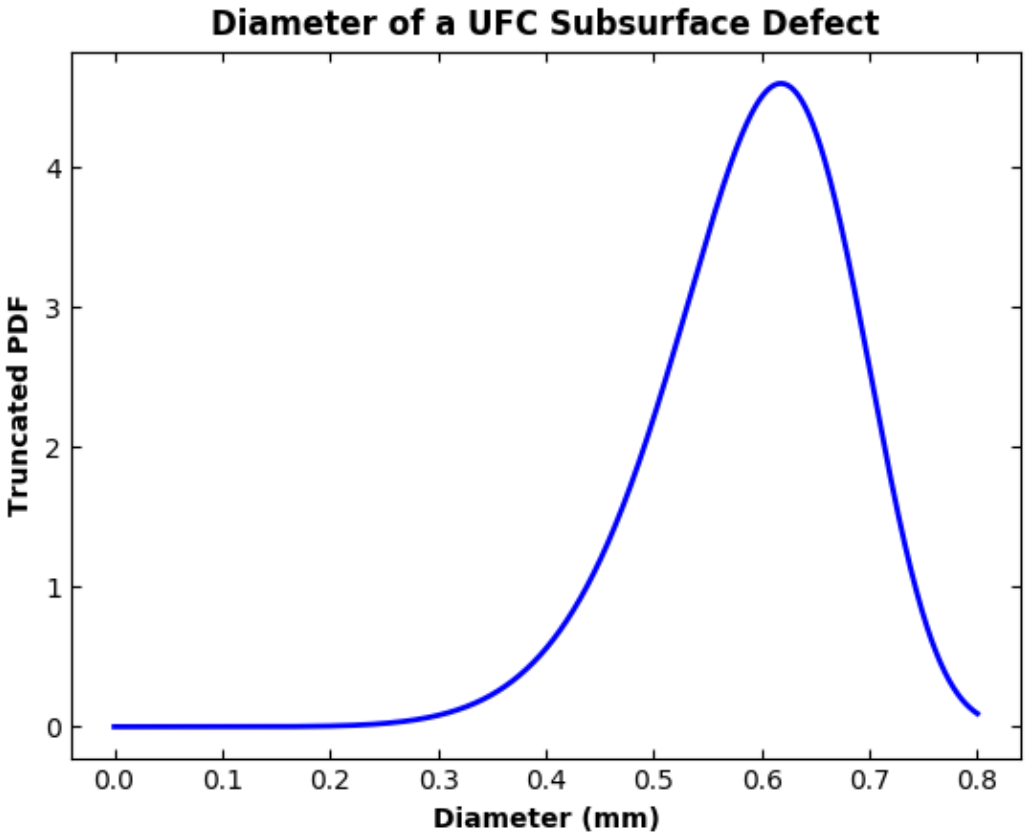

Figure 4.5: Postulated left-tail Weibull distribution for subsurface defect diameters for a defective UFC.

4.2 Repository Temperature Model Formulation

Similar to the methodologies employed by Johnson et al. (1994); Shoesmith et al. (1995, 1997), variation in cooling rates across a DGR may be modelled by creating two temperature zones, Figure 4.7, with corresponding temperature profiles, Figure 3.1, associated with an arbitrary point on the UFC surface (Guo, 2017). Two temperature zones is a simplification of actual temperature variations anticipated in the DGR but is consistent with the work presented in Guo (2017). The four interior panels comprise the high temperature zone (Zone I), or the zone for which cooling rates are lower than in other placement rooms in the DGR, and, therefore, UFCs in Zone I would sustain high temperatures (or

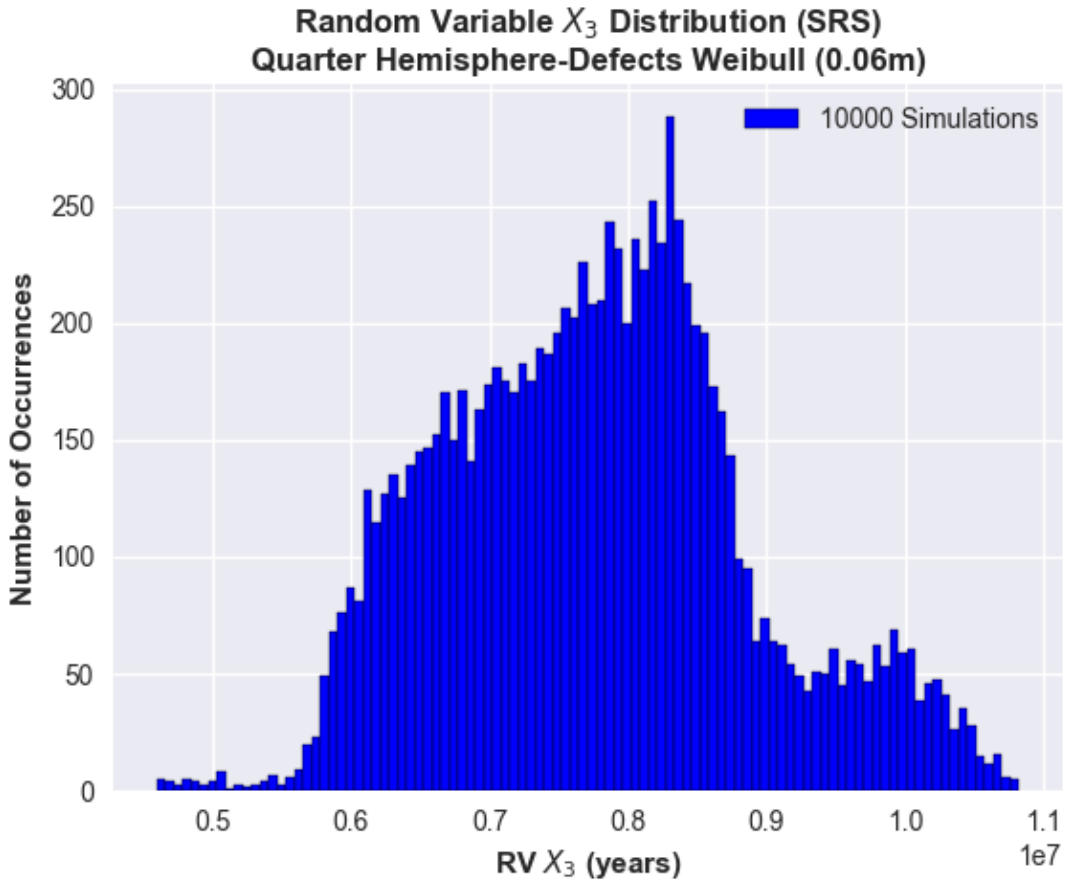

Figure 4.6: Estimated distribution for RV X_3, based on a 0.06-m mesh size and with probability p of subsurface defects modelled by a left-tail Weibull distribution.

dry-out periods) for a longer period of time than other UFCs in the DGR. The four exterior panels comprise the low temperature zone (Zone II), or the zone for which the cooling rate is higher than the placement rooms in Zone I. For the present work the UFC surface temperature profile at Panel F (Zone II) is considered.

Inflow of groundwater during saturation will be characterised by higher than ambient temperatures and will commence at different times for each of the two temperature zones due to differences in cooling rates. Consequently, the effect of higher than ambient temperatures in the advancing groundwaters will be reflected in higher porewater effective diffusion coefficients for HS^-. The effect of temperature on the diffusivity of ions in clays

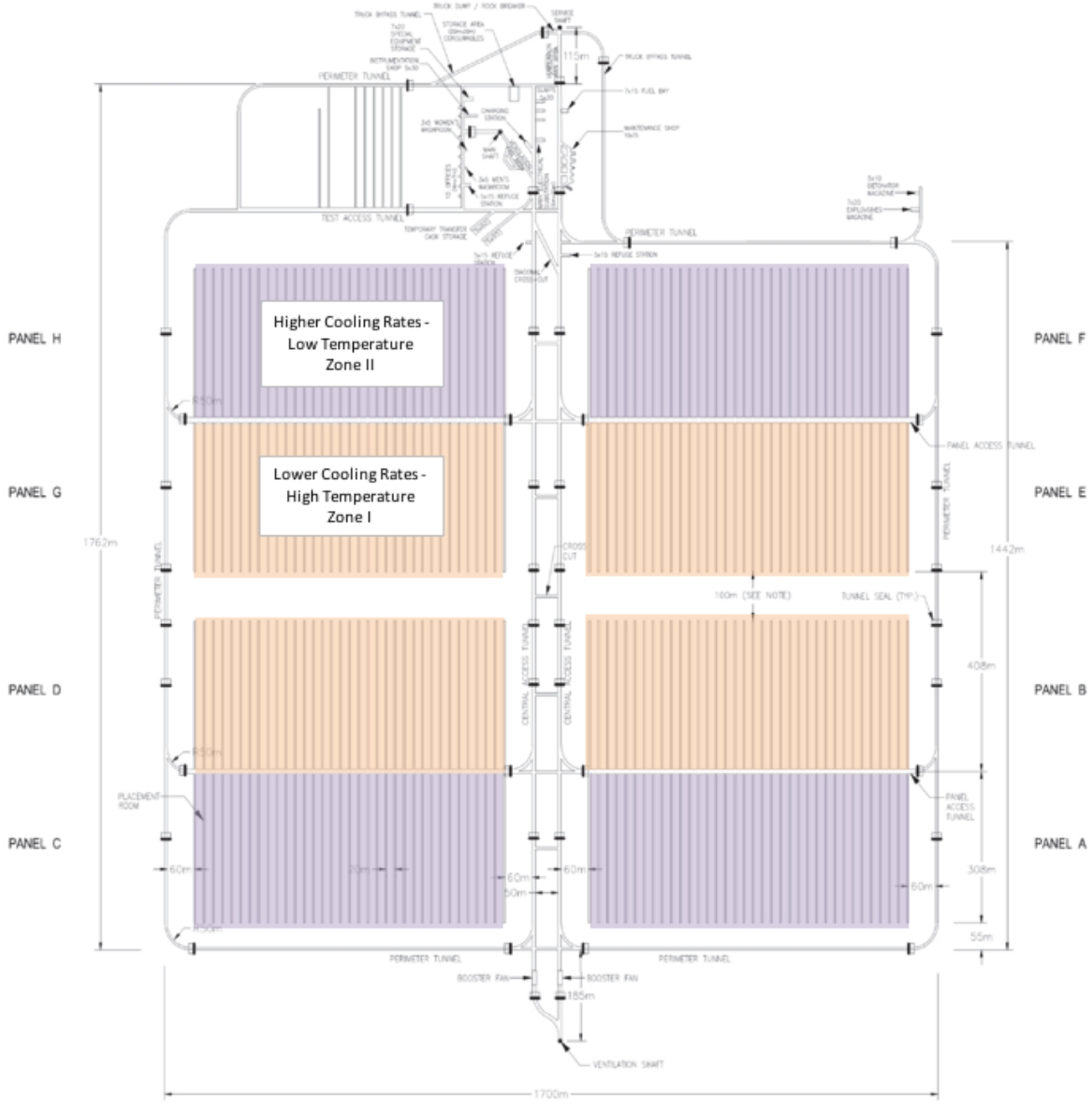

Figure 4.7: Simplified temperature zones within a hypothetical crystalline rock DGR (Noronha, 2016).

has been demonstrated by Mon et al. (2016) and Rowe et al. (2005) to be reasonably

approximated by the temperature correction applied to free-water diffusion:

$$\frac{D_{\mathrm{T}_i}}{D_{\mathrm{T}_j}} = \frac{T_i \eta_j}{T_j \eta_i}. \tag{4.5}$$

Equation 4.5 is the well-known Einstein-Stokes equation (Einstein, 1905) for a spherical particle under Brownian motion, with (absolute) temperatures T_i, T_j, temperature-dependent diffusion coefficients $D_{\mathrm{T}_i}, D_{\mathrm{T}_j}$, and the temperature-dependent dynamic or kinematic viscosity of water η_i, η_j, all associated with repository time periods i, j. For the present model, the effect of temperature on the effective diffusion coefficient of HS^- in bentonite buffer pore water is approximated by applying the correction proposed by Equation 4.5, with dynamic viscosity of water determined as per Huber et al. (2009). This approach was employed by Briggs et al. (2017) and more recently by Rashwan et al. (2022). To simplify computation, additional assumptions and approximations are employed as discussed below.

The near-field is assumed to attain full saturation by the time UFC surfaces reach peak temperature in Panel F (i.e., at approximately 83°C), which presently is estimated to occur roughly 50 years after repository closure. From a modelling perspective, this translates to effectively starting simulations approximately 50 years after repository closure, an error which is inconsequential relative to repository timescales and ignored in the calculations of UFC minimum times to failure. Additionally, the expected temperature gradient from the hotter UFC surfaces to the colder regions of the emplacement room walls is ignored, and the temperature to which the bentonite clay buffer is elevated as hydrogen sulphide ions diffuse from the geosphere to the UFC surfaces is taken as the estimated, time-dependent UFC surface temperature, Figure 3.1 (Panel F). This is a conservative assumption. Lastly, a step function is used to approximate the UFC surface cooling profile presented in Figure 3.1 (Panel F) over the range from peak temperature to ambient conditions. A correction factor derived from Equation 4.5 is applied subsequently at each temperature step for the step duration. Correction factors and time-temperature steps employed in the modelling are included in Table 4.6. Note, the correction factor is applied to the randomly drawn effective diffusion coefficient for HS^-.

The multi-level probabilistic formulation developed in Chapter 3 cannot be directly applied to account for temperature effects without some modification. In particular, the variable of interest at each time step is now the corrosion rate, or more specifically, the total corrosion damage (i.e., equivalent depth) sustained during each time-temperature step. Corrosion rate can be expressed using Equation 3.9, modified to account for the multi-level framework. Moreover, because the objective is first times to failure, the maximum

Table 4.6: Step function approximation of cooling curve on UFC surface, Panel F

Time Step r	Start Time (years)	End Time (years)	Step Length t_r (years)	Temp (°C)	Temp (°K)	Viscosity	Correction Factor (β_r)
1	44	100	56	83	356.15	0.0003425	4.800
2	100	230	130	75	348.15	0.0003785	4.246
3	230	500	270	70	343.15	0.0004046	3.915
4	500	900	400	66	339.15	0.00042804	3.657
5	900	1700	800	61	334.15	0.00046038	3.350
6	1700	3750	2050	54	327.15	0.00051294	2.944
7	3750	7000	3250	48	321.15	0.0005667	2.616
8	7000	11000	4000	42	315.15	0.00063006	2.309
9	11000	17000	6000	35	308.15	0.0007191	1.9789
10	17000	25085	8085	27	300.15	0.00085304	1.6249
11	25085	35100	10015	21	294.15	0.00097964	1.386
12	35100	45118	10018	16	289.15	0.00111104	1.201
13	45118	55134	10016	14	287.15	0.00117204	1.131
14	55134	65150	10016	12	285.15	0.00123952	1.062
15	65150	75167	10017	11.5	284.65	0.00125639	1.046
16	75167	85184	10017	11	284.15	0.00127326	1.030
17	85184	95200	10016	10.5	283.65	0.00129013	1.015
18	95200	100210	5010	10	283.15	0.001307	1

corrosion rate, labelled $X_{d_{\text{Corr}}}^{max}$, is the real variable of interest:

$$X_{d_{\text{Corr}}}^{max} \coloneqq max \left\{ \frac{X_{D_{\text{HS}}}^{j} X_{C_0}^{k} f_{\text{HS}} M_{\text{Cu}}}{l_{\text{eff}}^{i} \rho_{\text{Cu}}} \right\}. \tag{4.6}$$

The maximum corrosion rate $X_{d_{\text{Corr}}}^{max}$ is a RV and represents the quotient of the product

of two RVs ($X^j_{D_{\text{HS}}}$ and $X^k_{C_0}$) and l^i_{eff}, multiplied by a constant ($f_{\text{HS}} M_{\text{Cu}}/\rho_{\text{Cu}}$). With $X^{max}_{d_{\text{Corr}}}$ known, the total corrosion depth, labelled $X^{max}_{\text{depth},r}$, can be determined by multiplying the maximum corrosion rate for the rth time-temperature step by the time length t_r of the rth step; that is,

$$X^{max}_{\text{depth},r} \coloneqq X^{max}_{d_{\text{Corr}}} \times t_r. \tag{4.7}$$

Consistent with the previous formulation, Equations 4.6 and 4.7 identify two RVs of interest, representing respectively the maximum corrosion rates and depths for a given time step r. Separating out the components in Equation 4.6 that contribute to the overall corrosion rate allows use of the multi-level framework. For instance, a cursory inspection of Equation 4.6 reveals that from among the equation parameters, at the UFC level (i.e., Level 1), only the effective diffusion length l^i_{eff} varies (deterministically). This means that one must look beyond Level 1 to account for the variation in relevant properties within an emplacement room that contribute to maximum corrosion rates. More specifically, within a given emplacement room the only components of Equation 4.6 subject to variation are $X^j_{D_{\text{HS}}}$ and l^i_{eff}. Further, Equation 4.6 informs the reader that the maximum corrosion rate in any given emplacement room will occur on the UFC where the quotient $X^j_{D_{\text{HS}}}/l^i_{\text{eff}}$ is a maximum, since all other equation parameters are constant. An understanding of the levels in a DGR as discussed in Chapter 3 suggests that the maximum corrosion rate in an arbitrary emplacement room always occurs where l^i_{eff} is a minimum regardless of the value of $X^j_{D_{\text{HS}}}$. That this is clear, one needs only to consider an arbitrary emplacement room with 375 UFCs, each of which are surrounded by a single buffer box that takes on a single value (i.e., from section 3.5.2 the RV $X^j_{D_{\text{HS}}}$ is assigned a value randomly) from the baseline distribution for D_{HS}. Of all possible values across a single UFC (i.e., a fixed j) which the quotient $X^j_{D_{\text{HS}}}/l^i_{\text{eff}}$ assumes, the maximum occurs at the minimum $l^i_{\text{eff}} \forall i$. Extending this across all 375 UFCs in an arbitrary emplacement room, it is easy to see that the maximum value for $X^j_{D_{\text{HS}}}/l^i_{\text{eff}} \forall i, j$ occurs at the maximum of the set $\left\{X^j_{D_{\text{HS}}}/min\left\{l^i_{\text{eff}}\right\}\right\}$.

To account for the effect on temperature, the correction factor β_r from Table 4.6 is applied to $X^j_{D_{\text{HS}}}$. Therefore, for any arbitrary emplacement room, at time step r, corresponding to a cooling period during a temperature transient, the maximum corrosion rate occurs at $max\left\{\beta_r X^j_{D_{\text{HS}}}/min\left\{l^i_{\text{eff}}\right\}\right\}$. Define for Level 2 the RV Y^r_2 such that

$$Y^r_2 \coloneqq max\left\{\frac{\beta_r X^j_{D_{\text{HS}}}}{l^{min}_{\text{eff}}}\right\} \quad \forall j; j = 1, 2, \ldots, 375. \tag{4.8}$$

Equation 4.8 may be interpreted to mean that for any given emplacement room, the maximum corrosion rate will always occur at the jth UFC where $X^j_{D_{\text{HS}}}$ is maximum among all assumed (assigned) values and at the node associated with l^{min}_{eff}. This is true regardless of

β_r. Both β_r and l_{eff}^{min} are constants for any time step r in Equation 4.8. The RV Y_2^r points to where the maximum corrosion rate occurs—both in an arbitrary emplacement room and locally on the UFC sustaining the highest rate of corrosion. This does not mean that the first failure will occur here, however. A subtle but important point to understand.

Extending the above formulation to Level 3, by bringing the RV Y_2^r into the context of Equation 4.6, one can re-define $X_{d_{\text{Corr}}}^{max}$ as Y_3^r,

$$Y_3^r \coloneqq max \left\{ \frac{Y_2^r X_{C_0}^k f_{\text{HS}} M_{\text{Cu}}}{\rho_{\text{Cu}}} \right\} \quad \forall k; k = 1, 2, \ldots, 36. \tag{4.9}$$

With Equation 4.9, the interpretation becomes clearer such that for any given panel, the maximum corrosion rate will occur at the kth emplacement room associated with the greatest [HS^-], at the jth UFC with largest $X_{D_{\text{HS}}}^j$, and at the node associated with l_{eff}^{min}. As before, this does not mean that the first failure will occur here because (net) copper thickness varies across the UFC and may not necessarily be at a minimum at the node corresponding with l_{eff}^{min}.

To employ Equations 4.8 and 4.9, one needs to step through each time step, estimating at each time step the distribution of Y_3^r and multiplying the same by the length of the time step t_r from Table 4.6 to obtain an estimate of the maximum corrosion sustained during the time step. Accordingly, Equation 4.7 becomes

$$X_{\text{depth},r}^{max} \coloneqq Y_3^r \times t_r. \tag{4.10}$$

Consequently, the total maximum corrosion damage $X_{\text{depth,total}}^{max}$, sustained by the end of the cooling period, is given by

$$X_{\text{depth,total}}^{max} \coloneqq \sum_{1}^{r} Y_3^r \times t_r. \tag{4.11}$$

At each time step, a LHS scheme was employed with 10000 realisations to estimate Y_2^r and Y_3^r, similar to the approach used in section 3.5.2. The estimated distribution for $X_{\text{depth,total}}^{max}$ is depicted in Figure 4.8.

Once the cooling period is complete, the estimation of first times to failure can be determined by following the methodology described in section 3.5.2. The only exception is that now there is a correction to the RV X_1 defined in Equation 3.13 to account for the total "accelerated" corrosion damage sustained during the cool down. Consequently, also taking into the account the potential for coating defects (Equation 4.3), the effect of temperature on X_1 may be expressed as follows:

$$X_1 \coloneqq min(\mathbf{x}) = min \left\{ (X_{t_{\text{Cu}}}^{\text{net}} - X_{\text{depth,total}}^{max}) l_{\text{eff}}^i \right\} \quad \forall i; i = 1, 2, \ldots, n, \tag{4.12}$$

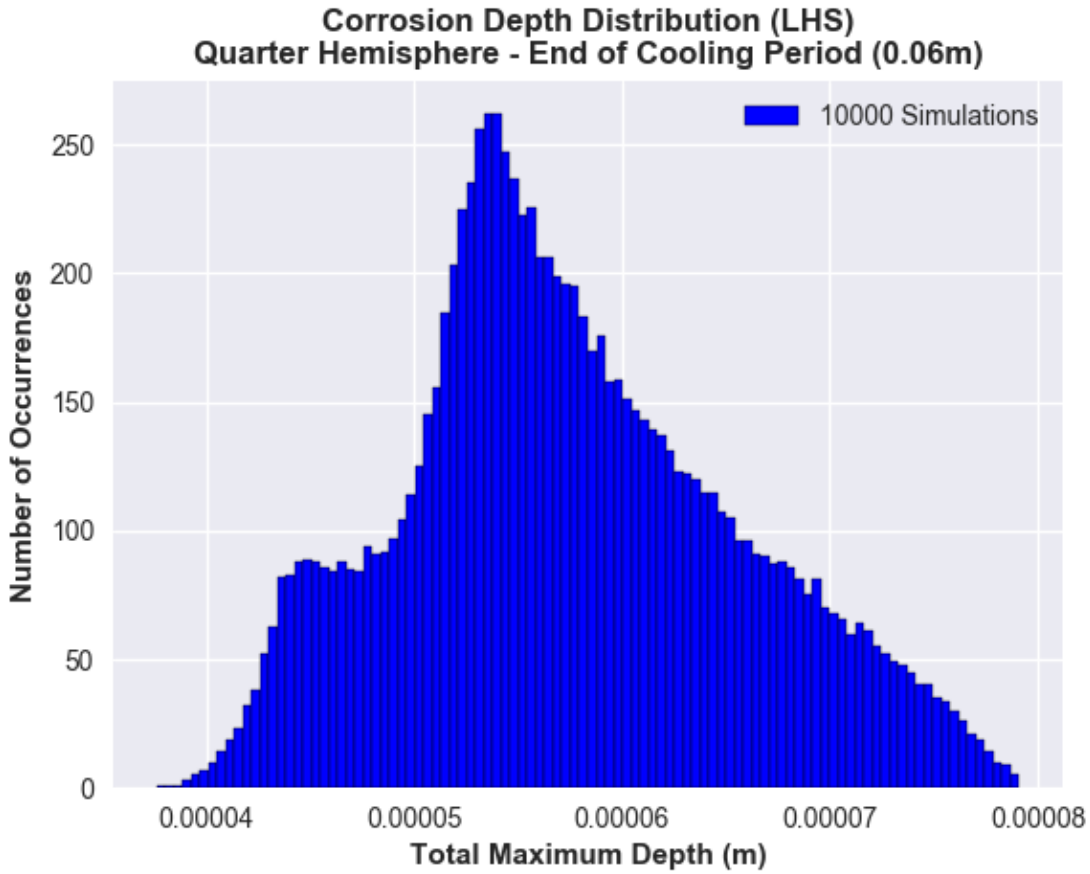

Figure 4.8: Estimated distribution for RV $X^{max}_{\text{depth,total}}$, representing the distribution in the total maximum corrosion depth at the end of the cooling period, for a 0.06-m mesh size.

where n is the number of nodes associated with the mesh size. With the potential for defects—and subsequently sparsely populated long left-tail distributions for X_1 and X_2—stratified random sampling with Neyman allocation was applied to Equation 4.12, along with the rest of the methodology described in section 3.5.2. To be consistent, computations for net copper thickness were carried out using the right-tail Lognormal function representation for the defect diameter distribution.

4.2.1 Time-to-Failure Predictions

Figure 4.9 illustrates the resulting first times to failure, with the summary statistics provided in Table 4.7. The results show that for the short cooling period defined by Figure 3.1, the combined effect of temperature and subsurface defects leads to a further reduction, on average, of approximately 400000 years on UFC first times to failure, which is approximately equal to the effect of subsurface defects alone (right-tail Lognormal representation). When compared with the minimum UFC lifetime predicted by the baseline model (i.e., 5.42×10^6 years, Table 3.5), the effect of temperature alone represents a decrease of approximately 7.4% on average in predicted minimum UFC lifetimes.

Table 4.7: Summary statistics for times to first UFC failures (Defect & Temperature Effect Model)

Statistic	Time (10^6 years)
Mean	7.65
Median	7.65
Standard Deviation	1.12
Minimum	4.60
Maximum	10.71

4.3 Summary

Incorporating latent defects into the baseline model leads naturally to shorter predicted UFC first times to failure, but the reduction in UFC lifetime is not too significant relative to DGR timescales of interest. This is in part attributed to the assumed distribution shape for defect diameters, which only becomes a significant factor in reducing UFC lifetimes—in the order of 800000 years—when a more pessimistic outlook on the distribution of defects is assumed (e.g., left-tail Weibull). The simple evaluation of epistemic uncertainty associated with the chosen distribution for defect diameters underscores the need to better characterise coating defects. While not assessed in this work, the distribution for p—the probability of a defective UFC coating—is a significant factor in determining the fraction of early UFC failures. Therefore, the fraction and timing of early failures will be governed by the

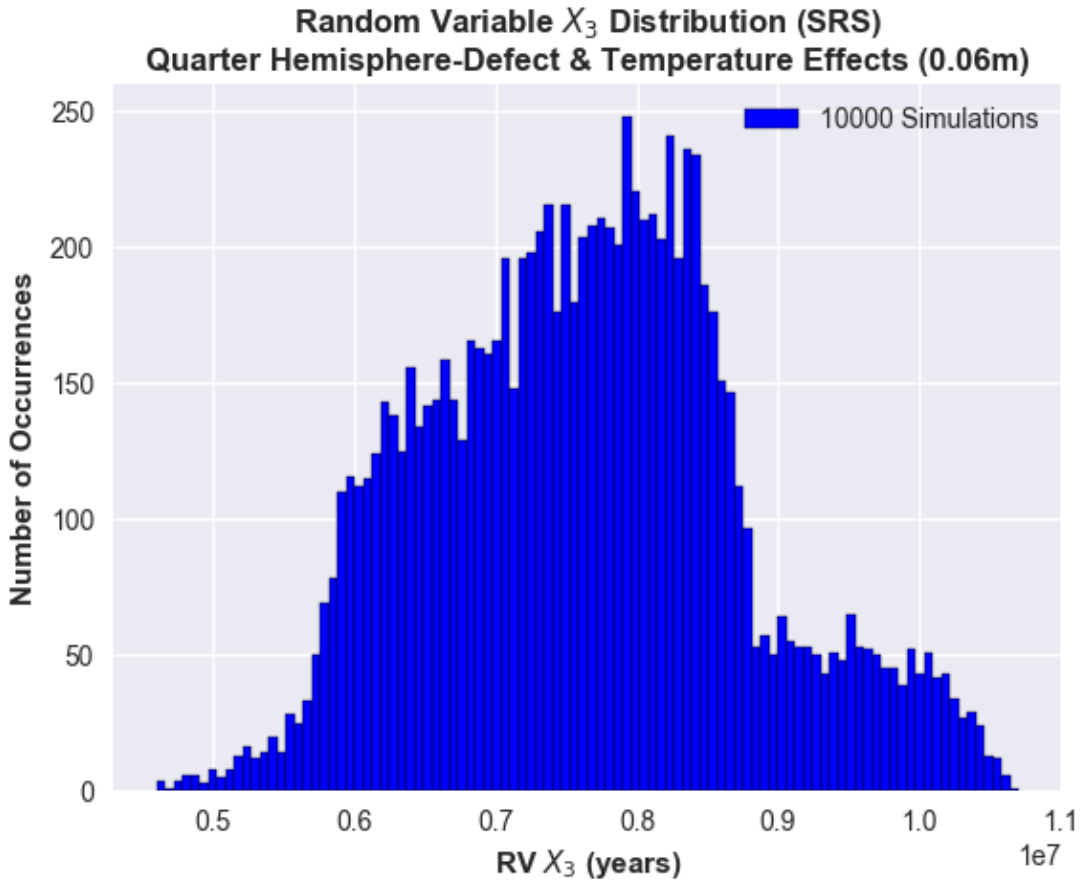

Figure 4.9: Estimated distribution for RV X_3, based on a 0.06-m mesh size. The distribution accounts for the probability p of subsurface defects modelled by a right-tail Lognormal distribution and temperature effects causing accelerated corrosion damage during a cooling period.

respective distributions chosen for p and defect diameters. Admittedly, a gap in knowledge exists concerning p as it pertains to UFC electrodeposited copper coatings, particularly within a large-scale manufacturing setting. Latent defects are not limited to subsurface coating defects, however, though this was the interpretation applied in the present model. In one respect, the interpretation of latent defects as being similar to coating porosity, for instance, precludes the use of p since it may be argued that all copper coatings will have porosity to varying degree (i.e., it is inherent to both the electrodeposition and cold spray processes). Although this is a valid perspective, the intent here was to develop a

framework that would allow for the incorporation of defects; and this was accomplished irrespective of the nature of the defects. But more work is required if there is a need to account for spatial variability such as the propensity for defects to manifest or cluster at specific surface regions of a UFC.

Latent defects can take the form of FOD introduced to the UFC surfaces on route from encapsulation to placement. In fact, FOD may result in defects that are effectively greater in depth than the maximum assumed subsurface coating defect diameter (i.e., 0.8 mm) not detectable by present NDE methods planned immediately following electrodeposition. The potential for latent defects due to FOD needs to be adequately assessed along the entire manufacturing-placement process route.

Under the present assumptions concerning the distributions of p and defect diameters, increasing the number of realisations from 10^4 to at least 10^5 would likely give rise to shorter UFC first times to failure. This point was made clear by the bounding (lower bound) point estimate results, where it was evident that the bounding point estimate was still noticeably lower than the predicted minimum UFC lifetime at 10^4 realisations though still within the same order of magnitude. Given the chosen distributions for p and defect diameters, and the multi-level probabilistic framework, it is anticipated that a significantly large number of realisations (e.g., $> 10^5$) would be required to approach the lower bound point estimate. The lower bound point estimate may be seen as a rare event, however.

The effect of temperature on UFC lifetimes was explored using a simple correction applied to the effective diffusion coefficient for HS^- based on the Einstein-Stokes equation. Several additional simplifying yet overall conservative assumptions were incorporated to permit computational estimates of UFC lifetimes under the effect of temperature. For the cooling period duration anticipated in a hypothetical Canadian crystalline rock DGR, temperature decreased the minimum UFC lifetimes by approximately 400000 years and had an equivalent effect to that of latent defects represented by a right-tail Lognormal distribution. Relative to the baseline model, the effect of temperature on average leads to an approximate 7.4% reduction in the predicted minimum UFC lifetime. This result is lower than that reported by Briggs et al. (2017), who estimated a 12% increase in the flux of HS^- arriving at the surface of the UFC over a timespan of 10^6 years when incorporating the effect of repository temperatures via the Einstein-Stokes equation. A possible explanation for this discrepancy is the fact that the repository temperature profile used by Briggs et al. (2017) was stated by the authors to over-predict the expected temperatures in the time interval from 200 to 2000 years, which is when the correction factor is relatively large. Assuming the approach employed to quantify the effect of temperature is reasonable, temperature can be seen as a contributing factor to reduced UFC lifetimes but one that is potentially less significant than latent defects, depending on the actual defect distribution.

Chapter 5

Stochastic Process Model

This chapter presents a stochastic process model to approximate pitting corrosion in the copper coating of UFCs. Pitting corrosion is assumed plausible during the brief oxic period postulated for the DGR environment. The chapter unfolds in the following way. A brief literature review of different stochastic processes used to model pitting corrosion is provided in Section 5.1, with an emphasis on the more prevalent approach. Introduced in Section 5.2 is the surrogate data employed in the model fitting. The chapter then turns to development of the stochastic process model, which requires two steps. The first formulates an expression to approximate the intensity of the pitting process in terms of occurrence and magnitude of pit depths consequential to UFC lifetimes. The NHPP and the GPD, with a POT framework, are employed in this step. The second incorporates the aforementioned intensity function into a first-order NHMP for the purpose of estimating pit depth distributions at some time t, representing the length of the oxic period. Estimation of pit depth distribution occurs by the propagation of an initial pit depth distribution across a Markov chain. The two steps are detailed in Section 5.3 and Section 5.4, respectively, with model efficacy demonstrated in Section 5.4. Assignment of relevant pit depths onto the surface of a UFC is covered separately in Section 5.5. Section 5.6 compares the results of the baseline model (Chapter 3) with that resulting from the combined effect of sulphide-induced and pitting corrosion. For completeness, this section also compares the more traditional extreme value statistical approaches for modelling evolution of pit depths with the present results. Lastly, Section 5.7 provides a brief summary of the chapter. The problem statement addressed in this chapter is to characterise the distribution of extreme pit depths for an arbitrarily selected time span, which is an approximation to the length of the oxic period in the DGR, and to determine subsequently a means to assign pit depths to a UFC for estimating lifetimes.

5.1 Brief Literature Review

Historically, stochastic processes used to model pit growth, or the growth of corrosion defects, include the stationary Gamma process (Cheng and Pandey, 2012; Zhang and Zhou, 2013), the Fokker-Planck process (Camacho et al., 2011), the inverse Gaussian process (Zhang et al., 2013), the geometric Brownian motion process (Zhang and Zhou, 2015), and the Itô linear stochastic process (Fontes et al., 2015). The Markov process, however, seems to be the most popular approach. A detailed literature review of pit growth modelled as a Markov process is found in Appendix A. Here, only a brief summary is provided.

Since Provan and Rodriguez III (1989), who appear to be the first to apply the Markov process—specifically a Markov chain—to pit growth, a host of authors such as Caleyo et al. (2009); He et al. (2019); Hong (1999a); McCallum et al. (2014); Ossai et al. (2016); Timashev et al. (2008); Valor et al. (2007, 2010, 2013); Xie et al. (2018) have applied the Markov process to pitting corrosion, corrosion defects, or environmentally-induced wear. But the approach put forward by Valor and colleagues has gained the most traction, being adopted entirely, or in part, by He et al. (2019); McCallum et al. (2014); Ossai et al. (2016), each with varying degrees of success.

What sets the work by Valor and colleagues apart is the simplicity with which a key process parameter is determined. Very briefly—as this is discussed in much more detail in the sections to follow, a Markov chain is used to model a process, whose possible states are represented by the points where the chain links connect. The process is said to transition from state to state along the chain, with a rate or intensity of transition (also called the intensity function) determined by a single parameter, often labelled λ (or $\lambda(t)$ if time-dependent). Without this parameter, a Markov chain cannot be employed. In addition to justifying the use of a Markov chain to model the evolution of a process, the major challenge facing a modeller is the determination of λ. If there is sufficient process data, time-independent λ may be obtained by solving sequentially a system of differential equations governing the state probabilities. When λ is a function of time, the functional form is required a priori. Until Valor et al. (2007), the formulations proposed for $\lambda(t)$ in earlier works were complicated and lacked physical justification or clear basis. Instead, Caleyo et al. (2009); Valor et al. (2007, 2010, 2013) proposed two formulations[1]:

1. $\lambda(t) = \chi\omega t^{\omega-1}$, where Weibull parameters χ and ω are determined through the minimisation of an error function comprising—in a very general sense—the difference

[1] Alma Valor is a co-author in Caleyo et al. (2009) and very likely the inspiration behind the formulations for $\lambda(t)$ presented in Caleyo et al. (2009).

in mean and variance of a limiting form of the cumulative distribution function for pit depth maxima and the Gumbel distribution fitted to data.

2. $\lambda(t) = \beta/(t-t_{sd})$, where the parameter β stems from the empirical power-law expression for the mean of pit depth maxima $\bar{D}(t) \coloneqq \alpha(t-t_{sd})^{\beta}$, with t and t_{sd} representing an arbitrary future time and the start of the pit growth process (i.e., after initiation), respectively.

Both formulations described above were employed in a pure-birth, linear-growth-rate (time-dependent) model of the Markov process, but only the second formulation was used by the authors in a Markov chain to propagate an initial distribution of pit depth maxima to a future time t. To facilitate the use of a Markov chain, Caleyo et al. (2009); Valor et al. (2013) employed Parzen's (Parzen, 2015) closed-form solution for the set of differential equations governing the state probabilities of a pure-birth, linear-growth-rate (time-dependent) model, substituting subsequently into that solution their expression for $\lambda(t)$. Consequently, the second formulation for $\lambda(t)$ is the focus of this brief review.

Caleyo et al. (2009); Valor et al. (2013) argue the validity of the second formulation based on the work by Cox and Miller (1987), who—for pedagogical reasons—present an analysis termed "deterministic" to gain insight into the (statistical) expectation of a population size, and to show thereby that this expectation is the same as that derived for the size of a population modelled as a pure-birth, linear-growth-rate stochastic process, with time independence. The equivalence of the "deterministic" and stochastic expectations is used by Caleyo et al. (2009); Valor et al. (2013) to justify their proposition that the empirical power-law expression for the mean of pit depth maxima $\bar{D}(t) \coloneqq \alpha(t-t_{sd})^{\beta}$ is equivalent to the expected population size when modelled by a pure-birth, linear-growth-rate stochastic process, with time dependence. Of note, Cox and Miller (1987) examined a time-independent process for both the "deterministic" and stochastic model. Caleyo et al. (2009); Valor et al. (2013) extend this equivalence to the time-dependent case for $\lambda(t)$, without proof or explicit justification. It turns out, as shown in Section A.2.2, that the illustration presented by Cox and Miller (1987) also holds for $\lambda(t)$ though with a slight change in formulation. For completeness, the three main points that underpin the assertion of equivalence by Caleyo et al. (2009); Valor et al. (2013) are summarised below (details are found in Section A.2.2):

1. (Cox and Miller (1987)) The size of a population $n(t)$ at time t is not random but "deterministic" and large enough to be treated as a continuous function of t. Further, let the intensity function be defined as the product of the intrinsic transition rate λ

and the size of the population (i.e., $n(t)\lambda$, which is analogous to a pure-birth, linear-growth-rate process), and for a small interval of time Δt the size of the population increases by $n(t)\lambda\Delta t$. Provided the limit $\Delta t \to 0$ exists, the expected size of the population at time t, given the initial population size n_0, is

$$n(t) = n_0 e^{\lambda \cdot t}. \tag{5.1}$$

2. (Cox and Miller (1987)) For a random population $N(t)$, modelled as a time-independent pure-birth, linear-growth-rate stochastic process, the expected size is

$$E[N(t)] = N_0 e^{\lambda \cdot t}, \tag{5.2}$$

where N_0 is the initial population size.

3. (Caleyo et al. (2009); Valor et al. (2013)) By virtue of 1 and 2, the expected size of a random population $N(t)$, modelled as a time-dependent pure-birth, linear-growth-rate stochastic process, is equivalent to the "deterministic" mean of pit depth maxima; that is,

$$E[N(t)] = N_0(t_0) e^{\Lambda(t) - \Lambda(t_0)} \equiv \bar{D}(t) \coloneqq \alpha (t - t_{sd})^{\beta}, \tag{5.3}$$

where $\Lambda(t, t_0) \coloneqq \int_{t_0}^{t} \lambda(\tau) d\tau$.[2] Thus, when $t_0 = 0$ and $N_0(t_0) = 1$,[3]

$$\Lambda(t) = \ln \left[\alpha (t - t_{sd})^{\beta} \right], \tag{5.4}$$

$$\frac{d\Lambda(t)}{dt} \equiv \lambda(t) = \frac{\beta}{(t - t_{sd})}. \tag{5.5}$$

Equation 5.3 is valid provided the increase in the deterministic pit depth, $\Delta \bar{D}$, over a short time Δt, may be defined as

$$\Delta \bar{D} \coloneqq \bar{\lambda}(t) \bar{D} \Delta t, \tag{5.6}$$

and $\bar{\lambda}(t)$, interpreted as the intrinsic transition rate for a deterministic pitting corrosion process, may be defined as $\bar{\lambda}(t) \equiv \lambda(t) \coloneqq \beta / (t - t_{sd})$.

The simple expression for $\lambda(t)$ (Equation 5.5) positions the Caleyo et al. (2009); Valor et al. (2013) approach well above others, and the equivalence "deterministic" $\equiv$ stochastic

[2] Note, Caleyo et al. (2009); Valor et al. (2013) use the label $\rho(t)$ instead of $\Lambda(t)$, but for consistency with the labelling used in this chapter, the latter has been used.

[3] To be precise, $t_0 \geq t_{sd} \geq 0$.

facilitates the use of experimental or field corrosion data, whose mean may be justifiably characterised by a power-law expression, or any other suitable regression fit. The last statement is altogether implied in their approach, though it is not explicitly stated as such. This indicates that the functional form of $\lambda(t)$ is dependent on the regression fit chosen to characterise the data, having no probabilistic basis. By extension, their approach should appply equally to say the average pit depth above a specified threshold. In other words, the assertion that any regression fit to corrosion data, whether pit depth maxima or pit depths above some threshold, may be equated to the expected size of a population modelled by a pure-birth, linear-growth-rate time-dependent stochastic process should still hold. The strength of this assertion appears to be the condition attached by Caleyo et al. (2009); Valor et al. (2013) that restricts the process by which a change in the deterministic pit depth occurs to that defined for a pure-birth, linear-growth-rate time-dependent process, Equation 5.6. Put differently, if the pitting process can be mimicked by a pure-birth, linear-growth-rate time-dependent process, then—argue Caleyo et al. (2009); Valor et al. (2013)—the assertion implied by Equation 5.3 is valid.

The work by Caleyo et al. (2009); Valor et al. (2013) focused on the propagation of pit depth maxima. Pit depths above a specified threshold were also examined in Rivas et al. (2008); Valor et al. (2010, 2013), but under the second $\lambda(t)$ formulation and entirely to improve the minimisation scheme and not as the distribution of pit depths to propagate. As far as this author can tell, the propagation of pit depths above a threshold (vs pit depth maxima) across a pure-birth, linear-growth-rate time-dependent CTMC has not been demonstrated in the literature.

The work presented in the sections to follow seeks to show that $\lambda(t)$ may be derived solely from stochastic and asymptotic arguments without the need to resort to an equivalence between a deterministic—empirically derived—regression expression for pit growth and a stochastic representation of the same. Moreover, an assertion will be made and demonstrated that $\lambda(t)$ for a NHPP is in fact equivalent to that characterising a NHMP, enabling its employment in a pure-birth, linear-growth-rate time-dependent CTMC. Lastly, it will also be demonstrated that pit depths above a specified threshold may be adequately propagated across a pure-birth, linear-growth-rate time-dependent CTMC, increasing the utility of existing data and enabling UFC lifetime predictions associated with the effect of pitting corrosion to be more realistic.

5.2 Surrogate Pitting Corrosion Data

The data used in this work originates from Li et al. (2019). This author reached out to the primary author for the full dataset since the article only focused on maximum pit depths. The full dataset was subsequently received with permission (private communication).

Figure 5.1 shows the evolution of pit depths with time. The data, which is left-truncated arbitrarily by Li et al. (2019), represents pooled results from 100 304-stainless-steel corrosion coupons, arranged into sets of ten samples (samples and coupons are used interchangeably throughout). The exposed corrosion coupon surface area was approximately 10 mm $\times$ 50 mm. Each set of samples was immersed in 3.5 wt% NaCl solution at 30°C for 7, 14, 21, 28, 30, 60, 90, 120, 150, and 180 days, respectively. At each exposure period, one set was removed and pits measured.

Importantly, the data consists of two distinct experiments. The first experiment, which includes exposure periods 7-28 days, was used by Li et al. (2019) to generate a simple power-law model that was subsequently applied to predict the results for exposure periods 30-180 days. One will note that there is a slight difference in the pit depth trends between the two experiments, which is most pronounced at the 28- and 30-day exposure periods. While the experiments were, in principle, identical in terms of conditions, clearly there was variability between the two. For this work, the two experiments were considered one experiment, and any goodness-of-fit effects were ignored. Additional background relating to the challenges in finding suitable data are further discussed in Appendix B, Section B.2

5.3 Occurrence of Extreme Pit Depths as a NHPP

The focus of this section is to formulate an expression for the intensity density function of the stochastic process model, which is proposed to approximate the occurrence and magnitude of pit depths consequential to UFC lifetimes. Before proceeding with model formulation, however, it is beneficial (to the reader) to formally define a stochastic process, a Homogeneous Poisson Process (HPP), and finally a NHPP. Additionally, the form of the likelihood function, which is used to estimate the parameters of the NHPP, is reviewed.

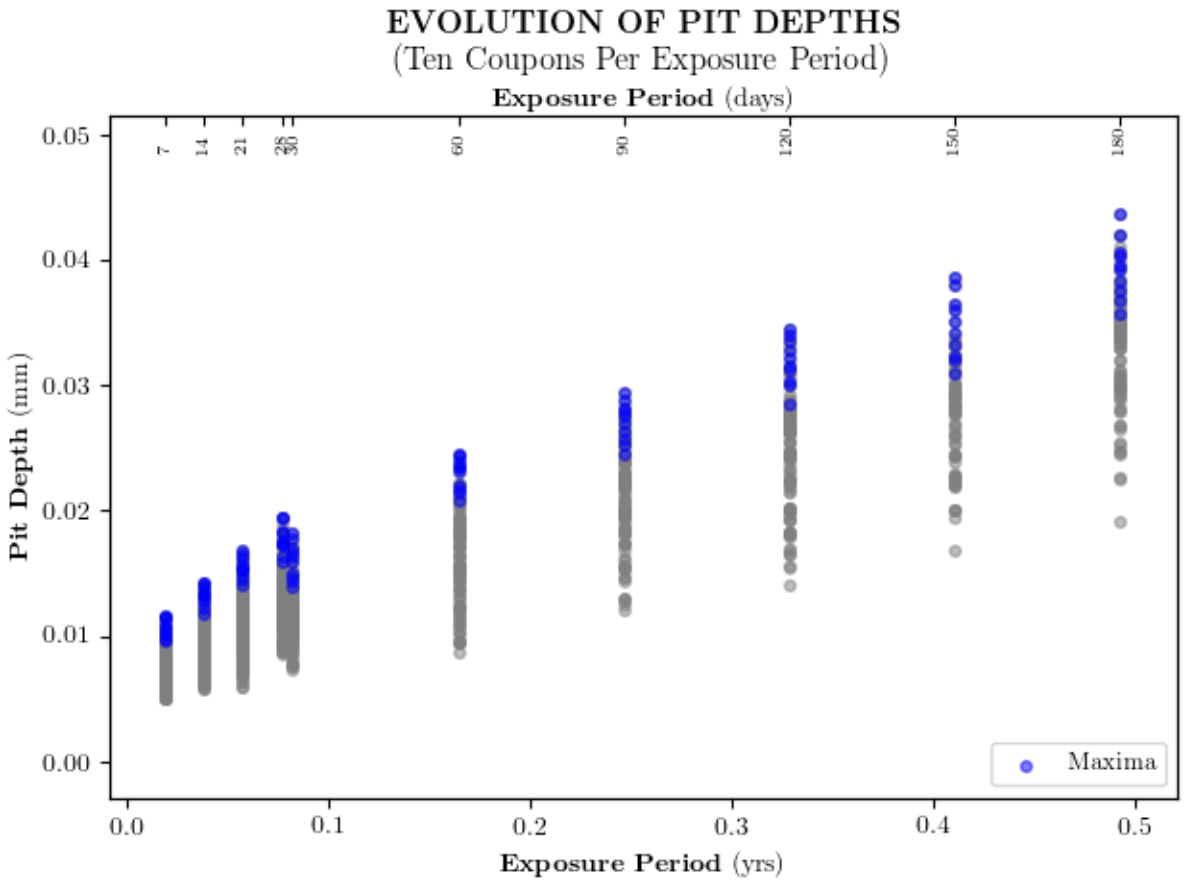

Figure 5.1: Pit depths versus time for 304 stainless steel coupons immersed in 3.5 wt% NaCl solution at 30°C (Li et al., 2019, by permission). The maxima per exposure period are highlighted in blue.

5.3.1 Preliminaries—Stochastic Process

Stochastic Process

Simply, a *stochastic*[4] process $\mathbf{X} := \{X(t); t \in \mathbf{T}\}$ is a collection (some authors use set, family, or ensemble) of RVs $X(t)$, which take on values at t in some state space $\mathbf{S}$, accord-

[4]The word *stochastic* is synonymous with "random" and originates from the Greek verb '$\sigma\tau o\chi\acute{\alpha}\zeta o\mu\alpha\iota$', which is understood to express the sentiment 'to shoot at, aim at, guess at', Grimmett and Stirzaker (2001, pg 213). Some authors use *random* processes instead (e.g., Gray and Davisson (1986); Grimmett and Stirzaker (2001); Hajek (2015); Peebles Jr. (2002)), but it is more common to associate *random* with

ing to some probability law[5]. The parameter t, sometimes referred to as the index of the process, takes on values in the parameter or index set $\mathbf{T}$. For the present work, $\mathbf{T}$ is the set of non-negative real numbers $\mathbb{R}_+$ (i.e., $\mathbf{T} \coloneqq [0, \infty)$), representing time typically defined in years, unless otherwise stated. A more elegant definition—one that emphasises the aim of this chapter—is: "*A stochastic process is the mathematical abstraction of an empirical process whose development is governed by probabilistic laws*," Doob (1953). Following Beichelt and Fatti (2002, pg 47), a stochastic process $\mathbf{X} \coloneqq \{X(t); t \in \mathbf{T}\}$ is completely determined if for all $n = 1, 2, \ldots$ and for all n-tuples $\{t_1, t_2, \ldots, t_n\}$, with $t_i \in \mathbf{T}$, the joint probability distribution functions of the random vectors $(X(t_1), X(t_2), \ldots, X(t_n))$ are known:

$$F_{X(t_1),X(t_2),\ldots,X(t_n)}(x_1, x_2, \ldots, x_n) = P(X(t_1) \leq x_1, X(t_2) \leq x_2, \ldots, X(t_n) \leq x_n). \tag{5.7}$$

The set of joint distribution functions defined by Equation 5.7 fully defines the probability distribution of the stochastic process $\mathbf{X}$. In the present work, $\mathbf{X} \coloneqq \{X(t); t \in \mathbf{T}\}$ represents a continuous parameter, continuous state space, stochastic process.

Homogeneous Poisson Process

For many real-life applications, stochastic processes are nothing more than a random distribution of points (Brémaud (2020b, pg vii), Resnick (1987, pg 300)) or a localisation of events as points in time (Kass et al., 2014, pg 564). In such cases, they are more commonly referred to as *point* processes. The "canonical" Point process is the one-dimensional HPP. The HPP defines the number of points, events, or shocks[6] in a prescribed interval of time; that is, the HPP is the underlying process that governs the *number of events by time* t. The event of interest is the occurrence of the RV $X(t)$.

Define arrival of events as points in time given by $\{t_0, t_1, t_2, \ldots, t_{i-1}, t_i, \ldots\}$, and define event inter-arrival times (i.e., times between events) by $\{\tau_1, \tau_2, \ldots, \tau_{i-1}, \tau_i, \ldots\}$, where $t_0 = 0$ and $\tau_1 = t_1 - t_0$. For the HPP, event inter-arrival times are Exponentially distributed; that is, $\tau_i \sim \text{Exp}(\lambda)$, where λ is the constant, instantaneous rate of arrivals. When λ is constant, it is time-invariant. This is the meaning of the term homogeneous. Moreover, for the HPP the number of counts $N(s, t)$ in a time interval $[s, t), s, t > 0$, is Poisson-distributed; that is, $N(s, t) \sim \text{Pois}(\lambda \Delta t)$, with $\Delta t = t - s$ signifying that the HPP exhibits the *stationary* increments property—the distribution of counts is dependent on the width of the interval but not on the location (time) of the process. A homogeneous instantaneous

variables and *stochastic* with processes (Gallager, 2013, pg 16).

[5]The very simple definition of a *probability law* is a probability distribution function $F_X(x)$, where $F_X(x) = P(X \leq x)$, of a numerical valued random phenomenon represented by X, Parzen (1960, pg 177).

[6]The expression "shocks" to a system are more common in reliability analysis (e.g., Cha and Finkelstein (2018)).

rate of arrival implies a process that is stationary. Subsequently, characterisation of a HPP often amounts to counting the number of points (events) within an interval of time. This is referred to as a *counting* or *arrival* process $\mathbf{N} \coloneqq \{N(t) : t \geq t_0\}$, where t_0 is the initial time, typically set to zero, and $N(t)$ counts the number of events in $[0, t]$. The HPP may also be characterised by the inter-arrival times. In the context of the pitting corrosion data and the stochastic model proposed, the focus will be on counting the occurrence of extreme pit depths.

Non-Homogeneous Poisson Process

For the NHPP (also referred to as inhomogeneous, non-stationary, or temporal), which by definition is also a counting process $\mathbf{N}$, the following properties hold (see Cha and Finkelstein (2018, pg 77); Çinlar (1975, pg 94); Kao (2019, pg 56); Parzen (2015, pg 125); and Snyder and Miller (1991, pg 41)):

1. $P(N(t_0) = 0) = 1$;
2. For $t_0 \leq s < t$, the increments $N(s, t) = N(t) - N(s)$ is Poisson-distributed with parameter $\Lambda(s, t) \coloneqq \Lambda(t) - \Lambda(s)$,

$$P(N(s,t) = n) = \frac{1}{n!}(\Lambda(t) - \Lambda(s))^n e^{-(\Lambda(t)-\Lambda(s))}, n = 0, 1, 2, \ldots, \tag{5.8}$$

   where $\Lambda(t)$ is the intensity measure of the process (also called the mean value function, the mean measure, parameter function, or cumulative rate), and is a finite-valued, non-negative, non-decreasing function of t. Simply put, $\Lambda(s, t)$ is the statistical expectation or the expected number of events in the interval $[s, t)$ (i.e., $E[N(s, t)] = \Lambda(s, t)$) If the following limit[7] exists

$$\lim_{\Delta t \to 0^+} \frac{1 - P(N(t + \Delta t) - N(t) = 0)}{\Delta t} = \lambda(t), \tag{5.9}$$

[7]This limit is also expressed as $\lim_{\Delta t \to 0^+} \frac{P(N(t+\Delta t) - N(t) = 1)}{\Delta t} = \lambda(t)$ and implies that $P(N(t + \Delta t) - N(t) = 1) \approx \lambda(t)\Delta t + o(\Delta t)$. The Landau symbol "*little o of* Δt," $o(\Delta t)$, represents a function of Δt such that

$$\lim_{\Delta t \to 0} \frac{f(\Delta t)}{\Delta t} = 0,$$

expressing the idea that the function $f(\Delta t)$ approaches zero faster than Δt (pg 124 Canuto and Tabacco, 2015).

then $\Lambda(t)$ is said to be differentiable, right-continuous, and can be expressed as

$$\Lambda(t) = \int_{t_0}^{t} \lambda(\tau) d\tau, \tag{5.10}$$

where $t_0 = 0$, typically. The function $\lambda(t)$ is termed the intensity (density) function, representing the instantaneous average rate of the process at time t—the instantaneous average rate that points (events) occur. One can then write

$$P(N(s,t) = n) = \frac{1}{n!} \left(\int_{s}^{t} \lambda(\tau) d\tau \right)^{n} e^{-\int_{s}^{t} \lambda(\tau) d\tau}, n = 0, 1, 2, \ldots \tag{5.11}$$

For Δt very small,

$$P(N(t + \Delta t, t) = 1) \approx \lambda(t) \Delta t, \tag{5.12}$$

and

$$\lim_{\Delta t \to 0^{+}} \frac{P(N(t + \Delta t) - N(t) > 1)}{\Delta t} \to 0,$$

indicating that the probability of more that one event is negligible over the interval Δt very small (i.e., $P(N(t+\Delta t) - N(t) \geq 2) = o(\Delta t)$). A counting process that has the probability defined in the latter parentheses is said to be *orderly* or *regular* (Cha and Finkelstein, 2018, pg 25 and Snyder and Miller, 1991, pg 44); that is, qualitatively speaking multiple events do not occur simultaneously. This is the assumption made in this work.

3. $\{N(t) : t \geq t_0\}$ has independent, non-stationary increments. Independence means that the number of counts observed over disjoint subintervals are independent.

4. Inter-arrival times for a NHPP are $\sim \text{Exp}(\Lambda(s,t))$

Likelihood Function for Non-Homogeneous Poisson Process

Suppose a sample path of an arbitrary NHPP $\mathbf{N}$ with intensity density function $\lambda(t : \eta)$, consisting of n events, is observed over the interval $(0, T]$ at times $t = t_1 < t_2 < \cdots < t_n$, with no events occurring in the interval $(t_n, T]$. Here, the intensity function is parametrised with some arbitrary parameter vector η. Define ρ as the *event* that the aforementioned sample path is observed[8]. With reference to Equation (5.11) and Equation (5.12), the

[8]More concretely, the event ρ is defined as the observed sample path of points and corresponding cumulative count (i.e., $\rho := \{t_1, t_2, \ldots, t_n, N(t) = n\}$) for an arbitrary NHPP $\mathbf{N} := \{N(t) = t_0 \leq t < T\}$ on the interval $[t_0, T)$.

probability of the event ρ is the probability of observing no events (i.e., points) in the interval $(0, t_1)$, one event in $[t_1, t_1 + \Delta t_1)$, no events in the interval $[t_1 + \Delta t_1, t_2)$, one event in $[t_2, t_2 + \Delta t_2), \ldots,$ up to no events occurring in the interval $[t_n + \Delta t_n, T]$ (see Cha and Finkelstein (2018, pg 78); Kao (2019, pg 59); and Snyder and Miller (1991, pg 61)). Consequently, the probability of the event ρ is

$$P(\rho) = \exp\left(-\int_0^{t_1} \lambda(\tau : \eta)d\tau\right) \cdot \lambda(\tau : \eta)\Delta t_1 \cdot \exp\left(-\int_{t_1+\Delta t_1}^{t_2} \lambda(\tau : \eta)d\tau\right) \cdot \lambda(\tau : \eta)\Delta t_2 \cdots \exp\left(-\int_{t_i+\Delta t_i}^{T} \lambda(\tau : \eta)d\tau\right).$$

The corresponding joint density $f_{\mathbf{N}}(\rho)$[9] for the occurrence of event ρ is obtained by taking the limit as $\Delta t_i \to 0^+$

$$\begin{aligned} f_{\mathbf{N}}(\rho) &= \lim_{\Delta t_i \to 0^+} \frac{P(\rho)}{\prod_{i=1}^{n} \Delta t_i} \\ &= \prod_{i=1}^{n} \lambda(t_i : \eta) \exp(-\Lambda(T)). \end{aligned}$$

Suppose further that m such paths are observed on intervals $(0, T_j]$, where $j = 1, 2, \ldots, m$, consisting of n_j events each, then the joint density (Lawless, 1987), which is the likelihood function, is

$$L(\eta \,|\, t) = \prod_{j=1}^{m} \left\{ \prod_{i=1}^{n_j} \lambda(t_{ij} : \eta) \exp(-\Lambda(T_j)) \right\}. \tag{5.13}$$

5.3.2 NHPP-GPD Model Postulates

The objective of this section is to transform a cumulative degradation process, such as pitting corrosion, into an "equivalent" Point process—specifically a NHPP—by interpreting extreme pit depths as events that arrive (on the surface of a corrosion coupon) according to some intensity. As discussed in Appendix D, Section D.3, this is accomplished by simply placing a point at $(t, X(t))$ on a timeline for any extreme pit depth observation $X(t)$ taken at time t. More formally, if the RV $X(t)$ represents the depth of a pit at time t, which equivalently is interpreted as an event at t, and if sequences of pit depths over time are represented by $\mathbf{X} \coloneqq \{X(t); t \in \mathbf{T}\}$, then a stochastic process is an adequate probabilistic

[9] Also referred to as the *sample-function density*, Snyder and Miller (1991, pg 60).

framework to characterise the occurrence of pit depths. This is a reasonable proposition, provided suitable probability laws exist for $X(t)$. Two probability laws are proposed. One to account for the occurrence of pit depths, specifically the number of pit depths in a specified interval of time. The other to govern the magnitude of pit depths over the same interval. Both are discussed below.

For this work, the occurrence of extreme pit depths across a corrosion coupon within a specified time interval is approximated by a NHPP. Concretely, the expected number or count of extreme pit depths, measured across a corrosion coupon, in the interval $[s,t], 0 \leq s \leq t$, is approximated by invoking the counting process $\mathbf{N} \coloneqq \{N(t) : t \geq t_0\}$ characterisation of a NHPP. Accordingly, for the surrogate data, the expected number of extreme pit depths recorded at each exposure period per coupon is $E[N(s,t)] \coloneqq \Lambda(s,t)$. Additionally, the corresponding probability law is $N(s,t) \sim \text{Pois}(\Lambda(s,t))$, Equation 5.8. Employing a NHPP approximation implies that there is an underlying process for extreme pit depths that may be characterised by the parameter $\Lambda(s,t)$. Extreme pit depths need definition, however.

Pit depths applied to a UFC must be consequential (conservative) to UFC lifetimes. In this model, consequential and extreme pit depths are synonymous and defined as pits characterised by the right tail region of a time-dependent pit depth distribution. To be precise, an extreme pit depth is any pit depth $X(t)$ greater than or equal to some specified depth u_t (i.e., $X(t) \geq u_t$). The variable u_t is termed a *threshold* pit depth and is time-dependent. Consequently, the proposed probability law governing $X(t) \geq u_t$ is the time-variant GPD (Equation 5.14), defined within a POT framework. The GPD is the limiting distribution of events above some threshold, referred to as *exceedances*. Hence, $X(t)|X(t) \geq u_t$ is a pit depth exceedance, an extreme pit depth:

$$GPD(x \mid \mu_t, \alpha_t, \kappa_t, u_t) \coloneqq \left\{ 1 - \left[1 - \kappa_t \frac{(x - u_t)}{{\alpha_t}^*} \right]^{1/\kappa_t} \right\}, \tag{5.14}$$

defined for $\kappa_t \neq 0$, $\alpha_t^* \geq 0$, and $1 - \kappa_t \dfrac{(x - u_t)}{\alpha_t^*} \geq 0$, with $\alpha_t^* \coloneqq \alpha_t - \kappa_t(u_t - \mu_t)$.

Here, x represents the realisation of the RV $X(t)$, and $\alpha_t, \mu_t, \kappa_t$ are respectively the scale, location, and shape parameters, defined as some functions of time t.

Counts of extreme pit depths $N(t)$ and the magnitude of extreme pit depths $X(t)|X(t) \geq u_t$ are assumed independent of each other, although both are dependent on the time location of events. Consequently, as proposed, the underlying stochastic process that governs the occurrence of $X(t) \geq u_t$ is the NHPP, with the magnitude of $X(t)|X(t) \geq u_t$ char-

acterised by the GPD, within a POT framework. This is also known as a *marked* Point process, specifically a marked Poisson Point process (Brémaud, 2020a, pg 6).

To summarise, the proposed stochastic model to approximate extreme pit depth occurrences and their magnitude includes the following postulates:

1. The occurrence of extreme pit depths $X(t)|X(t) \geq u_t$ as events observed in a corrosion coupon, within an arbitrary time interval $[s,t], 0 \leq s \leq t$, is governed by a NHPP.

2. The number of extreme pit depths $N(t)$ observed in a corrosion coupon, within an arbitrary time interval $[s,t], 0 \leq s \leq t$, are $\sim \text{Pois}(\Lambda(s,t))$, with intensity measure $\Lambda(s,t)$.

3. The magnitudes of extreme pit depths are independent of the number of extreme-pit-depth events observed in a corrosion coupon by time t and follow a time-variant GPD, within a POT framework.

5.3.3 Intensity Measure $\Lambda(t)$

To fit the aforementioned stochastic model to the surrogate pitting corrosion data, the likelihood function defined earlier for m paths of a general NHPP (Equation 5.13) must be modified to account for the number of corrosion coupons used to generate the data. More concretely, following the work of Smith (1994, pg 231), the 10 corrosion coupons used per exposure period are treated as if data were collected for 10 identical exposure periods, equivalent to the pooling of 10 time blocks into a single dataset. This modification is accomplished by inserting the factor C_p ($C_p = 10$ corrosion coupons) into Equation 5.13, as follows:

$$L(\eta \,|\, t) = \prod_{j=1}^{m} \left\{ \prod_{i=1}^{n_j} \lambda(t_{ij} : \eta) \exp(-C_p \Lambda(T_j)) \right\}. \tag{5.15}$$

For the surrogate pitting corrosion data, Equation 5.15 represents the likelihood function for $j = 1, 2, \ldots, 10$ exposure periods, with durations T_j from initial time $T_0 = 0$ and which consist of n_j pooled pit depths per exposure period. Equation 5.15 does not, however, satisfy the first postulate of the stochastic model as all pit depths are included in the variable n_j. The interest is in $X(t)|X(t) \geq u_t$. To do so, n_j must represent all the pooled, extreme pit depths per exposure period that are equal to or greater than a specified pit depth threshold u_t applicable to the exposure period. This requires the definition of a time-variant threshold. Similarly, $\Lambda(T_j)$ and $\lambda(t_{ij})$ also need to be formulated in agreement

with the three postulates defined above. Specifically, $\Lambda(T_j)$ takes on the meaning of the expected number of exceedances or extreme pit depths observed in a corrosion coupon by time T_j, with $\lambda(t_{ij})$ representing the instantaneous average rate that exceedances or extreme pit depths occur when at a specified magnitude of extreme pit depth at time t_{ij}. The intensity function $\lambda(t_{ij})$ may be viewed as an intrinsic parameter of the pitting process. For brevity, all of the algebraic details and assumptions associated with the equations for $\Lambda(T_j)$ and $\lambda(t_{ij})$, which follow shortly, are left to the appendices. Here, only the results are presented.

As shown in Appendix D, for limiting or asymptotic arguments, if, for an arbitrary exposure period of length t from initial time $t_0 = 0$, the magnitude of pit depth exceedances above some time-variant threshold u_t follow a time-variant GPD, and if the number of pit depth exceedances are $\sim$ Pois$(\Lambda(t \mid \boldsymbol{\theta}))$, then the intensity measure $\Lambda(t \mid \boldsymbol{\theta})$ may be formulated as

$$\Lambda(t \,|\, \boldsymbol{\theta}) = \left[1 - \kappa_t \left(\frac{u_t - \mu_t}{\alpha_t}\right)\right]^{\frac{1}{\kappa_t}}. \tag{5.16}$$

The parameter set $\boldsymbol{\theta} \coloneqq \{\mu_t, \alpha_t, \kappa_t\}$ represents the location, scale, and shape parameters of the limiting distribution of pit depth maxima (per corrosion coupon), and the subscript t signifies a formulation with time as co-variate. The relationship between the limiting distribution of pit depth maxima (see Appendix B, Equation B.5) and that for pit depth exceedances (Equation 5.14) is such that $\boldsymbol{\theta}$ is common to both (Castillo et al., 2005, pg 264).

Appendix C details the methodology used to arrive at suitable pit depth thresholds u_t. For the surrogate data, a power-law relationship (i.e., $u_t \coloneqq ut_j^c$, where j is the jth exposure period) adequately captures the change in pit depth threshold with time, Figure 5.2. In this figure, the thresholds are labelled $low1$, which is simply a designation arising from the approach applied to select appropriate thresholds (see Appendix C for further information). When applied to the surrogate data, the time-dependent thresholds result in pit depth exceedances, illustrated in Figure 5.3.

Time-dependent location and scale parameters μ_t and α_t were also adequately modelled using a power-law relationship with time as co-variate (i.e., $\mu_t \coloneqq \mu t_j^b$ and $\alpha_t \coloneqq \alpha t_j^b$, and j is the jth exposure period). For reasons described in Appendix B, the shape parameter κ was maintained constant and independent of time. The methodology, including assumptions and model fit assessment, are described first in Appendix B, which details the fitting of the GEV distribution to pit depth maxima, and subsequently in Appendix C, where the fit is verified against the GPD within a POT framework.

With the form of the time-dependent relationship well defined for u_t, μ_t, and α_t, the

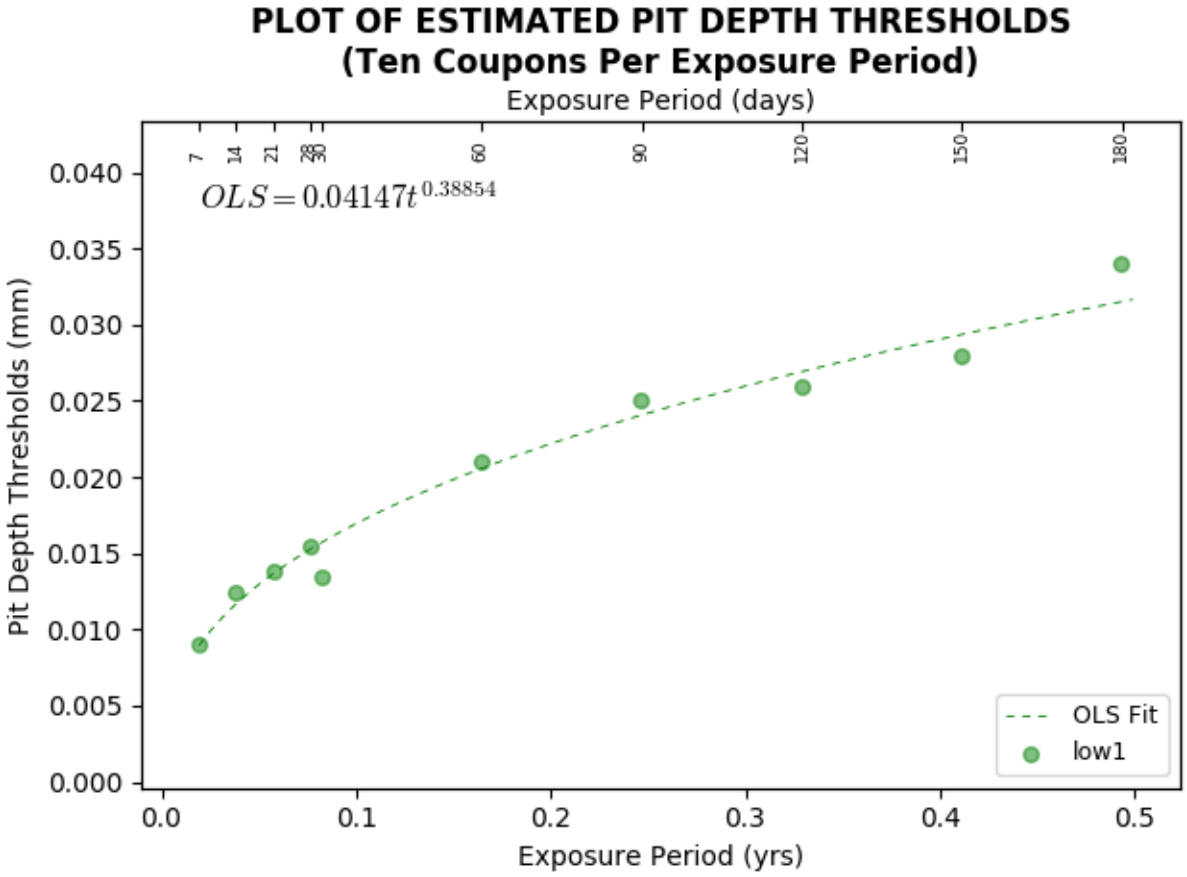

Figure 5.2: The change in the ($low1$) thresholds with time is captured by a power-law relationship, fitted by Ordinary Least Squares.

appropriate formulation for $\Lambda(t\,|\,\boldsymbol{\theta})$, satisfying the three postulates, is

$$\Lambda(t\,|\,\boldsymbol{\theta}) = \left[1 - \kappa\left(\frac{ut_j^c - \mu t_j^b}{\alpha t_j^b}\right)\right]^{\frac{1}{\kappa}}, \tag{5.17}$$

and, as per Smith (1994, pg 231), the corresponding intensity density function $\lambda(x_{i,j}\,|\,\boldsymbol{\theta})$ is

$$\lambda(x_{i,j}\,|\,\boldsymbol{\theta}) := -\frac{\partial\Lambda(x_{i,j}\,|\,\boldsymbol{\theta})}{\partial x} = \frac{1}{\alpha t_j^b}\left[1 - \kappa\left(\frac{x_{i,j} - \mu t_j^b}{\alpha t_j^b}\right)\right]^{\frac{1}{\kappa}-1}. \tag{5.18}$$

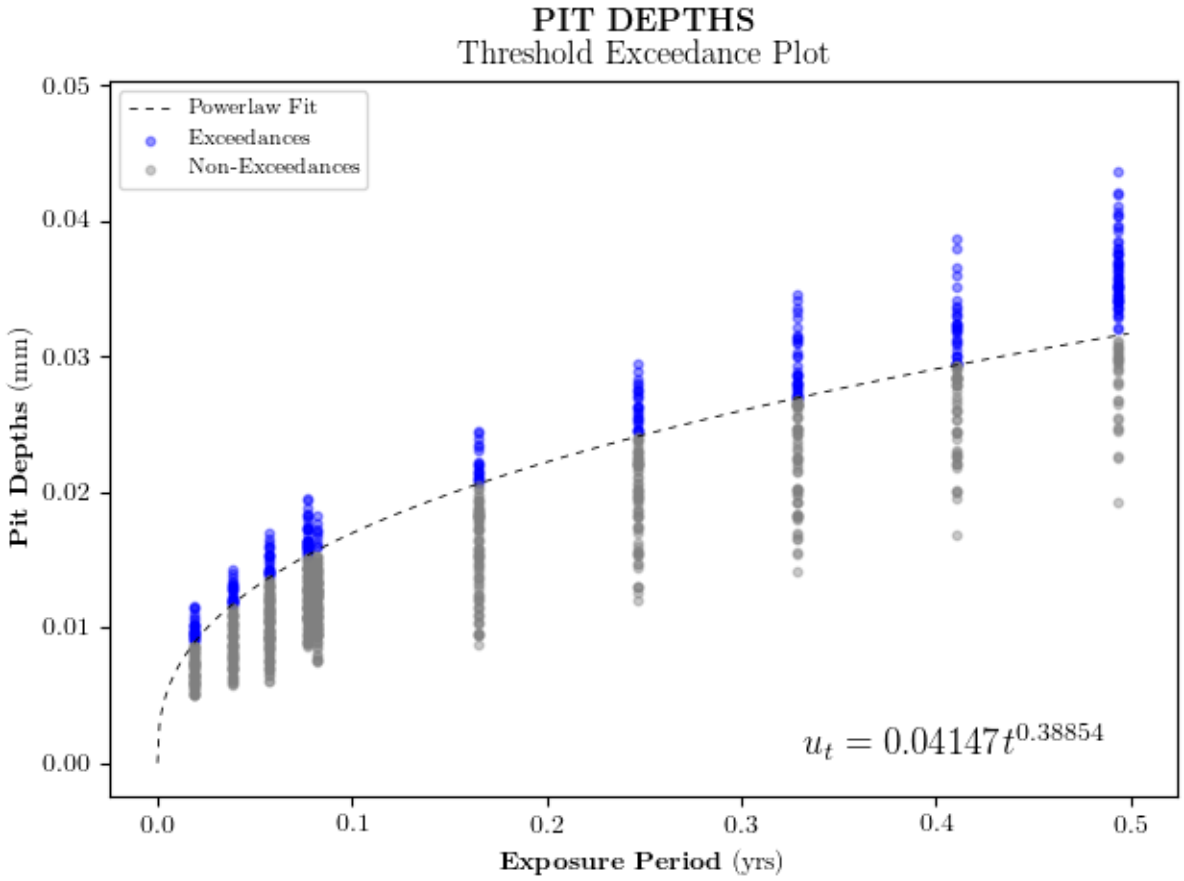

Figure 5.3: Scatter plot of exceedances arising from the employment of the ($low1$) thresholds.

In the partial derivative of Equation 5.18, the ith extreme pit depth—ith exceedance—associated with the jth exposure period, $x_{i,j}$, has replaced the time-variant threshold pit depth u_t. This is consistent with understanding that the intensity density function is dependent on the exceedance level $x_{i,j}$, a concept more readily understood within the alternative context of a limiting distribution of a Point process, Appendix D, Section D.1. The function $\lambda(x_{i,j}\,|\,\boldsymbol{\theta})$ stands in contrast to that proposed by Caleyo et al. (2009); Valor et al. (2013), Equation 5.5, which has no dependence on the magnitude of pit depths. It should also be noted that the non-homogeneity of the intensity density function is captured through the inclusion of time as co-variate in the location and scale model parameters μt_j^b and αt_j^b, respectively.

The complete form of the likelihood function for the surrogate data, satisfying the above postulates, becomes

$$L(\boldsymbol{\theta}\,|\,\mathbf{x},\mathbf{t}) = \prod_{j=1}^{N} \left\{ \exp\left\{ -C_p \cdot \left[1 - \kappa \left(\frac{ut_j^c - \mu t_j^b}{\alpha t_j^b} \right) \right]^{\frac{1}{\kappa}} \right\} \cdot \prod_{i=1}^{n_j} \frac{1}{\alpha t_j^b} \left[1 - \kappa \left(\frac{x_{i,j} - \mu t_j^b}{\alpha t_j^b} \right) \right]^{\frac{1}{\kappa}-1} \right\}. \quad (5.19)$$

In Equation 5.19, $N = 10$, $\boldsymbol{\theta} \coloneqq \{\mu, \alpha, \kappa, b\}$, $x_{i,j}$, and n_j represent respectively the number of exposure periods, the parameter vector for the NHPP with points marked by the GPD, the ith realisation of the exceedance RV at the jth exposure period, and the number of exceedances for exposure period j. The parameter set $\boldsymbol{\theta}$ to be estimated in the maximisation of the likelihood function does not include threshold power-law parameters u and c as these are predetermined (Appendix C). Numerical maximisation of the natural logarithm of Equation 5.19 (i.e., $l(\boldsymbol{\theta} \mid \mathbf{x}, \mathbf{t})$) was performed with Python 3.6.9, with the optimisation algorithm SLSQP. Constraints applied to the maximisation were $1/\alpha t^b > 0$, $1 - \kappa(ut^c - \mu t^b)/\alpha t^b \geq 0$, and $1 - \kappa(x_{i,j} - \mu t^b)/\alpha t^b \geq 0$. Results are presented in Table 5.1 for threshold level $low1$.

Figure 5.4 shows the expected number of extreme pit depths with time, estimated from the maximum likelihood estimators $\hat{\mu}, \hat{\alpha}, \hat{\kappa}, \hat{b}$. Included in Figure 5.5 are, respectively, plots of the instantaneous average rate of pit depth occurrences $\lambda(x_{i,j}|\boldsymbol{\theta})$ estimated for the 7-day and 180-day exposure periods. The intensity density function follows a very similar trend with respect to exceedances for all other periods. Note, the intensity density function is independent of the corrosion coupon size and is, therefore, a measure of the "intrinsic" propensity for the occurrence of extreme pit depths when at a specified pit depth exceedance $x_{i,j}$ at time t_j. Loosely speaking, this may be interpreted as the probability of growing a pit deeper than its current (extreme) depth. The trends in Figure 5.5 demonstrate that this propensity decreases almost linearly with pit depth exceedances, particularly for pit depths close to the threshold. Further away, the rate of decrease tapers gradually to an endpoint, which is consistent with the right endpoints exhibited by the limiting distribution for maxima (i.e., GEV) with a positive κ parameter (see Appendix B). Put another way, pit depths further away from a valid threshold become very rare. This definition is consistent with the probability statement expressed by Equation 5.12. Its significance will become more apparent in the next section. Figure 5.6 provides a complementary view as a function of time, at time-variant threshold levels. The physical meaning assigned to this plot is that it represents in graphical terms a measure of the likelihood of exceeding time-variant thresholds. Together with Figure 5.4, the overall picture is that the number of extreme events (i.e., pit depth exceedances) increases with time but at a

decreasing rate as the probability of exceeding an ever-increasing time-variant threshold diminishes with time.

Table 5.1: Maximum Likelihood Parameter Estimates for the NHPP with Exceedances ∼GPD

Threshold	$\hat{\mu}$	$\hat{\alpha}$	$\hat{\kappa}$	$\hat{b}$	$l(\hat{\boldsymbol{\theta}}\,\vert\,\mathbf{x},\mathbf{t})$
$low1$[1]	0.04876	0.00399	0.34450	0.40926	1660.94

[1] $u = 0.04147$ and $c = 0.38854$ (Appendix C).

By way of comparison, the intensity measure predicted by the formulation in Equation 5.4, as proposed by Caleyo et al. (2009); Valor et al. (2013), is plotted in Figure 5.7. In this plot, the parameters α and β were determined from a power-law fit to pit depth exceendances derived for the $low1$ thresholds. Their formulation was applied with $t_0 = 0$ and the time-to-initiate pits $t_{sd} \approx 0$, taken from Li et al. (2019). While the shape of the plot is similar to the one derived solely from asymptotic arguments (Figure 5.4), the function is negative, violating the definition given in Section 5.3.1. One would arrive at a similar conclusion regardless of the statistic chosen for fitting a power-law (i.e., whether pit depth thresholds, mean, or median), indicating that the proposed formulation, irrespective of the regression fit, simply doesn't satisfy the stochastic definition of an intensity measure. The unexpected outcome raises questions for this author, some of which are examined in greater detail in Appendix A, Section A.2.2. Here, suffice to say that Caleyo et al. (2009); Valor et al. (2013) do not appear to use the functional form of the intensity measure precisely as proposed by Equation 5.4, though they explicitly point to an identical equation in their work. Unfortunately, the precise form used is unknown. What follows is a synopsis of the findings in Section A.2.2, presented herein to shed light potentially on the functional form employed by Caleyo et al. (2009); Valor et al. (2013).

A direct application of Equation 5.4, using the power-law parameters (κ_t, ν_t from the two articles cited above) derived for their piping material and the "All Soils" condition, results in the plot shown in Figure 5.8. The actual plot provided in the two articles is reproduced in Figure 5.9 by a spline fit to eight arbitrarily selected data points. The two plots are clearly not in agreement. Further examination of Figure 5.9 informs the reader that the time axis starts at 5 years. This happens to be the year for which the pitting corrosion data in one example presented in the two articles was chosen to represent the initial pit depth distribution. The same was subsequently used to make predictions for a future time t. Consequently, let $t_0 = 5$, which implies that Equation 5.4 does not apply in

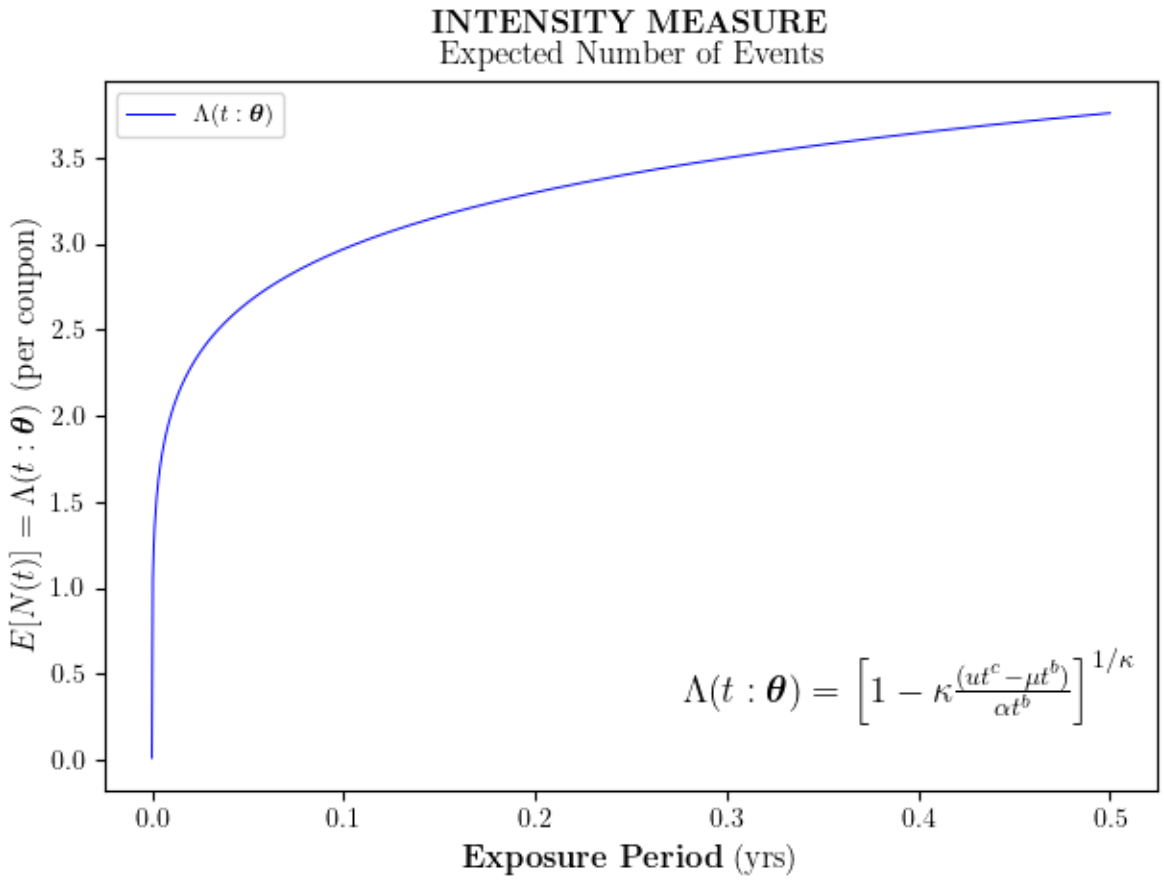

Figure 5.4: Expected number of extreme pit depths (events) $E[N(t)]$ per coupon by time t given $\Lambda(t:\boldsymbol{\theta})$.

its present form. However, as shown in Section A.2.2, when $t_0 \neq 0$ and $N(t_0) \neq 1$, the complete expression for $\Lambda(t)$ becomes

$$\Lambda(t) = \ln\left[\kappa_t\left(t - t_{sd}\right)^{\nu_t}\right] + \ln\left[\kappa_t\left(t_0 - t_{sd}\right)^{\nu_t}\right] - \ln N(t_{sd}) - \ln N(t_0). \tag{5.20}$$

Since t_{sd} is the time to initiate a pit, it would follow that the size of the population at t_{sd} should be $N(t_{sd}) = 1$. Working on this premise simplifies the expression for $\Lambda(t)$ to

$$\Lambda(t) = \ln\left[\kappa_t\left(t - t_{sd}\right)^{\nu_t}\right] + \ln\left[\kappa_t\left(t_0 - t_{sd}\right)^{\nu_t}\right] - \ln N(t_0), \tag{5.21}$$

but $N(t_0 = 5)$ is unknown; it is neither defined nor described in Caleyo et al. (2009); Valor et al. (2013). Subsequently, for exploratory reasons, let $\Lambda(t)$ be defined by the first two

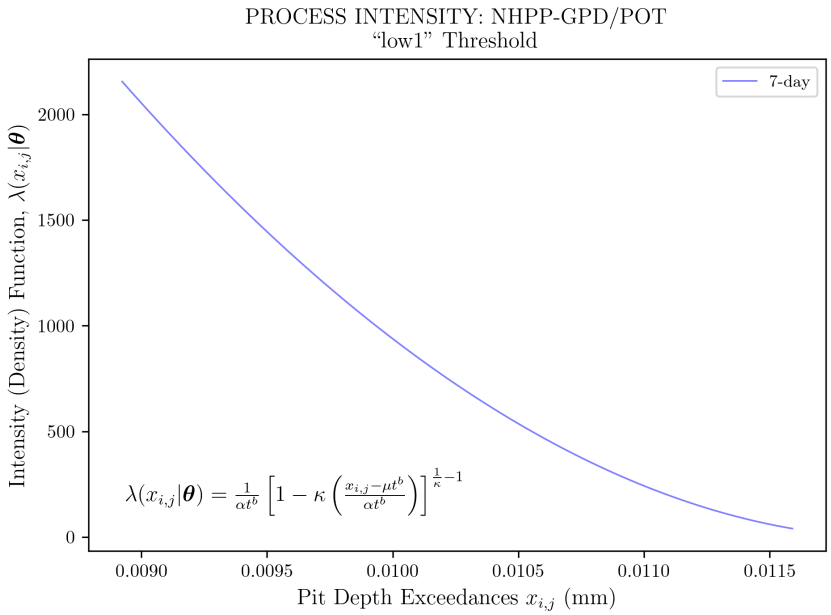

(a) 7-day Exposure Period

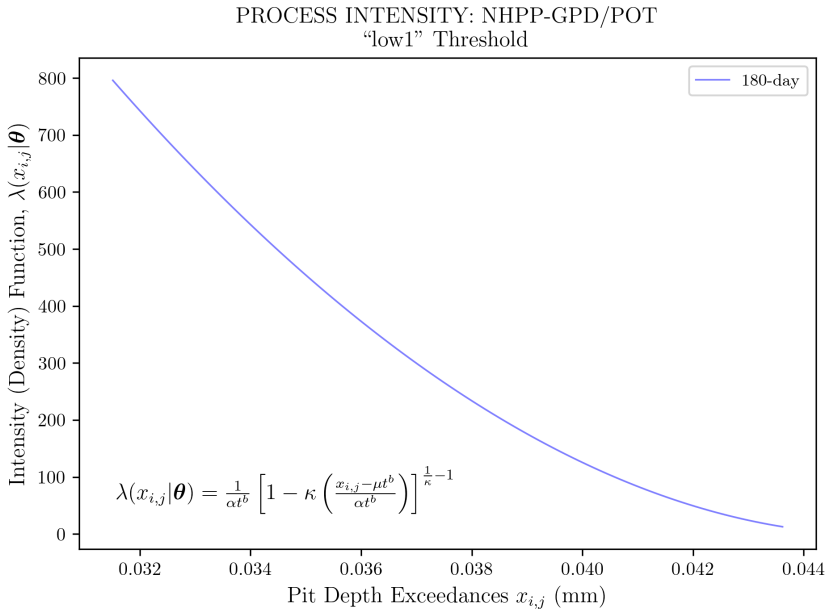

(b) 180-day Exposure Period

Figure 5.5: Instantaneous average rate of occurrence for pit depth exceedances, $\lambda(x_{i,j}|\boldsymbol{\theta})$, estimated for (a) the 7-day and (b) 180-day exposure period data.

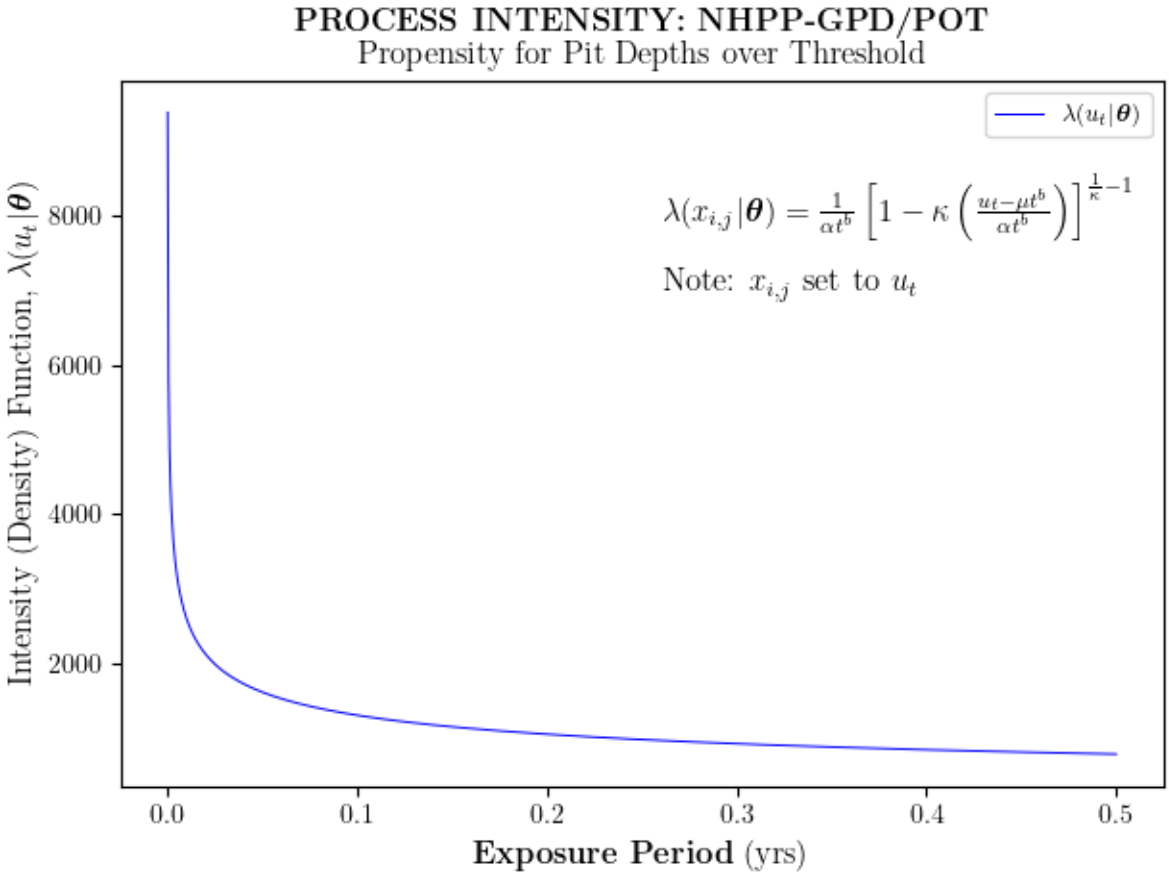

Figure 5.6: Instantaneous average rate of occurrence for pit depth exceedances, $\lambda(x_{i,j}|\boldsymbol{\theta})$, estimated at threshold level.

terms on the right side of the equality of Equation 5.21. A resulting plot of this two-term function, Figure 5.10, reveals a strikingly similar trend to the plot presented in the two articles, Figure 5.9, except that the two-term plot is translated down along the y-axis. More specifically, Figure 5.9 shows that $\Lambda(t=5)=1$. It's not immediately clear to this author why the expected number of events at $t=5$ years should be set to 1. However, if the difference in the two plots is simply a matter of translation, then an estimate for the value of the third term in Equation 5.21 (i.e., $N(t_0=5)$) may be deduced by setting $\Lambda(t=5)=1$. This leads to the plot shown in Figure 5.11, which includes the plot from Figure 5.9. Remarkably, the two plots are in very good agreement.

There are several problems, however, with the deduced final form for $\Lambda(t)$. Two are mentioned here briefly. First, the deduced value for $N(t_0 = 5) = 0.03148$ is nonsensical in the sense that $N(t)$ represents the size of a population—an integer value—and is analogous to the damage state of a discrete state Markov chain. Along the same line of argument, $N(t_0 = 5) \not< 1$, seeing $N(t_{sd} = 2.9) = 1$.[10] However, if one simultaneously treats the size of the population $N(t)$ as a positive, real-valued function—as postulated by Caleyo et al. (2009); Valor et al. (2013) in Section 5.1, then $N(t_{sd} = 2.9) = 0.03148$ would be consistent with their reasoning. Unfortunately, this leads to confusion. Two, there are no reasons known to this author why the expected number of events should be restricted in value, particularly to the value of 1, as was the case above. A careful re-read of the papers failed to provide further clarity, but it is possible that the size of the population—damage state of the Markov chain—was indeed 1.[11] Assuming that Equation 5.20 is correct, then it would appear that, at best, the approach proposed by Caleyo et al. (2009); Valor et al. (2013) lacks transparency. At worst, it is not a workable proposition; that is, it cannot be employed to estimate the expected number of events from $t_0 = 0$, starting with a population of size 1 ($N(t_0) = 1$). Consequently, the functional form proposed by Caleyo et al. (2009); Valor et al. (2013) will not be given further consideration in this work.

[10] Alternatively, one may set $N(t_0 = 5) = 1$ as demonstrated in Section A.2.2, which would then result in $N(t_{sd} = 2.9) = 0.03148$, but this would not alleviate the concerns with $N(t) \in \mathbb{R}_+$.

[11] This author made many attempts to contact Caleyo et al. (2009); Valor et al. (2013) by various means, but received no replies.

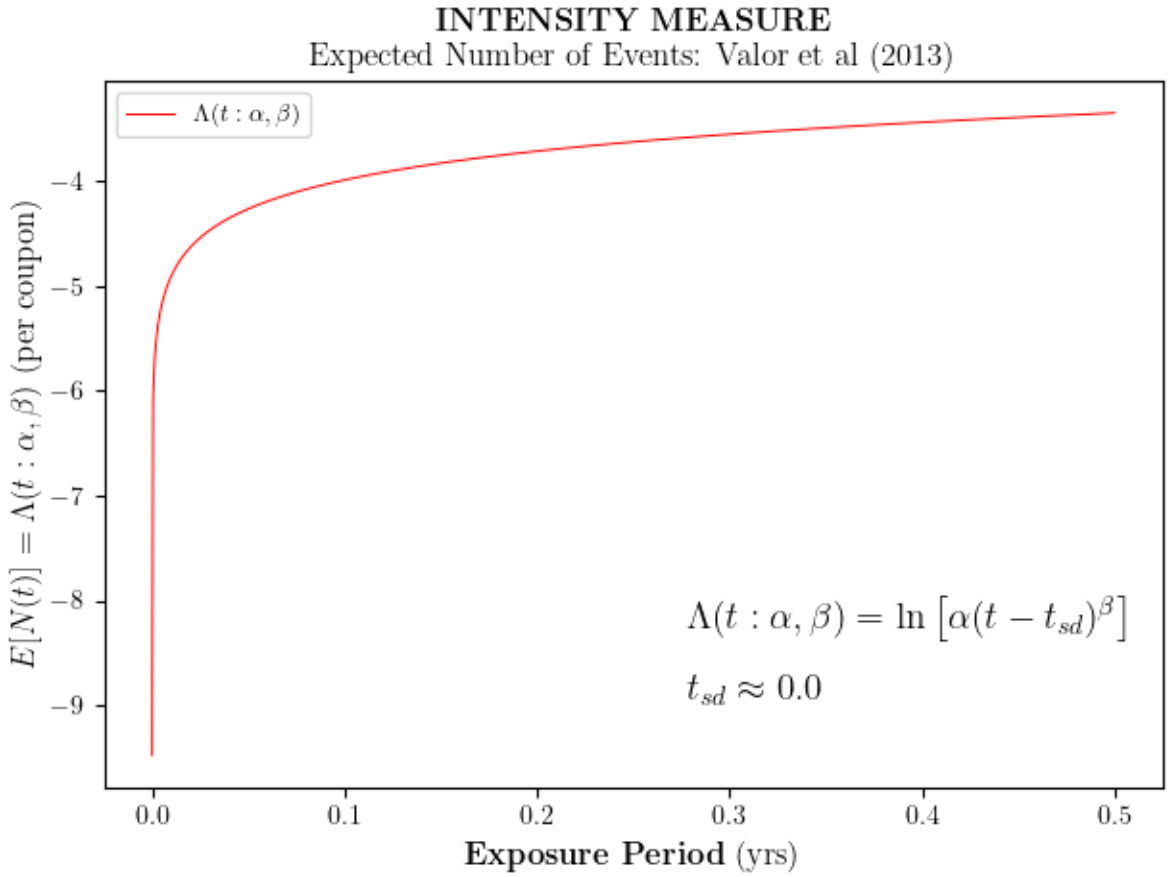

Figure 5.7: Expected number of extreme pit depths (events) $E[N(t)]$ per coupon by time t predicted by the approach proposed by Caleyo et al. (2009); Valor et al. (2013), with the parameters $\alpha = 0.04644$ and $\beta = 0.39762$ derived from a power-law fit to pit depth exceedances (low1).

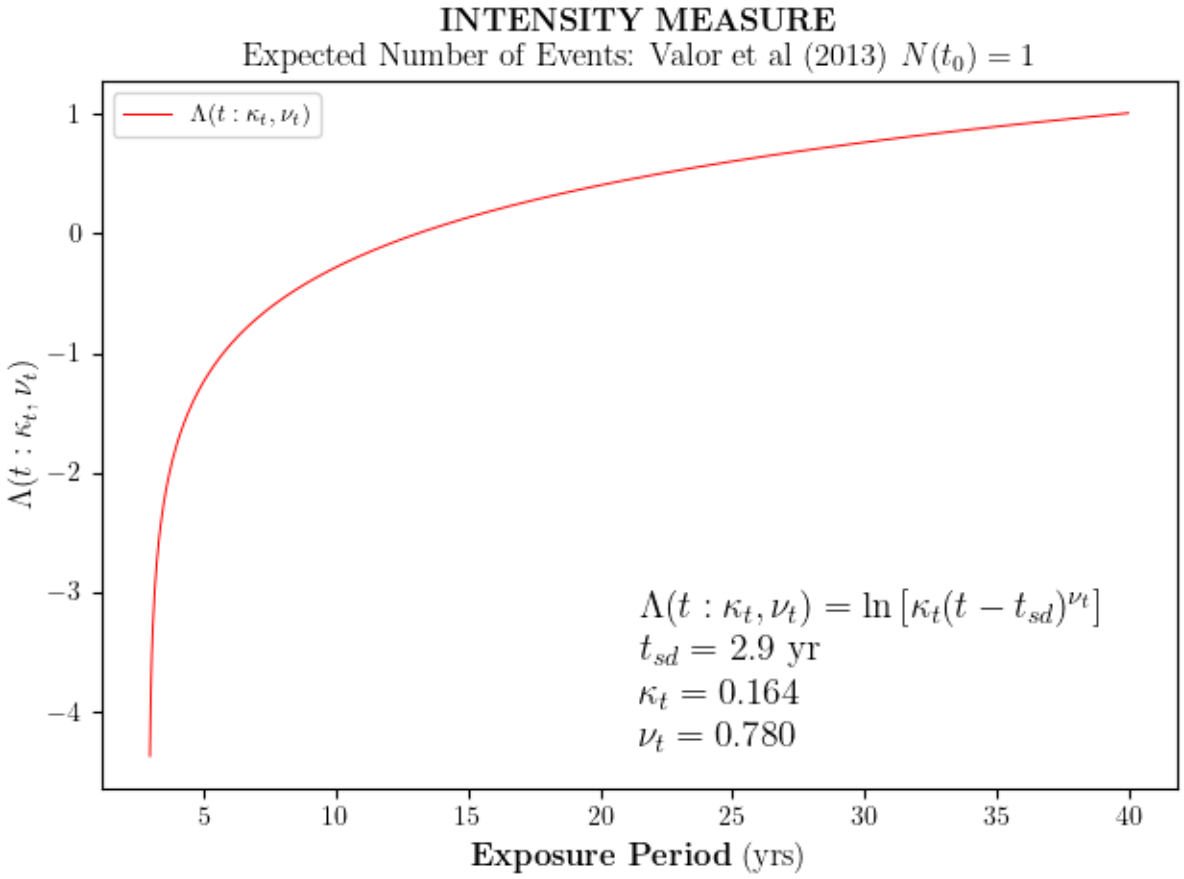

Figure 5.8: Expected number of extreme pit depths (events) $\Lambda(t)$ by time t predicted by the approach proposed by Caleyo et al. (2009); Valor et al. (2013), with the parameters $\kappa_t = 0.164$ and $\nu_t = 0.780$ taken from Tables 1 and 2, Valor et al. (2013).

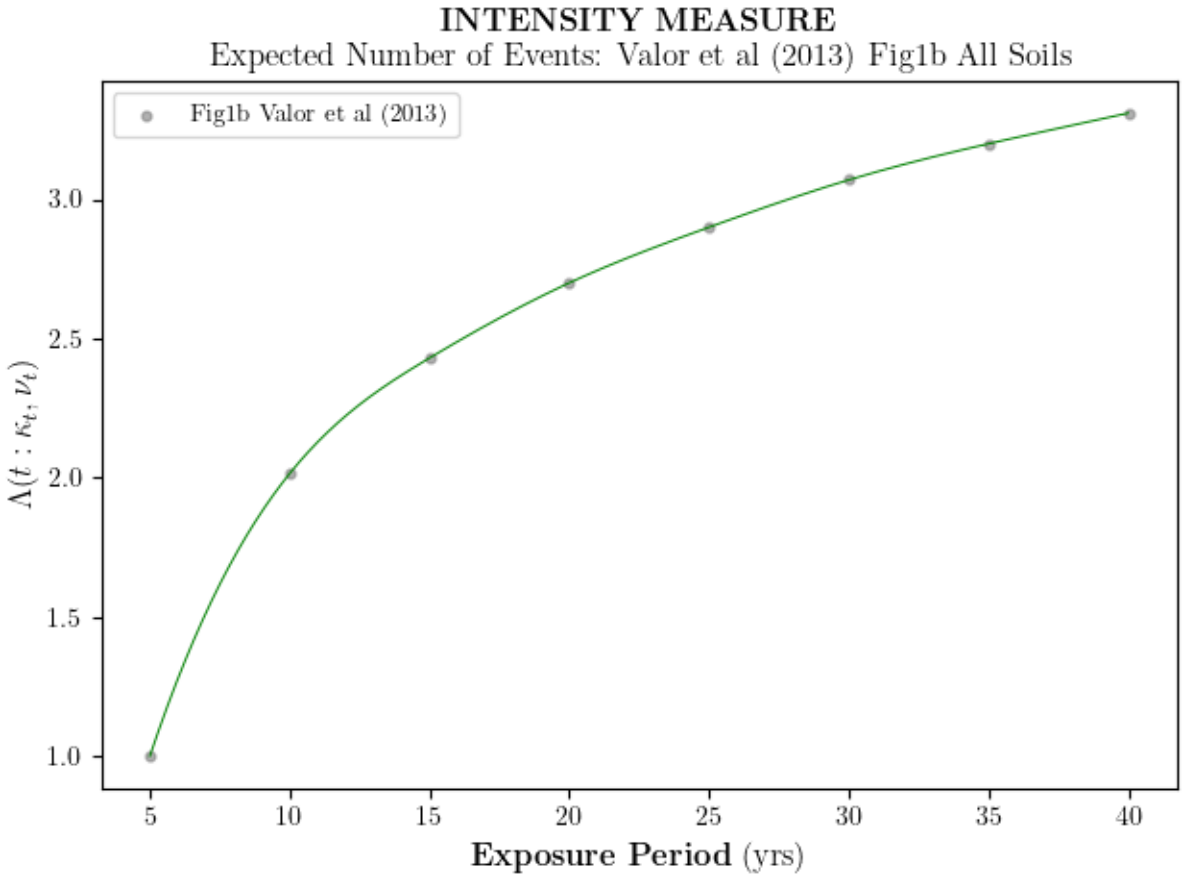

Figure 5.9: Expected number of extreme pit depths (events) $\Lambda(t)$ by time t, showing actual data points from Fig1b Valor et al. (2013).

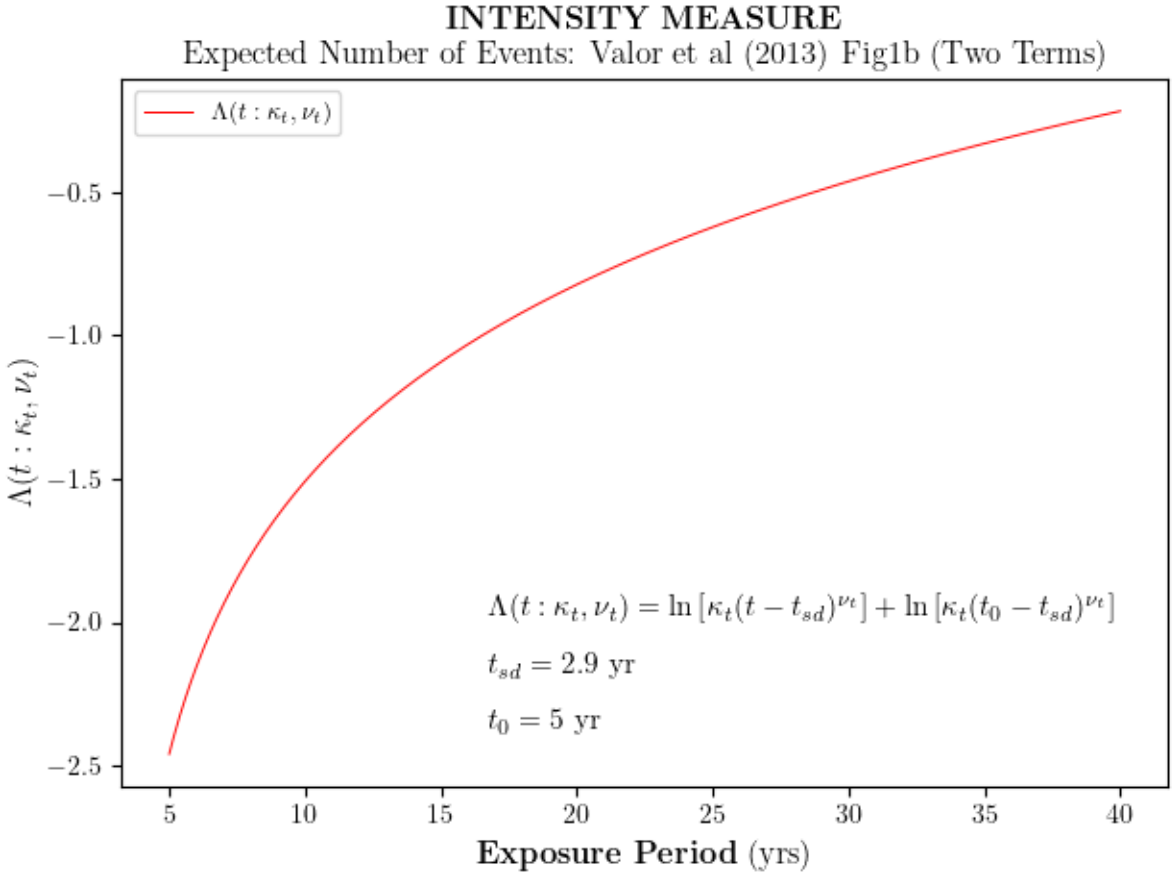

Figure 5.10: Expected number of extreme pit depths (events) $\Lambda(t)$ by time t, with the parameters $\kappa_t = 0.164$ and $\nu_t = 0.780$ taken from Tables 1 and 2, Valor et al. (2013), using the first two terms to the right of the equal sign in Equation 5.21.

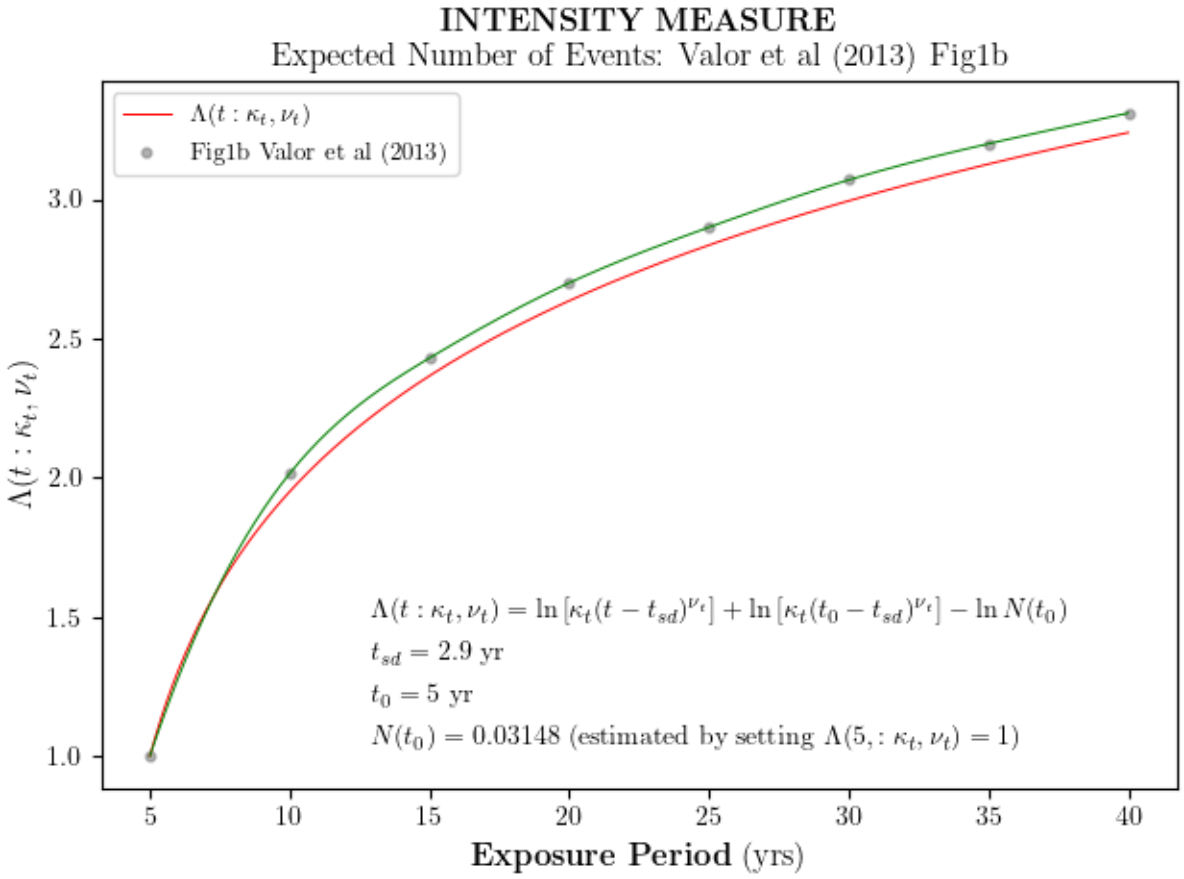

Figure 5.11: Expected number of extreme pit depths (events) $\Lambda(t)$ by time t, showing actual data points from Fig1b Valor et al. (2013) and a deduced plot with parameters taken from Tables 1 and 2, Valor et al. (2013).

5.4 Evolution of Extreme Pit Depths as a NHMP

The objective of this section is to model pit growth using a special class of stochastic processes called *Markov*. Motivation for doing so stems in part from their prevalence in modelling pitting corrosion (Section 5.1) and partly from the potential to improve on a specific aspect of the methodology widely adopted in the literature. More concretely, the first and most significant improvement proposed here is the replacement of the empirically derived *intensity of transition* function, employed by Valor et al. (2013) and others, by the asymptotically derived intensity density function defined by Equation 5.18, whose merit rests entirely on its origins as an intrinsic stochastic process parameter. Invoking the equivalence between a NHPP and a first-order NHMP process enables this proposal. A second improvement is the modelling of pit depth exceedances instead of pit depth maxima. The former not only supports better utilisation of available data but also facilitates assignment of more than one relevant pit depth to the surface of a UFC. These two improvements are considered meaningful contributions to the modelling of pit growth via Markov processes. To support development of the Markov model, some preliminaries are helpful.

5.4.1 Preliminaries—Markov Process

A Markov process is the label given to a physical or empirical system that exhibits properties that obey probability laws, for which the future state of the system—given the knowledge of the present—is independent of its prior history (Çinlar, 1975, pg 187). Markov processes are defined or classified by the characteristic or nature of their states and time parameter. A Markov process with discrete states, which may be integer-valued, denumerable, or finite, and sometimes countably infinite, is called a *Markov chain*, and a Markov chain with a continuous-time parameter is typically referred to as a Continuous-Time Markov chain CTMC.

Formally, a continuous-time, non-homogeneous stochastic process $\{S(t); t \geq 0\}$ with an arbitrary state space $\mathbb{N}_0 \coloneqq \{0, 1, 2, \dots\}$ is called a CTMC if, $\forall s < t,\ s, t \in \mathbb{R}_0^+, \forall i, j, k \in \mathbb{N}_0$,

$$\begin{aligned} p_{j,k}(s,t) &\coloneqq P(S(t)=j \,|\, S(s)=k, S(u)=i, 0 \leq u \leq s) \\ &= P(S(t)=j \,|\, S(s)=k), \end{aligned} \tag{5.22}$$

and

$$p_k(t) = P(S(t) = k). \tag{5.23}$$

Equation 5.23 defines the probability that the state of the process at time t is k. Similarly, $p_{j,k}(s,t)$ defines the conditional probability that the state of the process at time t is k

given that at time s the process was in state j. The function $p_{j,k}(s,t)$ is referred to as the *transition probability function*. Equivalently, $p_{j,k}(s,t)$ represents the conditional probability of transitioning from j to k over the time interval $t-s$, when at time s. Note, $p_{j,k}(s,t)$ is conditionally dependent on s and is, therefore, time non-homogeneous. Conditional dependence on the current state of the process defines a first-order Markov process.

Computationally, it is more expedient to work with matrices when analysing a CTMC. Consequently, define the *probability transition matrix* $\mathbf{P}(s,t)$,

$$\mathbf{P}(s,t) \coloneqq \{p_{j,k}(s,t)\} \quad \forall j,k \in \mathbb{N}_0 \text{ and } t > s \geq 0. \tag{5.24}$$

The family $\{\mathbf{P}(s,t)\}\,\forall s,t \geq 0,\, t>s$ represents the transition probability matrices for the non-homogeneous CTMC. One of the attractive features of non-homogeneous (and homogeneous) Continuous-Time Markov Chains (CTMCs) is that they can be uniquely determined by their initial state distribution and their transition probability matrices (e.g., see Brémaud (2020b, pg 298) and Stroock (2005, pg 84)). Subsequently, for a non-homogeneous CTMC with an arbitrary state space $\mathbb{N}_0$, let the row vector $\mathbf{v}_s \coloneqq \{P(N(s)=i)\}\,\forall i \in \mathbb{N}_0$ represent the initial state distribution at time s. Then,

$$\mathbf{v}_t \coloneqq \mathbf{v}_s \mathbf{P}(s,t) \tag{5.25}$$

defines the state distribution of a non-homogeneous CTMC at future time t. An expression for $\mathbf{P}(s,t)$ is derived by invoking the assumption that there exist particular limit functions[12], also called *infinitesimal transition* functions (or infinitesimal transition rates or probabilities), defined as follows.

Infinitesimal Transition Functions

For each state $j \in \mathbb{N}_0$ in a non-homogeneous CTMC, there is a non-negative continuous function $q_j(t)$ defined by the limit

$$\lim_{\Delta t \to 0^+} \frac{1}{\Delta t} \{1 - p_{j,j}(t, t+\Delta t)\} = q_j(t) \quad 0 < q_j(t) < \infty, \forall j \in \mathbb{N}_0, \tag{5.26}$$

and for each pair of states j and k, with $j \neq k$, $k \in \mathbb{N}_0$, there is a non-negative continuous function $q_{j,k}(t)$ defined by the limit

$$\lim_{\Delta t \to 0^+} \frac{1}{\Delta t} p_{j,k}(t, t+\Delta t) = q_{j,k}(t). \tag{5.27}$$

[12]This is equivalent to prescribing that such functions exist—in the limit—for the empirical system modelled as a Markov process

The rate at which the process leaves or transitions out of state j at time t is given by $q_j(t)$, also called the *intensity of passage*. Simply put, $1-p_{j,j}(t, t+\Delta t)$ is the probability of a jump from state j to another state within the infinitesimally small time interval $[t, t+\Delta t]$, which is approximately equal to $q_j(t)\Delta t + o(\Delta t)$. By extension, $p_{j,k}(t, t+\Delta t)$ is the probability of transitioning from states j to k during an infinitesimally small time interval $[t, t+\Delta t]$, which is also approximately equal to $q_{j,k}(t)\Delta t + o(\Delta t)$. The function $q_{j,k}(t)$ is called the *intensity of transition* to state k given that at time t the state was j. The infinitesimal transition functions $q_j(t)$ and $q_{j,k}(t)$, along with the transition probability function $p_{j,k}(s,t)$, lead to the formulation of *Kolmogorov's Forward Differential* equation (Parzen, 2015):

$$\frac{\partial}{\partial t} p_{j,k}(s,t) = -q_k(t)p_{j,k}(s,t) + \sum_{i \neq k} p_{j,i}(s,t)q_{i,k}(t). \tag{5.28}$$

A useful interpretation of the right side of Equation 5.28 is minus the *rate of probability flow* out of state k plus the rate of probability flow into state k from all other states (Hajek, 2015, pg 127). The solution to Kolmogorov's Forward Differential equation ultimately leads to an expression $\mathbf{P}(s,t)$, to be shown later in this chapter.

5.4.2 NHMP Model Postulates

In this work, following the example of others (see Section 5.1), a special class of CTMC models, called *pure-birth, linear-growth-rate*, will be employed to express the evolution of corrosion pits. In the pure-birth, linear-growth-rate stochastic model, also referred to as the *Yule process* (see Kao (2019, pg 249) and Taylor and Karlin (1998, pg 334)), the underlying or instantaneous rate of the process is directly proportional to the state of the process, which is represented by the size of the population for some living organism (e.g., bacteria). While the Yule Process analogy is useful, it is necessary to move from a state space defined by population sizes to one that maps pit depth to an integer-valued damage state. Formulating pit growth as a pure-birth, linear-growth-rate non-homogeneous CTMC requires several postulates, which are discussed below.

Pure-birth, Linear-growth-rate Model

In the context of a CTMC, the pure-birth, linear-growth-rate stochastic process means:

1. Transitions can only occur to the next adjacent state (i.e., $j \to j+1$), which means there are only births and no deaths. This is the sentiment expressed by *pure birth*.
2. The intensity of passage out of state j at time t, $q_j(t)$, is equivalent to the intensity of transition to state $j+1$ during the time interval $[t, t+\Delta t]$.

3. The process population always begins with a single member, so the state space is the set of all non-negative integers $\mathbb{N}_1 \coloneqq \{1, 2, \dots\}$.

4. Each member of the population can give birth at the same rate. Given that the state space of the pure-birth, linear-growth-rate process represents the set of all possible sizes for the population, it follows that the intensity of transition $q_j(t)$ for a population of size j at time t is linearly (directly) proportional to the population size and re-defined

$$q_j(t) \coloneqq \lambda_j(t) = j\lambda(t). \tag{5.29}$$

   Equation 5.29 implies a *linear growth rate*. The term $\lambda(t)$ is re-introduced here because it represents the intrinsic (single) member rate of transition, which, when Equations 5.9 and 5.26 are compared, it is immediately evident that for a population of size $j = 1$ (i.e., a single member) $q_j(t) \equiv \lambda(t)$.

Owing to the four points above, one can describe the pure-birth, linear-growth-rate non-homogeneous CTMC by a simple *transition rate diagram*, Figure 5.12:

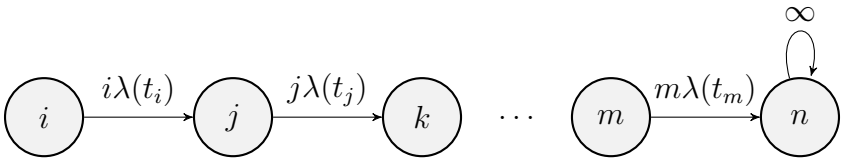

Figure 5.12: Transition rate diagram for a pure-birth, linear-growth-rate non-homogeneous CTMC, with states $\{i, j, k, m, n \in \mathbb{N}_1\}$ and absorbing state n (i.e., $\lambda_n(t) \coloneqq n\lambda(t) = 0$), shown with an infinite transition rate into itself to illustrate the point that it is an absorbing state. The times $\{t_i, t_j, \dots, t_m\}$ represent respectively the times when the process is at states $\{i, j, \dots, m\}$.

It follows that the set of Kolmogorov's forward equations (Parzen (2015)), for the pure-birth, linear-growth-rate non-homogeneous CTMC, may be derived for the set of arbitrary times $\{s, t\}$ and states $\{j, k\}$ as

$$\begin{aligned} \frac{\partial}{\partial t} p_{j,k}(s,t) &= -k\lambda(t) p_{j,k}(s,t) + j\lambda(t) p_{j,j}(s,t), \\ \frac{\partial}{\partial t} p_{j,j}(s,t) &= -j\lambda(t) p_{j,j}(s,t), \end{aligned} \tag{5.30}$$

or in more general, compact notation (i.e., $\lambda_j(t) = j\lambda(t)$ and j, k arbitrary and not necessarily sequential)

$$\begin{aligned} \frac{\partial}{\partial t} p_{j,k}(s,t) &= -\lambda_k(t) p_{j,k}(s,t) + \lambda_{k-1}(t) p_{j,k-1}(s,t), \\ \frac{\partial}{\partial t} p_{j,j}(s,t) &= -\lambda_j(t) p_{j,j}(s,t). \end{aligned} \tag{5.31}$$

Conveniently, Parzen (2015, pg 302) demonstrates, by means of a probability generating function transformation of $p_{j,k}(s,t)$ and Lagrange's method for solving a first-order linear partial differential equation, that the above equations can be solved explicitly without the need to resort to numerical methods. Accordingly, a closed-form expression for the probability transition function $p_{j,k}(s,t)$, for the pure-birth, linear-growth-rate non-homogeneous CTMC, is given by the Negative Binomial distribution $\text{NegBin}(k-j, p)$, with parameters $k-j$ and p:

$$p_{j,k}(s,t) = \binom{k-1}{k-j} p^j (1-p)^{k-j}, \qquad \text{for } k \geq j+1, \tag{5.32}$$

where

$$p = e^{-[\Lambda(t) - \Lambda(s)]} \tag{5.33}$$

$$\Lambda(t) = \int_0^t \lambda(\tau) d\tau. \tag{5.34}$$

Consequently, for a finite (i.e., n-state), integer-valued (i.e., $j, k \in \mathbb{N}_1$), non-homogeneous (i.e, $\lambda(t)$, $t \geq 0$) CTMC, modelled as a pure-birth, linear-growth-rate process (i.e., $\lambda_j(t) = j\lambda(t)$), the probability of $k-j$ jumps, or equivalently the probability of transitioning from states j to k, over the time interval $[s,t]$, is a discrete RV $\sim \text{NegBin}(k-j, p)$, having parameter $p \coloneqq \exp\{-[\Lambda(t) - \Lambda(s)]\}$. Moreover, the corresponding probability transition matrix $\mathbf{P}(s,t)$ for the pure-birth, linear-growth-rate non-homogeneous CTMC is

$$\mathbf{P}(s,t) = \begin{bmatrix} p_{i,i}(s,t) & p_{i,j}(s,t) & p_{i,k}(s,t) & \dots & p_{i,m}(s,t) & p_{i,n}(s,t) \\ 0 & p_{j,j}(s,t) & p_{j,k}(s,t) & \dots & p_{j,m}(s,t) & p_{j,n}(s,t) \\ 0 & 0 & p_{k,k}(s,t) & \dots & p_{k,m}(s,t) & p_{k,n}(s,t) \\ \vdots & \vdots & \vdots & \ddots & \vdots & \vdots \\ 0 & 0 & \dots & 0 & p_{m,m}(s,t) & p_{m,n}(s,t) \\ 0 & 0 & 0 & \dots & 0 & p_{n,n}(s,t) \end{bmatrix}, \tag{5.35}$$

which is a square $n \times n$, upper triangular matrix, consistent with the four points above.

Event $E(t)$ and Damage State $D(t)$

Let the stochastic event $E_i(t) \subseteq \mathbb{R}_+$ be defined by the interval $[y_i, y_i + \Delta y)$, where $i = 1, 2, \ldots, n_D$ for some positive integer n_D, $t > 0$, and $y_i, \Delta y \in \mathbb{R}_+$ (Δy a constant). Further, let $y_i \leq X(t) - u_t < y_i + \Delta y$, where $X(t)$ is the time-variant RV pit depth exceedance, and u_t is the time-variant pit depth threshold. Consequently, let the event space $\mathbf{E} \coloneqq \{E_i(t) : y_i \leq X(t) - u_t < y_i + \Delta y\}$. Put simply, $\mathbf{E}$ is the set of n_D real-valued semi-open intervals containing all possible[13] time-variant pit depth excesses. As per Section 5.3, $X(t)|X(t) \geq u_t$ is characterised by the GPD, within a POT framework, and $u_t \coloneqq ut^c$.

Define the finite damage state space $\mathbf{D} \coloneqq \{D(t) = i; i = 1, 2, \ldots, n_D\}$ of a pure-birth, linear-growth-rate non-homogeneous CTMC, and let f be a function that maps $E_i(t)$ to $D(t) = i$, $f : \mathbf{E} \to \mathbf{D}$.

$$X(t) - u_t \to \begin{cases} 1, & \text{if } y_1 < X(t) - u_t < y_2; \\ 2, & \text{if } y_2 \leq X(t) - u_t < y_3; \\ \vdots & \\ n_D, & \text{if } y_{n_D - 1} \leq X(t) - u_t < y_{n_D}. \end{cases}$$

Then, let

$$p_i(t) \coloneqq P(D(t) = i) = P(y_i \leq X(t) - u_t < y_i + \Delta y). \tag{5.36}$$

Equation 5.36 defines the probability of being in state i at time t as the probability that a pit depth excess $X(t) - u_t$ at time t, falls in the interval $[y_i, y_i + \Delta y)$, with Δy representing the event interval width.

Heuristically speaking, Δy is chosen such that calculated pit depth excesses can be readily binned to produce reasonable density histograms, which necessarily implies having a minimum number of events (i.e., pit depth exceedances). Based on the current pit depth data, setting $\Delta y = 0.001$ mm yields reasonable distributions across all exposure periods. With the interval width known, the number of states n_D in the non-homogeneous CTMC is defined by establishing reasonable bounds for the range of expected pit depth excesses. From the data (e.g., see Figure 5.3), an upper bound labelled L was selected as 0.050 mm. Typically, L represents the distance traversed by a degradation mechanism through a structural member (e.g., thickness of plate, shell, etc.) and is normally known beforehand. In the present case, L was chosen to reflect the maximum anticipated pit growth sustained in the present model for the time interval of interest, which was chosen arbitrarily to

[13] Within measurement instrument precision, it is implied that all measured pit depths and pit depth excesses calculated to the same precision are contained within the set of semi-open intervals.

represent the short oxic period. For $\Delta y = 0.001$ mm and $L = 0.050$ mm, the number of states in the Markov chain was defined as the quotient $L/\Delta y$, or $n_D = 50$ states. By this formulation, the event space $\mathbf{E} \coloneqq \{(0, 0.001), [0.001, 0.002), \ldots, [0.049, 0.050)\}$ is mapped to the finite damage state space $\mathbf{D} \coloneqq \{D(t) = i; i = 1, 2, \ldots, 50\}$, facilitating employment of a non-homogeneous CTMC as a mathematical abstraction to model the evolution of pit depth excesses in time. The finite damage state space $\mathbf{D}$ is a subset of $\mathbb{N}_1$.

Equivalence of a NHPP and a NHMP

It has already been mentioned that for a single member (i.e., $j = 1$) $q_j(t) \equiv \lambda(t)$. This suggests that the NHPP and the NHMP are equivalent. To discuss their equivalence, it is convenient to speak of the Markov process as a *jump process*, which is defined as a stochastic process that transitions between discrete states at times that can be fixed or random (Ibe, 2013, pg 50). For the jump process of interest here, the system enters a state, spends a random amount of time in the state, which is referred to as holding (also dwell, occupancy, or sojourn) time, and then jumps (i.e., transitions) to another adjacent state, where it dwells for another random period of time before it jumps again. As discussed in Section 5.3.1, for a HPP inter-arrival times—equivalent to dwell times in the present context—are $\sim \text{Exp}(\lambda)$, whilst for the NHPP, inter-arrival times are $\sim \text{Exp}(\Lambda(s, t))$, where $\Lambda(s, t) = \Lambda(t) - \Lambda(s)$. For a positive, integer-valued, homogeneous CTMC, the dwell times are $\sim \text{Exp}(\lambda)$ (see Ibe, 2013, pg 86 and Breuer, 2003, pg 331). By extension, the dwell times for a positive, integer-valued, non-homogeneous CTMC are $\sim \text{Exp}(\Lambda(s, t))$ (Gokhale et al., 2004). Consequently, a positive, integer-valued, homogeneous CTMC is a HPP, and a positive, integer-valued, non-homogeneous CTMC is a NHPP (Gokhale et al., 2004). That this equivalence holds true when a non-homogeneous CTMC is modelled as a pure-birth, linear-growth-rate process is self-evident as the system transitions to the next damage state whenever one of the population members gives birth first. The time to give birth is the inter-arrival time: it is independent[14] of the size of the population but dependent on the time of the last birth. The probability that a birth will occur is proportional to the population size, however.

Based on the foregoing, the equivalence of NHPP and NHMP means that $\Lambda(t)$ represents the expected number of extreme pit depth events ($\equiv$ expected number of stochastic events) by time t, or in the context of a non-homogeneous CTMC the expected number of state transitions. This, however, is different from the expected state of the chain $E[D(t)]$, which, as shown in Section A.2.2 is

$$E[D(t)] = e^{\Lambda(t)}, \tag{5.37}$$

[14]It is independent in the sense that there is no factor applied explicitly to the Exponential distribution to account for the size of the population. Instead, the effect of the size of the population is captured within the intensity measure formulation, specifically the threshold equation.

when the non-homogeneous CTMC is modelled as pure-birth, linear-growth-rate stochastic process and the initial state of the chain is 1. Using Equation 5.17 with parameters from Table 5.1, the expected state of a non-homogeneous Markov chain $E[D(t)]$, whose event space $\mathbf{E} \coloneqq \{E_i(t) : y_i \leq X(t) - u_t < y_i + \Delta y\}$ is mapped to the damage state space $\mathbf{D} \coloneqq \{D(t) = i; i = 1, 2, \ldots, n_D\}$, is shown in Figure 5.13.

To summarise, the proposed stochastic model to approximate the growth of extreme pit depths embraces the following postulates:

1. The magnitude of extreme pit depths $X(t)|X(t) \geq u_t$, which represent time-variant events observed in a corrosion coupon, can be organised into real-valued semi-open intervals representing all possible values of pit depth excesses $X(t) - u_t|X(t) \geq u_t$. The collection of such intervals is defined as the event space $\mathbf{E}$,

$$\mathbf{E} \coloneqq \{E_i(t) : y_i \leq X(t) - u_t < y_i + \Delta y\}\,.$$

   Definition of the event space is possible provided reasonable allowance is made for the anticipated maximum pit depth excess sustained by time t in the structure of interest and sufficient prior pit depth data exists to define an interval width adequately.

2. The mapping of the event space to a subset of the non-negative integer line allows pit depth excesses $X(t) - u_t|X(t) \geq u_t$ to be represented by an equivalent discrete, finite damage state space $\mathbf{D}$,

$$\mathbf{D} \coloneqq \{D(t) = i; i = 1, 2, \ldots, n_D\}\,,$$

   mimicking states of damage through which a structure undergoing pitting corrosion transitions.

3. The process of transitioning through discrete damage states is modelled by a pure-birth, linear-growth-rate non-homogeneous CTMC, whose intensity of transition $\lambda(x_{i,j}\,|\,\boldsymbol{\theta})$,

$$\lambda(x_{i,j}\,|\,\boldsymbol{\theta}) \coloneqq -\frac{\partial \Lambda(x_{i,j}\,|\,\boldsymbol{\theta})}{\partial x} = \frac{1}{\alpha t_j^b}\left[1 - \kappa\left(\frac{x_{i,j} - \mu t_j^b}{\alpha t_j^b}\right)\right]^{\frac{1}{\kappa}-1}\,,$$

   is derived from the NHPP representation of extreme pit depth occurrences, with $X(t)|X(t) \geq u_t \sim$ GPD. This is possible because of the equivalence of event inter-arrival times of a NHPP and the process dwell times of a NHMP. Transitioning through the states is simulated by propagating an initial damage distribution $\mathbf{v}_s$

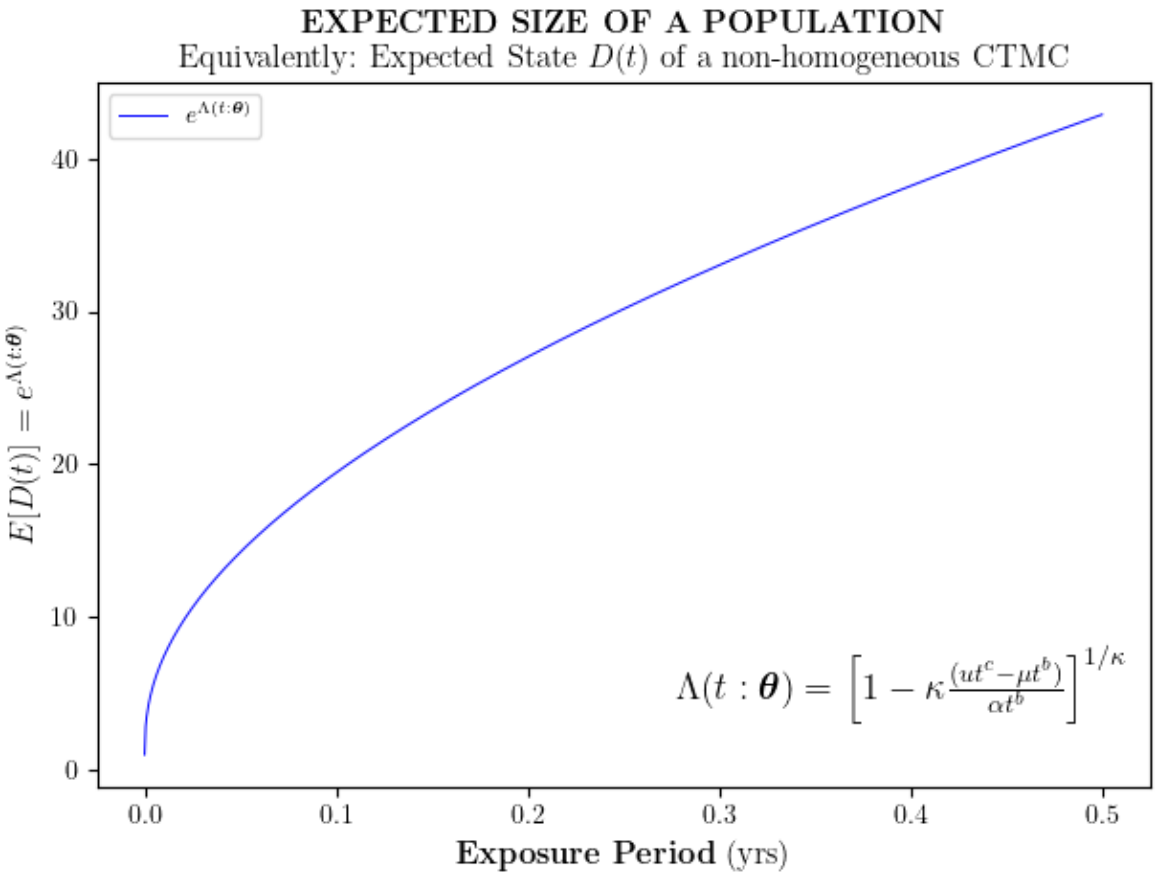

Figure 5.13: Expected state of a pure-birth, linear-growth-rate non-homogeneous CTMC, whose event space $\mathbf{E} \coloneqq \{E_i(t) : y_i \leq X(t) - u_t < y_i + \Delta y\}$ is mapped to the damage state space $\mathbf{D} \coloneqq \{D(t) = i; i = 1, 2, \ldots, n_D\}$, with intensity measure $\Lambda(t)$ given by Equation 5.17 with parameters from Table 5.1. The chain starts at state $i = 1$ at $t = 0$. Note, the chain exists only at integer-valued states, but for convenience $E[D(t)]$ is plotted as a real-valued function.

through the CTMC to predict a damage distribution $\mathbf{v}_t$ at time t by means of a probability transition matrix $\mathbf{P}(s,t)$:

$$\mathbf{v}_t \coloneqq \mathbf{v}_s\mathbf{P}(s,t)$$

5.4.3 NHMP Model Efficacy

The efficacy of the pure-birth, linear-growth-rate non-homogeneous CTMC model is assessed for the current pitting corrosion data by propagating an initial distribution of pit depth excesses through the Markov chain and subsequently comparing qualitatively predicted distributions at each exposure period with those observed. This was accomplished as follows.

For an initial distribution, pit depths from the 7-day exposure test (i.e., $\mathbf{v}_s, s=7/365$) were selected. Corresponding pit depth excesses were calculated by substracting the $low1$ threshold from the data. Due to the limited number of data points (i.e., pit depth excesses) for the 7-day exposure test, however, the initial (empirical) distribution was approximated with a GPD (Equation (5.14)) using the parameters from Table 5.1. This approach provided a well-defined density histogram as an initial distribution. The "observed" distribution of pit depth excesses at each remaining exposure period (i.e., $t = 14/365, 21/365, \ldots, 180/365$) were similarly determined. The initial distribution of pit depth excesses was then mapped to the damage state space, resulting in initial damage state distribution. This damage state distribution was propagated subsequently across the Markov chain by means of Equation 5.25 to produce the "predicted" distribution (histograms) of damage states. A backward mapping of the damage states to the event space yielded a set of predicted pit depth excess distributions. Adding the $low1$ thresholds generated a set of pit depth exceedance distributions, depicted in Figure 5.14, which were subsequently compared with the "observed" distributions.

Generally, the Markov-based predictions tend towards longer tails when compared with the fitted GPD. Certainly, fine tuning Δy and n_D would improve the qualitative goodness of fit, but that is not the objective here. The results clearly demonstrate the efficacy of modelling pit depth exceedances with a non-homogeneous Markov process, specifically the class of Markov models defined by the pure-birth, linear-growth-rate process. Moreover, the use of the NHPP rate $\lambda(t)$ for the infinitesimal transition rate in the non-homogeneous CTMC has been validated for the surrogate data, and modelling pit depth exceedances economises the use of available data over that limited to only predicting pit depth maxima. The last two points, in particular, are considered meaningful contributions to the existing body of knowledge.

The efficacy of the NHMP can be further illustrated by comparing predicted, expected pit depth exceedances with those observed. Effectively, this is achieved by calculating the expectation of the Negative Binomial distribution (Equation 5.32). More concretely, Equation A.13 from Section A.2.2 and Equation 5.37 are used to first estimate the expected damage state of the Markov chain from some initial time t_0 to an arbitrary future time t. Here, the initial time t_0 is once again taken as the 7-day exposure period (i.e., 7/365 years), and $t > 7/365$. Subsequently, the expected damage state of the Markov chain at time t, given that at time t_0 the damage state was D_0, is

$$E[D(t)] = D_0 e^{\Lambda(t)-\Lambda(t_0)}. \tag{5.38}$$

The initial damage state of the Markov chain D_0 can be approximated by mapping to the damage state space $\mathbf{D}$ the observed average pit depth excess at $t_0 = 7/365$ years. Such a mapping leads to $D_0 \approx 1.38$, which rounding to the nearest whole number (i.e., $D(t) \subseteq \mathbb{N}_1$) results in $D_0 = 1$.

To facilitate comparison with observed pit depth exceedances, the results of Equation 5.38 need to be mapped back to the event space characterised by pit depth excesses, whereupon the corresponding time-dependent thresholds are added. Backward mapping was carried out by fitting a simple linear regression formula to the relationship between the central point of each interval in the event space $\mathbf{E}$ and the damage state space $\mathbf{D}$. Figure 5.15 compares the expected pit depth exceedances derived from the NHMP with those observed for $low1$ thresholds along with an Ordinary Least Squares (OLS) fitted to pit depth exceedances. The agreement between the NHMP-based expected pit depth exceedances and the OLS fit is exceptionally good.

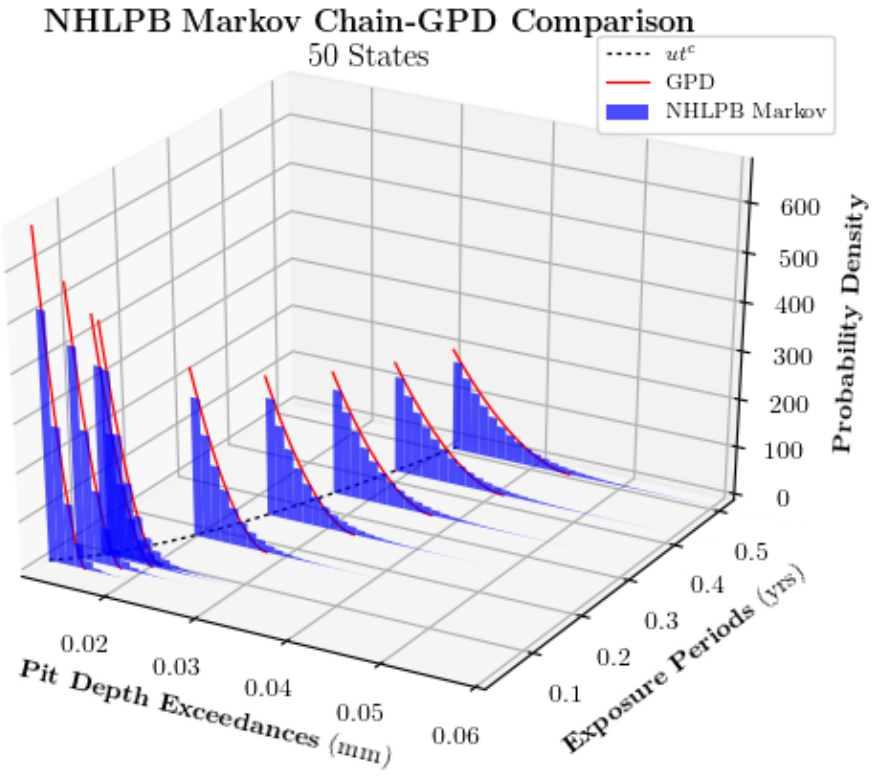

Figure 5.14: Distribution of pit depth exceedancess across all exposure periods, with the initial distribution represented by the 7-day exposure period exceedances and the *low*1 threshold level plotted as dashed line. The figure compares the "predicted" distributions from the Markov process model (here represented by the shortened abbreviation non-homogeneous linear pure birth (NHLPB)) and the "observed" distributions represented by fitting the GPD to the observed exceedances.

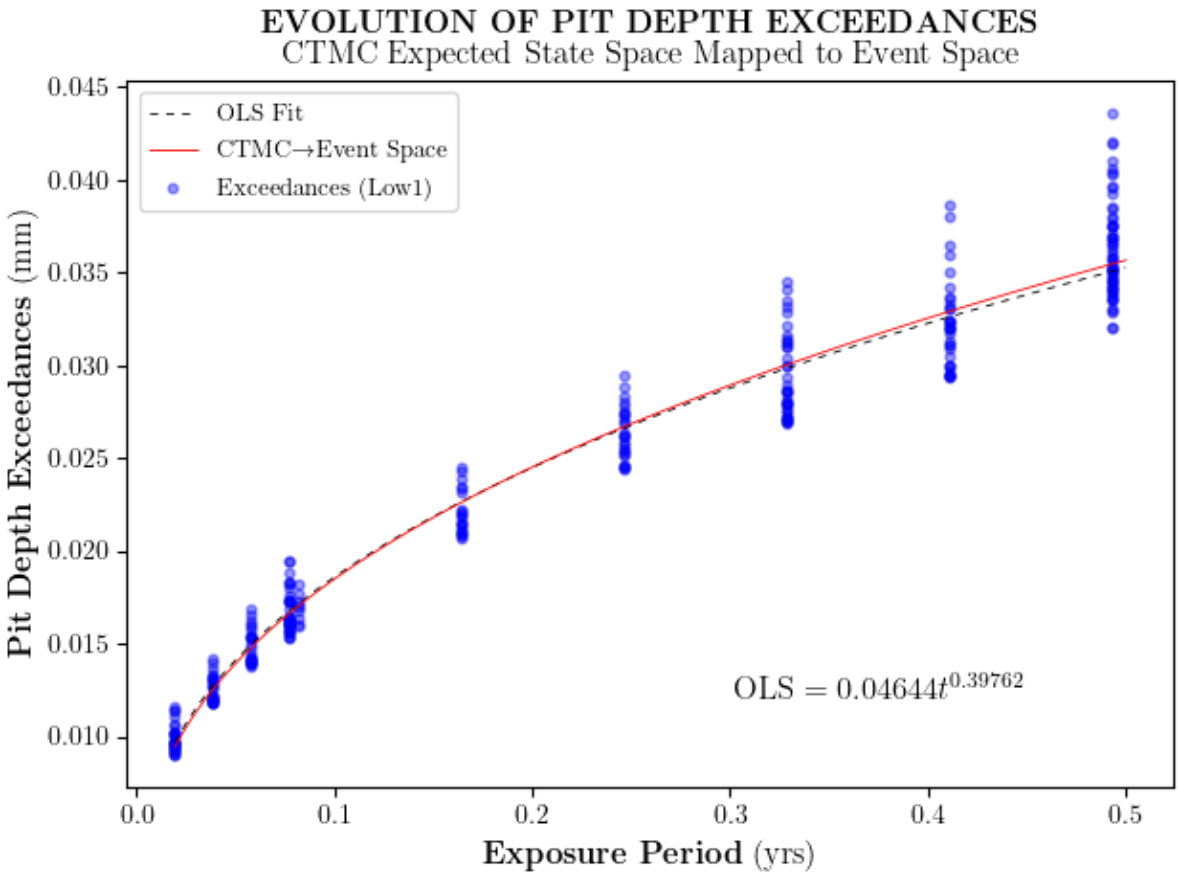

Figure 5.15: Plot of pit depth exceedancess across all exposure periods. The figure compares "predicted" expected pit depth exceedance (red line), estimated from the Markov process model, with observed exceedances. Also included is the OLS fit to pit depth exceedances, plotted by a dashed line. For the CTMC, the 7-day exposure period exceedances ($low1$ threshold level) were used for the initial distribution.

5.5 Algorithm to Assign Pit Depth Exceedances

The basic approach to assign a random pit depth exceedance to each discretised panel on a UFC is to sample from the "predicted" Markov-based distribution, labelled $f_{Markov}(x,t)$, at the desired time period t. The underlying assumption is that in the future, data similar to the one employed in this work will be generated for copper under relevant repository conditions over timescales that, ideally, permit either interpolation (i.e., bound the expected oxic period) or at most some level of extrapolation (i.e., outside the timescales of the experiment) without necessarily introducing significant uncertainty.

Consequently, the algorithm receives as input the timescales for the early, dry oxic period where pitting corrosion is considered a potential degradation mechanism. For simplicity, this could be represented by a time vector, T, covering the minimum and maximum timescales t_{min}, t_{max} anticipated (i.e., $T = [t_{min}, t_{max}]$). Additional inputs include the total number of panels m on the UFC, the ratio M of the UFC surface area to corrosion coupon area (also referred to as *size effect*), the intensity measure $\Lambda(t;\hat{\boldsymbol{\theta}})$, which defines for a single corrosion coupon the expected number of exceedances at projected time period t, and the distribution of initial copper coating thickness, $f_{t_{\mathrm{Cu}}}$.

From Section 3.5, the number of panels m for the 0.06-m mesh size model is 255. The ratio M of the surface area of the quarter hemispherical end-cap and a single corrosion coupon is 251. Consequently, the total expected number of pit depth exceedances n_t assignable to the quarter hemispherical end-cap for time t, consisting potentially of a maximum of one pit depth exceedance per panel, is $M\Lambda(t;\hat{\boldsymbol{\theta}})$ or 255 if $M\Lambda(t;\hat{\boldsymbol{\theta}}) > 255$.

In words, the algorithm selects a time t_i from T and calculates n_t, which is compared with m. The initial distribution $f_{Markov}(x,t_0)$ is then propagated across the Markov chain to the desired time t_i, resulting in "predicted" distribution of pit depth exceedances $f_{Markov}(x,t_i)$. The algorithm then samples randomly n_t thicknesses from the initial copper coating thickness distribution. Arrays of pit depth exceedances $(D_{tmin}, D_{t_{max}})$ are generated by sampling n_t pit depth exceedances from $f_{Markov}(x,t_i)$. Modified arrays of copper coating thickness are subsequently created by subtracting from the initial copper coating thickness array pit depth exceedances from each time segment. The modified initial copper coating thickness arrays are then fed into the original UFC lifetime code for continued processing (not shown here). Algorithm 4 summarises the approach.

Algorithm 4 Pit Depth Exceedance Assignment—NHMP Process

Require: $T, m, M, \Lambda(t;\hat{\boldsymbol{\theta}}), f_{t_{\text{Cu}}}, f_{Markov}(x,t_0)$

Initialise variables, arrays: $t, D_{t_{min}}, D_{t_{max}}, Cu, Cu_{t_{min}}, Cu_{t_{max}}$
$u_k, c_k \leftarrow$ select threshold level k
for t_i in T **do**
    $n_t \leftarrow \text{int}(M\Lambda(t_i;\hat{\boldsymbol{\theta}}))$
    if $n_t > m$ **then**
        $n_t \coloneqq m$
    $f_{Markov}(x,t_i) \leftarrow f_{Markov}(x,t_0)$
    $Cu \leftarrow$ sample randomly n_t thicknesses from $f_{t_{\text{Cu}}}$
    if $t_i == min(T)$ **then**
        $D_{t_{min}} \leftarrow$ sample randomly n_t pit depth exceedances from $f_{Markov}(x,t_i)$
        $Cu_{t_{min}} \leftarrow Cu - D_{t_{min}}$
    else
        $D_{t_{max}} \leftarrow$ sample randomly n_t pit depth exceedances from $f_{Markov}(x,t_i)$
        $Cu_{t_{max}} \leftarrow Cu - D_{t_{max}}$

5.6 Effect of Sulphide-induced & Pitting Corrosion

In this section, the effect of sustaining pitting corrosion during the oxic period, followed by sulphide-induced corrosion, is compared against the baseline sulphide-induced corrosion model of Chapter 3. Specifically, a comparison is made between the NHMP (or CTMC) model developed in the previous sections and competing EVA approaches such as modelling growth of maximum pit depths by the GEV distribution (Appendix B) and pit depth exceedances directly via the GPD within a POT framework (Appendix C). Another approach to compare with the Markov process is to use directly the stochastic process defined in Section 5.3 to predict pit depth exceedances (Appendix D), which here is labelled Point process. Note, this approach is essentially the same as that shown in Appendix C, with the exception that the number of pit depth exceedances assigned to the UFC are governed by $M\Lambda(t;\hat{\boldsymbol{\theta}})$. These approaches are described in detail in their respective appendices, along with the algorithms for assigning pit depths to a UFC. For brevity, these details are omitted here. The comparison is performed by simulating pit growth for an arbitrary two-year oxic period and by making a few minor modifications to the baseline UFC lifetime model (Chapter 3). These modifications are discussed below.

The first modification represents the employment of the UFC discretised model with a mesh size of 0.02 m. Refining the mesh size from 0.06 m to 0.02 m increases the number of

panels on the quarter hemispherical end-cap from 255 to 1599 and allows for the algorithms associated with the Point process and the CTMC to assess the expected number of exceedances at a future time of interest against the number of panels. Without this change the algorithms would be—relatively speaking—uninteresting because $M\Lambda(t;\hat{\boldsymbol{\theta}})$ would always be greater than 255, restricting n_t to 255. The second modification targets the number of realisations executed at each level of the UFC model. To expedite the simulations, without loss of generality—particularly since this is surrogate data, the number of realisations for RVs X_2 and X_3 are reduced respectively from 10000 each to 5000 and 1000. A reduction in the number of realisations impacts the ability to sample more accurately from the tails of the respective distributions. This effect also manifests in a final distribution for RV X_3 that is different than that shown in Figure 3.17. For the purpose of comparing the various models, this loss in sampling accuracy and change in distribution shape is of little impact.

Figure 5.16 shows the Gaussian Kernel density estimation distributions, derived from the density histograms of predicted UFC lifetimes, estimated from the GEV distribution (extrapolated in time and space, Equation B.35), the GPD, the non-homogeneous Point process, and the pure-birth, linear-growth-rate non-homogeneous CTMC. Also included in the figure is the density histogram and corresponding Gaussian Kernel density estimation distribution for the baseline UFC lifetime model (i.e., sulphide-induced corrosion only). Table 5.2 lists the mean and standard deviation estimated from the respective distributions.

Consistent with the respective pit depth assignment algorithms, the mean UFC lifetime was the lowest for the GEV distribution, extrapolated in time and space, since a single maximum pit depth was assigned to each panel. This is very conservative, but in comparison to the mean lifetimes predicted by the other models, the results suggest that it is not overly conservative. The algorithm for the assignment of pit depths using the GPD also assigns a single pit depth to each panel but from pit depth exceedances, which results in slightly longer mean lifetime than that predicted by the GEV distribution extrapolated in time and space. In contrast, the algorithms for both the Point process and the CTMC determine the number of pit depth exceedances to assign from the expected number of exceedances after accounting for size effects, which is the ratio M. If this number is less than the number of panels, then a lower number of pit depth exceedances are assigned when compared with that assigned by the GEV and GPD algorithms. After two years of pit growth, the expected number of exceedances after accounting for size effects was in fact less than the number panels. Generally speaking, the results are consistent and quite similar, indicating that any one of the four modelling approaches is a viable option. For the reasons just discussed, the trend in the mean minimum lifetime is also observed in the standard deviation trend.

From the perspective of the effect of pitting corrosion on UFC mean lifetimes, the results

indicate that for the surrogate data, pitting corrosion during a 2-yr oxic period reduces the average minimum UFC lifetimes (i.e., baseline) by approximately 10^5 years. This is a negligible amount when compared with the mean minimum lifetimes, which are in the order of 10^6 years. However, when coupled with the potential for latent defects and the effect of the single repository temperature transient, and when a greater number of realisations are applied, minimum UFC lifetimes may sustain noticeable reductions. Again, due to the fact that results are based on surrogate data, one is advised to exercise a measure of caution. This is particularly true when one seeks from this work to quantify the effect of pitting corrosion on UFC lifetimes or to draw premature conclusions concerning the adequacy—or lack thereof—of the present corrosion allowance. Indeed, the important point to emphasise is that should pitting corrosion be a credible cause for concern, a probabilistic model has been presented that offers a fresh perspective into the interpretation of pitting corrosion as a series of stochastic events. With the NHMP model for pitting corrosion discussed in this chapter, not only does a user have the ability to propagate a distribution of pits forward in time, the user also gains insight into the intrinsic intensity of the pitting process. From an engineering perspective, the latter is significant because one can both speak about the number of expected pits greater than some critical depth at some future time of interest and account for the same in any model that is concerned with the number of potential radioactive waste leak sites on a UFC surface.

Table 5.2: Mean and Standard Deviations for the UFC Minimum Lifetimes Predicted by the GEV Distribution, the GPD, the Point process, and CTMC

Statistic	Baseline[1]	GEV^{M}[2]	GPD	Point Process	CTMC
Mean (10^6 yrs)	8.4528	8.1519	8.1757	8.2496	8.3422
Std Dev (10^6 yrs)	1.7528	1.6747	1.6474	1.7112	1.7202

[1] Minimum UFC lifetimes due to sulphide-induced corrosion

[2] GEV^{M} is the GEV distribution extrapolated in time and space, Equation B.35.

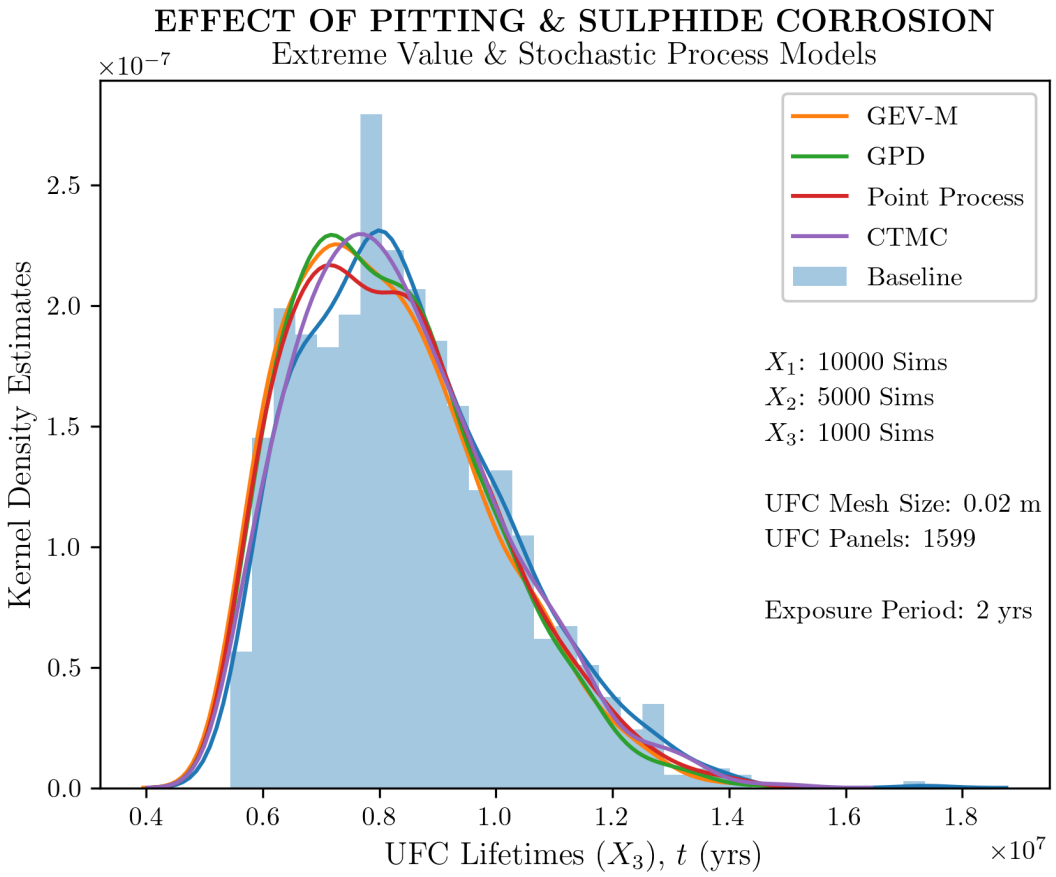

Figure 5.16: Distribution of predicted minimum UFC lifetimes (X_3), estimated from EVA models such as the GEV distribution and the GPD (both time- and space-extrapolated) and from the stochastic process models Point and CTMC. Pit depths are estimated for a two-year oxic period and for a UFC mesh size of 0.02 m, which is equivalent to 1599 nodes or panels. Computational effort was minimised by reducing the number of realisations (i.e., Sims) required to generated an empirical distribution for X_2 and X_3. Minimum lifetimes due to sulphide-induced corrosion are represented by the histogram results labelled Baseline and corresponding Kernel density estimation (blue line).

5.7 Summary

A pure-birth, linear-growth-rate non-homogeneous CTMC has been applied successfully to model the evolution of pit depth exceedances in the quarter hemispherical end-cap of a UFC. While others in the literature have employed Markov chains to model pit depth maxima, as far as this author is aware, this is the first time pit depth exceedances have been modelled by a CTMC. Moreover, the non-homogeneous Markov process model presented here is unique in the incorporation of a well-defined intensity measure and intensity density function, both having direct and transparent origins in the NHPP and the asymptotic basis underpinning the GEV distribution. This contrasts the semi-empirical approach prevalent in the literature for formulating an expression for the pit growth process intensity, which again has been restricted to pit depth maxima applications. For the surrogate data employed in this work, the assumptions made concerning the length of the oxic period, and the limited simulations carried out, pitting corrosion was shown to reduce on average the mean minimum UFC lifetimes by approximately 10^5 years, relative to the mean minimum lifetime predicted as a result of sulphide-induced corrosion alone. When compared with the mean minimum UFC lifetimes, which are in the order of 10^6 years, the effect of pitting corrosion is not considered significant or consequential to the current corrosion allowance. However, this needs to be placed within the context of this work. Additionally, the engineering significance of the stochastic model is further demonstrated by its ability to estimate the expected number of extreme pit depths on the surface of a UFC. Owing to the reasonable assumption that extreme pit depths can be likely sites for the perforation of UFC copper coatings and eventual leakage of radioactive waste, the ability to estimate the number of leak sites is considered important from an engineering perspective.

Chapter 6

Conclusions

6.1 Summary

A baseline UFC copper-coating lifetime model, developed on the basis that sulphide-induced corrosion is the only degradation mechanism of concern, has been successfully developed to account for the effect of critical variables presently understood to be of significance to UFC lifetimes. These include copper coating thickness, HS^- effective diffusion coefficient in compacted bentonite, and $[HS^-]$ in the geosphere. Building upon the probabilistic framework of the baseline model, the present work has also integrated the required formulation to account for the effects of both latent copper-coating defects and repository temperatures within the existing 1-D, multi-level representation of the sulphide-induced corrosion problem. Model utility has been demonstrated in the incorporation of uncertainty for UFC life-limiting variables such as HS^- diffusivity in bentonite clay, emplacement room $[HS^-]$, UFC copper coating thickness and potential defects, and repository emplacement room temperatures (via enhanced corrosion rates).

The question of how to account for the potential for pitting corrosion within the probabilistic framework described above was examined in this work using a stochastic process model applied to surrogate data. This resulted in two meaningful contributions to the general body of literature associated with modelling pit growth via Markov chains, as discussed below. Overall, within the context of the surrogate data used in this work, the effect of pitting corrosion during the short oxic period postulated for the DGR was found to have negligible effect on UFC lifetimes, relative to repository timescales, and inconsequential to the existing corrosion allowance.

From an engineering perspective, the significance of the combined model was illustrated in the ability to provide a distribution of minimum UFC lifetimes, from which fraction of first failures over timescales of interest may be computed. Further engineering significance was highlighted by the facility to quantify the number of potential locations on the UFC surface where deep pits can lead to leaks of radioactive fuel—sites for release of contaminants into the geosphere. While not explicitly demonstrated though discussed, the combined model also allows for the identification of sites on the UFC surface where leaks will first occur. This can be extended to which UFCs in an emplacement room will leak first and to which emplacement rooms within a panel will exhibit first leaks. The modelling results of this work are for the purpose of illustrating a potential methodology.

6.2 Research Contributions

- The primary and most significant research contribution from this work is the formulation of a probabilistic framework for predicting UFC lifetimes based on both sulphide-induced and pitting corrosion. Presently, to the author's best knowledge, no such model exists for copper-coated UFCs or copper-clad used fuel waste containers.
- The second research contribution is the successful employment of a pure-birth, linear-growth-rate non-homogeneous Markov process to propagate pit depth exceedances across a CTMC. To the best of this author's estimation, pit depth exceedances have not been modelled in this manner before.
- The third and final research contribution is the use of the NHPP intensity measure and intensity density function for modelling growth of pit depth exceedances in a CTMC. The value of this contribution is that the intensity of a pitting process may be derived solely from stochastic and asymptotic arguments without the need to resort to popular methods that invoke an equivalence between a deterministic—empirically derived—expression for pit growth and a stochastic representation of the same.

6.3 Future Work

One of the significant assumptions employed in the current model is that distributed properties assigned to the factors associated with the DGR/engineered barriers are time invariant. For example, the distribution assigned to the $[HS^-]$ is assumed to remain fixed over the

timescales of the DGR. The same assumption applies to the distribution of the HS^- effective diffusion coefficient in the bentonite buffer box, which is also assumed to be isotropic and constant throughout. Future conditions in the evolving repository environment may violate these assumptions. One hypothetical scenario is the delayed hydraulic activation of fractures in the EDZ of emplacement room walls, which could lead to non-uniform groundwater saturation and potentially localised growth of SRB. However, the likelihood of this and other potential scenarios that are hypothesised to violate these assumptions need to be thoroughly assessed by qualified experts. Should such an assessment establish a reasonable likelihood of occurrence, one approach that could be considered in future work is to treat these scenarios as "shocks" in the timescale of the DGR.

A very significant limitation of the current probabilistic model is the need to "recalibrate" the effective diffusion length against some numerical diffusion analysis every time the design of the UFC and buffer box change. Future work may consider a completely different framework to eliminate this dependency.

Lastly, this work has considered only a very small part of a very complex problem. While the research to date points to sulphide-induced corrosion as the most consequential degradation mechanism for the copper coatings, there are many other factors that can contribute to failure of a UFC. Future work may consider expanding the definition of failure adopted in this model.

References

Anderson, T. W. (2011). Anderson–darling tests of goodness-of-fit. In Lovric, M., editor, *International Encyclopedia of Statistical Science*, pages 52–54. Springer Berlin Heidelberg, Berlin, Heidelberg.

Anderson, T. W. and Darling, D. A. (1954). A TEST OF GOODNESS OF FIT. *Journal of the American Statistical Association*, 49(268):765–769.

Bader, B., Yan, J., and Zhang, X. (2018). Automated threshold selection for extreme value analysis via ordered goodness-of-fit tests with adjustment for false discovery rate. *The Annals of Applied Statistics*, 12(1):310–329.

Bath, A. (2014). Independent assessment of groundwater sulphide content in the long-term: Main review phase. Technical Note Technical Note 2014:48, Swedish Radiation Safety Authority.

Beichelt, F. E. and Fatti, L. P. (2002). *Stochastic Processes and Their Applications*. CRC Press LLC.

Beirlant, J., Goegebeur, Y., Segers, J., and Teugels, J. L. (2004). *Statistics of Extremes: Theory and Applications*. Wiley.

Berger, J. O. (1985). *Statistical Decision Theory and Bayesian Analysis*. Springer, 2nd edition.

Bojinov, M., Laitinen, T., Mäkelä, K., Snellman, M., and Werme, L. (2004). Corrosion of copper in 1M NaCl under strictly anoxic conditions. *MRS Online Proceedings Library*, 807:6.

Bojinov, M. and Makela, K. (2003). Corrosion of copper in anoxic 1M NaCl solution. Working Report WR-2003-45, Posiva.

Bolstad, W. M. (2010). *Understanding Computational Bayesian Statistics*. John Wiley & Sons, 1st edition.

Brémaud, P. (2020a). *Point Process Calculus in Time and Space: An Introduction with Applications*. Probability Theory and Stochastic Modelling. Springer International Publishing, 1st edition.

Brémaud, P. (2020b). *Probability Theory and Stochastic Processes*. Universitext. Springer International Publishing, 1st edition.

Breuer, L. (2003). *From Markov Jump Processes to Spatial Queues*. Springer, Dordrecht, 1st edition.

Briggs, S., Lilja, C., and King, F. (2021). Probabilistic model for pitting of copper canisters. *Materials and Corrosion*, 72(1–2):308–316.

Briggs, S., McKelvie, J., Sleep, B., and Krol, M. (2017). Multi-dimensional transport modelling of corrosive agents through a bentonite buffer in a Canadian deep geological repository. *Science of The Total Environment*, 599-600:348–354.

Brown, S. J., Caesar, J., and Ferro, C. A. T. (2008). Global changes in extreme daily temperature since 1950. *Journal of Geophysical Research: Atmospheres*, 113(D5).

Bücher, A. and Segers, J. (2017). On the maximum likelihood estimator for the generalized extreme-value distribution. *Extremes*, 20(4):839–872.

Bullen, D. B. (1996). A model for container performance in an unsaturated repository. *Nuclear Technology*, 113:29–45.

Caleyo, F., Velázquez, J., Valor, A., and Hallen, J. (2009). Markov chain modelling of pitting corrosion in underground pipelines. *Corrosion Science*, 51(9):2197–2207.

Camacho, E., Melo, P., Saldanha, P., and Silva, E. D. (2011). A fokker-planck model of pitting corrosion in underground pipelines to support risk-informed decision making. In Berenguer, C., Grall, A., and Soares, C. G., editors, *Advances in Safety, Reliability and Risk Management*.

Cannon, A. J. (2010). A flexible nonlinear modelling framework for nonstationary generalized extreme value analysis in hydroclimatology. *Hydrological Processes*, 24(6):673–685.

Canuto, C. and Tabacco, A. (2015). *Mathematical Analysis I*. UNITEXT - La Matematica per il 3+2, Volume 84. Springer International Publishing Switzerland, 2nd edition.

Cao, X. and Spall, J. C. (2012). Relative performance of expected and observed fisher information in covariance estimation for maximum likelihood estimates. In *2012 American Control Conference (ACC)*, pages 1871–1876.

Casella, G. and Berger, R. L. (2002). *Statistical Inference*. Brooks/Cole, 2nd edition.

Castillo, E. (1988). *Extreme Value Theory in Engineering*. Academic Press.

Castillo, E., Hadi, A. S., Balakrishnan, N., and Sabaria, J. M. (2005). *Extreme value and related models with applications in engineering and science*. Wiley-Interscience, Hoboken, New Jersey.

Çinlar, E. (1975). *Introduction to Stochastic Processes*. Dover.

Cha, J. H. and Finkelstein, M. (2018). *Point processes for reliability analysis : shocks and repairable systems*. Springer series in reliability engineering. Cham, Switzerland: Springer.

Chen, J., Qin, Z., Martino, T., Guo, M., and Shoesmith, D. (2018). Copper transport and sulphide sequestration during copper corrosion in anaerobic aqueous sulphide solutions. *Corrosion Science*, 131:245–251.

Chen, J., Qin, Z., Martino, T., and Shoesmith, D. (2017a). Non-uniform film growth and micro/macro-galvanic corrosion of copper in aqueous sulphide solutions containing chloride. *Corrosion Science*, 114:72–78.

Chen, J., Qin, Z., Martino, T., and Shoesmith, D. W. (2017b). Effect of chloride on Cu corrosion in anaerobic sulphide solutions. *Corrosion Engineering, Science and Technology*, 52:40–44.

Chen, J., Qin, Z., and Shoesmith, D. (2011). Long-term corrosion of copper in a dilute anaerobic sulfide solution. *Electrochimica Acta*, 56:7854–7861.

Chen, J., Qin, Z., and Shoesmith, D. W. (2010). Kinetics of Corrosion Film Growth on Copper in Neutral Chloride Solutions Containing Small Concentrations of Sulfide. *Journal of The Electrochemical Society*, 157:C338.

Chen, J., Qin, Z., and Shoesmith, D. W. (2014). Key parameters determining structure and properties of sulphide films formed on copper corroding in anoxic sulphide solutions. *Corrosion Engineering, Science and Technology*, 49:415–419.

Cheng, T. and Pandey, M. D. (2012). An accurate analysis of maintenance cost of structures experiencing stochastic degradation. *Structure and Infrastructure Engineering*, 8(4):329–339.

Chijimatsu, M., Fujita, T., Sugita, Y., Amemiya, K., and Kobayashi, A. (2001). Field experiment, results and THM behavior in the Kamaishi mine experiment. *International Journal of Rock Mechanics and Mining Sciences*, 38(1):67–78.

Choulakian, V. and Stephens, M. A. (2001). Goodness-of-fit tests for the generalized pareto distribution. *Technometrics*, 43(4):478–484.

Coles, S. (2001). *An introduction to statistical modeling of extreme values*. Springer-Verlag, London, England.

Coles, S. and Pericchi, L. (2003). Anticipating catastrophes through extreme value modelling. *Journal of the Royal Statistical Society. Series C (Applied Statistics)*, 52(4):405–416.

Coles, S., Pericchi, L. R., and Sisson, S. (2003). A fully probabilistic approach to extreme rainfall modeling. *Journal of Hydrology*, 273(1–4):35–50.

Coles, S. and Tawn, J. (2005). Bayesian modelling of extreme surges on the uk east coast. *Philosophical Transactions: Mathematical, Physical and Engineering Sciences*, 363(1831):1387–1406.

Coles, S. G. and Dixon, M. J. (1999). Likelihood-based inference for extreme value models. *Extremes*, 2(1):5–23.

Coles, S. G. and Tawn, J. A. (1996). A bayesian analysis of extreme rainfall data. *Journal of the Royal Statistical Society. Series C (Applied Statistics)*, 45(4):463–478.

Cox, D. R. and Miller, H. D. (1987). *The Theory of Stochastic Processes*. Science Paperbacks.

Cox, D. R. and Snell, E. J. (1968). A general definition of residuals. *Journal of the Royal Statistical Society. Series B (Methodological)*, 30(2):248–275.

Datla, S. V., Jyrkama, M. I., and Pandey, M. D. (2008). Probabilistic modelling of steam generator tube pitting corrosion. *Nuclear Engineering and Design*, 238(7):1771–1778.

Davison, A. C. and Hinkley, D. V. (1997). *Bootstrap Methods and their Application*. Cambridge Series in Statistical and Probabilistic Mathematics. Cambridge University Press.

Davison, A. C. and Ramesh, N. I. (2000). Local likelihood smoothing of sample extremes. *Journal of the Royal Statistical Society: Series B (Statistical Methodology)*, 62(1):191–208.

Davison, A. C. and Smith, R. L. (1990). Models for exceedances over high thresholds. *Journal of the Royal Statistical Society. Series B (Methodological)*, 52(3):393–442.

Denison, I. A. and Romanoff, M. (1950). Soil-corrosion studies, 1946 and 1948: copper alloys, lead, and zinc. *Journal of Research of the National Bureau of Standards*, 44:259–289.

Dessirier, B., Frampton, A., Fransson, Å., and Jarsjö, J. (2016). Modeling early in situ wetting of a compacted bentonite buffer installed in low permeable crystalline bedrock: MODELING EARLY IN SITU WETTING OF A COMPACTED BENTONITE. *Water Resources Research*, 52(8):6207–6221.

Dessirier, B., Åkesson, M., Lanyon, B., Frampton, A., and Jarsjö, J. (2017). Reconstruction of the water content at an interface between compacted bentonite blocks and fractured crystalline bedrock. *Applied Clay Science*, 142:145–152.

DOE (U.S. Department of Energy) (2002). Yucca Mountain Science and Engineering Report Technical Information Supporting Site Recommendation Consideration. Technical Report DOE/RW-0539-1 Revision 1, DOE.

DOE (U.S. Department of Energy) (2008). Yucca Mountain repository license application, safety analysis report. Technical Report DOE/RW-0573, DOE.

Doob, J. L. (1953). *Stochastic Processes*. John Wiley & Sons.

Doubt, G. (1984). Assessing reliability and useful life of containers for disposal of irradiated fuel waste. Technical Report AECL-8328, AECL, Chalk River Nuclear Laboratories.

Efron, B. and Tibshirani, R. (1994). *An Introduction to the Bootstrap*. Chapman and Hall/CRC, 1st edition.

Einstein, A. (1905). Über die von der molekularkinetischen theorie der wärme geforderte bewegung von in ruhenden flüssigkeiten suspendierten teilchen. *Annalen der Physik*, 322(8):549–560.

El Adlouni, S., Ouarda, T. B. M. J., Zhang, X., Roy, R., and Bobée, B. (2007). Generalized maximum likelihood estimators for the nonstationary generalized extreme value model. *Water Resources Research*, 43(3).

Fernández, A. M. and Villar, M. V. (2010). Geochemical behaviour of a bentonite barrier in the laboratory after up to 8 years of heating and hydration. *Applied Geochemistry*, 25(6).

Fontes, G., Frutuoso e Melo, P., and De Martin Alves, A. (2015). An itô model of pit corrosion in pipelines for evaluating risk-informed decision making. *Nuclear Engineering and Design*, 293:485–491.

Gallager, R. G. (2013). *Stochastic Processes: Theory for Applications*. Cambridge University Press.

Garisto, F. (2012). Fourth Case Study: Features, Events and Processes. Technical Report TR-2012-14, NWMO.

Garisto, F. (2013). Fifth Case Study: Reference Data and Codes. Technical Report TR-2013-06, NWMO.

Gierszewski, P., Avis, J., Calder, N., D'Andrea, A., Garisto, F., Kitson, C., Melnyk, T., Wei, K., and Wojciechowski, L. (2004). Third Case Study - Postclosure Safety Assessment. Technical Report 06819-REP-01200-10109-R00, OPG.

Gokhale, S., Lyu, M., and Trivedi, K. (2004). Analysis of software fault removal policies using a non-homogeneous continuous time markov chain. *Software Quality Journal*, 12:211–230.

Gray, R. M. and Davisson, L. D. (1986). *Random Processes: A Mathematical Approach for Engineers*. Prentice-Hall Information and System Sciences Series. Prentice-Hall Inc., New Jersey, 1st edition.

Grimmett, G. R. and Stirzaker, D. R. (2001). *Probability and Random Processes*. Oxford University Press, United States of America, 3rd edition.

Groen, E., Heijungs, R., Bokkers, E., and de Boer, I. (2014). Methods for uncertainty propagation in life cycle assessment. *Environmental Modelling & Software*, 62:316–325.

Guo, R. (2015). Thermal Modelling of a Mark II Container. Technical Report NWMO-TR-2015-06, NWMO.

Guo, R. (2016). Thermal Response of a Mark II Conceptual Deep Geological Repository in Crystalline Rock. Technical Report NWMO-TR-2016-03, NWMO.

Guo, R. (2017). Thermal response of a Canadian conceptual deep geological repository in crystalline rock and a method to correct the influence of the near-field adiabatic boundary condition. *Engineering Geology*, 218.

Hajek, B. (2015). *Random Processes for Engineers*. Cambridge University Press, United Kingdom, 1st edition.

Hall, D. S., Behazin, M., Jeffrey Binns, W., and Keech, P. G. (2021). An evaluation of corrosion processes affecting copper-coated nuclear waste containers in a deep geological repository. *Progress in Materials Science*, 118:100766.

Hall, W. J. and Wellner, J. A. (2017). Estimation of mean residual life. *arXiv: Statistics Theory*.

Hansen, C., Behie, G., Bier, A., Brooks, K., Chen, Y., Helton, J., Hommel, S., Lee, K., Lester, B., Mattie, P., Mehta, S., Miller, S., Sallaberry, C., Sevougian, S., and Vo, P. (2014). Uncertainty and sensitivity analysis for the nominal scenario class in the 2008 performance assessment for the proposed high-level radioactive waste repository at Yucca Mountain, Nevada. *Reliability Engineering & System Safety*, 122:272–296.

He, X., Xu, X., Tian, W., Li, Y., Jin, W., and Zhou, M. (2019). Markov stochastic process modeling for evolution of wear depth in steam generator tubes. *Advances in Mechanical Engineering*, 11(5):1–9.

Hong, H. P. (1999a). Application of the stochastic process to pitting corrosion. *Corrosion*, 55(1):10–16.

Hong, H. P. (1999b). Inspection and maintenance planning of pipeline under external corrosion considering generation of new defects. *Structural Safety*, 21(3):203–222.

Hosking, J. R. M. (1990). L-moments: Analysis and estimation of distributions using linear combinations of order statistics. *Journal of the Royal Statistical Society. Series B (Methodological)*, 52(1):105–124.

Hosking, J. R. M., Wallis, J. R., and Wood, E. F. (1985). Estimation of the generalized extreme-value distribution by the method of probability-weighted moments. *Technometrics*, 27(3):251–261.

Huber, M. L., Perkins, R. A., Laesecke, A., Friend, D. G., Sengers, J. V., Assael, M. J., Metaxa, I. N., Vogel, E., Mareš, R., and Miyagawa, K. (2009). New international formulation for the viscosity of h2o. *Journal of Physical and Chemical Reference Data*, 38(2):101–125.

Ibe, O. C. (2013). *Markov Processes for Stochastic Modeling*. Elsevier, 2nd edition.

Ibrahim, B., Zagidulin, D., Behazin, M., Ramamurthy, S., Wren, J., and Shoesmith, D. (2018). The corrosion of copper in irradiated and unirradiated humid air. *Corrosion Science*, 141.

Ikonen, K. and Raiko, H. (2015). Thermal analysis of KBS-3H repository. Technical Report WR 2015-01, Posiva.

Järvine, A. K., Murchison, A. G., Keech, P. G., and Pandey, M. D. (2019). A probabilistic model for estimating life expectancy of used nuclear fuel containers in a canadian geological repository: Baseline model. *Nuclear Engineering and Design*, 352:110202.

Järvine, A. K., Murchison, A. G., Keech, P. G., and Pandey, M. D. (2020). A probabilistic model for estimating life expectancy of used nuclear fuel containers in a canadian geological repository: Effects of latent defects and repository temperature. *Nuclear Technology*, 206(7):1036–1058.

Jenkinson, A. F. (1955). The frequency distribution of the annual maximum (or minimum) values of meteorological elements. *Quarterly Journal of the Royal Meteorological Society*, 81(348):158–171.

Johnson, L. H., LeNeveu, D. M., King, F., Shoesmith, D. W., Kolar, M., Oscaron, D. W., Sunder, S., Onofrei, J. L., and Crosthwaite, J. L. (1996). The disposal of Canada's nuclear fuel waste- A study of postclosure safety of in-room emplacement of used CANDU fuel in copper containers in permeable plutonic rock- volume 2- Vault model. Technical Report AECL-11494-2, COG-96-552-2, AECL.

Johnson, L. H., LeNeveu, D. M., Shoesmith, D. W., Oscaron, D., Gray, M. N., Lemire, R., and Garisto, N. (1994). The Disposal of Canada's Nuclear Fuel Waste: The Vault Model for Postclosure Assessment. Technical Report AECL-10714, COG-93-4, AECL Research.

Kalton, G. (1983). *Introduction to Survey Sampling*. Sage Publications.

Kao, E. P. (2019). *An Introduction to Stochastic Processes*. Dover.

Kass, R. E., Eden, U., and Brown, E. (2014). *Analysis of Neural Data*. Springer Series in Statistics. Springer-Verlag New York, 1st edition.

Katz, R. W., Parlange, M. B., and Naveau, P. (2002). Statistics of extremes in hydrology. *Advances in Water Resources*, 25(8):1287–1304.

Khaliq, M., Ouarda, T., Ondo, J.-C., Gachon, P., and Bobée, B. (2006). Frequency analysis of a sequence of dependent and/or non-stationary hydro-meteorological observations: A review. *Journal of Hydrology*, 329(3):534–552.

Kharin, V. V. and Zwiers, F. W. (2005). Estimating extremes in transient climate change simulations. *Journal of Climate*, 18(8):1156 – 1173.

King, F. (2014). Predicting the lifetimes of nuclear waste containers. *JOM*, 66:526–537.

King, F., Hall, D. S., and Keech, P. G. (2017). Nature of the near-field environment in a deep geological repository and the implications for the corrosion behaviour of the container. *Corrosion Engineering, Science and Technology*, 52:25–30.

King, F. and LeNeveu, D. M. (1991). Prediction of the lifetimes of copper nuclear waste containers. In *Conference on Nuclear Waste Packaging*, Las Vegas, NV. American Nuclear Society.

King, F. and Lilja, C. (2013). Localised corrosion of copper canisters in bentonite pore water. Technical Report TR-13-27, SKB.

King, F. and Lilja, C. (2014). Localised corrosion of copper canisters. *Corrosion Engineering, Science and Technology*, 49(6):420–424.

King, F. and Stroes-Gascoyne, S. (1995). Microbially Influenced Corrosion of Nuclear Fuel Waste Disposal Containers. Proceedings of the International Conference on Microbially Influenced Corrosion, New Orleans, Louisiana. NACE.

Kolar, M. and King, F. (1995). Modelling the Consumption of Oxygen by Container Corrosion and Reaction with Fe(II). volume 412. Materials Research Society.

Kremer, E. P. (2017). Durability of the Canadian used fuel container. *Corrosion Engineering, Science and Technology*, 52(sup1):173–177.

Kwong, G. M. (2011). Status of Corrosion Studies for Copper Used Fuel Containers Under Low Salinity Conditions. Technical Report TR-2011-14, NWMO.

Lawless, J. F. (1987). Regression methods for poisson process data. *Journal of the American Statistical Association*, 82(399):808–815.

Laycock, P. J., Cottis, R. A., and Scarf, P. A. (1990). Extrapolation of extreme pit depths in space and time. *Journal of The Electrochemical Society*, 137(1):64–69.

Leadbetter, M. R., Lindgren, G., and Rootzen, H. (1983). *Extremes and Related Properties of Random Sequences and Processes*. Springer, New York, NY.

Lehmann, E. and Casella, G. (1998). *Theory of Point Estimation*. Springer, 2nd edition.

Li, X., Zhao, Y., Qi, W., Wang, J., Xie, J., Wang, H., Chang, L., Liu, B., Zeng, G., Gao, Q., Sun, H., Zhang, T., and Wang, F. (2019). Modeling of pitting corrosion damage based on electrochemical and statistical methods. *Journal of The Electrochemical Society*, 166(15):C539–C549.

Martino, T., Chen, J., Qin, Z., and Shoesmith, D. W. (2017). The kinetics of film growth and their influence on the susceptibility to pitting of copper in aqueous sulphide solutions. *Corrosion Engineering, Science and Technology*, 52:61–64.

Martino, T., Partovi-Nia, R., Chen, J., Qin, Z., and Shoesmith, D. W. (2014). Mechanisms of Film Growth on Copper in Aqueous Solutions Containing Sulphide and Chloride under Voltammetric Conditions. *Electrochimica Acta*, 127:439–447.

Martins, E. S. and Stedinger, J. R. (2000). Generalized maximum-likelihood generalized extreme-value quantile estimators for hydrologic data. *Water Resources Research*, 36(3):737–744.

McCallum, K., Zhao, J., Workman, M., Iannuzzi, M., Kappes, M., Payer, J., Clemons, C., Chawla, S., Kreider, K., Mimoto, N., and Young, G. (2014). Localized corrosion risk assessment using markov analysis. *Corrosion*, 70(11):1114–1127.

McKay, M. D., Beckman, R. J., and Conover, W. J. (1979). Comparison of Three Methods for Selecting Values of Input Variables in the Analysis of Output from a Computer Code. *Technometrics*, 21(2):239–245.

McMurry, J. (2004). Reference water compositions for a deep geologic repository in the Canadian Shield. Technical Report 06819-REP-01200-10135-R00, Ontarion Power Generation.

Mon, E. E., Hamamoto, S., Kawamoto, K., Komatsu, T., and Moldrup, P. (2016). Temperature effects on solute diffusion and adsorption in differently compacted kaolin clay. *Environmental Earth Sciences*, 75(7).

Morco, R. P., Joseph, J. M., Hall, D. S., Medri, C., Shoesmith, D. W., and Wren, J. C. (2017). Modelling of radiolytic production of HNO $_3$ relevant to corrosion of a used fuel container in deep geologic repository environments. *Corrosion Engineering, Science and Technology*, 52(sup1).

Naylor, J. C. and Smith, A. F. M. (1982). Applications of a method for the efficient computation of posterior distributions. *Journal of the Royal Statistical Society. Series C (Applied Statistics)*, 31(3):214–225.

Noronha, J. (2016). Deep Geological Repository Conceptual Design Report Crystalline / Sedimentary Rock Environment. Technical Report APM-REP-00440-0015 R001, NWMO.

Northrop, P. J. and Coleman, C. L. (2014). Improved threshold diagnostic plots for extreme value analyses. *Extremes*, 17:289–303.

NWMO (2012). Adaptive Phased Management: Used Fuel Repository Conceptual Design and Postclosure Safety Assessment in Crystalline Rock. Pre-Project Report TR-2012-16, NWMO.

NWMO (2017). Sixth Case Study Features, Events, and Processes. Technical Report TR-2017-08, NWMO.

Ossai, C. I., Boswell, B., and Davies, I. (2016). Markov chain modelling for time evolution of internal pitting corrosion distribution of oil and gas pipelines. *Engineering Failure Analysis*, 60:209–228.

Panagoulia, D., Economou, P., and Caroni, C. (2014). Stationary and nonstationary generalized extreme value modelling of extreme precipitation over a mountainous area under climate change. *Environmetrics*, 25(1):29–43.

Parzen, E. (1960). *Modern Probability Theory and Its Applications*. A Wiley Publication in Mathematical Statistics. John Wiley & Sons, Inc., 1st edition.

Parzen, E. (2015). *Stochastic Processes*. Dover.

Pawitan, Y. (2013). *In all likelihood: Statistical Modelling and Inference Using Likelihood*. Claredon Press-Oxford, 1st edition.

Peebles Jr., P. Z. (2002). *Probability, Random Variables and Random Signal Principles*. McGraw Hill Education (India) Private Limited, 4th edition.

Pensado, O. and Pabalan, R. (2008). Probabilistic methodology to estimate environmental conditions for localized corrosion and stress corrosion cracking of Alloy 22 in a high-level radioactive waste repository setting. *Journal of Nuclear Materials*, 381:231–241.

Pickands, J. (1971). The two-dimensional poisson process and extremal processes. *Journal of Applied Probability*, 8(4):745–756.

Pickands, J. (1975). Statistical inference using extreme order statistics. *The Annals of Statistics*, 3(1):119–131.

Provan, J. W. and Rodriguez III, E. S. (1989). Part i: Development of a markov description of pitting corrosion. *Corrosion*, 45(3):178–192.

Qin, Z. and Shoesmith, D. (2008). Failure model and Monte Carlo simulations for titanium (grade-7) drip shields under Yucca Mountain repository conditions. *Journal of Nuclear Materials*, 379:169–173.

R Core Team (2021). *R: A Language and Environment for Statistical Computing*. R Foundation for Statistical Computing, Vienna, Austria.

Rashwan, T. L., Asad, M. A., Molnar, I. L., Behazin, M., Keech, P. G., and Krol, M. M. (2022). Exploring the governing transport mechanisms of corrosive agents in a canadian deep geological repository. *Science of The Total Environment*, page 153944.

Rechard, R. P., Lee, J. H., Hardin, E. L., and Bryan, C. R. (2014a). Waste package degradation from thermal and chemical processes in performance assessments for the Yucca Mountain disposal system for spent nuclear fuel and high-level radioactive waste. *Reliability Engineering & System Safety*, 122:145–164.

Rechard, R. P., Wilson, M. L., and Sevougian, S. D. (2014b). Progression of performance assessment modeling for the Yucca Mountain disposal system for spent nuclear fuel and high-level radioactive waste. *Reliability Engineering & System Safety*, 122:96–123.

Renard, B., Sun, X., and Lang, M. (2013). Bayesian methods for non-stationary extreme value analysis. In AghaKouchak, A., Easterling, D., Schubert, K. H. S., and Sorooshian, S., editors, *Extremes in a Changing Climate: Detection, Analysis and Uncertainty*, pages 39–96. Springer, Dordrecht.

Resnick, S. I. (1987). *Extreme Values, Regular Variation and Point Processes*. Springer-Verlag New York.

Rice, J. A. (2007). *Mathematical Statistics and Data Analysis*. Cengage, 3rd edition.

Rivas, D., Caleyo, F., Valor, A., and Hallen, J. (2008). Extreme value analysis applied to pitting corrosion experiments in low carbon steel: Comparison of block maxima and peak over threshold approaches. *Corrosion Science*, 50(9):3193–3204.

Rowe, R. K., Mukunoki, T., and Sangam, H. P. (2005). BTEX Diffusion and Sorption for a Geosynthetic Clay Liner at Two Temperatures. *Journal of Geotechnical and Geoenvironmental Engineering*, 131(10):1211–1221.

Rutqvist, J., Börgesson, L., Chijimatsu, M., Nguyen, T., Jing, L., Noorishad, J., and Tsang, C.-F. (2001). Coupled thermo-hydro-mechanical analysis of a heater test in fractured rock and bentonite at Kamaishi Mine — comparison of field results to predictions of four finite element codes. *International Journal of Rock Mechanics and Mining Sciences*, 38(1):129–142.

Salas, J., Sena, C., and Arcos, D. (2014). Hydrogeochemical evolution of the bentonite buffer in a KBS-3 repository for radioactive waste. Reactive transport modelling of the LOT A2 experiment. *Applied Clay Science*, 101:521–532.

Saltelli, A., Ratto, M., Andres, T., Campolongo, F., Cariboni, J., Gatelli, D., Saisana, M., and Tarantola, S. (2008). *Global Sensitivity Analysis: The Primer*. Wiley.

Saltelli, A., Tarantola, S., Campolongo, F., and Ratto, M. (2004). *Sensitivity Analysis in Practice: A Guide to Assessing Scientific Models*. Wiley.

Samper, J., Mon, A., and Montenegro, L. (2018). A revisited thermal, hydrodynamic, chemical and mechanical model of compacted bentonite for the entire duration of the FEBEX in situ test. *Applied Clay Science*, 160:58–70.

Scarf, P. (1992). Estimation for a four parameter generalized extreme value distribution. *Communications in Statistics—Theory and Methods*, 21(8):2185–2201.

Scarf, P. (1993). On the limiting joint distribution of the extreme order statistics. *Applied Stochastic Models and Data Analysis*, 9(3):267–278.

Scarf, P., Cottis, R., and Laycock, P. (1992). Extrapolation of extreme pit depths in space and time using the r deepest pit depths. *Journal of The Electrochemical Society*, 139(9):2621–2627.

Scarf, P. A. and Laycock, P. J. (1994). Applications of extreme value theory in corrosion engineering. *Journal of Research of the National Institute of Standards and Technology; (United States)*, 99(4):313–320.

Scarf, P. A. and Laycock, P. J. (1996). Estimation of extremes in corrosion engineering. *Journal of Applied Statistics*, 23(6):621–644.

Shibata, T. (1994). Application of extreme value statistics to corrosion. *Journal of Research of the National Institute of Standards and Technology; (United States)*, 99(4):327–336.

Shoesmith, D. W., Ikeda, B. M., Bailey, M. G., Quinn, M. J., and LeNeveu, D. M. (1995). A Model for Predicting the Lifetimes of Grade-2 Titanium Nuclear Waste Containers. Technical Report AECL-10973, COG-94-558, AECL.

Shoesmith, D. W., Ikeda, B. M., and LeNeveu, D. M. (1997). Modeling the Failure of Nuclear Waste Containers. *CORROSION*, 53:820–829.

SKB (2010a). Corrosion calculations report for the safety assessment SR-Site. Technical Report TR-10-66, SKB.

SKB (2010b). Data report for the safety assessment SR-Site. Technical Report TR-10-52, SKB.

SKB (2011). Long-term safety for the final repository for spent nuclear fuel at Forsmark - Main report of the SR-Site project - Volume I. Technical Report TR-11-01, SKB.

Smith, J. M. (2007). *The corrosion and electrochemistry of copper in aqueous, anoxic sulphide solutions.* PhD thesis, Library and Archives Canada = Bibliothèque et Archives Canada, Ottawa. OCLC: 665191350.

Smith, J. M., Wren, J. C., Odziemkowski, M., and Shoesmith, D. W. (2007). The Electrochemical Response of Preoxidized Copper in Aqueous Sulfide Solutions. *Journal of The Electrochemical Society*, 154(8):C431.

Smith, R. L. (1985). Maximum likelihood estimation in a class of nonregular cases. *Biometrika*, 72(1):67–90.

Smith, R. L. (1989). Extreme value analysis of environmental time series: An application to trend detection in ground-level ozone. *Statistical Science*, 4(4):367–377.

Smith, R. L. (1994). Multivariate threshold methods. In Galambos J., Lechner J., S. E., editor, *Extreme Value Theory and Applications*, pages 225–248. Springer, Boston, MA.

Smith, R. L. (2003). Statistics of extremes, with applications in environment, insurance and finance. In Finkenstadt, B. & Rootzen, H., editor, *Extreme Values in Finance, Telecommunications, and the Environment*, page 78. Chapman and Hall/CRC, 1st edition edition.

Smith, R. L. and Naylor, J. C. (1987). A comparison of maximum likelihood and bayesian estimators for the three- parameter weibull distribution. *Journal of the Royal Statistical Society. Series C (Applied Statistics)*, 36(3):358–369.

Snyder, D. L. and Miller, M. I. (1991). *Random Point Processes in Time and Space*. Springer-Verlag New York.

Solari, S., Egüen, M., Polo, M. J., and Losada, M. A. (2017). Peaks Over Threshold (POT): A methodology for automatic threshold estimation using goodness of fit p-value. *Water Resources Research*, 53(4):2833–2849.

Standish, T., Chen, J., Jacklin, R., Jakupi, P., Ramamurthy, S., Zagidulin, D., Keech, P., and Shoesmith, D. (2016). CORROSION OF COPPER-COATED STEEL HIGH LEVEL NUCLEAR WASTE CONTAINERS UNDER PERMANENT DISPOSAL CONDITIONS. *Electrochimica Acta*, 211.

Stephens, M. A. (1986). Tests based on edf statistics. In D'Agostino, R. B. and Stephens, M. A., editors, *Goodness-of-Fit-Techniques*. Marcel Dekker, New York.

Stephenson, A. (2016). Bayesian inference for extreme value modelling. In Dey, D. K. and Yan, J., editors, *Extreme Value Modelling and Risk Analysis*, pages 257–279. Chapman and Hall/CRC, New York.

Stroock, D. W. (2005). *An Introduction to Markov Processes*. Graduate Text in Mathematics 230. Springer, 1st edition.

Taylor, H. M. and Karlin, S. (1998). *An Introduction to Stochastic Modeling*. Academic Press, 3rd edition.

Timashev, S. A., Malyukova, M. G., Poluian, L. V., and Bushinskaya, A. V. (2008). Markov description of corrosion defects growth and its application to reliability based inspection and maintenance of pipelines. volume Volume 4 of *7th International Pipeline Conference*, pages 525–533.

Valor, A., Caleyo, F., Alfonso, L., Rivas, D., and Hallen, J. (2007). Stochastic modeling of pitting corrosion: A new model for initiation and growth of multiple corrosion pits. *Corrosion Science*, 49(2):559–579.

Valor, A., Caleyo, F., Alfonso, L., Velázquez, J., and Hallen, J. (2013). Markov chain models for the stochastic modeling of pitting corrosion. *Mathematical Problems in Engineering*, 2013.

Valor, A., Caleyo, F., Rivas, D., and Hallen, J. (2010). Stochastic approach to pitting-corrosion-extreme modelling in low-carbon steel. *Corrosion Science*, 52(3):910–915.

van der Vaart, A. W. (2000). *Asymptotic Statistics*. Cambridge, 1st edition.

van Noortwijk, J. (2009). A survey of the application of gamma processes in maintenance. *Reliability Engineering & System Safety*, 94(1):2–21. Maintenance Modeling and Application.

Wadsworth, J. L. (2016). Exploiting structure of maximum likelihood estimators for extreme value threshold selection. *Technometrics*, 58(1):116–126.

Wadsworth, J. L. and Tawn, J. A. (2012). Likelihood-based procedures for threshold diagnostics and uncertainty in extreme value modelling. *Journal of the Royal Statistical Society. Series B (Statistical Methodology)*, 74(3):543–567.

Wasserman, L. (2010). *All of Statistics: A Concise Course in Statistical Inference*. Springer, 1st edition.

Werme, L., Sellin, P., and Kjellbert, N. (1992). COPPER CANISTERS FOR NUCLEAR HIGH LEVEL WASTE DISPOSAL. CORROSION ASPECTS. Technical Report TR-92-6, SKB.

Xie, Y., Zhang, J., Aldemir, T., and Denning, R. (2018). Multi-state markov modeling of pitting corrosion in stainless steel exposed to chloride-containing environment. *Reliability Engineering & System Safety*, 172:239–248.

Yang, G. L. (1978). Estimation of a biometric function. *The Annals of Statistics*, 6(1):112–116.

Yoon, S., Cho, W., Heo, J.-H., and Kim, C. E. (2010). A full bayesian approach to generalized maximum likelihood estimation of generalized extreme value distribution. *Stochastic Environmental Research and Risk Assessment*, 24(5):761–770.

Zhang, S. and Zhou, W. (2013). System reliability of corroding pipelines considering stochastic process-based models for defect growth and internal pressure. *International Journal of Pressure Vessels and Piping*, 111-112:120–130.

Zhang, S. and Zhou, W. (2015). Probabilistic characterisation of metal-loss corrosion growth on underground pipelines based on geometric brownian motion process. *Structure and Infrastructure Engineering*, 11(2):238–252.

Zhang, S., Zhou, W., and Qin, H. (2013). Inverse gaussian process-based corrosion growth model for energy pipelines considering the sizing error in inspection data. *Corrosion Science*, 73:309–320.

Zhao, X., Zhang, Z., Cheng, W., and Zhang, P. (2019). A new parameter estimator for the generalized pareto distribution under the peaks over threshold framework. *Mathematics*, 7(5).

Zheng, L., Samper, J., and Montenegro, L. (2011). A coupled THC model of the FEBEX in situ test with bentonite swelling and chemical and thermal osmosis. *Journal of Contaminant Hydrology*, 126(1-2):45–60.

APPENDICES

Appendix A

Pit Growth with Markov Process—Detailed Literature Review

The purpose of this appendix is to provide a more detailed literature review of the application of Markov processes for modelling pit growth. The focus is primarily on the more prevalent approach proposed by Valor and colleagues for propagating a distribution of pit depths across a non-homogeneous CTMC.

A.1 Early Work on Pit Growth as Markov Process

Essential to the Markov process is the identification of the intrinsic rate(s) at which the state of the process transitions. The plural form is used here because, for non-homogeneous processes, transition rates are time dependent, and depending on the class of Markov models employed, transition rates may also be state-dependent. Transition rates are also referred to as intensities of the process, analogous to the intensities of the Point process discussed in Appendix D. For a discrete state space Markov process, one speaks of a Markov chain, and the overlapping links of the chain are viewed as discrete nodes or states of the process. Consequently, finding the appropriate formulation to express the transition rates or intensities of the process is a task faced by all modellers.

Provan and Rodriguez III (1989), who appear to be the first to apply a CTMC to pitting corrosion, presented an expression for the intensity of the process at an arbitrary

state j and time t

$$\lambda_j = j\lambda\frac{(1+\lambda t)}{(1+\lambda t^{\kappa})}, \qquad \lambda, \kappa > 0.$$

The parameters λ and κ were determined by an iterative process that minimised the difference between the mean and variance of the actual and predicted distribution of maximum pit depths, at specified times (i.e., exposure periods). To do so, Provan and Rodriguez III (1989) transformed actual maximum pit depths into probability histograms, with bin widths corresponding to 1/100 of the thickness of corrosion coupons—implying a discrete Markov chain with 100 states. While remarkably good agreement was observed qualitatively for the actual and predicted probability histograms, particularly for one of the two alloy systems assessed, the reasons for choosing the specific algebraic expression for the intensity function was never discussed, leaving questions as to the basis for choosing the formulation. Moreover, the minimisation scheme was not sufficiently clear, and neither was the methodology for generating pit depth distributions from the Markov model parameters. The latter is normally achieved by propagating through the Markov chain an initial distribution of pit depths. Lastly, while transition rates were defined as functions of state and time, the transition probabilities were not formulated explicitly, and these are required to fully specify the Markov model. Provan and Rodriguez III (1989) specified the differential equations—called the Kolmogorov differential equations—that govern the rate of change of the transition probabilities. The solution to the Kolmogorov differential equations yield the transition probabilities of the Markov chain, also known as the transition probability function. Unfortunately, Provan and Rodriguez III (1989) did not discuss how the Kolmogorov equations were solved, especially in the context of their intensity function.

Following the work by Provan and Rodriguez III (1989), Hong (1999a,b) modelled the evolution of maximum pit depths in piping with a homogeneous Markov process (discrete state). By modelling the Markov process as homogeneous, which means the intensity of the process is time invariant, transition probabilities were obtained without difficulty since solutions for the Kolmogorov differential equations are readily available.

Timashev et al. (2008) applied a homogeneous pure-birth Markov model to pit growth in piping by solving the closed-form solution to the Kolmogorov differential equations sequentially. In their case, λ was state-dependent but time-independent.

All of these authors were—to varying degrees—successful in modelling pit growth as a Markov process, but only Provan and Rodriguez III (1989) presented a time-dependent formulation for the intensity function.

A.2 Pit Growth Modelling by Valor & Colleagues

Of importance to this work are the two derivations for $\lambda(t)$ proposed by Valor and colleagues. These are discussed below in chronological order.

A.2.1 First Formulation for $\lambda(t)$

Valor et al. (2007) modelled pit growth as a non-homogeneous Markov process, represented by a pure-birth, linear-growth-rate model. A Weibull process was proposed to express the time-dependent intensity function $\lambda(t)$ used subsequently in the Markov process:

$$\lambda(t) = \chi\omega\,(t - t_k)^{\omega-1}\,, \tag{A.1}$$

with

$$\rho(t) = \int^t \lambda(\tau)d\tau = \chi\,(t - t_k)^{\omega} \quad \omega < 1. \tag{A.2}$$

Here, t_k is the time to initiate a pit for the kth pit, assuming pit initiation times are distinct.

To solve for parameters χ and ω, Valor et al. (2007) proposed a minimisation scheme whose objective function comprises the means and variance of two distribution functions: a Gumbel distribution directly fitted to pit depth maxima, and a limiting distribution function for pit depth maxima "calibrated" against a Gumbel distribution. The process is somewhat involved, requiring simultaneous adjustment of five parameters, two of which define the parameters of a separate Weibull distribution for initiation time t_k, one of which represents the number of pits initiated m, and the last two which are used in $\lambda(t)$. The limiting distribution of pit depth maxima, which is calibrated against the Gumbel distribution, originates from the transition probability function $p_{1,j}(t - t_k)$ derived by Parzen (2015) for the transition from state 1 to some discrete state j over the time interval $[t - t_k]$, for a stochastic process modelled as pure-birth, linear-growth-rate. Valor et al. (2007) did not use the complete transition probability function $p_{j,k}(s, t)$ for any states j, k and times s, t presented in Parzen (2015), but chose instead to define the underlying Cumulative Distribution Function (CDF) of a single pit by the sum of $p_{1,j}(t - t_k)$ for all values of j. More concretely, for a discrete RV S, representing the state of a Markov chain, the CDF may be expressed as

$$F_S(i, t - t_k) \coloneqq \sum_{j=1}^{i} p_{1,j}(t - t_k) = 1 - \left\{1 - e^{[-\rho(t-t_k)]}\right\}^i, \tag{A.3}$$

with $\rho(t-t_k)$ given by Equation A.2. In words, Equation A.3 represents the probability that the state of Markov process will be i or less. It is also simply a re-arrangement of Equation (5.25) in Parzen (2015, pg 304), which is represents the Geometric distribution.

From the theory of EVA (see Appendix B), the limiting distribution of state maxima, for large m, may be approximated by the GEV family of distributions. But Valor et al. (2007) argue, by solving for the normalisation constants and testing for the appropriate domain of attraction (e.g., see Castillo (1988, pg 100)), that $F_S(i, t-t_k)$ is in the Gumbel domain of attraction. Thus,

$$[F_S(i,t-t_k)]^m = \left(1-\left\{1-e^{[-\rho(t-t_k)]}\right\}^i\right)^m \approx Gmbl(x) = \exp\left\{\exp\left[-\alpha_e(x-\beta_e)\right]\right\}, \quad \text{(A.4)}$$

where x is pit depth, and α_e, β_e are the *estimated* parameters of the Gumbel distribution. To solve for α_e and β_e, $[F_S(i,t-t_k)]^m$ is computed for $i = 1, 2, \ldots, n$, where n is the final state of the chain, across all initiation times t_k, for a single (corrosion experiment) exposure time t, and subsequently extracted from a Gumbel probability paper plot, for example. In compact form, the set of points to plot (after transforming the state i to its corresponding pit depth x) on a Gumbel probability paper plot (Castillo, 1988, pg 134) is, after assuming t_k are iid,

$$\{[F_S(i,t-t_k)]^m : \forall i\} \coloneqq \left\{\prod_{k=1}^{m} F_S(1,t-t_k), \prod_{k=1}^{m} F_S(2,t-t_k), \ldots, \prod_{k=1}^{m} F_S(n,t-t_k)\right\} \quad \text{(A.5)}$$

Once α_e, β_e are estimated from the Gumbel probability paper plot for a particular set $\{[F_S(i,t-t_k)]^m : \forall i\}$, the corresponding Gumbel distribution mean and variance μ_e, σ_e^2 are estimated. At the same time, the Gumbel distribution is fitted directly to the experimental data to obtain the *observed* Gumbel distribution mean and variance μ_o, σ_o^2. This is repeated for all N exposure times. Finally, the objective function E_T, which is proposed by Valor et al. (2007) to approximate the total error, is calculated:

$$E_T \coloneqq \sum_{T=1}^{N}\left[\sqrt{(\mu_o^T-\mu_e^T)^2}+\sqrt{(\sigma_o^{2T}-\sigma_e^{2T})^2}\right]. \quad \text{(A.6)}$$

A Monte Carlo procedure was employed by the authors to generate sets of initiation times of size m. No information was provided with respect to the values explored for m. Minimisation of E_T leads to estimates of χ and ω, and subsequently $\lambda(t)$.

The approach by Valor et al. (2007) was subsequently revised by limiting the states of the Markov process—to be applied in the minimisation of E_T—to only the equivalent pit

depths greater than or equal to a specified percentile, obtained from the observed Gumbel distribution (Rivas et al., 2008; Valor et al., 2010, 2013). Specifically, the argument made was that an improvement between observed (direct Gumbel fit to data) and estimated (Markov process calibrated against Gumbel distribution) pit depth maxima distributions is possible only if pit depths above some threshold u are used in the underlying distribution $F_S(i, t - t_k)$. Threshold levels approximated using a mean residual life plot (e.g., see Figure C.1 for a similar application) were compared with the $\alpha = 0.005$ percentile values, designated u_α, estimated from the observed Gumbel distribution fitted at each exposure period. The resulting good agreement was subsequently used as a basis by Valor et al. (2010) to justify shifting the Markov states from i to $i + u_\alpha$ in Equation A.5. This meant, effectively, using pit depth exceedances. Further, Rivas et al. (2008) suggested $\{0.0005, 001, 005\}$ as possible values for α in u_α based on a comparison between the average number of observed exceedances at each u_α on a corrosion coupon and those estimated by solving for the expression of expected number of exceedances λ. The latter was derived by assuming the number of exceedances at any exposure period was $\sim$ Pois(λ), with time-independent parameter λ, and the magnitude of exceedances follow a time-invariant GPD, with Gumbel as the associated limiting distribution for maxima.[1] Valor et al. (2010) applied this improved approach to the minimisation scheme discussed earlier and obtained estimated Gumbel distribution parameters for $\{[F_S(i, t - t_k)]^m : \forall i\}$, with i replaced by $i + u_\alpha$, $u_\alpha = 0.0005$, and assuming all pits initiated at the same time (i.e., $t_k = 0$). The last adjustment simplified the computations significantly by reducing to three the adjustable parameters (i.e., χ, ω, m). In particular, the number of pits m was no longer associated with number of initiated pits, but rather with the number of exceedances. The same application was subsequently reproduced in Valor et al. (2013), where it was disclosed that $m = 7.6$, and where it was concluded that $m = 7.6 \approx 8$ compared well with the expected number of exceedances $\lambda = \{10, 5, 12, 9, 6, 9\}$ estimated at the six exposure periods examined. The estimation for λ was, as stated earlier, estimated for exceedances $\sim$ GPD and the number of exceedances $\sim$ Pois(λ).

Admittedly, it is quite easy to miss a few subtleties in the work by Rivas et al. (2008); Valor et al. (2007, 2010, 2013). Perhaps, of greatest consequence to the question of validity is that originally, the derivation proposed in Valor et al. (2007) and subsequently extended in Valor et al. (2010, 2013), the parameter m was presented as the number of pit depths observed in a corrosion coupon, which, when approaching a large number (e.g., $m \to \infty$), permits the approximation of $[F_S(i, t - t_k)]^m$ by the limiting Gumbel distribution for maxima. Perhaps an objection could be raised that $m = 7.6$ is hardly considered a

[1] The time-invariant GPD associated with the Gumbel for maxima is the Exponential distribution, Exp(λ).

large number. Asymptotic theory states that for large enough m, the probability that the maximum of the sequence $X_1, X_2, \cdots, X_m$, where $X_i \sim F$, is less than x, converges to the limiting distribution as m approaches a large number. In other words, it is a long sequence of RVs, representing pit depths, whose probability $P(max\{X_1, X_2, \cdots, X_m\} < x)$ converges. This is the justification given in Appendix B, where it is assumed for the surrogate data that a sufficiently large number of pits were initiated within a coupon for the asymptotic condition to hold. Moreover, the asymptotic requirement for the sequence to be long still applies even when the sequence of RVs is conditioned on $X_i > u$, where u is some large enough threshold. This is effectively demonstrated in the derivation for the intensity measure, Section D.2, where the summation is taken to ∞. Additionally, that good agreement was reported between $\lambda = \{10, 5, 12, 9, 6, 9\}$ and $m \approx 8$ in Valor et al. (2013) speaks potentially to a misunderstanding of the meaning of the parameter m. The expected number of exceedances λ is an average, whereas m is the size of the sequence of exceedances. While this author does not deny the obviously good results presented in Valor et al. (2013, Figure 5), where the Gumbel fit to experimental pit depth maxima are compared with a distribution derived by the minimisation scheme at each exposure period, it could be argued that the good agreement may have more to do with forcing a good fit between one Gumbel distribution (observed) and another Gumbel distribution (estimated) by adjusting χ, ω, m and u_α, and less to do with the validity of the proposed Markov model. Lastly, while Valor et al. (2007, 2010, 2013) do model pit growth as a pure-birth, linear-growth-rate non-homogeneous Markov process, a Markov chain is not explicitly employed in a classical sense in producing the estimated distributions of pit depth maxima. Valor et al. (2013) do use the word "chain" but in the context of converting pit depths to interger-valued damage states in $\{[F_S(i, t - t_k)]^m : \forall i\}$. To be clear, this formulation of $\lambda(t)$ was not used to propagate an initial distribution of pit depths across a CTMC. The second formulation for $\lambda(t)$ proposed by Valor et al. (2010) does. This is discussed next.

A.2.2 Second Formulation for $\lambda(t)$

The second formulation for $\lambda(t)$ proposed by Caleyo et al. (2009); Valor et al. (2013) is

$$\lambda(t) \coloneqq \frac{\nu_t}{t - t_{sd}}. \tag{A.7}$$

The parameter ν_t in Equation A.7 represents the exponent in a power-law fit to pit depth maxima, t is a future time, and t_{sd} the time to initiate a pit. The origins of Equation A.7 can be traced to a statement made by Cox and Miller (1987, pg 157), who equate the size a population, modelled as a *deterministic* function, to the expected size of a population

modelled as particular *stochastic* process—a pure-birth, linear-growth rate model, with time-independent rate. Caleyo et al. (2009); Valor et al. (2013) borrow this equivalence and apply the term "deterministic" to an empirical expression for the average maximum pit depth. In what follows, the equivalence statement from Cox and Miller (1987) is explored to fully appreciate the implications in the use of the formulation for $\lambda(t)$ proposed by Caleyo et al. (2009); Valor et al. (2010).

Cox and Miller (1987) present a simple analysis, which they term "deterministic," to gain intuition for the expectation of the size of a population, which is eventually modelled as a pure-birth, linear-growth-rate (time-independent rate) stochastic process (i.e., $\{N(t), t \geq 0\}$, where $N(t)$ represents the size or state of the population at time t). The "deterministic" analysis assumes that the size of the population $n(t)$ is not random but large enough to be treated as a continuous function of t (thereby allowing for the limit to exist, as will be discussed shortly). Additionally, the "deterministic" analysis defines an intensity function $\lambda n(t)$, representing the rate at which the population increases, to be the product of the actual or intrinsic transition rate λ and the population size $n(t)$. This definition implies a pure-birth, linear-growth-rate process. Subsequently, for a small time interval Δt, the population size increases by $\lambda n(t)\Delta t$. Then,

$$\begin{aligned} n(t+\Delta t) - n(t) &= \lambda n(t)\Delta t \\ \lim_{\Delta t \to 0} \frac{n(t+\Delta t) - n(t)}{\Delta t} &= \lambda n(t) \\ \frac{dn(t)}{dt} &= \lambda n(t), \end{aligned}$$

whose solution is simply

$$n(t) = n_0 e^{\lambda t},$$

and where n_0 is the initial condition for the size of the population.

Cox and Miller (1987) then proceed to show, by solving the set of Kolmogorov's differential equations for a pure-birth, linear-growth-rate (time-independent rate) stochastic process, that the expectation for $N(t)$, $E[N(t)]$, is

$$E[N(t)] = n_0 e^{\lambda t},$$

assuming initial conditions $t_0 = 0$ and $N(0) = n_0$. Consequently, (Cox and Miller, 1987, pg 159) assert that the "deterministic" analysis (theory) produces exactly the "stochastic" mean. But these authors qualify their statement, which is quoted verbatim:

> In later examples, this agreement will not always occur. A sufficient condition for equality is that for an arbitrary positive integer r, the structure of the process starting from rn_0 individuals is identical with that of the sum of r separate systems each starting individually from initial state n_0. Note, that even when deterministic theory and stochastic mean do agree, they do not necessarily give a good idea of the behaviour of individual realizations. (pg 159, Cox and Miller, 1987)

Based on the assertion of equivalence between deterministic theory and stochastic mean, Caleyo et al. (2009); Valor et al. (2013) proceed to assert that the "deterministic" function for the average maximum pit depth $\bar{D}(t)$, derived empirically by fitting a power-law function to pit depth maxima, is equal to the stochastic mean of a population $E[N(t)]$, modelled by a pure-birth, linear-growth-rate stochastic process, with a time-dependent rate. Mathematically,

$$\bar{D}(t) \coloneqq \kappa_t (t - t_{sd})^{\nu_t} \equiv E[N(t)] = N_0(t_0) e^{\rho(t) - \rho(t_0)}. \tag{A.8}$$

Taking as initial conditions $t_0 = 0$ and $D(0) = 1$, where $D(0)$ is the initial damage state of the pitting process (analogues to the initial size of the population N_0), and under a further assumption that the change in the average maximum pit depth $\Delta\bar{D}$ during a small interval of time Δt is adequately described by $\bar{\lambda}(t)\bar{D}\Delta t$, Caleyo et al. (2009); Valor et al. (2013) further propose that

$$E[D(t)] = D_0(t_0) e^{\rho(t) - \rho(t_0)} \equiv \bar{D}(t) \coloneqq \kappa_t (t - t_{sd})^{\nu_t}, \tag{A.9}$$

Upon substitution for initial conditions, followed by re-arranging for $\rho(t)$, leads to

$$\rho(t) = \ln\left[\kappa_t (t - t_{sd})^{\nu_t}\right], \tag{A.10a}$$

$$\lambda(t) \coloneqq \frac{d}{dt}\rho(t) = \frac{\nu_t}{t - t_{sd}}. \tag{A.10b}$$

If pit initiation times t_{sd} are assumed to be negligibly small relative to inspection intervals for field data or exposure periods for experimental data, Eqn A.10b reduces further to simply the quotient ν_t/t. Surprisingly, this approach leads to very good predictions of Monte-Carlo simulated maximum pit depth distributions (e.g., Figure 5 in Caleyo et al. (2009)) and generally reasonable predictions of experimental corrosion coupon data (e.g., Figure 9 in Caleyo et al. (2009)). This formulation for $\lambda(t)$ appears to also have become the de facto approach for modelling evolution of pits with a Markov chain, as evidence by its

adoption for modelling—to varying degrees of success—maximum pit depths (McCallum et al. (2014); Ossai et al. (2016); Xie et al. (2018)) and evolution of wear depths in steam generator tubes (He et al., 2019).

While arguably the appeal of the second formulation for $\lambda(t)$ is its simplicity, there are a few observations worthy of note. First, Cox and Miller (1987) use a time-independent rate analogy to arrive at their equivalence statement. Caleyo et al. (2009); Valor et al. (2013) apply it directly to a time-dependent stochastic process, without clarification or justification. However, as will be shown shortly, the stochastic mean of a population modelled with a time-dependent rate is in fact equal to $E[N(t)]$, right side of identically equal sign in Equation A.8. For example, for a pure-birth, linear-growth-rate (time-dependent rate) stochastic process, the characteristic function $\varphi_{N(t)-N(s)}(u)$ for the change in population size $N(t) - N(s)$ over a time interval $[s, t]$, where $t > s \geq 0$, conditioned on the fact that the size of the population at time s is m, is

$$\varphi_{N(t)-N(s)}(u) = E\left[e^{iu\{N(t)-N(s)\}}|N(s) = m\right] = \left\{\frac{e^{-[\rho(t)-\rho(s)]}}{1-(1-e^{-[\rho(t)-\rho(s)]})e^{iu}}\right\}^m. \tag{A.11}$$

The first derivative of the characteristic function yields the first moment or expectation of a RV. Thus,

$$\begin{aligned} i^{-1}\left[\frac{d}{du}\varphi_{N(t)-N(s)}(u)\right]_{u=0} &= E\left[N(t) - N(s)|N(s) = m\right] \\ &= me^{[\rho(t)-\rho(s)]}\left(1 - e^{-[\rho(t)-\rho(s)]}\right) \\ &= m\left(e^{[\rho(t)-\rho(s)]} - 1\right), \end{aligned} \tag{A.12}$$

which, for initial conditions $s = 0$ and $N(0) = 1$, simplifies to

$$E[N(t)] = E[N(t) - N(0)] + 1 = e^{[\rho(t)-\rho(0)]} = e^{\rho(t)} \tag{A.13}$$

Second, a plot of $\rho(t)$, Equation A.10a, for $\kappa_t = 0.164$, $\nu_t = 0.780$, and $t_{sd} = 2.9$, which represent power-law fitting parameters and initiation times, respectively, for the "All soils" class applicable to pitting in underground piping modelled by Caleyo et al. (2009), is presented in Figure A.1. This plot, which is reproduced by directly applying Equation A.10a with $D(t_0) = 1$—the condition applied to derive this equation, is compared with Figure A.2. The last figure is a reproduction of Figure 2a in Caleyo et al. (2009) and Figure 1b in Valor et al. (2013) for the "All Soils" condition and same parameters. It is important to note that Caleyo et al. (2009); Valor et al. (2013) explicitly reference the formulation $\rho(t) = \ln\left[\kappa_t(t - t_{sd})^{\nu_t}\right]$ as the means by which to generate the plot in Figure A.2. A comparison of Figure A.2 with Figure A.1 would suggest that this was not the case.

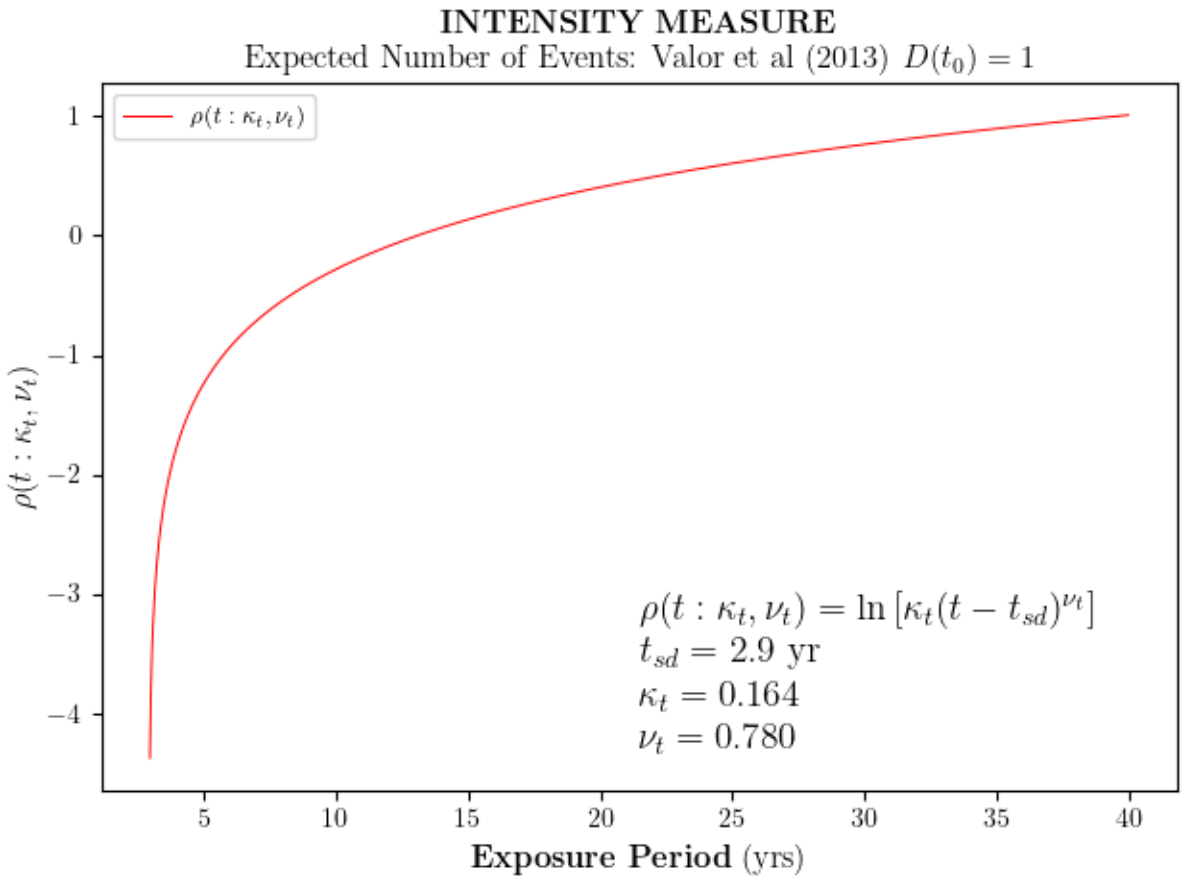

Figure A.1: Expected number of extreme pit depths (events) by time t predicted by the approach proposed by Caleyo et al. (2009); Valor et al. (2013), with parameters $\kappa_t = 0.164$ and $\nu_t = 0.780$ taken from Tables 1 and 2, Valor et al. (2013).

To arrive at a plausible formulation employed by Caleyo et al. (2009); Valor et al. (2013) to generate Figure A.2, one should observe that in Figure A.2 $\rho(5) = 1$, suggesting $t_0 \neq 0$. In fact, $t_0 = 5$ represents one time period used by the authors to facilitate comparison with predictions generated for a later time. Thus, it would appear that $t_0 = 5$ was used to generate Figure A.2, implying that one must revisit Equation A.9 to arrive at a complete

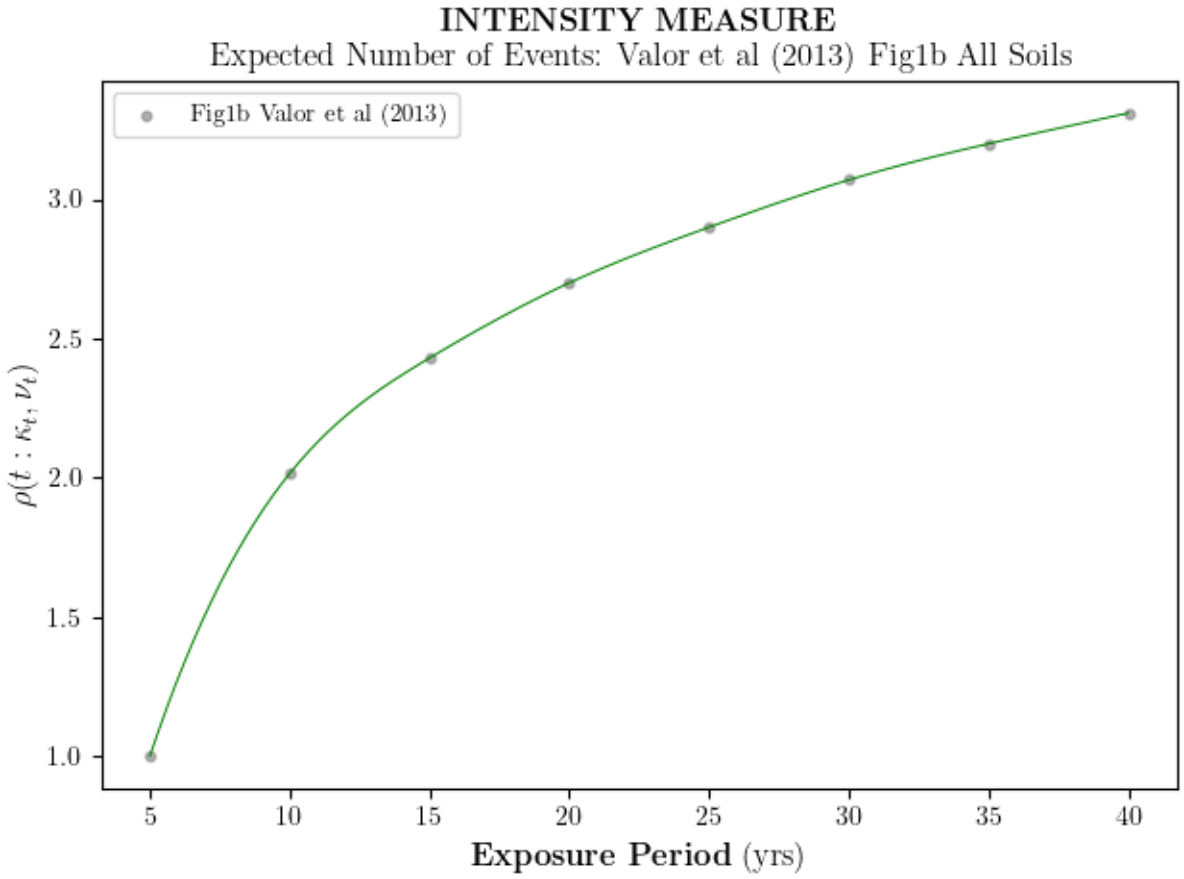

Figure A.2: Expected number of extreme pit depths (events) by time t predicted by the approach proposed by Caleyo et al. (2009); Valor et al. (2013), with the parameters $\kappa_t = 0.164$ and $\nu_t = 0.780$ taken from Tables 1 and 2, Valor et al. (2013).

expression for $\rho(t)$. For instance,

$$\begin{aligned} D_0(t_0)e^{\rho(t)-\rho(t_0)} &= \kappa_t(t-t_{sd})^{\nu_t} \\ \ln D_0(t_0) + \rho(t) - \rho(t_0) &= \ln\left[\kappa_t(t-t_{sd})^{\nu_t}\right] \\ \rho(t) &= \ln\left[\kappa_t(t-t_{sd})^{\nu_t}\right] - \ln D_0(t_0) + \rho(t_0). \end{aligned} \tag{A.14}$$

If it is true that $\rho(t) = \ln\left[\kappa_t(t-t_{sd})^{\nu_t}\right]$, then it stands to reason that $\rho(t_0) = \ln\left[\kappa_t(t_0-t_{sd})^{\nu_t}\right]$, provided $D_{t_{sd}}(t_{sd}) = 1$, else $\rho(t_0) = \ln\left[\kappa_t(t_0-t_{sd})^{\nu_t}\right] - \ln D_{t_{sd}}(t_{sd})$. Consequently,

$$\rho(t) = \ln\left[\kappa_t(t-t_{sd})^{\nu_t}\right] + \ln\left[\kappa_t(t_0-t_{sd})^{\nu_t}\right] - \ln D_0(t_0) - \ln D_{t_{sd}}(t_{sd}), \tag{A.15}$$

which presents two unknowns $D_0(t_0)$ and $D_{t_{sd}}(t_{sd})$.

A possible process of elimination to deduce the values of these unknowns, assuming $t_0 = 5$, is to plot the first two terms to the right of the equality sign in Equation A.15. The resulting plot, shown in Figure A.3, is very similar in shape and almost identical in height to that displayed in Figure A.2. Additionally, if one assumes $D_0(t_0) = 1$; that is, if one lets the damage state at $t_0 = 5$ be equal to 1, Equation A.15 is further reduced to three terms. Since the two-term plot appears to be identical to the actual plot, but only that it is translated down on the ordinate, the magnitude of $D_{t_{sd}}(t_{sd})$ may be deduced by shifting the two-term plot along the ordinate until $\rho(5) = 1$. The quantity of this shift approximates $-\ln D_{t_{sd}}(t_{sd})$. Figure A.4 shows the shifted plot along with the results from Figure A.2. Almost perfect agreement is observed, suggesting that Equation A.15 is the likely formulation applied by Caleyo et al. (2009); Valor et al. (2013). From the foregoing, there are three points worthy of consideration.

One is that in general $D(t)$, $D_0(t_0)$, or $D_{t_{sd}}(t_{sd})$ represent integer-valued damage states, analogous to the size of a population. The result $D_{t_{sd}}(t_{sd}) = 0.03148$, while mathematically convenient and consistent (i.e., $D_{t_{sd}}(t_{sd}) < D_0(t_0)$), cannot represent an integer-valued damage state. It is inconsistent to define it as an integer-valued state of a Markov chain, as is the case in Caleyo et al. (2009); Valor et al. (2013), while at the same time use it as a positive, real-valued function. Two, there is nothing in Caleyo et al. (2009); Valor et al. (2013) to explain why $\rho(5) = 1$. Strictly speaking, $\rho(t)$ is an average mean rate of occurrence, or equivalently the expected number of stochastic events—the expected number of transitions in a Markov chain from $t = 0$ to t (see Section 5.3.1). There is no obvious reason to fix the expected number of events or transitions to a set number for any time t. Three, taken together the formulation proposed in Equation A.10a is not a workable solution for $t_0 = 0$ since the function is negative (Figure A.1): this is a violation of the fundamental definition of $\rho(t)$ for a stochastic process (Section 5.3.1).

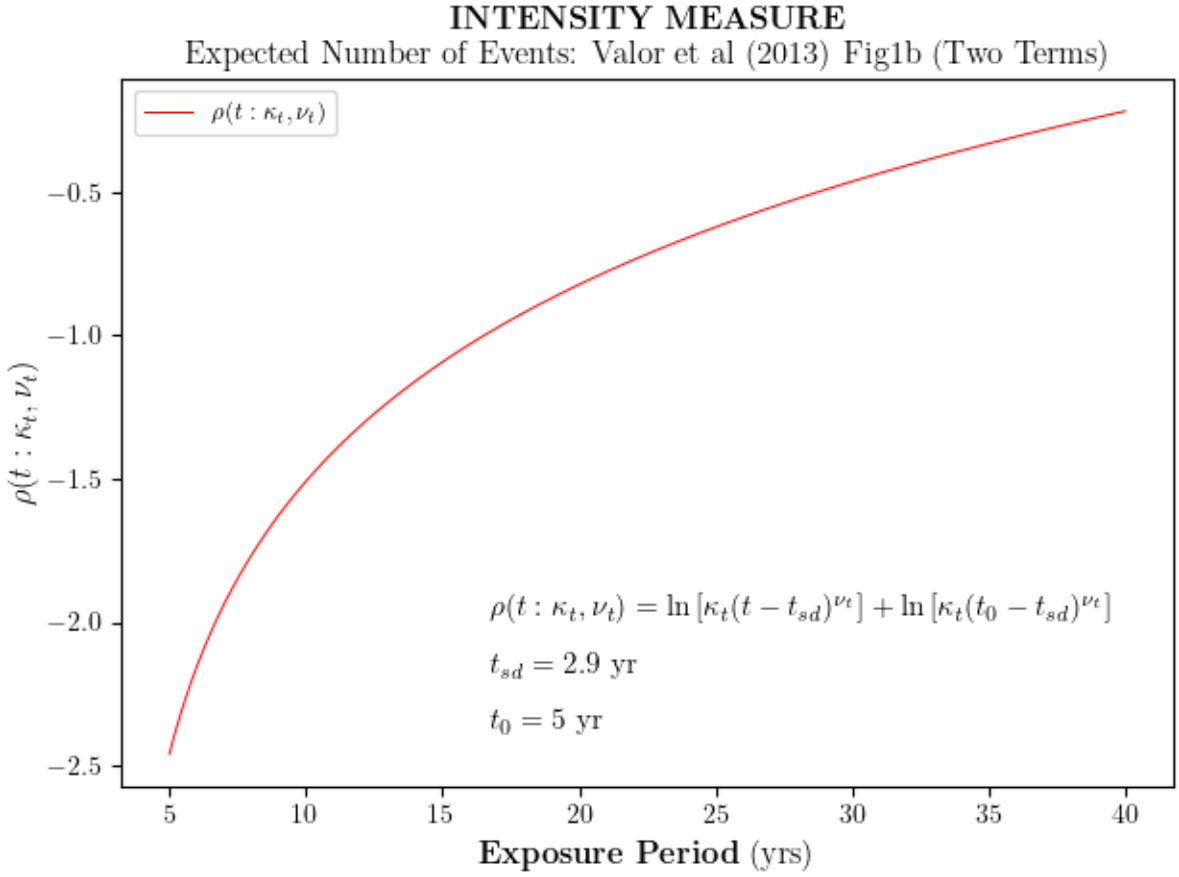

Figure A.3: Expected number of extreme pit depths (events) by time t, with the parameters $\kappa_t = 0.164$ and $\nu_t = 0.780$ taken from Tables 1 and 2, Valor et al. (2013), using the first two terms to the right of the equal sign in Equation A.15.

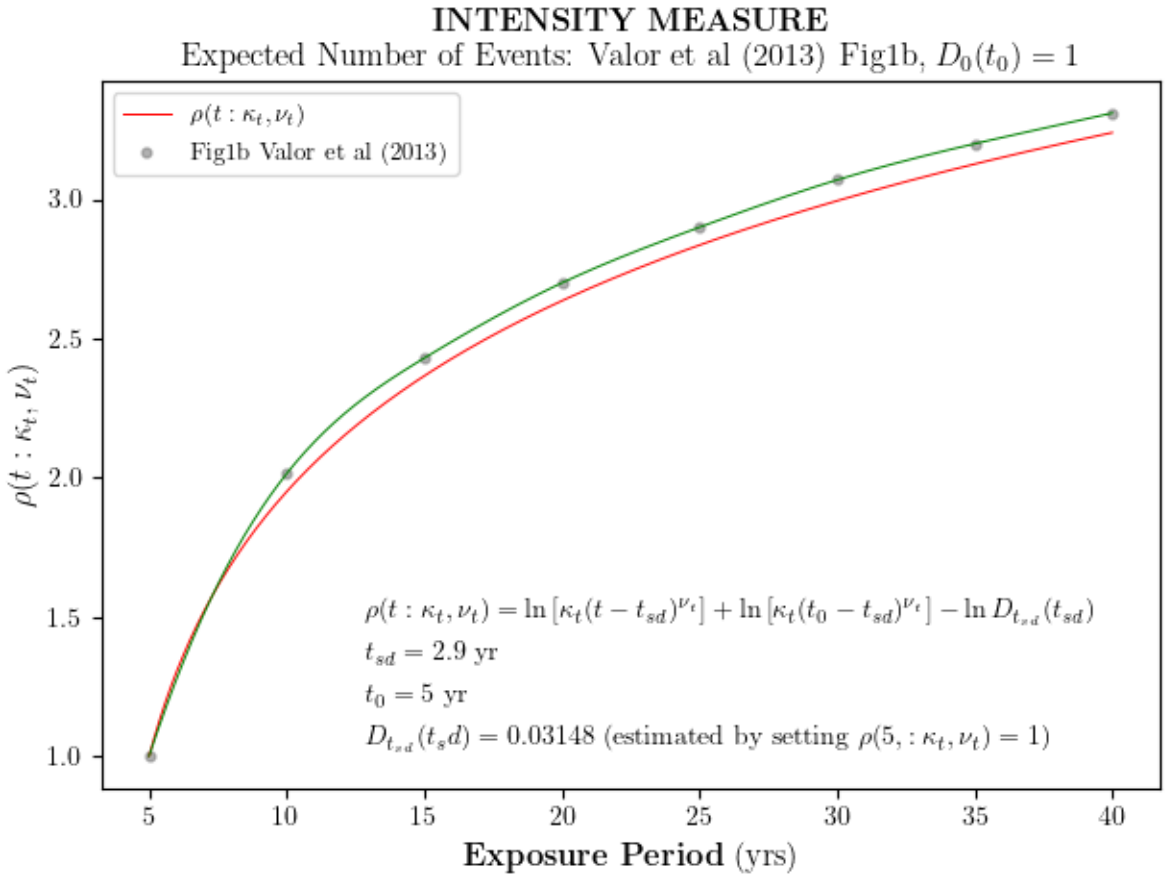

Figure A.4: Expected number of extreme pit depths (events) by time t, showing actual data points from Fig1b Valor et al. (2013) and a deduced plot with parameters taken from Tables 1 and 2, Valor et al. (2013).

Appendix B

Extreme Value Analysis

The objective of this appendix is to provide the mathematical details leading to the use of parameters $\mu, \alpha, \kappa,$ and b in the intensity measure formulation, Equation 5.17, in Chapter 5, Section 5.3.3. Owing to the fact that the first three of these parameters have their origin in the limiting distribution of maxima, also referred to as the GEV family of distributions, this chapter includes sufficient EVA background framed in the context of pit depth maxima. This framework is also helpful in understanding the GPD, which represents the limiting distribution of exceedances. Moreover, because both the work on the GPD in Appendix C and the stochastic process model developed in Chapter 5 heavily rest on the confidence of fitted GEV parameters, significant effort is placed on the goodness-of-fit assessments and validity of model assumptions. Questions such as why use the Maximum Likelihood Estimator (MLE) as a parameter point estimator, what about the effect of small sample size (e.g, surrogate data) on the bias of MLE, etc. are also addressed—almost exhaustively—in this appendix. Consequently, this appendix is necessarily detailed.

B.1 Generalised Extreme Value

For completeness, let $X_1, X_2, \ldots, X_n$ be a sequence of iid RVs, with common but unknown distribution function F. Define M_n as

$$M_n \coloneqq max(X_1, X_2, \ldots, X_n), \tag{B.1}$$

and

$$P(M_n \leq x) = P(X_1 \leq x, X_2 \leq x, \ldots, X_n \leq x) = [F(x)]^n = F^n(x), x \in \mathbb{R}. \tag{B.2}$$

In the present case, the RV X and the sequence of RVs $X_1, X_2, \ldots, X_n$ represent the depth of a corrosion pit and $x_1, x_2, \ldots, x_n$ a sequence of corrosion pit depths observed on a corrosion coupon. Following the theory of extreme value (see Coles, 2001, pg 47; Castillo et al., 2005, pg 54; Resnick, 1987, Ch 0; and Leadbetter et al., 1983, Ch 1), with appropriate sequence of normalising constants $\{a_n > 0\}$ and $\{b_n \in \mathbb{R}\}$, referred to typically as scale and location respectively, the sequence $M_n^* \coloneqq \{(M_n - b_n)/a_n\}$ converges in distribution as $n \to \infty$, such that

$$P\left(M_n^* \leq z\right) = P\left(\left(M_n - b_n\right)/a_n \leq z\right) = F^n(a_n z + b_n) \xrightarrow{d} H(z) \text{ as } n \to \infty. \tag{B.3}$$

The cumulative distribution function $H(z)$ is referred to as an "extremal distribution function," Pickands (1975), and $F(x)$ is said to be in the "maximal domain of attraction" of $H(z)$ if Equation (B.3) is satisfied for at least one pair of normalising constants $\{a_n > 0\}$ and $\{b_n \in \mathbb{R}\}$, Castillo, 1988, pg 195. Without the normalising constants, $F^n(x)$ degenerates as $n \to \infty$. Visually, this means that the PDF of M_n shifts to the right and its variance decreases as n increases, and the CDF of M_n (i.e., $F^n(x)$) also moves to the right, acquiring a large positive slope as n increases. Together, this indicates that the distribution of M_n degenerates to a point mass (i.e., a one-point distribution) on its upper endpoint. More precisely, for any $x < x_+$, where $x_+ \coloneqq \sup\{x : F(x) < 1\}$ is the upper endpoint of F (or in words, x_+ is the smallest value of x where $F(x) = 1$), $F^n(x) \to 0$ as $n \to \infty$. Therefore, in the limit, $F^n(x)$ takes only values 0 or 1, satisfying the definition of a degenerate distribution:

$$\lim_{n\to\infty} F^n(x) = \begin{cases} 1, & \text{if } F(x) = 1, \\ 0, & \text{if } F(x) < 1. \end{cases} \tag{B.4}$$

Consequently, provided the normalising constants exist, $H(z)$ is non-degenerate and converges or belongs to one of three types of limiting distributions (i.e., Gumbel type, Fréchet type, and the Weibull type). As discussed by Jenkinson (1955), the three types of limiting distributions may be combined into a single family of distributions—the GEV distribution family, having the form shown in Equation (B.5). To be clear, $H(z)$ is the GEV CDF shown in Equation (B.5). In practice, the need to determine the normalising constants is avoided by recognising that for large n, $P(M_n^* \leq z) \approx H(z)$ and $P(M_n \leq z) \approx H((z - b_n)/a_n)$ that, as $n \to \infty$, is equal to $H^*(z)$, representing another member of the GEV distribution family. Since both distributions $H(z)$ and $H^*(z)$ require a different set of fitted parameters, it's immaterial which distribution is chosen (see Coles, 2001, pg 49). Consequently, provided n is large, one works directly with M_n, and z can be replaced by x without loss of generality.

The formulation for the GEV CDF employed in this thesis is taken from Castillo et al., 2005, pg 64:

$$GEV(M_n \leq x) = GEV(x \,|\, \mu, \alpha, \kappa) = \exp\left\{ -\left[1 - \kappa\left(\frac{x-\mu}{\alpha}\right)\right]^{\frac{1}{\kappa}} \right\}; 1 - \kappa\left(\frac{x-\mu}{\alpha}\right) \geq 0, \tag{B.5}$$

where $\mu \in \mathbb{R}$, $\alpha > 0$, and $\kappa \neq 0$ are the location, scale, and shape parameters, respectively, and x represents maximum pit depth observed over a given area of interest. Equation B.5 is identical to the more popular expression given in Coles, 2001, pg 47, except for κ, which is the negative of the one used in Coles (2001). However, the form used in Equation B.5 is more common in the environmental literature, which has proved to be a good source of many helpful references in handling Peaks-Over-Threshold in this work. One additional note, from this point onward the RV X represents the maximum pit depth for a given corrosion coupon and x the observed maximum pit depth. The use of X in lieu of M_n (or Z, for example) is to limit the number of variables used throughout though at times M_n will be used simply to emphasise its definition (Equation B.1).

To employ Equation B.5, pit depth maxima are obtained by arranging "observed" maximum pit depth data (i.e., $x_1, x_2, \ldots, x_m$) into m "blocks." In the present context, "blocks" represent corrosion coupons, and the maximum pit depths for each coupon represent the block maxima (i.e., $x_1, x_2, \ldots, x_m$). The GEV distribution is then fit to the block maxima. Since $GEV(x)$ is an asymptotic model, the number of observed pits n per coupon should be sufficiently large to satisfy asymptotic assumptions. As discussed below, the number of pits per coupon for which depth measurements were recorded was on average greater than ten. However, the corrosion coupon data is left-truncated, which means the originators of the data chose to ignore pits smaller than an arbitrary depth, suggesting that n per coupon was likely much greater than ten, but unknown. For this work, it is assumed that a sufficient number of pits were generated per coupon, though not measured, to satisfy asymptotic assumptions. Additionally, since n is unknown, but assumed to be large, the approximation $P(M_n^* \leq z) \approx H(z)$ is implied in this thesis wherever the equal sign occurs.

The corresponding PDF for the GEV CDF is obtained by taking the derivative of Equation B.5 with respect to x, holding all previous parameter constraints:

$$g(x \,|\, \mu, \alpha, \kappa) = \frac{1}{\alpha}\left[1 - \kappa\left(\frac{x-\mu}{\alpha}\right)\right]^{\frac{1}{\kappa}-1} \exp\left\{ -\left[1 - \kappa\left(\frac{x-\mu}{\alpha}\right)\right]^{\frac{1}{\kappa}} \right\}; 1 - \kappa\left(\frac{x-\mu}{\alpha}\right) \geq 0. \tag{B.6}$$

For most of the analysis covered in this work, the GEV CDF and PDF will suffice to adequately provide the necessary probability laws. In most extreme value analysis problems, however, the interest more often than not lies with predicting the magnitude of a rare event, or the quantile x_p of the GEV distribution, where p is called the non-exceedance probability (adopting the terminology from Castillo et al. (2005), whereas Coles (2001) refers to p as the exceedance probability). For a non-exceedance probability p, the quantile x_p is derived by inverting Equation B.5:

$$x_p = \mu + \frac{\alpha}{\kappa}\left[1 - (-\ln p)^{\kappa}\right]; \kappa \neq 0. \tag{B.7}$$

The quantile x_p will feature prominently in the explanatory discussions under Section B.4 and is included herein for that purpose only.

B.2 Surrogate Data

Ideally, data from the Denison and Romanoff (1950) study would be a good starting point, but a few issues explained below render it unsuitable for the task at hand. The Denison and Romanoff data is approximately 74-88 years old (as at the time of the writing of this thesis). It represents long-term (14 years) underground (shallow trench) tests for copper and various copper alloy pipe specimens buried in a range of soil conditions across many sites in the United States of America. Five exposure periods were sampled over the 14 years, with two pipe specimens, each approximately 305 mm long and 43 mm in outer diameter, sampled per exposure period. The results, which comprised measured maximum and average pit depths, were ultimately fit to a power-law relationship in time. While important from many points of view, including a test duration well exceeding most small-specimen laboratory tests, the number of specimens sampled per exposure period was very limited (e.g., sometimes just two specimens were sampled) and the observed variability large, resulting in a sparse dataset that offered limited scope for additional analysis (i.e., it would be difficult to be confident of extrapolation in time, to say the least). Additionally, soil conditions surveyed were not necessarily representative of postulated DGR environments (only two soil conditions were considered in the Briggs et al., 2021 model, further limiting the utility of the data). While soil condition is not necessarily a deterrent for employing the Denison and Romanoff data in this work, it does represent a source of additional variability (i.e., lack of experimental control) that is undesirable. More importantly, the available data effectively restricts any study to potentially a block maxima analysis—but such an endeavour would be highly dubious since the number of blocks (i.e.,

the number of corrosion coupons) is, statistically speaking, too small. Consequently, no further consideration was given to the Denison and Romanoff data for this analysis.

It is important for the reader to note that King and LeNeveu (1991) applied EVA to the Denison and Romanoff data in their modelling of pitting corrosion in 25-mm thick copper shell containers. Specifically, King and LeNeveu (1991) fitted a simple two-parameter Gumbel distribution using least squares to some of the Denison and Romanoff maximum pit depth data, on a per period basis. Pit data for some of the copper alloy types and soil conditions, spanning the six test periods including the 14-year period, was combined to form a single data set. One of the two fitted parameters was argued to exhibit some time dependence and was subsequently represented by a simple linear equation in logarithmic time scale. This formulation allowed for the extrapolation in time and space (i.e., size effect) of the Gumbel distribution for maximum pit depths to repository timescales. The work by King and LeNeveu (1991) is simply mentioned here for completeness and to credit their efforts. However, the lack of data remains a problem and, in particular, the poor fit employed to represent the time dependence of one of the Gumbel distribution parameters makes it is difficult for this author to justify their approach here.

The data used in this work originates from Li et al. (2019). This author reached out to the primary author for the full dataset since the paper focused on maximum pit depths only. The full dataset was subsequently received with permission (private communication).

Figure B.1 shows the evolution of pit depths with time. The data, which is left-truncated arbitrarily by Li et al. (2019), represents pooled results from 100 304 stainless steel corrosion coupons, arranged into sets of ten samples (samples and coupons are used interchangeably throughout). Each sample having an exposed surface area 10 mm $\times$ 50 mm. The sets of samples were immersed in 3.5 wt% NaCl solution at 30°C for 7, 14, 21, 28, 30, 60, 90, 120, 150, and 180 days, respectively. At each exposure period, one set was removed and pits measured. With the exception of two exposure periods, the number of pooled pit depths recorded per exposure period was greater than 100. Of the two exposure periods with less than 100 pooled recorded pit depths, 82 and 92 pooled pit depths, respectively, were recorded. Formally, for the block maxima GEV modelling, a block is represented by the size of each coupon, and there are ten blocks for each exposure period. The block maxima (i.e., the maximum pit depths for each coupon per exposure period) are highlighted in blue in Figure B.1.

It is important to note that the data consists of two distinct experiments. The first experiment, which included exposure periods 7-28 days, was used by Li et al. (2019) to generate a simple power-law model that was subsequently applied to predict the results for exposure periods 30-180 days. One will note that there is a slight difference in the

pit depth trends between the two experiments, which is most pronounced at the 28- and 30-day exposure periods. While the experiments were, in principle, identical in terms of conditions, clearly there was variability between the two. A small effect was noticed when fitting the block maxima data. (A greater effect was noticed for the threshold function discussed later in this document.)

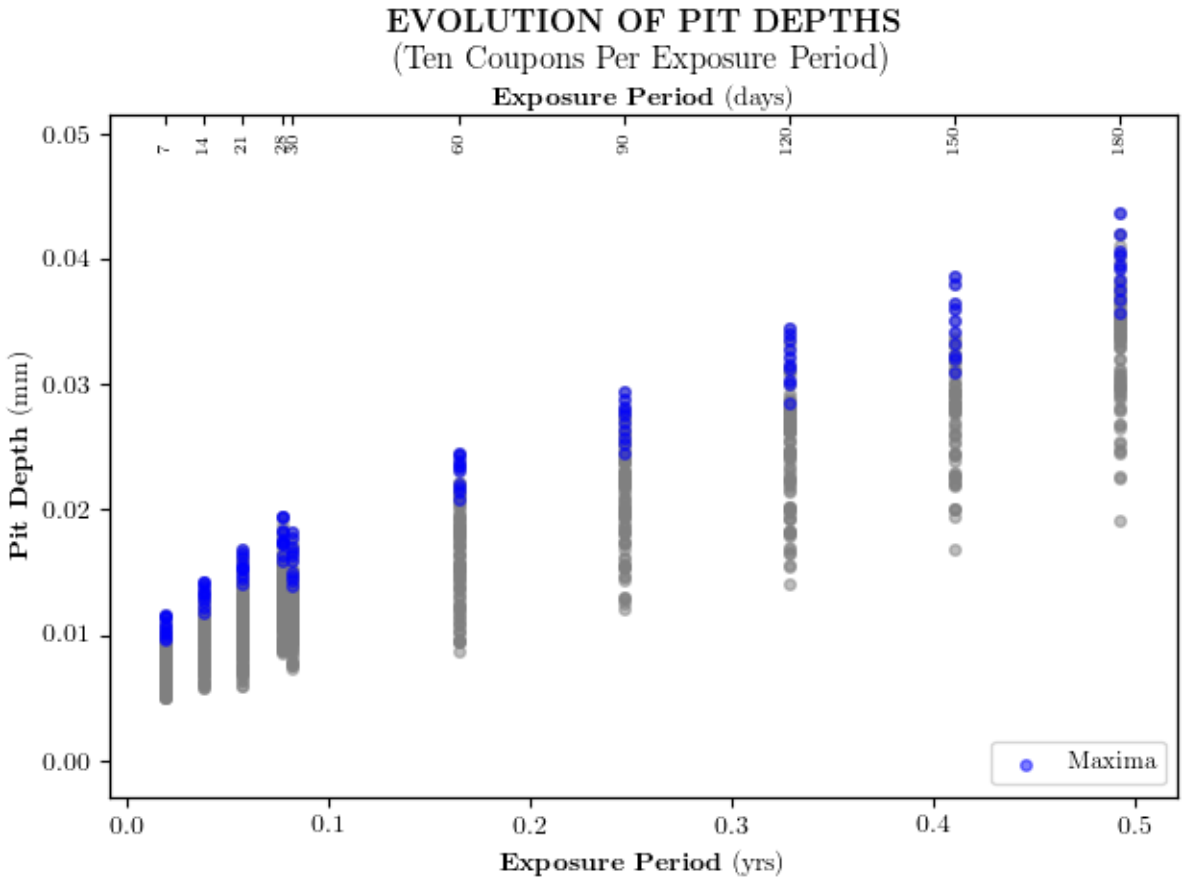

Figure B.1: Pit depths versus time for 304 stainless steel coupons immersed in 3.5 wt% NaCl solution at 30°C (Li et al., 2019, by permission). The maxima per exposure period are highlighted in blue.

B.3 Extrapolation in Time

To model evolution of maximum pit depth with time, a decision was made to assume a power-law relationship for the location (μ) and scale (α) parameters, each having a common exponential term, while leaving the shape (κ) parameter invariant to time. Strictly speaking, $\mu_t \coloneqq \mu t^b, \alpha_t \coloneqq \alpha t^b,$ and κ are parameters of the model, and $\mu, \alpha,$ and b hyperparameters. For simplicity, however, the term "parameters" will be adopted for μ, α, κ and b. That the location and scale are chosen—seemingly arbitrarily—to increase by the same exponent b, is a choice based on the behaviour observed typically for carbon steels (Laycock et al., 1990) and is assumed here to be true for 304 stainless steels immersed in 3.5 wt% NaCl solution at 30°C. Also, the decision to leave the shape parameter constant is consistent with the approach adopted successfully by Laycock et al. (1990); Scarf (1992); Scarf et al. (1992); Scarf and Laycock (1994), particularly for modelling stainless steels. Consequently, the revised GEV distribution with time as covariate and the corresponding density function are shown respectively in Equation B.8 and Equation B.9:

$$GEV(x,t\,|\,\mu,\alpha,\kappa,b) = \exp\left\{-\left[1-\kappa\left(\frac{x-\mu t^b}{\alpha t^b}\right)\right]^{\frac{1}{\kappa}}\right\}; 1-\kappa\left(\frac{x-\mu t^b}{\alpha t^b}\right) \geq 0; \tag{B.8}$$

$$g(x,t\,|\,\mu,\alpha,\kappa,b) = \frac{1}{\alpha t^b}\left[1-\kappa\left(\frac{x-\mu t^b}{\alpha t^b}\right)\right]^{\frac{1}{\kappa}-1} \exp\left\{-\left[1-\kappa\left(\frac{x-\mu t^b}{\alpha t^b}\right)\right]^{\frac{1}{\kappa}}\right\}. \tag{B.9}$$

Equation B.8 is the non-stationary representation (as chosen in this work) of the stationary GEV distribution given in Equation B.5. Assuming that a confidence interval for the shape parameter κ does not include zero, the support of $GEV(x,t\,|\,\mu,\alpha,\kappa,b)$ is $x \leq \mu t_j^b + \alpha t_j^b/\kappa$, which results in an upper endpoint $x_+ = \mu t_j^b + \alpha t_j^b/\kappa$.

B.4 Parameter Estimation and Goodness-of-Fit

The literature offers many methods for deriving point estimates of the stationary GEV distribution parameters. Traditionally, the most popular methods are Probability-Weighted Moments (PWM), Hosking et al. (1985); L-Moments (LM), Hosking (1990), which are related to the method of PWM; and Maximum Likelihood (ML), Smith (1985). A review

of the literature would show that in surprisingly many instances, authors simply state the selected parameter estimation method without due consideration for the implications of their choice. However, among these there are at times more discriminating authors who include a statement to the effect that any necessary conditions associated with the parameter estimation method are assumed to apply. Fortunately, the literature is replete with examples where more careful thought is given to the consequence of choosing one estimation method over another on predictions concerning extreme events—whether these are in finance, insurance, or civil and environmental engineering. The point being made is that given the purpose of this thesis—to develop a probabilistic model for UFC lifetime predictions—it is incumbent on this author to offer at least a justification for the parameter estimation method chosen and to state simply the implications for ensuing analyses. The intent, however, is not to provide an exhaustive review of the various methods and their merits, but rather to grant the reader a measure of appreciation for the choice made.

The method of ML is preferred by this author simply because of both its intuitiveness and flexibility in handling the non-stationary GEV. However, there are other benefits that attract many users to ML. These include: (*i*) the ability to estimate standard errors—and by extension confidence intervals—for estimated model parameters by invoking asymptotic normality assumptions, and (*ii*) the relative ease with which a simple approach (e.g., deviance statistic) can be applied to assess whether a complex model (in the sense of more parameters) is a better fit to data than a simpler model (i.e., a simpler model whose set of parameters is contained within the set of parameters of the more complex model). A very good, accessible summary of these benefits are provided in Coles (2001, Sec. 2.6.3), Beirlant et al. (2004, Sec. 5.1), and Castillo et al. (2005, Ch. 5.1).

There are three main concerns with the method of ML, however. First, the so-called "regularity conditions" that govern the applicability of asymptotic normality assumptions are restricted to $\kappa < 0.5$, Smith (1985)[1]. Second, for small-sized samples the ML method can lead to both unrealistic estimates for κ and large bias and variance for the GEV parameter estimations, including large bias and variance for quantile estimates of extreme events (i.e., for return levels associated with some very small exceedance probability), Hosking et al., 1985. By small sample size it is meant $m \leq 25$, as demonstrated by Hosking et al., 1985 through simulations. The results of Hosking et al., 1985 have been replicated by several authors (e.g., see Coles and Dixon, 1999 and Martins and Stedinger, 2000) and represent legitimate concerns. The last concern is the potential for convergence problems when maximising the likelihood function by numerical algorithms. In the present work, this problem was not experienced and is not discussed further. Regularity conditions

[1]For a more recent assessment of the asymptotic normality assumptions in the context of the GEV distribution and a critique on the paper by Smith (1985), see Bücher and Segers (2017).

are assumed met, but the interested may consult Casella and Berger, 2002, pg 516, and Lehmann and Casella, 1998, pg 440 for a detailed description of regularity conditions. The effect of small sample size is discussed separately below. However, to better understand the ensuing discussion the method of ML is presented first.

B.4.1 The Maximum Likelihood Method

What follows has been adapted from many of the references already cited above, but of particular noteworthiness is the book by Pawitan (2013) that—aside from being somewhat of an exhaustive yet very readable exposition of the maximum likelihood method—provides the reader with some great historical perspectives on the evolution of the concept of statistical inference.

Assume that $X_1, X_2, \dots$ are iid RVs, representing a sequence of corrosion pits on a particular coupon with density $g_{\boldsymbol{\theta}}(x, t)$, where the subscript $\boldsymbol{\theta}$ implies a fixed parameter vector (i.e., $g_{\boldsymbol{\theta}}(x) = g(x, t \,|\, \boldsymbol{\theta})$), and $\boldsymbol{\theta} \coloneqq (\mu, \alpha, \kappa, b)$. Under the assumption of independence, the joint distribution of $X_1, X_2, \dots$ is expressed by

$$g_{\boldsymbol{\theta}}(x_1, x_2, \dots, t) = \prod_{i=1}^{m} g_{\boldsymbol{\theta}}(x_i, t). \tag{B.10}$$

A note of clarification is required here. Equation B.10 describes the joint distribution for m corrosion pit maxima at a fixed exposure time t. For k distinct exposure times, where m maxima are observed for each, the joint distribution of a sequence of RVs $X_{1,1}, X_{2,1}, \dots, X_{m,k}$, where $X_{i,j}$ is the random variable associated with the observed maximum corrosion pit $x_{i,j}$ of the ith coupon at the jth exposure period, takes the following form

$$g_{\boldsymbol{\theta}}(x_{1,1}, x_{2,1}, \dots, t_1, t_2, \dots) = \prod_{j=1}^{k} \left\{ \prod_{i=1}^{m} g_{\boldsymbol{\theta}}(x_{i,j}, t_j) \right\}. \tag{B.11}$$

The assumption that m maxima between exposure periods are *independent and identically distributed* is worthy of a brief discussion. Suppose for a moment the m maxima represent a univariate time series of consecutive observations across all exposure periods. It could then be said that the data exhibit "temporal" dependence in the form of a nonlinear trend with time (e.g., see Figure B.1). Such a trend would raise questions as to the validity of the limiting GEV distribution since Equation B.5 indicates clearly that it is invariant to time. Fortunately, the limiting GEV distribution is still applicable provided non-hyperparameters (i.e., μ_t and α_t, in the present case) are defined as functions of time

(Coles, 2001, Ch 6), as is the case in Equation B.8. One can thus say that non-stationarity or temporal dependence in the data, which violates the assumption of *identically distributed*, is overcome—more accurately "relaxed"—by defining the parameters of the GEV model as functions of time and thereby assigning a single distribution to the RV $X_{i,j}$. The question of independence of m maxima between exposure periods is also satisfied. For example, events $\{X_{1,1}=x_{1,1}\}$ and $\{X_{1,2}=x_{1,2}\}$ are independent in that the value of the former provides no information on the value of the latter. Intuitively, this is consistent with our understanding that the corrosion tests at each exposure period are distinct and non-interacting subsets of the larger corrosion experiments (and were not generated as a result of consecutive observations). Consequently, the m maxima between exposure periods are *iid* (i.e., $\overset{iid}{\sim} g(x,t\,|\,\boldsymbol{\theta})$), which is understood to mean that maxima across all time periods are independent and are (loosely speaking) also identically distributed as per the parametrisation of the non-stationary GEV model . With the assumption of iid justified, the form of Equation B.11 holds. (The concept of dependence is revisited in the next chapter under the Markov process model for the evolution of pit depth exceedances over a specified threshold.)

Assuming $X_{1,1}, X_{2,1}, \ldots, X_{m,k} \overset{iid}{\sim} g(x,t\,|\,\boldsymbol{\theta})$, then the *likelihood function* L, which represents the likelihood of observing the data $x_{1,1}, x_{2,1}, \ldots$ across k exposure periods (i.e., $\{t_j \in \mathbb{R}_+ : j = 1, 2, \ldots, k\}$), for a given parameter vector $\boldsymbol{\theta}$, is defined by

$$L(\boldsymbol{\theta}\,|\,x_{1,1}, x_{2,1}, \ldots, t_1, t_2, \ldots) = \prod_{j=1}^{k} \left\{ \prod_{i=1}^{m} g_{\boldsymbol{\theta}}(x_{i,j}, t_j) \right\}. \tag{B.12}$$

Subsequently, the MLE of $\boldsymbol{\theta}$ is defined as

$$\hat{\boldsymbol{\theta}} = \arg\max_{\boldsymbol{\theta}\in\boldsymbol{\Theta}} L(\boldsymbol{\theta}\,|\,x_{1,1}, x_{2,1}, \ldots, t_1, t_2, \ldots). \tag{B.13}$$

For the sample observed $x_{1,1}, x_{2,1}, \ldots$, the MLE $\hat{\boldsymbol{\theta}}$ is the estimate for $\boldsymbol{\theta}$ that maximises L across the parameter space $\boldsymbol{\Theta}$, where $\boldsymbol{\theta} \in \boldsymbol{\Theta}$ and $\boldsymbol{\Theta} \subseteq \mathbb{R}^d$, d an integer ≥ 1. Put in other words, L is the likelihood of $\boldsymbol{\theta}$, with $\boldsymbol{\theta}$ treated as a variable, conditional on the observed data. It is often more convenient to work with the *log-likelihood function* l, which represents the natural logarithm of Equation B.12:

$$l(\boldsymbol{\theta}\,|\,x_{1,1}, x_{2,1}, \ldots, t_1, t_2, \ldots) = \sum_{j=1}^{k} \left\{ \sum_{i=1}^{m} \ln g_{\boldsymbol{\theta}}(x_{i,j}, t_j) \right\}. \tag{B.14}$$

This is possible because the solution to the maximisation problem (Equation B.13) is invariant to the natural logarithm of L (i.e, invariant to a strictly monotone increasing transformation—*the natural logarithm function is strictly increasing on the interval* $(0, \infty)$). Consequently, $\hat{\boldsymbol{\theta}}$ may be defined as

$$\hat{\boldsymbol{\theta}} = \arg\max_{\boldsymbol{\theta} \in \boldsymbol{\Theta}} l(\boldsymbol{\theta} \,|\, x_{1,1}, x_{2,1}, \ldots, t_1, t_2, \ldots). \tag{B.15}$$

To simplify notation, let $\mathbf{x}, \mathbf{t} \coloneqq \{x_{1,1}, x_{2,1}, \ldots, t_1, t_2, \ldots\}$. The maximisation problem requires taking the partial derivatives of L or l with respect to $\boldsymbol{\theta}$ and setting the same to zero. Consequently, $\hat{\boldsymbol{\theta}}$ is the solution to the *likelihood equation* that, for the multi-parameter case of the non-stationary GEV distribution, is expressed as the vector of component-wise partial derivates set to zero

$$\nabla l(\hat{\boldsymbol{\theta}} \,|\, \mathbf{x}, \mathbf{t}) = \left(\frac{\partial l(\hat{\boldsymbol{\theta}} \,|\, \mathbf{x}, \mathbf{t})}{\partial \mu}, \frac{\partial l(\hat{\boldsymbol{\theta}} \,|\, \mathbf{x}, \mathbf{t})}{\partial \alpha}, \frac{\partial l(\hat{\boldsymbol{\theta}} \,|\, \mathbf{x}, \mathbf{t})}{\partial \kappa}, \frac{\partial l(\hat{\boldsymbol{\theta}} \,|\, \mathbf{x}, \mathbf{t})}{\partial b} \right)^{\mathrm{T}} = \mathbf{0}, \tag{B.16}$$

where $(\cdot)^{\mathrm{T}}$ represents transpose and $\mathbf{0}$ is a 4×1 zero column vector. For the non-stationary GEV distribution, it is more convenient to solve for $\hat{\boldsymbol{\theta}}$ in Equation B.15 by applying suitable numerical maximisation algorithms (more precisely, minimisation routines applied to the negative log-likelihood function (i.e., $-l(\boldsymbol{\theta} \,|\, \mathbf{x}, \mathbf{t})$). $\nabla l(\boldsymbol{\theta} \,|\, \mathbf{x}, \mathbf{t})$ is also known as the *score vector* $\mathbf{S}(\boldsymbol{\theta} \,|\, \mathbf{x}, \mathbf{t})$, and the MLE satisfies the condition $\mathbf{S}(\hat{\boldsymbol{\theta}} \,|\, \mathbf{x}, \mathbf{t}) = \mathbf{0}$. Also, under certain regularity conditions, the expectation of $\mathbf{S}(\boldsymbol{\theta} \,|\, \mathbf{x}, \mathbf{t})$ is equal to zero (i.e., $E\left[\mathbf{S}(\boldsymbol{\theta} \,|\, \mathbf{x}, \mathbf{t})\right] = \mathbf{0}$).

The covariance of $\mathbf{S}$ (i.e., $Cov\left[\mathbf{S}\right] = E\left[\mathbf{S}\mathbf{S}^T\right] - E\left[\mathbf{S}\right] E\left[\mathbf{S}\right]^T$), which is a $d \times d$ matrix, is called the *Fisher information matrix* $\mathbf{I}(\cdot)$ and represents the negative expectation (taken with respect to the RV $X_{i,j}$) of the *Hessian* $\mathbf{H}$—the matrix of second partial derivatives of the log-likelihood function:

$$\mathbf{H}(\boldsymbol{\theta} \,|\, \mathbf{x}, \mathbf{t}) = \frac{\partial \mathbf{S}(\boldsymbol{\theta} \,|\, \mathbf{x}, \mathbf{t})}{\partial \boldsymbol{\theta}} = \frac{\partial^2 l(\boldsymbol{\theta} \,|\, \mathbf{x}, \mathbf{t})}{\partial \boldsymbol{\theta} \partial \boldsymbol{\theta}^T} = \begin{pmatrix} \frac{\partial^2 l(\boldsymbol{\theta} | \mathbf{x}, \mathbf{t})}{\partial \mu \partial \mu} & \cdots & \frac{\partial^2 l(\boldsymbol{\theta} | \mathbf{x}, \mathbf{t})}{\partial \mu \partial b} \\ \vdots & \ddots & \vdots \\ \frac{\partial^2 l(\boldsymbol{\theta} | \mathbf{x}, \mathbf{t})}{\partial b \partial \mu} & \cdots & \frac{\partial^2 l(\boldsymbol{\theta} | \mathbf{x}, \mathbf{t})}{\partial b \partial b} \end{pmatrix}, \tag{B.17}$$

and

$$\mathbf{I}(\boldsymbol{\theta} \,|\, \mathbf{x}, \mathbf{t}) = -E\left[\mathbf{H}(\boldsymbol{\theta} \,|\, \mathbf{x}, \mathbf{t})\right]. \tag{B.18}$$

The *Fisher information matrix* $\mathbf{I}$ is a measure of the expected curvature of the log-likelihood function, which intuitively *informs* us as to the *shape*—flat or peaked—of the

log-likelihood function in the vicinity of its maximum (i.e., evaluated at $\boldsymbol{\theta}=\hat{\boldsymbol{\theta}}$). While in practice this is not directly exploited, it has been observed that when $-l$ is minimised via numerical algorithms, difficulties in convergence or numerical instabilities may arise when l is very flat in the neighbourhood of its maximum. Again, in the present work this was not experienced.

For a random maxima sample of size m, observed across k exposure periods, the above equations signify

$$\mathbf{H}(\boldsymbol{\theta}\,|\,\mathbf{x},\mathbf{t}) = \sum_{j=1}^{k}\left\{\sum_{i=1}^{m}\frac{\partial^2}{\partial\boldsymbol{\theta}\partial\boldsymbol{\theta}^T}\ln g_{\boldsymbol{\theta}}(x_{i,j},t_j)\right\} = \sum_{j=1}^{k}\left\{\sum_{i=1}^{m}\mathbf{H}(\boldsymbol{\theta}\,|\,x_{i,j},t_j)\right\}, \tag{B.19}$$

and, therefore,

$$\mathbf{I}(\boldsymbol{\theta}\,|\,\mathbf{x},\mathbf{t}) = -\sum_{j=1}^{k}\left\{\sum_{i=1}^{m}E\left[\mathbf{H}(\boldsymbol{\theta}\,|\,x_{i,j},t_j)\right]\right\}. \tag{B.20}$$

Distributing the expectation into the *Hessian* can be messy algebraically (e.g., see Equation B.25). Alternatively, one can compute the *Observed information matrix* $\mathbf{I_O}(\cdot)$ that, in the present context, is defined as the negative of the *Hessian*

$$\mathbf{I_O}(\boldsymbol{\theta}\,|\,\mathbf{x},\mathbf{t}) = -\mathbf{H}(\boldsymbol{\theta}\,|\,\mathbf{x},\mathbf{t}). \tag{B.21}$$

Coles (2001, pg 32) suggests that estimates of parameter confidence intervals (to be discussed shortly) derived using $\mathbf{I_O}(\cdot)$ are often more accurate than those estimated with $\mathbf{I}(\cdot)$. Further, Castillo et al. (2005, pg 111) state that if l is approximately quadratic in the neighbourhood of the maximum, then $\mathbf{I}(\cdot) \approx \mathbf{I_O}(\cdot)$, evaluated at $\boldsymbol{\theta}=\hat{\boldsymbol{\theta}}$. It is certainly simpler to perform the computations for $\mathbf{I_O}(\cdot)$ than for $\mathbf{I}(\cdot)$ (e.g., see Scarf (1992) for a complete computation for the non-stationary GEV distribution), but when used to estimate parameter uncertainties both forms of the *Fisher information matrix* lead to the same vulnerability to small-sized sample effects. Moreover, recently Cao and Spall (2012) showed that under a mean squared error criterion $\mathbf{I}(\cdot)$ outperforms $\mathbf{I_O}(\cdot)$ in estimating the covariance matrix of the MLE $\hat{\boldsymbol{\theta}}$. Consequently, while computationally attractive, there are no immediate compelling reasons to consider $\mathbf{I_O}(\cdot)$ for estimation of parameter uncertainties.

It is now possible to speak more specifically of the reasons why the ML method remains a popular statistical inference tool. Under certain regularity conditions, the MLE $\hat{\boldsymbol{\theta}}$ exhibits desirable properties (Castillo et al., 2005, pg 110), which are: it is a consistent, efficient, and an asymptotically normal estimator of $\boldsymbol{\theta}$. In few words, consistent means that as $m \to \infty$, $\hat{\boldsymbol{\theta}} \to \boldsymbol{\theta}$, or the variance of $\hat{\boldsymbol{\theta}} \to 0$. Efficient speaks to the characteristic that as an

estimator it has minimum variance. Asymptotically normal highlights that it convergences in distribution to the normal distribution N_d with mean vector $\boldsymbol{\theta}$ and covariance matrix equal to the inverse of the *Fisher information matrix* (i.e., $\hat{\boldsymbol{\theta}} \xrightarrow{d} \mathrm{N}_d(\boldsymbol{\theta}, \mathbf{I}(\boldsymbol{\theta}\,|\,\mathbf{x}, \mathbf{t})^{-1})$, where the subscript d in N_d denotes $d - dimensional$). The last point, in particular, allows for estimation of parameter uncertainty via the computation of symmetrical confidence intervals. More precisely, the square root of the diagonals of $\mathbf{I}(\boldsymbol{\theta} \mid \mathbf{x}, \mathbf{t})^{-1}$, evaluated at $\boldsymbol{\theta} = \hat{\boldsymbol{\theta}}$, yields estimates of the standard errors $(\hat{\sigma}_{\hat{\mu}}, \hat{\sigma}_{\hat{\alpha}}, \hat{\sigma}_{\hat{\kappa}}, \hat{\sigma}_{\hat{b}})$ for the MLEs $\hat{\mu}, \hat{\alpha}, \hat{\kappa},$ and $\hat{b}$, from which the respective $(1-\alpha)100\%$ confidence intervals $\hat{\mu} \pm z_{\alpha/2}\hat{\sigma}_{\hat{\mu}}, \hat{\alpha} \pm z_{\alpha/2}\hat{\sigma}_{\hat{\alpha}}, \hat{\kappa} \pm z_{\alpha/2}\hat{\sigma}_{\hat{\kappa}},$ and $\hat{b} \pm z_{\alpha/2}\hat{\sigma}_{\hat{b}}$ follow, with $z_{\alpha/2}$ equal to the standard normal quantile and α the confidence level.

From the foregoing, one can better appreciate that the *Fisher information matrix* provides a "number" that equates to a bound on the variance of $\hat{\boldsymbol{\theta}}$. The larger the value of the *Fisher information matrix*, the more "information" is derived about $\boldsymbol{\theta}$ from the observed sample $x_{1,1}, x_{2,1}, \ldots, t_1, t_2, \ldots,$ and the smaller the bound on the variance of $\hat{\boldsymbol{\theta}}$ (Casella and Berger, 2002, pg 338). The above discussion has only but touched on the ML method and its properties. The interested reader is encouraged to examine the following references, which this author found to be of substantial benefit in appreciating the subject matter. They are listed in order of increasing difficulty, with respect to required level of mathematics and statistics: Rice, 2007, Ch 8 Estimation of Parameters and Fitting of Probability Distributions; Wasserman, 2010, Ch 9 Parametric Inference; Casella and Berger, 2002, Ch 10 Asymptotic Evaluation; Pawitan, 2013; and van der Vaart, 2000, Ch 5 M- and Z-Estimators.

Small Sample Size

Coles and Dixon (1999) showed that indeed large bias and large mean square error are computed for the GEV ML estimators $\hat{\mu}, \hat{\alpha},$ and $\hat{\kappa}$ when the number of samples is less than 25. In their assessment, they noted that the difference between the GEV ML and PWM quantile estimators was due mainly to the negative skewness in the distribution of the shape parameter estimate $\hat{\kappa}$, which in turn led to large bias in quantile estimations. They attributed the better performance of the PWM quantile estimators to the implicit assumption used in the PWM methodology, which assumes $\kappa > -1$. This assumption effectively maps the unbounded κ parameter space $(-\infty, \infty)$ to the bounded-below $\hat{\kappa}$ parameter space $(-1, \infty)$. Coles and Dixon (1999) subsequently argued that the constraint $\kappa > -1$ acts very much as prior information, an argument they then used to develop a "penalised" MLE. Effectively, in the penalised scheme the likelihood function is multiplied

by a user-defined probability distribution, in a manner similar to some extent to that of a Bayesian formulation for parameter estimation. Penalised ML quantile estimators exhibit both improved bias and mean square error for small samples.

Around the same time as Coles and Dixon (1999) were submitting their manuscript for the "penalised" MLE, Martins and Stedinger (2000) were developing a modified ML method approach for small samples, which they called Generalised Maximum Likelihood (GML)[2] and whose parameter estimate was defined as the Generalised Maximum Likelihood Estimator (GMLE). The assertion made by Martins and Stedinger (2000) was that for hydrologic data it is reasonable to expect κ to lie within a certain range. When this assertion is viewed from the perspective of a "belief," it permits explicit definition of a prior distribution $\pi(\cdot)$ for κ, $\pi(\kappa)$, whose domain is bounded (i.e., $\kappa \coloneqq [\kappa_L, \kappa_U]$), where L and U are lower and upper, respectively. Based on experience and some analysis, a Beta distribution was chosen for $\pi(\kappa)$, and the Generalised Likelihood (GL) function was defined as the product of the likelihood function and the Beta prior. (As an aside, Martins and Stedinger (2000) defined the domain of $\pi(\kappa)$ as $[-0.5, 0.5]$, which effectively addressed concerns with satisfying regularity conditions (Smith, 1985)). Point estimates for $\mu, \alpha,$ and κ were obtained by numerical maximisation, using the Newton-Raphson method, of the GL function. With the GMLEs acquired, ensuing Monte Carlo simulations demonstrated lower Root Mean Square Error (RMSE)—in comparison with the methods of ML and PWM—for quantiles calculated across non-exceedance probabilities ranging from 0.001 to 0.999 and $\kappa \leq 0$, and for a sample of size 25. Maximisation of the GL function led to GMLEs $\hat{\mu}, \hat{\alpha},$ and $\hat{\kappa}$ that, in the context of a Bayesian formulation, represented the mode—not the mean—of the respective Bayesian posterior parameter distributions. However, for clarification, maximisation of the GL function resulted in point estimates, not posterior parameter distributions. Martins and Stedinger (2000) acknowledged that the method of GL was a semi-Bayesian analysis procedure suitable were insufficient regional data (domain know-how, in the context of this thesis) precluded definition of priors for μ and α.

Perhaps it could be argue that Coles and Tawn (1996) were the first[3] to carry out a full

[2]The expression *generalized maximum likelihood* was used by Berger (1985, pg 133) in reference to the use of the mode of the model parameter posterior distribution as one of several potential parameter point estimates.

[3]From the point of view that Coles and Tawn (1996) were the first to exploit fully a Bayesian framework by utilising the computational efficiencies offered by a Markov Chain Monte Carlo (MCMC) procedure to estimate the posterior parameter distribution $\pi(\boldsymbol{\theta} \mid \mathbf{x})$. Smith and Naylor (1987) were the first to apply a Bayesian framework in the context of extreme value analysis but for the three-parameter Weibull and with a numerical (integration) methodology invoking asymptotic normality assumptions for the posterior parameter distribution (i.e., assuming explicitly that $\pi(\boldsymbol{\theta} \mid \mathbf{x})$ is multi-variate normal—see Naylor and Smith (1982) for further details).

Bayesian analysis of extreme data—in their case rainfall data. Unlike others before them, Coles and Tawn (1996) chose to develop informative priors for quantiles (namely quantile differences) rather than for the GEV model parameters directly. Specifically, quantiles were determined for particular exceedance probabilities (i.e., rainfall return levels for specified return periods) by eliciting the knowledge of subject matter experts. Coles and Tawn (1996) opined that "*it was unlikely that prior beliefs on extremal behaviour could be adequately elicited directly in terms of GEV parameters.*" Consequently, the joint prior distribution of the quantiles (modelled arbitrarily by Gamma distributions) were defined and subsequently transformed into a prior distribution $\pi(\boldsymbol{\theta})$ for the GEV parameter vector $\boldsymbol{\theta}$, where $\boldsymbol{\theta} \coloneqq (\mu, \alpha, \kappa)$. The posterior parameter vector distribution $\pi(\boldsymbol{\theta} \,|\, \mathbf{x})$, where $\mathbf{x}$ represents the observed data (i.e., $\mathbf{x} \coloneqq x_1, x_2, \dots$), was calculated by multiplying $\pi(\boldsymbol{\theta})$ by the likelihood function, which was expressed in terms of a non-homogeneous Poisson point process. The latter requires an estimate of the threshold level for the determination of exceedances that, as will be discussed later, brings with it additional uncertainty—an uncertainty Coles and Tawn (1996) partly addressed. Subsequently, a MCMC method was applied to estimate the marginal posterior distributions for $\hat{\mu}, \hat{\alpha}$, and $\hat{\kappa}$. The authors subsequently showed that, when expert knowledge can be elicited, the full Bayesian formulation has definite advantages in both reducing standard errors for model parameter estimates and providing more realistic quantile confidence intervals—credible intervals—for very long return periods. This is particularly true for quantile predictions, where the use of the Bayesian predictive distribution (i.e., $f(x_{n+1} \,|\, x_1, x_2, \dots, x_n) \propto \int_{\boldsymbol{\Theta}} f(x_{n+1} \,|\, \boldsymbol{\theta}) \pi(\boldsymbol{\theta} \,|\, x_1, x_2, \dots, x_n) d\boldsymbol{\theta}$, where x_{n+1} is the new observation of interest[4], see Bolstad, 2010, pg 54) is viewed as "*the most natural summary of an extreme value inference*" (quoted in a follow-up paper by Coles and Pericchi (2003) in reference to Coles and Tawn (1996)).

With respect to the work by Coles and Pericchi (2003), including the work by Coles et al. (2003), a full Bayesian formulation was applied to extreme-value analysis of daily rain-fall data spanning approximately 50 years of record taking on the coast of Venezuela. Using a point process formulation for the likelihood function and zero-mean normal priors for $\mu, \ln \alpha$, and κ (i.e., $\mu, \ln \alpha \sim \mathrm{N}(0, 10^4)$, and $\kappa \sim \mathrm{N}(0, 10^2)$), the posterior marginal parameter distributions for each were estimated by the MCMC method. Similarly, Coles and Tawn (2005) analysed extreme surges on the east coast of the United Kingdom with a full Bayesian framework, but with seasonality accounted for by the incorporation of time as a covariate only in the formulation of $\mu(t)$ and $\alpha(t)$, holding κ time invariant. While Coles

[4]Namely, for a quantile of interest z_p, the formula is $P(Z_L < z_p \,|\, \mathbf{x}) = \int_{\boldsymbol{\Theta}} P(Z < z_p \,|\, \boldsymbol{\theta})^L \pi(\boldsymbol{\theta} \,|\, \mathbf{x}) d\boldsymbol{\theta}$, where Z_L is a maximum for some future period L (Coles and Tawn, 1996). The integral can be readily estimated by the MCMC procedure. A very good explanation of the predictive distribution in the setting of extreme value analysis is provided by Renard et al. (2013) and Stephenson (2016).

and Tawn (2005) do not specify the use of priors for the hyper-parameters associated with $\mu(t)$ and $\alpha(t)$, they do present normal marginal posterior distributions for each, suggesting that independent vague normal priors were used, as is typically the case when there is no information to suggest otherwise (Stephenson, 2016). The point of highlighting the full Bayesian approach adopted by Coles and Pericchi (2003), Coles et al. (2003), and Coles and Tawn (2005), is to demonstrate that an apparent change of mind can occur even when one expresses a strong opinion about the identification of priors. For instance, the reader may recall that Coles and Tawn (1996) expressed their incredulity in the validity of assigning meaningful priors for the GEV model parameters, which led them to do so for quantiles after eliciting expert opinion. In contrast, the last set of investigators abandoned this thought and adopted what are referred to as vague normal priors for parameter or hyper-parameters. In doing so, computations are greatly simplified, but the impact to parameter bias and RMSE remains unknown as these were not evaluated by the last set of investigators.

Notwithstanding, the attraction of the GML method remained strong as several authors (e.g., El Adlouni et al. (2007) and Yoon et al. (2010)) continued to pursue it as an improvement to method of ML for small-sized samples. For El Adlouni et al. (2007), the GML method proposed by Martins and Stedinger (2000) was adopted for parameter estimation in several non-stationary GEV models, with μ expressed as a linear or quadratic function of time, α as an exponential function of time, and a Beta prior for κ. But instead of employing numerical maximisation routines, El Adlouni et al. (2007) estimated the posterior GEV parameter distribution $\pi(\boldsymbol{\theta} \mid \mathbf{x})$ and corresponding marginal posterior parameter distributions for $\hat{\mu}, \hat{\alpha},$ and $\hat{\kappa}$ via the MCMC method. From each they chose the mode to represent the GMLEs. Perhaps the real attraction in the GML method—at least for El Adlouni et al. (2007)—was the flexibility with which covariates, such as time, could be integrated into various non-stationary GEV models, which they considered and subsequently fitted to data. Arguably, because the GML method defines an informative prior only for one parameter (i.e., the Beta prior for κ), integrating non-stationarity into the rest of the model parameters did not significantly challenge the computational efficiency of the MCMC method.

Concerning the work of Yoon et al. (2010), the GML method proposed by Martins and Stedinger (2000) was extended to a full Bayesian framework for the stationary GEV distribution by including vague[5] prior distributions for μ and α, with $\mu, \ln \alpha \sim \mathrm{N}(0, 10^4)$. In comparison with the full Bayesian approach applied by Coles and Pericchi (2003), the method by Yoon et al. (2010) replaces the prior distribution for κ, $\kappa \sim \mathrm{N}(0, 10^2)$, with the

[5]For normal priors (e.g., $\sim \mathrm{N}(0, 10^2 - 10^4)$, the terms "proper" (Coles and Pericchi, 2003) and "vague" (Yoon et al. (2010) and Stephenson (2016)) are synonymous.

Martins and Stedinger (2000) Beta prior but with a slight change to the Beta parameter values, which were derived by minimising a separate parameter selection criterion. Both approaches—vague priors vs vague priors for μ and $\ln \alpha$ but informative (Beta) prior for κ—in the context of small sample size were formally assessed by Yoon et al. (2010) via simulation for a sample size of 30. Their results showed that the vague prior approach leads to larger positive bias and RMSE for quantile estimates at high non-exceedance probabilities (i.e., $p > 0.99$). In fact, Yoon et al. (2010) found that the vague priors approach did not differ significantly from the ML method, which they postulated to be due to a lack of constrain in the domain of the vague prior for κ. This conclusion indicates that, for small sample size, a full Bayesian framework with vague priors is still subject to high bias and RMSE for quantile estimates at high non-exceedance probabilities, and this vulnerability appears to be linked to the selection of a vague prior for κ. (The field of Bayesian inference in extreme value analysis has grown significantly over the last few decades, especially with the availability of the freely available statistics software program R (R Core Team, 2021). Only a brief review has been presented herein. For a more detailed and relatively recent review of Bayesian inference within the context of extreme value analysis and R, the reader is referred to Stephenson (2016).)

Reasons for Choosing the ML Method

When viewed from the perspective of facility to estimate the marginal distributions for $\hat{\mu}, \hat{\alpha}$, and $\hat{\kappa}$, a full Bayesian framework is advantageous, particularly when compared with the ML method, which requires additional steps to obtain estimates of parameter confidence intervals, or the various modified ML methods presented above, which are not fully Bayesian. Additionally, with the potential to reduce bias and RMSE for small-sized samples, under appropriate selection of informative prior for κ, a natural question to ask is "why not adopt a full Bayesian approach right from the start and forego the penalised ML or GML methods?" The answer is simply that expert knowledge is not always available to support definition of an appropriate, informative prior for κ, and eliciting subject matter experts is no mean task. Depending on the design situation and the necessity for highly reliable quantile estimates, it could be argued that the extra effort is worth it—perhaps required. This point was brought into sharp focus by Coles and Pericchi (2003) in the context of the 1999 catastrophic rainstorm in Venezuela. Admittedly, with UFC lifetime predictions in view, the natural recommendation for this thesis (and for those wishing to apply extreme value statistics to estimate lifetimes of UFCs) would be to adopt a full Bayesian framework for the estimation of the GEV parameters. Unfortunately, due in part to lack of relevant Cu pitting corrosion data (i.e., for postulated repository conditions)

and a desire to eventually adopt into the present model some aspects of the active/passive mechanistic pitting approach presented in the model by Briggs et al. (2021), it is simply beyond the scope of this thesis to pursue a full Bayesian formulation at this time. But clearly, this is a recommendation for future work arising from this study (possibly even a stand-alone thesis topic).

While this work does not pursue a Bayesian framework (either full or partial), it would not be accurate to say that any meaningful prior knowledge is therefore ignored in the process of determining the MLEs. On the contrary, work on pitting corrosion in some stainless steels indicates $0 < \kappa < 0.5$ (Laycock et al., 1990). It follows that one can incorporate this prior knowledge and simultaneously satisfy regularity conditions and mitigate small sample size effects by defining the parameter set for κ by the closed interval $[0, 0.5]$. Indeed, this is the approach followed herein.

Lastly, to further support the adoption of the ML method, the reader may recall that a small sample is 25 or less observations (as defined by Hosking et al. (1985)), which in the block maxima context means $m \leq 25$. In this work, the number of block maxima per exposure period was fixed a priori at 10 (i.e., $m = 10$) by Li et al. (2019). As a consequence, had the stationary GEV model been fitted separately to each exposure period and subsequently used to predict quantile maximum pit depths for some very small exceedance probability, the ensuing prediction would be expected to exhibit large bias and variance, even when $\kappa \coloneqq [0, 0.5]$. However, as will be demonstrated below, the non-stationary GEV model (i.e., Equation B.8) was fitted simultaneously to the data comprising all 10 exposure periods, representing a combined sample size of 100 block maxima. It is proposed—without proof—that the resulting bias and variance inherent in the MLE $\hat{\boldsymbol{\theta}}$ are thereby significantly reduced.

B.4.2 Parameter Point Estimations

Point estimates of the GEV distribution parameters by ML method were obtained by minimising the negative likelihood function (Equation B.22) or the negative log-likelihood function (Equation B.23), with the constraints $1 - \kappa\left(x - \mu t^b/\alpha t^b\right) \geq 0$, $\alpha t^b > 0$, and $\kappa \coloneqq [0, 0.5]$, where $\boldsymbol{\theta_1}$ represents the model parameter vector (i.e., $\boldsymbol{\theta_1} = \{\mu, \alpha, \kappa, b\}$):

$$L(\boldsymbol{\theta_1} \,|\, \mathbf{x}, \mathbf{t}) = \prod_{j=1}^{10} \left\{ \prod_{i=1}^{n_j} \frac{1}{\alpha t_j^b} \left[1 - \kappa \left(\frac{x_{i,j} - \mu t_j^b}{\alpha t_j^b} \right) \right]^{\frac{1}{\kappa} - 1} \exp \left\{ - \left[1 - \kappa \left(\frac{x_{i,j} - \mu t_j^b}{\alpha t_j^b} \right) \right]^{\frac{1}{\kappa}} \right\} \right\}, \tag{B.22}$$

$$l(\boldsymbol{\theta_1}\,|\,\mathbf{x},\mathbf{t}) = \sum_{j=1}^{10}\left\{-n_j\ln\alpha - b\sum_{i=1}^{n_j}\ln t_j - (1-\kappa)\sum_{i=1}^{n_j} y_{i,j} - \sum_{i=1}^{n_j} e^{-y_{i,j}}\right\}, \tag{B.23}$$

with $y_{i,j}$ defined as

$$y_{i,j} = -\left(\frac{1}{\kappa}\right)\ln\left[1-\kappa\left(\frac{x_{i,j}-\mu t_j^b}{\alpha t_j^b}\right)\right]. \tag{B.24}$$

In Equation B.22 and Equation B.23 the index n_j is the number of maxima observed for the jth exposure period. For coding purposes, this formulation is more general than adopting m maxima per exposure period (e.g., Equation B.14), though in this work n_j was constant for all j and equal to m (i.e., $j{=}m{=}10$).

Two optimisation algorithms from the Scipy Optimize module for Python, the Limited Broyden-Fletcher-Goldfarb-Shanno (L-BFGS-B) and the Sequential Least Squares Programming (SLSQP), were utilised in a script written in Python 3.6.9. Verification and validation of the Python results was accomplished in parallel by the minimisation of the negative log-likelihood function in Excel and in LibreOffice Calc spreadsheets, using respectively the Generalized Reduced Gradient for Nonlinear Programming (GRG) and the DEPS Evolutionary Algorithm (DEPS-EA) solvers. The Scipy and the GRG were in excellent agreement, while the DEPS-EA solver converged to a slightly lower log-likelihood function value.

Initial values $\mu_0, \alpha_0, \kappa_0,$ and b_0 were required to facilitate numerical minimisation for all algorithms. A four-step approach was employed to obtain initial estimates. First, the Quantile Least Squares method (see Castillo et al. (2005, pg 224)) was used to obtain pre-initial estimates for $\mu_0, \alpha_0,$ and κ_0. Second, using the pre-initial parameter estimates, the stationary GEV model was fitted to the data from each exposure period, resulting in a 10-element vector for each of $\mu_{t_j}, \alpha_{t_j},$ and κ_{t_j}, where t_j refers to the jth exposure period. Third, a power-law fit of the form $y = a_1 x^{a_2}$ was fitted to the vectors for μ and α versus exposure time to yield an initial estimate for μ and α (i.e., $a_1 = \mu$ or α). Additionally, the exponential term a_2 from each of the two power-law fits was averaged to obtain an estimate for b (both exponential terms were quite close in value). Lastly, an estimate for κ was obtained by averaging the individual shape parameters derived from the stationary GEV model fit. This estimate, rounded to four decimal points, was $\bar{\kappa} = 0.0466$. For completeness, rounded to four decimal points, the initial starting values $\mu_0, \alpha_0, \kappa_0,$ and b_0 were $(0.0477, 0.0027, 0.0466, 0.3969)$. Overall, convergence took in the order of fractions of seconds for the Python scripts and approximately < 2 seconds for the Excel and LibreOffice Calc spreadsheets. Actual times will vary depending on the CPU processors utilised. Note that there is a discontinuity at $\kappa = 0$, so the actual bound used was $\kappa = [0.01, 0.5]$.

Table B.1 lists the ML estimates of the GEV distribution parameters to sufficient number of decimal points to facilitate comparison with those to be determined later in this chapter for the GPD. Of particular interest is $\hat{\kappa}$, which is well within the bounded interval $[0.01, 0.5]$ imposed on the numerical solution, indicating on first inspection that the Gumbel distribution, derived by taking the limit $\kappa \to 0$ in Equation B.8, is not a more valid model based on the data. Also included are the standard error (SE) and 95% Confidence Interval (CI), both of which were derived from the Bootstrap method (to be discussed). Figure B.2 shows the maximum pit depths per coupon per exposure period. Also included in the figure is the fitted GEV model and the expected maximum, Equation B.25 (Laycock et al. (1990)), which is bounded above and below by the two standard deviations determined from Equation B.26 as per Laycock et al., 1990. In Equation B.25 and Equation B.26, the model parameters are replaced by the estimates in Table B.1. For comparison, a simple power-law relationship was obtained via Ordinary Least Squares (OLS) and included in the figure. Overall, the GEV model fits the data well relatively speaking, but there are some obvious issues.

Table B.1: GEV Likelihood Function Parameters, Equation B.22

$\hat{\mu}$ (SE)[1] [95%CI][2]	$\hat{\alpha}$ (SE) [95%CI]	$\hat{\kappa}$ (SE) [95%CI]	$\hat{b}$ (SE) [95%CI]	$l(\hat{\boldsymbol{\theta}}_{\mathbf{1}} \mid \mathbf{x}, \mathbf{t})$
0.04788425	0.00400945	0.34294222	0.40294282	498.96
(0.00078)	(0.00035)	(0.07447)	(0.00716)	
[0.04632, 0.04943]	[0.00326, 0.00464]	[0.22442, 0.52428]	[0.38875, 0.41681]	

[1] Standard error of Bootstrap sampling distribution (10,000 repetitions)
[2] Based on percentile method of Bootstrap parameters

$$E\left[M_n\right] = \mu t^b + \frac{\alpha t^b}{\kappa} - \frac{\alpha t^b}{\kappa}\Gamma(1+\kappa); \kappa > -1. \tag{B.25}$$

$$\sigma\left(M_n\right) = \frac{\alpha t^b}{\kappa}\left\{\Gamma(1+2\kappa) - \left[\Gamma(1+\kappa)\right]^2\right\}^{1/2}; \kappa > -\frac{1}{2}. \tag{B.26}$$

As mentioned before, a distinct shift downward in the data occurs at 30 days of exposure, which coincides with the onset of the second set of experiments. While this shift

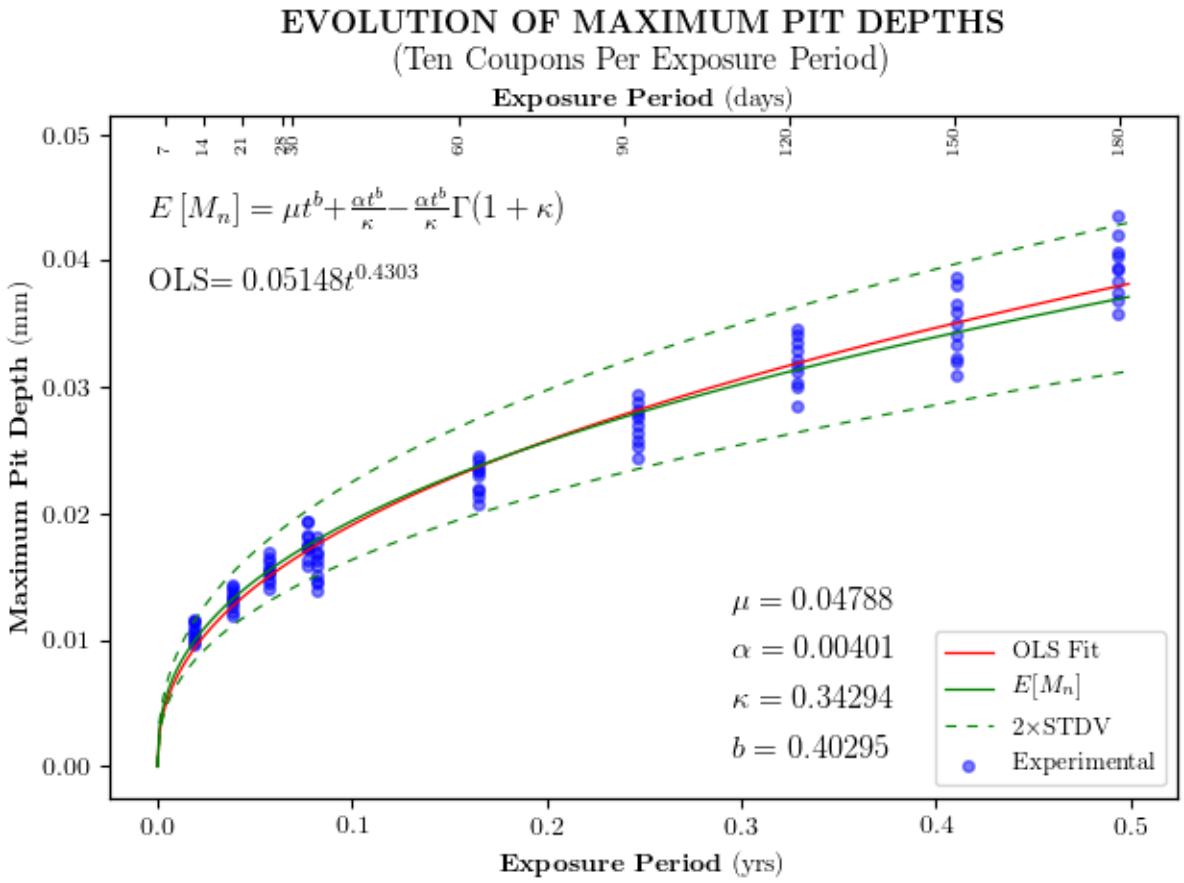

Figure B.2: Maximum pit depths versus time for 304 stainless steel coupons immersed in 3.5 wt% NaCl solution at 30°C Li et al. (2019)

clearly affects the overall accuracy of the fit, the effect is ignored for the sake of having a larger dataset from which to work. The data also exhibits an increase in variance with exposure time, which is consistent with typical corrosion experiments where time tends to cause a divergence in results. Unfortunately, this implies that the GEV distribution becomes more dispersed with time, leading to greater uncertainty in predictions. Figure B.3 captures this trend.

Model diagnostics were carried out by Goodness-of-Fit tests, the first of which was performed graphically using a Quantile-Quantile (Q-Q) plot (Beirlant et al., 2004, pg 3), followed thereafter by a hypothesis test via a likelihood ratio test (Castillo et al., 2005, pg 243).

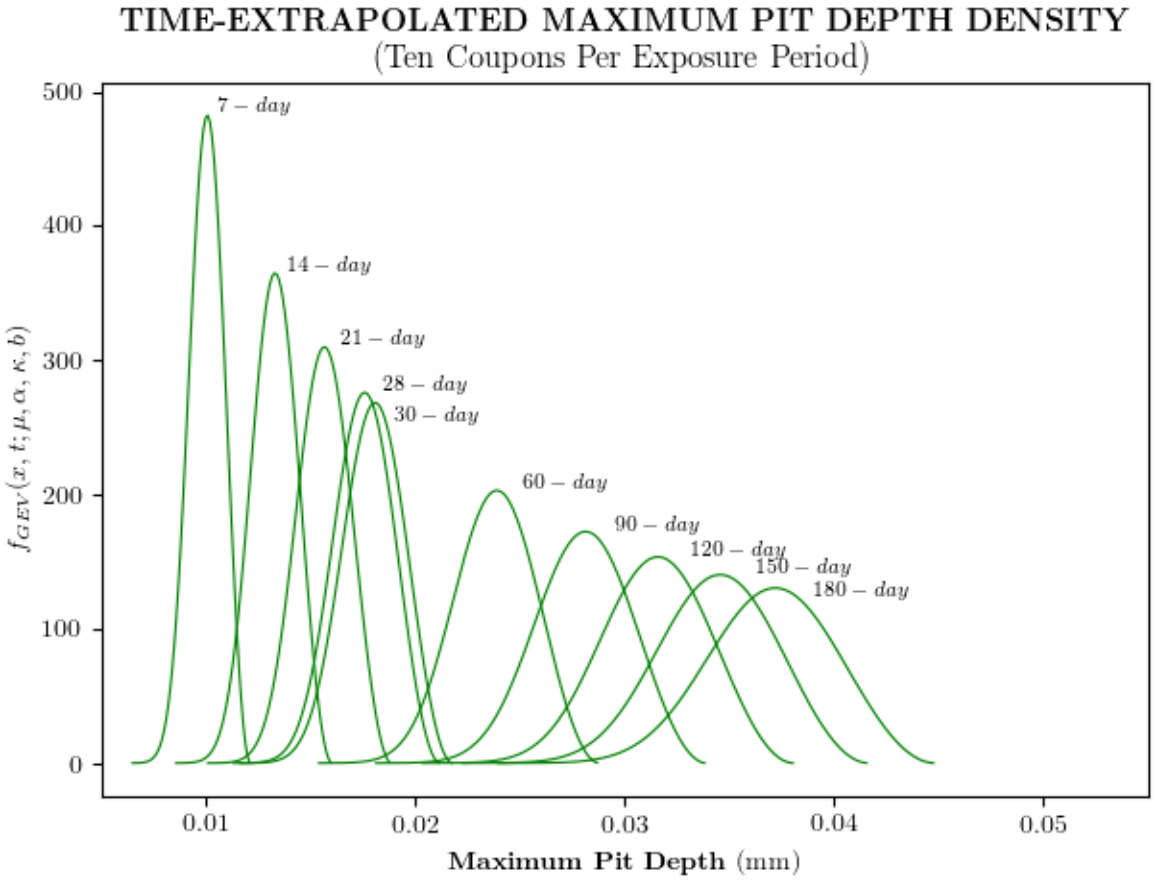

Figure B.3: Maximum pit depth density functions for 304 stainless steel coupons immersed in 3.5 wt% NaCl solution at 30°C Li et al. (2019).

Standard errors were also estimated for $\hat{\mu}, \hat{\alpha}, \hat{\kappa}$ and $\hat{b}$ to further confirm—in particular—that $\hat{\kappa} \neq 0$ (i.e., the rejection of the Gumbel model as a better fit to the data). Model diagnostics are further described and discussed below.

Due to the strict violation of the identically distributed requirement, the data used to fit the non-stationary GEV model needed to be transformed to iid RVs. The two most common options are transformations to the Gumbel or Exponential distributions (see Coles (2001, pg 110) and Beirlant et al. (2004, pg 216)). For this work, the transformation to the standard Exponential distribution is preferred as it naturally leads to the use of the Bootstrap method (Efron and Tibshirani (1994) and Davison and Hinkley (1997)) for the

estimation of parameter standard errors and confidence intervals. The empirical (discontinuous) quantile function of the standard Exponential distribution (Exp(1)) is defined as $\hat{Q}(p_{i,n}) \coloneqq -\ln(1-p_{i,n})$, where the plotting position p is defined as $p_{i,n} \in (0,1); i/(n+1) < p_{i,n} \leq (i+1)/(n+1)$. Other formulations of the plotting position are available, but the most commonly used has been adopted here. To assess if the non-stationary GEV model with the estimated parameters fits the data well via the Q-Q plot, two steps are required. One, the non-stationary GEV model with the estimated parameters is evaluated at the observed pit depths across all exposure periods. Two, the resultant percentiles $GEV(\mathbf{x}, \mathbf{t} \,|\, \hat{\boldsymbol{\theta}}_1)$ are ordered, subsequently transformed into standard Exponential quantiles, defined as $-ln(1-GEV_{i,n})$, where $GEV_{i,n} \in (0,1)$ are the ordered GEV model percentiles, and plotted in the vertical axis of the Q-Q plot. For reasons that will become obvious shortly, let the residual r_i be defined as $r_i \coloneqq -ln(1-GEV_{i,n})$. Subsequently, on the horizontal axis are plotted the empirical quantiles $\hat{Q}(p_{i,n})$ determined from the plotting positions for $GEV_{i,n}$.

Figure B.4 shows the resultant Q-Q plot. Generally, a large majority of the data falls on or is clustered around the 1:1 diagonal, which is a strong indication that the observed data fits the proposed model well despite the fact the data comprises two distinct datasets. Approximately four data points located within the last six transformed quantiles exhibit poor fit, however. Inspection of the data reveals that these are associated with the two deepest maximum pits on days 7 and 180. This result is not too surprising given the trend depicted in Figure B.2. On balance, the Q-Q plot provides strong evidence in favour of the non-stationary GEV model though it offers no information on the Gumbel goodness-of-fit. The likelihood ratio provides this insight.

For the Likelihood Ratio (LR) test, the objective is to test the null hypothesis H_0, which is that the underlying distribution of the maximum pit depths is Gumbel, with $\kappa = 0$ (i.e., $\boldsymbol{\theta}_0 = \{\mu, \alpha, 0, b\}$), against the alternative hypothesis H_1 (i.e., $\boldsymbol{\theta}_1 = \{\mu, \alpha, \kappa, b\}$) that the underlying distribution is GEV, or at least that it is a better fit to the data. Specifically, this test compares the difference in the log-likelihoods evaluated at the proposed parameter vectors:

$$LR = 2\left\{ l(\hat{\boldsymbol{\theta}}_1 \,|\, \mathbf{x}, \mathbf{t}) - l(\hat{\boldsymbol{\theta}}_0 \,|\, \mathbf{x}, \mathbf{t}) \right\}. \tag{B.27}$$

Under suitable regularity conditions and large n, $LR \sim \chi^2$ with 1 degree of freedom, and χ^2 is the Chi-square distribution. The null hypothesis H_0 is rejected at the significance level α if $LR > {\chi_1}^2(1-\alpha)$. For $\alpha = 0.05$, the critical $(1-\alpha)$ quantile of the ${\chi_1}^2$ distribution is 3.8415. Consequently, after re-arrangement of Equation B.27, H_0 is rejected if the differences between the two log-likelihoods is greater than 1.92075, or equivalently $l(\hat{\boldsymbol{\theta}}_0 \,|$

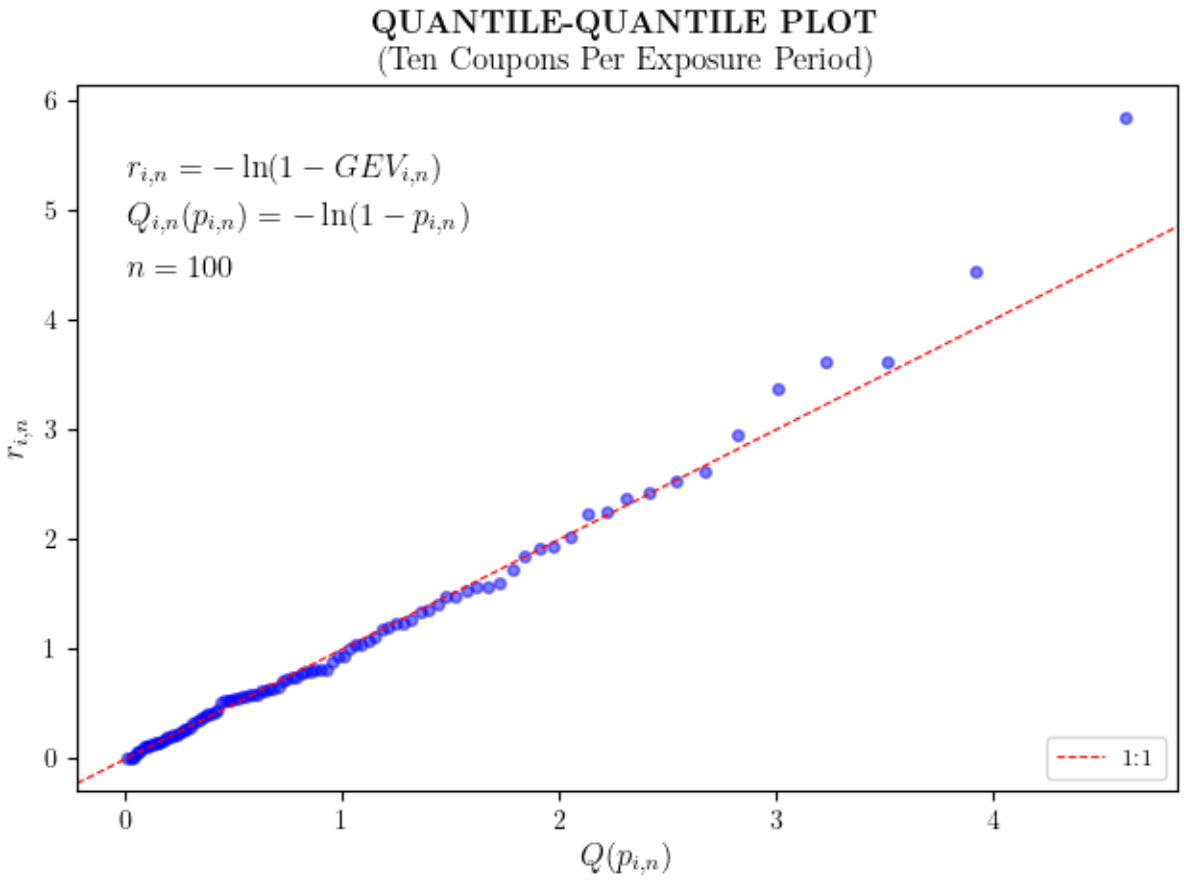

Figure B.4: Quantile-Quantile plot of maximum pit depths fitted to the non-stationary GEV model using the parameter set listed in Table B.1

$\mathbf{x}, \mathbf{t}) < 497.04$. The Gumbel distribution and density functions are

$$Gmbl(x, t \,|\, \mu, \alpha, b) = \exp\left[-\exp\left(\frac{\mu t^b - x}{\alpha t^b}\right)\right], \tag{B.28}$$

$$gmbl(x, t \,|\, \mu, \alpha, b) = \frac{1}{\alpha t^b} \exp\left[-\exp\left(\frac{\mu t^b - x}{\alpha t^b}\right)\right] \exp\left(\frac{\mu t^b - x}{\alpha t^b}\right), \tag{B.29}$$

and the corresponding likelihood and log-likelihood functions are

$$L(\boldsymbol{\theta}_0 \,|\, \mathbf{x}, \mathbf{t}) = \prod_{j=1}^{10} \left\{ \prod_{i=1}^{n_j} \frac{1}{\alpha {t_j}^b} \exp\left[-\exp\left(\frac{\mu {t_j}^b - x_{i,j}}{\alpha {t_j}^b}\right)\right] \exp\left(\frac{\mu {t_j}^b - x_{i,j}}{\alpha {t_j}^b}\right) \right\}, \tag{B.30}$$

$$l(\boldsymbol{\theta}_0 \,|\, \mathbf{x}, \mathbf{t}) = \sum_{j=1}^{10} \left\{ -n_j \ln \alpha - b \sum_{i=1}^{n_j} \ln t_j - \sum_{i=1}^{n_j} \exp\left[-\left(\frac{x - \mu t^b}{\alpha t^b} \right) \right] - \sum_{i=1}^{n_j} \left(\frac{x - \mu t^b}{\alpha t^b} \right) \right\} \tag{B.31}$$

Point estimates of the Gumbel parameters were determined in three steps. First, the Probability Paper Plot method (see Castillo et al. (2005, pg 141)) was employed to obtain stationary Gumbel model initial parameter estimates for each exposure period. Essentially, this method transforms the Gumbel distribution function into a linear form, which allows plotting and subsequent estimation of parameters from the slope and intercept derived from a linear regression fit to the plotted data. The result of this analysis is a 10-element vector of stationary parameter estimates. Second, as with the GEV model fitting, fitting a power-law to the elements of the μ and α vectors with time led to both an initial estimate of μ_0 and α_0 from the respective coefficients of the power-law fit and an estimate of b_0 based on the average of the exponential terms of the power-law fits. The last step involved modifying the Python script to minimise numerically the negative of the log-likelihood function, Equationn B.31, based on the initial estimates $(0.0475, 0.0031, 0.3947)$ for $\mu_0, \alpha_0,$ and b_0, rounded to four decimal points. On average, algorithm convergence occurred in fraction of a second; and the results, listed in Table B.2, are strikingly similar to those shown in Table B.1. However, at a 5% level of significance, there is sufficient evidence to reject the null hypothesis H_0; that is, $l(\hat{\boldsymbol{\theta}}_0 \,|\, \mathbf{x}, \mathbf{t}) = 487.01 < 497.04$. Altogether, the observed data better supports the GEV model over the Gumbel.

Table B.2: Gumbel Likelihood Function Parameters, Equation B.30

$\hat{\mu}$	$\hat{\alpha}$	$\hat{b}$	$l(\hat{\boldsymbol{\theta}}_0 \,\|\, \mathbf{x}, \mathbf{t})$
0.0477146	0.00408946	0.4084677	487.01

The final steps in model diagnostics involved estimating the standard error and confidence intervals for $\hat{\boldsymbol{\theta}}_1$. Although these have already been presented in Table B.1 (without discussion), the application of the Bootstrap method to estimate confidence intervals or standard errors for the non-stationary GEV model parameters requires the same transformation to the data as with the method applied to generate the Q-Q plot. However, this transformation is extended one step further to simplify the sampling process. For example, the Boostrap method involves sampling the original data with replacement. For the non-stationary GEV model, the data is not iid, and the transformation $-ln(1 - GEV_{i,n})$, which results in a quantity that is independent and identically $\sim$ Exp(1), is required before

sampling can take place. As before, let $r_i \coloneqq -ln(1 - GEV_{i,n})$, then

$$\begin{aligned} r_i &= -ln(1 - GEV_{i,n}) \\ e^{-r_i} &= 1 - GEV_{i,n} \\ GEV_{i,n} &= 1 - e^{-r_i} \\ \ln GEV_{i,n} &= \ln\left(1 - e^{-r_i}\right) \\ \left[1 - \kappa\left(\frac{x_{i,n} - \mu t^b}{\alpha t^b}\right)\right]^{\frac{1}{\kappa}} &= -\ln\left(1 - e^{-r_i}\right). \end{aligned} \tag{B.32}$$

Equation B.32 informs the reader that the expression to the left of the equal sign is also $\sim$ Exp(1)—a conclusion arrived at by considering the definition of a Cox-Snell residual. Briefly, from classical survival analysis the cumulative hazard function $H(t)$ is the negative of the natural logarithm of the survival function $S(t)$, or reliability function $R(t)$, given by $1 - F(t)$, where $F(t)$ is the cumulative distribution function of an arbitrary RV T. Cox and Snell (1968) showed that values for $H(t)$, referred to as Cox-Snell residuals ϵ, may be considered as originating from censored samples, exponentially distributed with parameter equal to 1 (i.e., $H(t) \sim \text{Exp}(1)$). Subsequently, it should become apparent to the reader that F, where $F \coloneqq e^{-r_i}$ is the same as GEV, and consequently the Cox-Snell residual $\epsilon_{i,j}$[6] may be defined as

$$\epsilon_{i,j}(\mathbf{x}, \mathbf{t} \,|\, \boldsymbol{\theta}_1) = \left[1 - \kappa\left(\frac{x_{i,j} - \mu t_j^b}{\alpha t_j^b}\right)\right]^{\frac{1}{\kappa}}. \tag{B.33}$$

Sampling of $\epsilon_{i,j}$, with replacement and with $\boldsymbol{\theta}_1$ replaced by $\hat{\boldsymbol{\theta}}_1$, permits estimation of parametric Bootstrap standard errors and confidence intervals. The basic procedure (Brown et al., 2008; Cannon, 2010; Davison and Ramesh, 2000; Katz et al., 2002; Khaliq et al., 2006; Kharin and Zwiers, 2005; Panagoulia et al., 2014) is as follows:

1. Transform the maximum pit depth data $x_{i,j}$ into time-corresponding Cox-Snell residuals as per Equation B.33.

2. Sample randomly with replacement from $\epsilon_{i,j}$, while keeping track of the exposure period t_j to obtain a Boostrap sample of residuals $\epsilon_{i,j}^{bs}$

[6]The reader should also note that the ordered Cox-Snell residuals and corresponding plotting positions could also have been implemented in the Q-Q plot since $\epsilon_{i,j} \sim$Exp(1).

3. Transform the Bootstrap sample of residuals $\epsilon_{i,j}^{bs}$ into corresponding Bootstrap maximum pit depths $x_{i,j}^{bs}$ according to the expression in Equation B.34.

4. Fit the non-stationary GEV model to the Bootstrap maximum pit depths $x_{i,j}^{bs}$ and store the estimated model parameters $(\hat{\mu}_{bs}, \hat{\alpha}_{bs}, \hat{\kappa}_{bs}, \hat{b}_{bs})$.

5. Repeat steps 2-5 for the desired number of repetitions.

The transformed maximum pit depths are obtained by re-arranging Equation B.33 to isolate $x_{i,j}$ and using the initial GEV model parameters $\hat{\boldsymbol{\theta}}_1$:

$$x_{i,j}^{bs} = \hat{\alpha} t_j^{\hat{b}} \frac{\left(1 - \epsilon_{i,j}^{\hat{\kappa}}\right)}{\hat{\kappa}} + \hat{\mu} t_j^{\hat{b}}. \tag{B.34}$$

For this work, $j \times n_j = 100$ random samples were drawn with replacement from $\epsilon_{i,j}$, with $10^2, 10^3,$ and 10^4 repetitions. For comparison, stratified sampling was also employed to ensure equal representation from each block. To ensure sufficient coverage of the estimated model parameters by the numerical minimisation algorithm (and to assure oneself of validating the preceding model diagnostic results), the bounds for all parameters were broadened, particulary κ, whose closed interval was revised to $[-0.1, 0.8]$. Standard errors were determined by calculating the standard deviation of the respective parameter Bootstrap sampling distribution. Two approaches were employed for estimating the 95% confidence intervals; namely, the simple percentile method of ordered Bootstrap parameters (i.e., lower $L_{\alpha/2}$, upper $U_{1-\alpha/2}$), and the "basic Bootstrap" confidence interval, which is $[2\hat{\boldsymbol{\theta}}_1 - U_{1-\alpha/2}, 2\hat{\boldsymbol{\theta}}_1 - L_{\alpha/2}]$. As will be seen shortly in the resultant sampling distributions, the need to employ more "accurate" confidence interval estimation methods, such as *Studentized* and *bias-corrected and accelerated*, was unwarranted; that is, it was clear that improving the accuracy of the estimated intervals would not alter the conclusion concerning the validity of the parameter estimates—especially the rejection of the null hypothesis H_0.

As a simple visual check against the statement that $\epsilon_{i,j} \sim \text{Exp}(1)$, a histogram of $\epsilon_{i,j}$ is plotted along with the standard Exponential density function (i.e., $f_{\text{Exp}}(\epsilon_{i,j}) = e^{-\epsilon_{i,j}}$), Figure B.5. The resultant histogram closely resembles the standard Exponential density function, confirming the Cox-Snell assertion. While this can be more formally evaluated with the Anderson-Darling goodness-of-fit test (Anderson, 2011; Anderson and Darling, 1954; Stephens, 1986), it is not critical to do so for the objective at hand. The Anderson-Darling goodness-of-fit test will be utilised later for assessing thresholds in the GPD assessment. Figures B.6-B.9 illustrate respectively the parametric Bootstrap sampling distributions for

$\hat{\mu}, \hat{\alpha}, \hat{\kappa},$ and $\hat{b}$, for 10,000 repetitions, which was sufficient to achieve stable estimates for standard errors and confidence intervals. Similar results were obtained for stratified sampling. However, stratified sampling led to slightly smaller standard errors and narrower confidence intervals and was not pursued further. Most critical to model diagnostic is the sampling distribution for $\hat{\kappa}$, which clearly confirms that the data does not support the Gumbel distribution. Overall, there is strong confidence in the fit and resultant parameters, allowing for sufficient assurance to proceed with the balance of the modelling efforts in this thesis (i.e., GPD, NHPP, and NHMP), which are highly dependent on the validity of the GEV model.

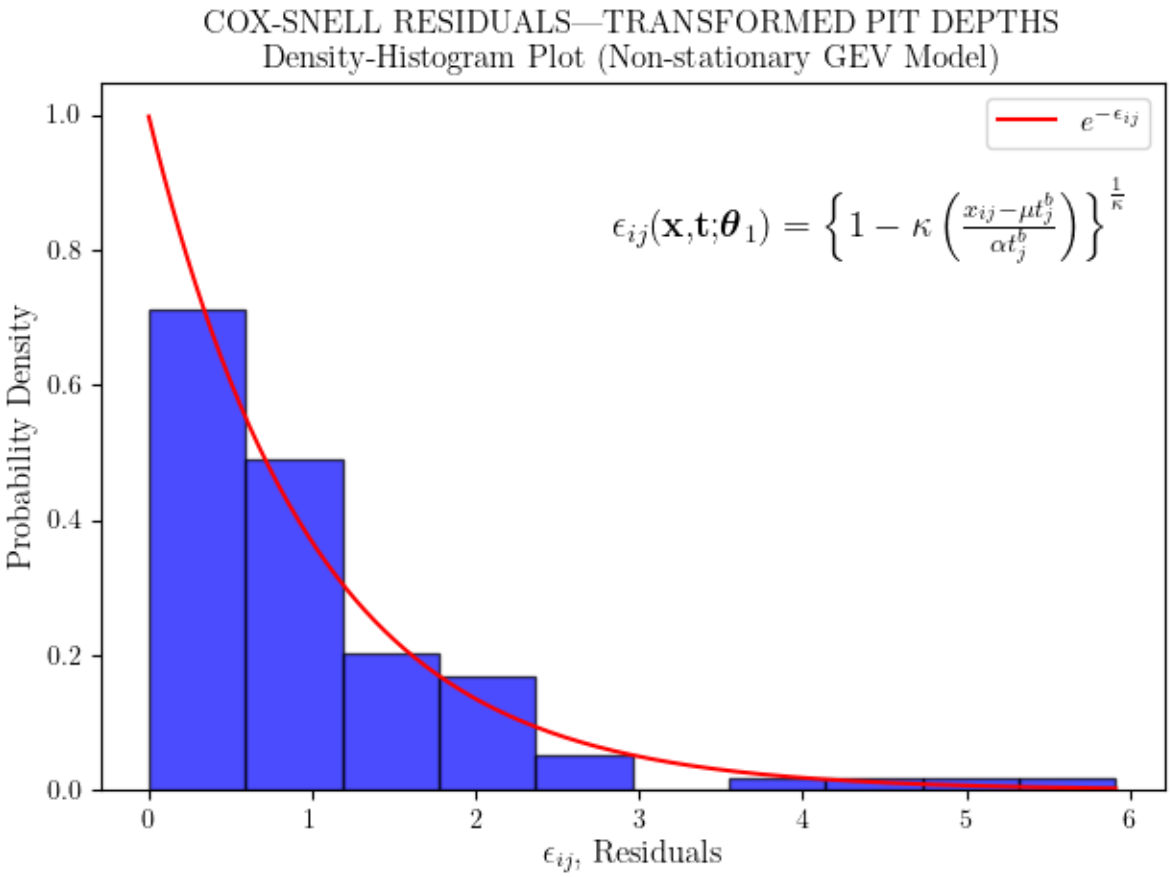

Figure B.5: Plot of Cox-Snell residuals for the maximum pit depths fitted to the non-stationary GEV model using the parameter set listed in Table B.1

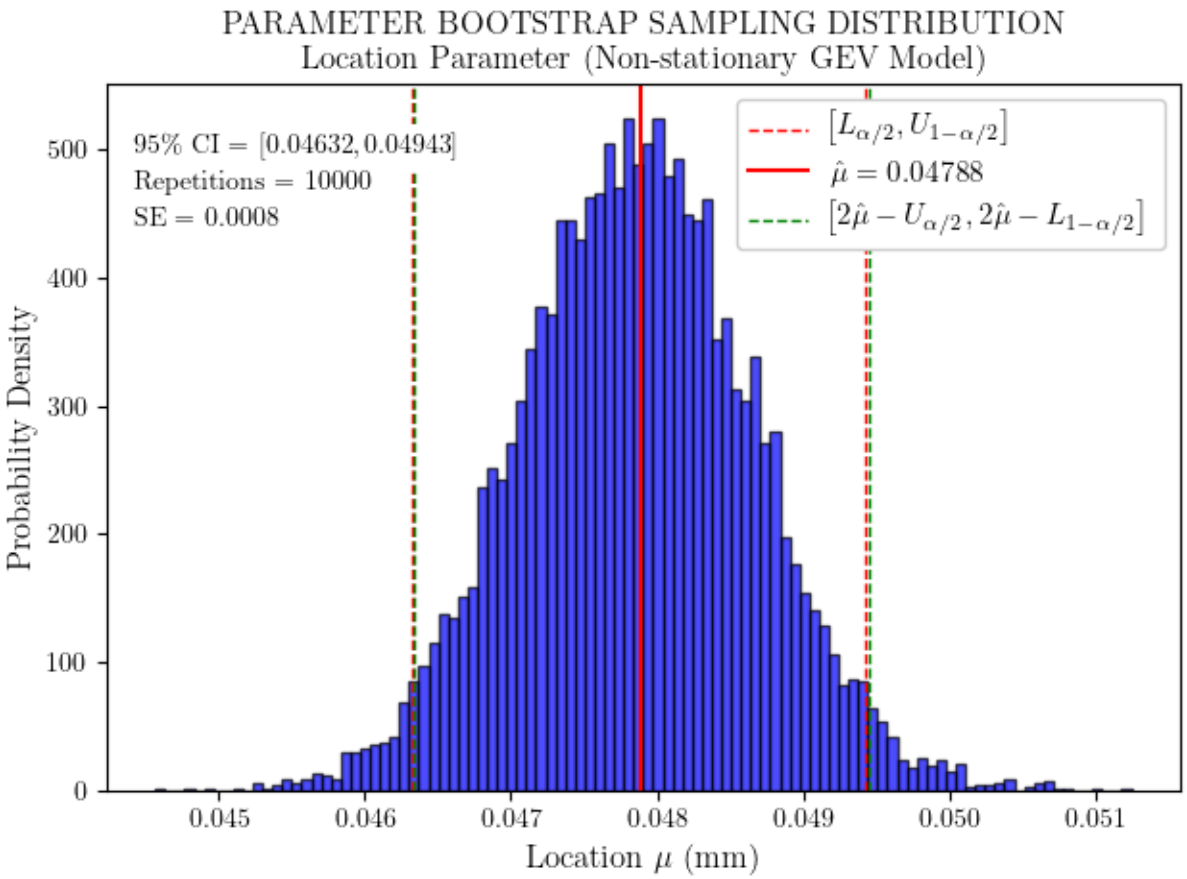

Figure B.6: Bootstrap sampling distribution for the non-stationary GEV model location parameter $\hat{\mu}$. Included in the plot as vertical dashed lines are the percentile and "basic Bootstrap" 95% confidence intervals, with the numerical values of the former also listed in the plot.

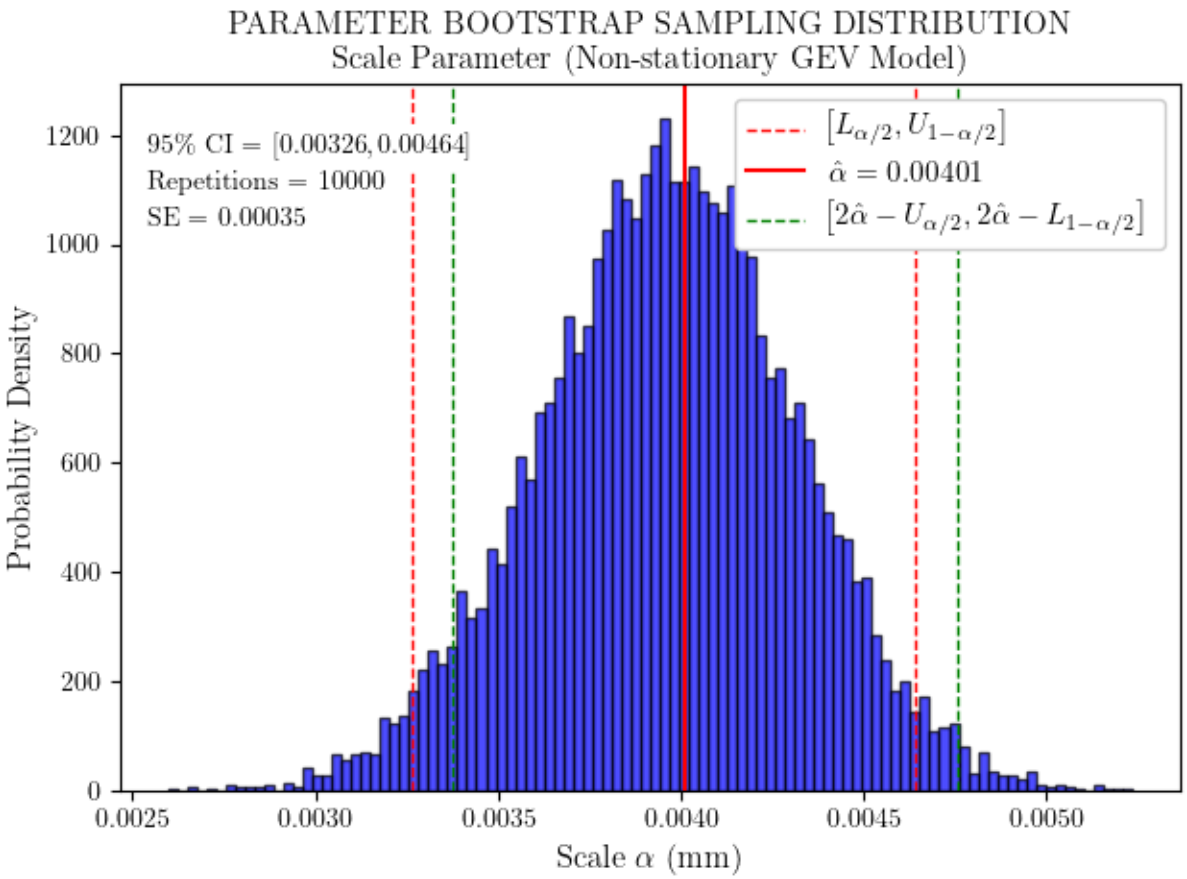

Figure B.7: Bootstrap sampling distribution for the non-stationary GEV model scale parameter $\hat{\alpha}$. Included in the plot as vertical dashed lines are the percentile and "basic Bootstrap" 95% confidence intervals, with the numerical values of the former also listed in the plot.

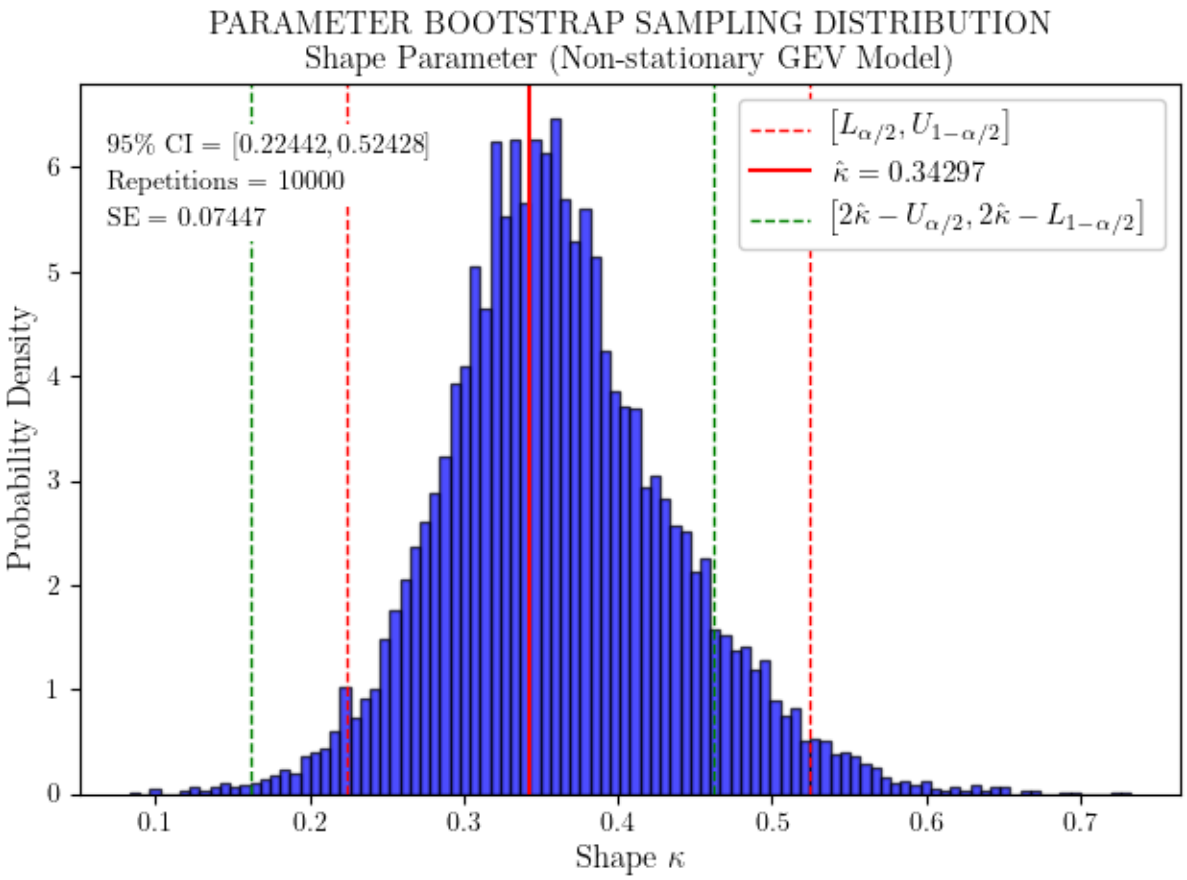

Figure B.8: Bootstrap sampling distribution for the non-stationary GEV model scale parameter $\hat{\kappa}$. Included in the plot as vertical dashed lines are the percentile and "basic Bootstrap" 95% confidence intervals, with the numerical values of the former also listed in the plot.

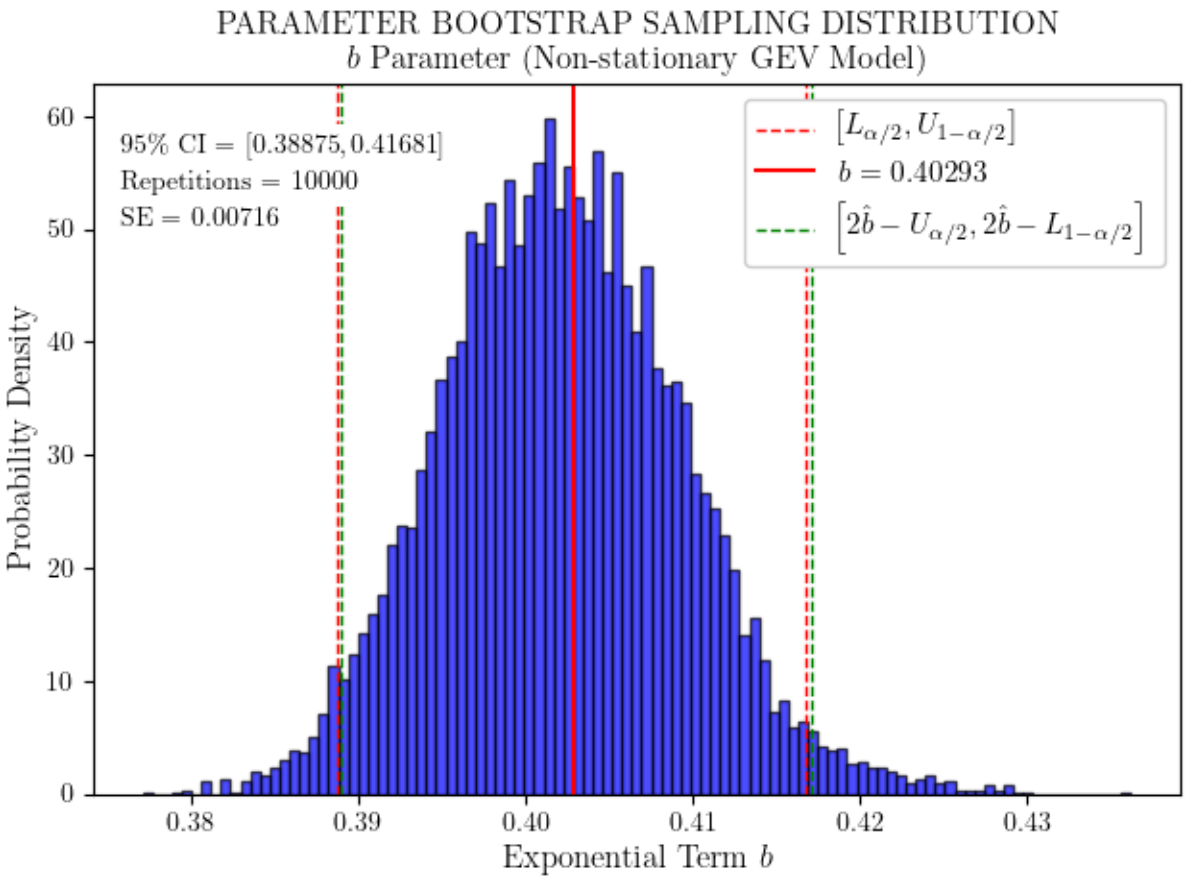

Figure B.9: Bootstrap sampling distribution for the non-stationary GEV model time exponential parameter $\hat{b}$. Included in the plot as vertical dashed lines are the percentile and "basic Bootstrap" 95% confidence intervals, with the numerical values of the former also listed in the plot.

B.4.3 Extrapolation in Time and Space

Size effect is an important step in the transfer of experimental results derived from small coupons to real structures. This concept, however, is not new, and has been in practice for quite some time but in the context of a return period (e.g., Shibata, 1994). Here, size effect is applied directly to the limiting distribution of the maximum over M units of area. Subsequently, the GEV distribution, Equation B.8, is modified following the approach in Laycock et al., 1990 and Scarf, 1993, as show in Equation B.35, which leads to the corresponding density function, Equation B.36. The size effect, typically labelled M, is the ratio of the UFC surface area to the corrosion coupon area and is approximately equal to 251.

$$\left(GEV(x,t;\theta_1)\right)^M = \left\{ \exp\left\{ -\left[1-\kappa\left(\frac{x-\mu t^b}{\alpha t^b}\right)\right]^{\frac{1}{\kappa}} \right\} \right\}^M \tag{B.35}$$

$$f(x,t;\mu_M,\alpha_M,\kappa,b,M) = \frac{M^\kappa}{\alpha t^b}\left[1-\kappa\left(\frac{x-\mu_M}{\alpha_M}\right)\right]^{\frac{1}{\kappa}-1} \exp\left\{ -\left[1-\kappa\left(\frac{x-\mu_M}{\alpha_M}\right)\right]^{\frac{1}{\kappa}} \right\} \tag{B.36}$$

Where the re-parametrisation of the location and scale parameters as μ_M and α_M is:

$$\mu_M = \mu t^b + \frac{\alpha t^b}{\kappa}\left[1-M^{-\kappa}\right] \tag{B.37}$$

$$\alpha_M = \alpha t^b M^{-\kappa} \tag{B.38}$$

Figure B.10 shows the UFC-area-extrapolated maximum pit depth with time. Also shown is the expected maximum for the area-extrapolated maximum pit depths, which is based on Equation B.39. The size-effect significantly reduces the variance Equation B.40 of the area-extrapolated density, noted most prominently when Figure B.11 and Figure B.3 are compared.

$$E\left[M_n\right]_M = \mu t^b + \frac{\alpha t^b}{\kappa} - \frac{\alpha t^b M^{-\kappa}}{\kappa}\Gamma(1+\kappa); \kappa > -1 \tag{B.39}$$

$$\sigma\left(M_n\right)_M = \frac{\alpha t^b M^{-\kappa}}{\kappa}\left\{\Gamma(1+2\kappa) - \left[\Gamma(1+\kappa)\right]^2\right\}^{1/2}; \kappa > -\frac{1}{2} \tag{B.40}$$

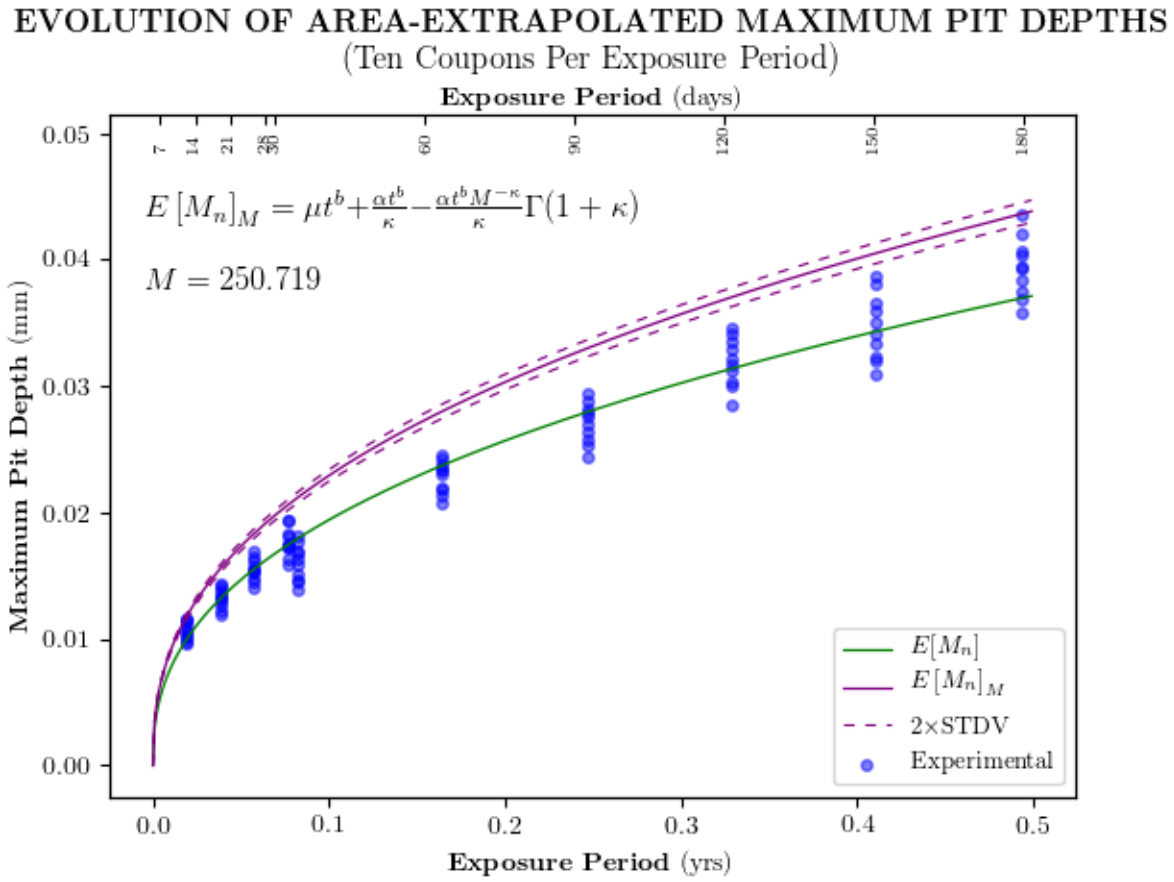

Figure B.10: Maximum pit depths versus time for 304 stainless steel coupons immersed in 3.5 wt% NaCl solution at 30°C Li et al. (2019). Extrapolation to UFC surface area included.

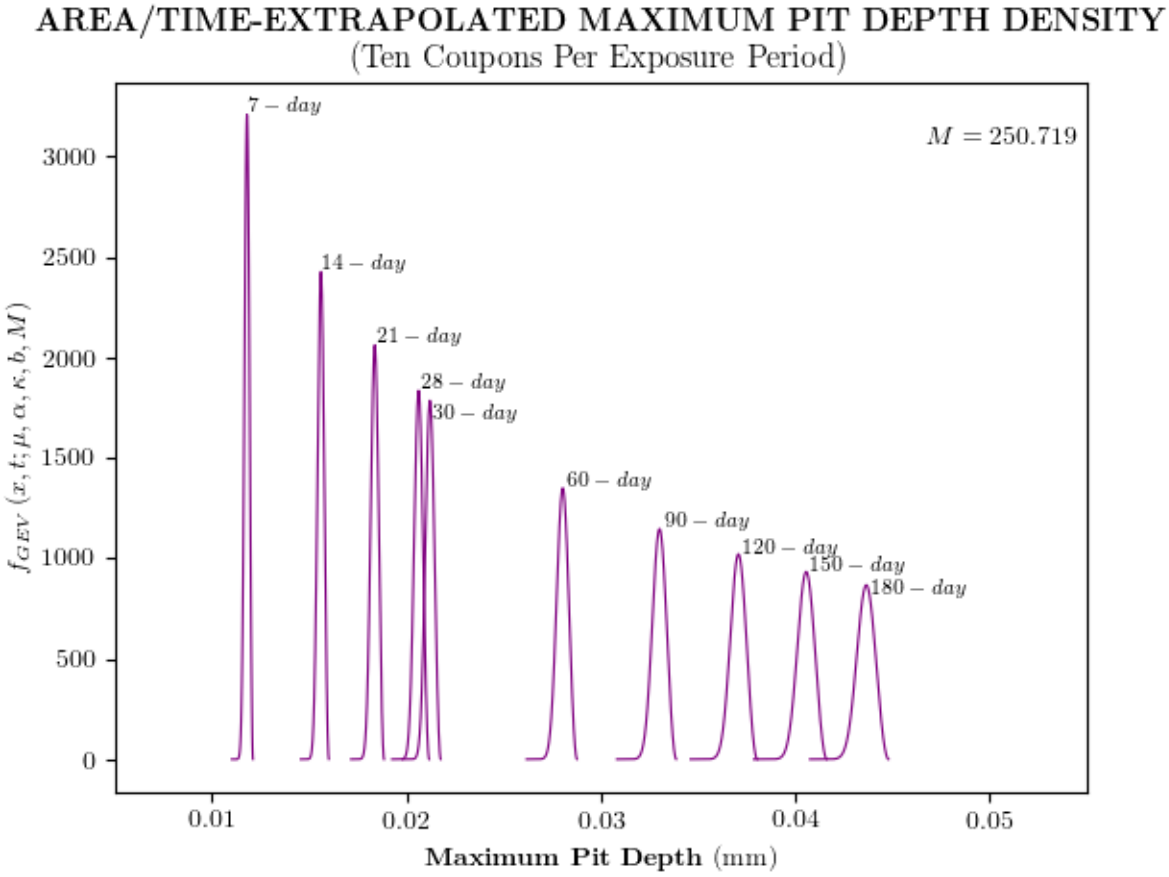

Figure B.11: Maximum pit depth density functions for 304 stainless steel coupons immersed in 3.5 wt% NaCl solution at 30°C Li et al. (2019). Extrapolation to UFC surface area included.

B.4.4 Algorithm to Assign Maximum Pit Depths

The basic approach to assign a random maximum pit depth to each discretised panel on the UFC is to sample from the appropriate time-and-space-extrapolated GEV density function (e.g., Figure B.11). The underlying assumption is that in the future, data similar to the one employed in this work will be generated for copper under relevant repository conditions over timescales that, ideally, permit either interpolation (i.e., bound the expected oxic period) or

at most some level of extrapolation (i.e., outside the timescales of the experiment) without necessarily introducing significant uncertainty.

Consequently, the algorithm receives as input the timescales for the early, dry oxic period where pitting corrosion is considered a potential degradation mechanism. For simplicity, this could be represented by a time vector, T, covering the minimum and maximum timescales t_{min}, t_{max} anticipated (i.e., $T = [t_{min}, t_{max}]$). Additional inputs include the total number of panels on the UFC, which represent the number of samples to draw randomly from the appropriate time-and-space-extrapolated GEV density function, and the distribution of the initial copper coating thickness. The copper coating thicknesses are log-normally distributed (i.e., $f_{t_{\mathrm{Cu}}} \sim$ Lognorm)).

Presently, because of both symmetry and the location on the UFC surface anticipated to sustain the greatest sulphide flux, the UFC lifetime model (Järvine et al., 2019, 2020) simulates sulphide corrosion for only one quarter of one of the UFC hemispherical end-caps. For the 0.06-m mesh size, the quarter hemispherical end-cap is discretised into $m = 255$ panels.

In words, the algorithm samples randomly m maximum pit depths from the GEV distribution extrapolated in both times t_{min}, t_{max} and space M, where $M \approx 251$ is the ratio of the UFC quarter hemispherical end-cap area to the corrosion coupon area. The sampling generates two arrays of maximum pit depths ($D_{tmin}, D_{t_{max}}$), one for each time segment. The algorithm then samples randomly m thicknesses from the initial copper coating thickness distribution, creating an array of thicknesses. A new array is created by subtracting from the copper coating thickness array the maximum pit depths. This is done twice, once for each time segment, to generate two modified initial copper coating thickness arrays, which would then be fed into the rest of the original UFC lifetime code for continued processing (not shown here). The algorithm is summarised in Algorithm 5.

Algorithm 5 Max Pit Depth Assignment—GEV

Require: $T, M, m, f(x, t; \mu_M, \alpha_M, \kappa, b, M), f_{t_{\mathrm{Cu}}} \sim Lognorm$

Initialise variables, arrays: $t, D_{t_{min}}, D_{t_{max}}, Cu, Cu_{t_{min}}, Cu_{t_{max}}$
$Cu \leftarrow$ sample randomly m thicknesses from $f_{t_{\mathrm{Cu}}}$
for t_i in T **do**
    $f(\theta_M) \leftarrow f(x, t_i; \mu_M, \alpha_M, \kappa, b, M)$
    if $t_i == min(T)$ **then**
        $D_{t_{min}} \leftarrow$ sample randomly m maximum pit depths from $f(\theta_M)$
        $Cu_{t_{min}} \leftarrow Cu - D_{t_{min}}$
    else
        $D_{t_{max}} \leftarrow$ sample randomly m maximum pit depths from $f(\theta_M)$
        $Cu_{t_{max}} \leftarrow Cu - D_{t_{max}}$

Appendix C

Peaks-Over-Thresholds

The objective of this appendix is to provide the mathematical details governing the fitting of the GPD, within a POT framework, to pit depth exceedances. Particular attention is given to the methodology applied to select appropriate pit depth thresholds, as this is critical to the validity of the stochastic process model developed in Chapter 5. The excellent agreement obtained with GEV distribution parameters further strengthens support of the methodologies adopted.

C.1 GPD within a POT Framework

The GPD in the POT framework is used to model excesses or exceedances over a threshold u, and like the GEV distribution it represents the family of generalised Pareto distributions. It can be shown (Pickands, 1975) that when u is large (i.e., near the upper end of the distribution of a RV X) those realisations of X that exceed u follow a GPD. In other words, the distribution function of $(X-u)$, conditional on $X > u$, is approximately that shown in Equation C.1. Formally, all $X \geq u$ are referred to as exceedances and $(X-u)$ as excesses. The immediate implication is that if the block maxima for X follow approximately the limiting GEV distribution, then the exceedances over a large enough threshold follow approximately the limiting GPD (see Castillo et al., 2005, pg 263; and Coles, 2001, pg 75). This also means that, other than u, the GPD parameters are equivalent to those determined by fitting the GEV distribution. Consequently, the parameters of the GPD are the location μ, scale α, and shape κ parameters from the GEV distribution, Table B.1. Since for the current data $\kappa > 0$ (see Table B.1), the primary constraints applied to Equation C.1 are $\alpha^* = \alpha - \kappa(u-\mu) \geq 0$ and $1 - \kappa(x-u)/\alpha^* \geq 0$. Here, the random variable X is the

observed pit depth within a block, and $X > u$. As with the fitting of Equation B.8 for block maxima, a GPD model is fit to data by pooling together all blocks per exposure period (see Figure B.1).

$$GPD(x \mid \mu, \alpha, \kappa, u) = \left\{ 1 - \left[1 - \kappa \frac{(x-u)}{\alpha^*} \right]^{1/\kappa} \right\}; \kappa \neq 0, \alpha* \geq 0, 1 - \kappa \frac{(x-u)}{\alpha^*} \geq 0, \quad \text{(C.1)}$$

$$\alpha^* = \alpha - \kappa(u - \mu). \quad \text{(C.2)}$$

C.2 Extrapolation in Time

The re-parametrisation of Equation C.1 with time as covariate follows the same formulation as that for maximum pit depth (i.e., Equation B.8). The challenge with the GPD model, however, is the proper selection of a threshold, which often begins with a trade off between model bias and variance. (This is also true for the GEV, but in the current work the number of blocks, which govern bias and variance, were already fixed by Li et al. (2019)). Low thresholds result in the realisation of many exceedances that can compromise the validity of the asymptotic assumptions intrinsic to the limiting GPD, leading to bias in the model estimates. With larger thresholds, however, there is stronger support for the asymptotic assumptions, but the result is a reduced number of exceedances and an increased variance in the model estimates (i.e., higher estimate uncertainty). The challenge is compounded when the threshold are time variant and the form of the threshold expression when parametrised with time needs to be adequately defined.

Generally, expert judgment is often the default approach to selecting a threshold level. In lieu of a subject matter expert, such as in the present case, the literature presents several methodologies for determining threshold levels. The more classical approach is the graphical method or the assessment of a Mean Residual Life (MRL) plot (also referred to as mean excess plot), popularised by Coles (2001), Davison and Smith (1990), and Smith (2003), but underpinned by the work of Hall and Wellner (2017) and Yang (1978). The other approach is loosely divided in two camps. The first performs a sequential, point-wise goodness-of-fit test (e.g., Bader et al., 2018; Choulakian and Stephens, 2001). The second, with increasing complexity, performs threshold diagnostics (e.g., Northrop and Coleman, 2014; Wadsworth, 2016; Wadsworth and Tawn, 2012). And of course, there are many variants on these approaches.

The MRL plot was chosen for this study as a base estimator of appropriate thresholds. To this was added a sequential, point-wise goodness-of-fit test with the Anderson-Darling

(Anderson, 2011; Anderson and Darling, 1954; Stephens, 1986) test statistic AD^2 to validate independently MRL plot threshold estimates. Lastly, in anticipation of the Non-homogeneous Poisson Point Process (NHPPP) approach (Appendix D), two additional assessments were included. One, thresholds must be greater than the lower endpoints of the limiting GEV distribution. Two, thresholds must satisfy the requirement that when x is replaced by u in $\Lambda(x)$ (Equation D.2), $V(u)$ is a finite-valued, non-negative, non-decreasing function of time.

C.3 Mean Residual Life Plot

Briefly, the MRL plot is a graphical means to assess the existence of an empirical, linear relationship between the expected value of $(X - u)$, given $X > u$ and u (Smith, 1994), as implied by the $-\kappa/(1 + \kappa)u$ term in Equation C.3:

$$E[X - u|X > u] = \frac{\alpha^*}{1 + \kappa} = \frac{\alpha - \kappa(u - \mu)}{1 + \kappa}. \tag{C.3}$$

In practice, due to the extent of scatter typically observed in the MRL plot, one simply looks for a region where there is a trend in the data that reasonably resembles a straight line (Smith, 1994), and one subsequently chooses the minimum threshold in that range. While the slope in the straight-line region of the MRL plot can be used to estimate κ (e.g., Castillo et al., 2005, pg 281), scatter in the data makes this estimate unreliable (Smith, 2003, pg 24). One does, however, confirm visually that the sign of the slope and that of the estimated κ (per exposure period) agree.

Figure C.1 provides an example of an MRL plot for the corrosion pit depth data after seven days of exposure. Approximate, symmetrical 95% confidence intervals are included under the assumption that means are normally distributed. Confidence intervals can also be estimated with a point-wise bootstrap approach (e.g., Smith, 2003, pg 24), but there was no obvious advantage to doing so for the objective at hand. To the untrained eye, a linear trend could be discerned from the lowest threshold (i.e., $u = 0.005$ mm) to approximately $u = 0.0085$ mm. However, this range can be divided into several subregions with different slopes, and one would need to decide which subregion is the correct one. If one were to pick an intermediate subregion within this range, thereby rejecting preceding and ensuing subregions, this would contradict one of the attractive properties of the GPD, which is that it is stable with respect to truncations from the left (see Castillo et al., 2005, pg 263). This means that if u_0 leads to the GPD being a valid model for the data (i.e., $(X - u_0) \sim$

$GPD(\alpha - \kappa(u_0 - \mu), \kappa))$, then for $u_1 > u_0$ $GPD(\alpha - \kappa(u_1 - \mu), \kappa)$ would also be a valid model. Based on this, it is better to identify a linear trend in the data by working from the right to the left of the MRL plot. Data points at the right end of the MRL plot will exhibit significant variability simply because of the limited number of data points. As one moves further to the left in the plot, the variability decreases, and one looks for the first consistent linear trend. In Figure C.1, this linear trend region occurs approximately in the range 0.009 mm to 0.010 mm.

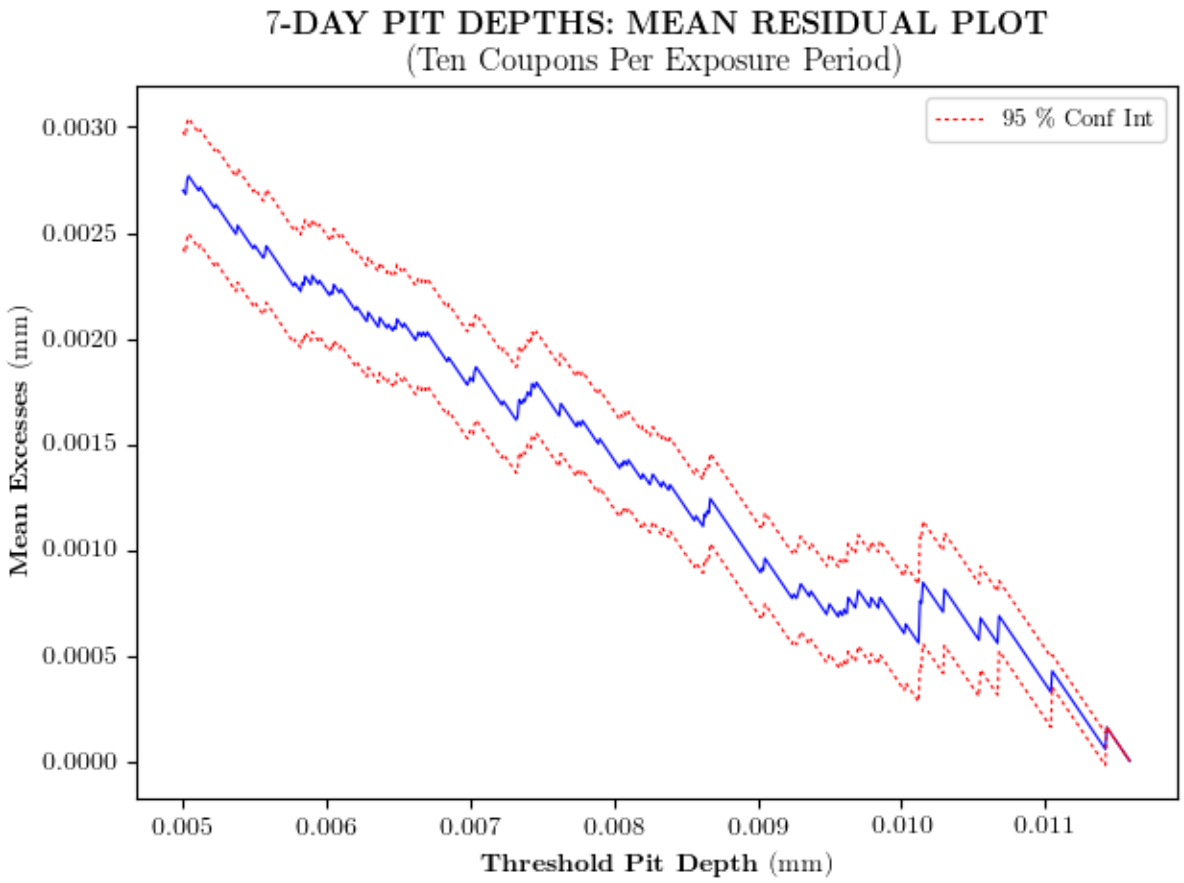

Figure C.1: Mean residual life plot for the 7-day exposure period pit depths

For the current analysis, four threshold levels, labelled *low*1, *low*2, *med*, and *high*, were selected arbitrarily within the linear region identified above. The reasonableness of the four threshold levels was assessed qualitatively by fitting the GPD to the excesses, using

α^* in the unexpanded form, and gauging the goodness of fit with both a Q-Q plot and a histogram of excesses overlaid with the density function of the GPD. Examples of Q-Q and density histogram plots for the "$low1$" thresholds, seven days of exposure, are displayed in Figure C.2 and Figure C.3, respectively. Good agreement between model predictions and observed quantiles (typified by a locus of points lying along the 45° line) in the Q-Q plot and the relative capture of the trend in the histogram by the model density function suggest that the "$low1$" threshold $u = 0.009$ mm is reasonable. The aforementioned methodology was repeated for the rest of the exposure periods, leading to a set of potential threshold levels, Table C.1.

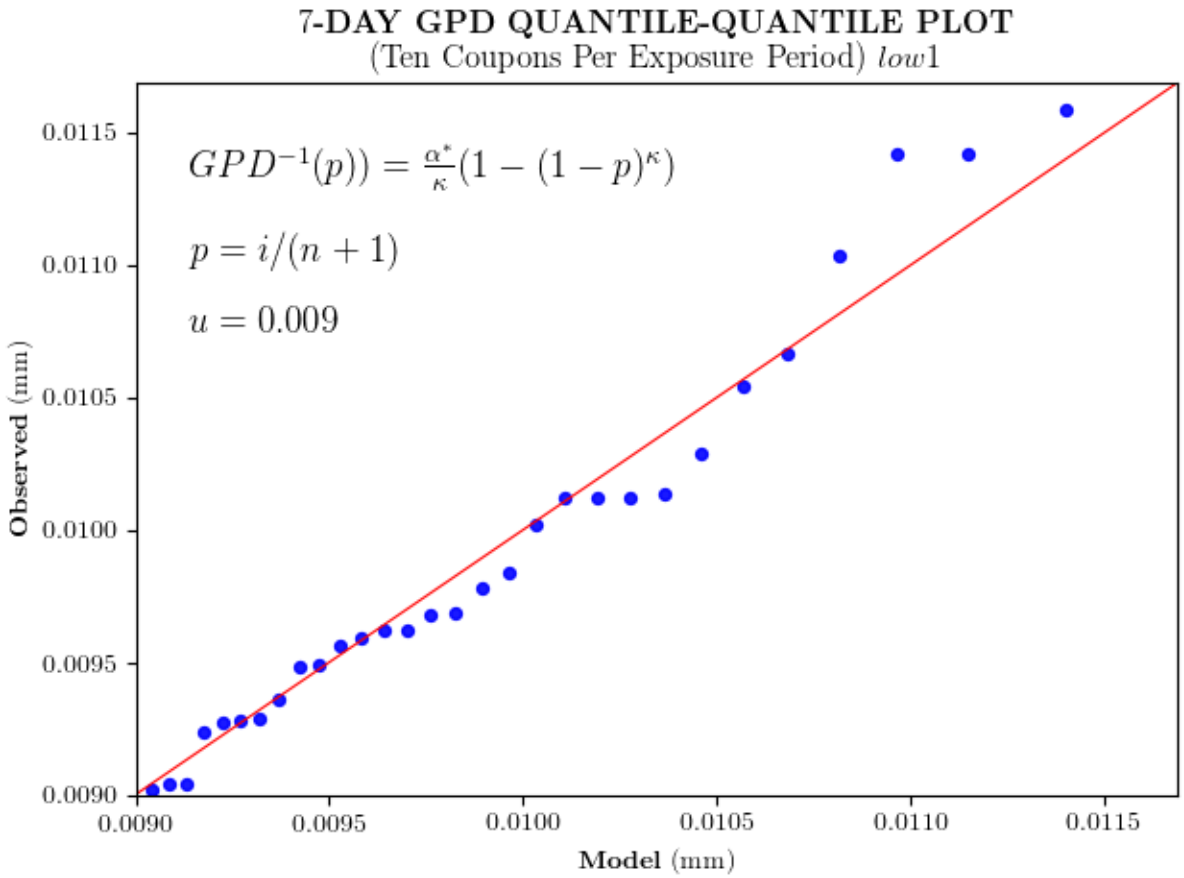

Figure C.2: Quantile-Quantile plot for the 7-day exposure period pit depths ($low1$)

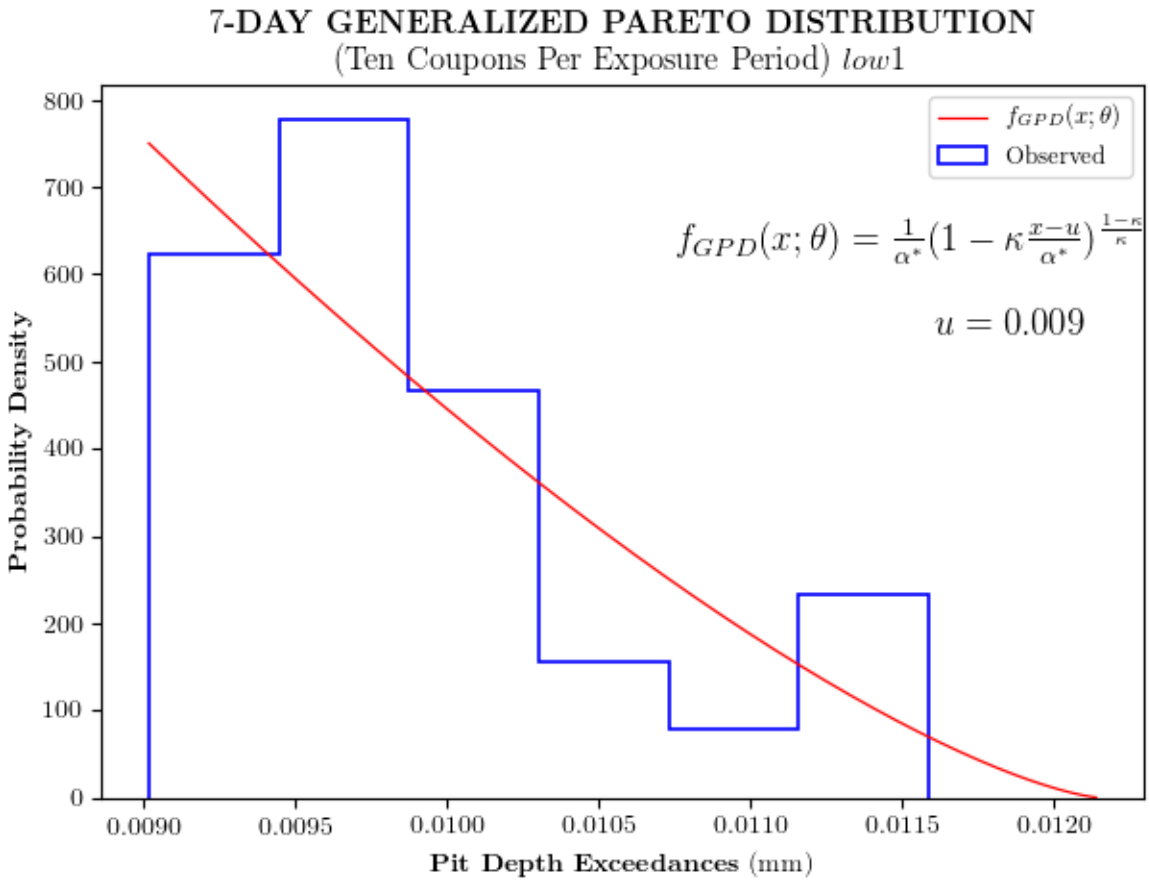

Figure C.3: Density-histogram for the 7-day exposure period pit depths ($low1$)

C.3.1 Sequential Goodness-of-Fit Tests

Mean residual life plots suffer from a high degree of subjectivity and those generated in this study are no exception. To underpin the proposed threshold levels presented in Table C.1, sequential, point-wise goodness-of-fit tests were conducted using the Anderson-Darling statistic AD^2 for the null hypothesis that Cox-Snell residuals are exponentially distributed with rate parameter $\lambda = 1$. Recall, from classical survival analysis the cumulative hazard function $H(t)$ is the negative of the natural logarithm of the survival function $S(t)$, or reliability function $R(t)$, given by $1 - F(t)$, where $F(t)$ is the cumulative distribution function of an arbitrary RV T. Cox and Snell (1968) showed that values for $H(t)$, referred to as Cox-Snell residuals ϵ, may be considered as originating from censored samples, exponen-

Table C.1: Mean Residual Life Plot Threshold Levels

Exposure Period (days)	*low*1[1]	*low*2	*med*	*high*
7	0.009	0.00901	0.0091	0.0092
14	0.0125	0.012505	0.0126	0.0127
21	0.0138	0.0141	0.0144	0.0148
28	0.0155	0.015503	0.0156	0.0157
30	0.0135	0.013505	0.0136	0.0137
60	0.021	0.02106	0.0212	0.0214
90	0.025	0.0255	0.026	0.027
120	0.026	0.0266	0.027	0.028
150	0.028	0.0286	0.029	0.030
180	0.034	0.0344	0.035	0.036

[1] All thresholds in mm

tially distributed with parameter equal to 1 (i.e., $H(t) \sim \text{Exp}(1)$). This means that for exceedances X over threshold u, the Cox-Snell residuals ϵ are

$$\epsilon = H(x) = -\ln S(x) = -\ln[1 - F(x)] = -\ln[1 - GPD(x, u \mid \boldsymbol{\theta})], \tag{C.4}$$

or

$$\epsilon = -\frac{1}{\kappa} \ln \left[1 - \kappa \frac{(x-u)}{\alpha^*} \right]. \tag{C.5}$$

Consequently, if a model is a good fit to data, the residuals (Equation C.5) are $\sim \text{Exp}(1)$, which means the ECDF for ϵ ($F_{\epsilon_i} = i/n$), should closely match that for $\epsilon \sim \text{Exp}(1)$, or $\epsilon \sim 1 - e^{-\epsilon}$. The Anderson-Darling test, which is an ECDF-based goodness-of-fit test (Stephens, 1986), is applied to the exceedances derived from a GPD model via Equation C.5, with the null hypothesis H_0 defined as $H_0 \coloneqq \epsilon \sim \text{Exp}(1)$. At a level of significance $\alpha = 0.05$—chosen arbitrarily, there is sufficient evidence to reject H_0 if the $p-$value < 0.05. To calculate the $p-$value, the Anderson-Darling statistic AD^2, Equation C.6, is computed for the observed residuals and compared against the AD^2 calculated for Bootstrap residual samples. This approach is widely used in the environmental science literature (e.g., Brown et al., 2008; Cannon, 2010; Davison and Ramesh, 2000; Katz et al., 2002; Khaliq et al., 2006; Kharin and Zwiers, 2005; Panagoulia et al., 2014).

$$AD^2 = -n + -\frac{1}{n} \sum_{i=1}^{n} (2i-1) \ln F_{\epsilon_i} - \frac{1}{n} \sum_{i=1}^{n} (2n - 2i + 1) \ln F_{\epsilon_i} \tag{C.6}$$

The sequential procedure (i.e., as u is allowed to vary) has been applied by various authors, with varying degrees of automation (see Bader et al., 2018; Choulakian and Stephens, 2001; Northrop and Coleman, 2014; Wadsworth, 2016; Wadsworth and Tawn, 2012; Solari et al., 2017; Zhao et al., 2019). The concern with the sequential, point-wise automated procedure, as raised by Bader et al. (2018), is the potential for premature stoppage (i.e., $p-$value > 0.05) due to random effects leading to false threshold selection, which Bader et al. (2018) mitigate through a proposed modification. For the present analysis, the application of the Anderson-Darling test is more sequential and point-wise than automated; that is, there is no stoppage criteria applied. The resulting $p-$values are plotted in a diagnostic plot to validate the MRL-derived threshold estimates and random effects, which do occur, are simply observed. Figure C.4 demonstrates the Bootstrap distribution of the AD^2 statistic for the 7-day exposure period, at $u = 0.009$ mm.

The resultant $p-$value is > 0.05, indicating that there is insufficient evidence to reject H_0. Figure C.5 compares the ECDFs for the Cox-Snell residuals F_{ϵ_i} and that for $\epsilon \sim \text{Exp}(1)$, for the 7-day exposure period at $u = 0.009$ mm. Qualitatively, there is reasonable overlap and no significant vertical distance separations between the two distributions, consistent with the calculated $p-$value.

Figure C.6 shows a typical diagnostic plot of the point-wise goodness-of-fit test performed by the aforementioned procedure. In this particular plot, for the 7-day exposure period, there is support for the "subjective" conclusion reached by the MRL plot, which is that candidate thresholds are in the region defined by $0.0009 < u < 0.0010$ mm.

The sequential, point-wise goodness-of-fit test methodology discussed above was conducted for the pooled pit depth data at each exposure period. The minimum threshold, u_{min}, was defined as that level for which subsequent thresholds $> u_{min}$ resulted in $p-$values approximately consistently above 0.05. The resultant minimum thresholds are included in Table C.2, along with the MRL plot thresholds, for comparison. Remarkably, there is very good agreement between these two methods, adding confidence to the estimates derived from the MRL plots.

C.3.2 Point Process Constraints

To support the Point process modelling in Chapter D, the thresholds must be greater than the lower endpoints of the limiting GEV distribution (Equation B.5) at each exposure period (the reason for this is explained in Chapter D, Section D.1). There is no finite lower endpoint for the GEV distribution (z_-), however, so a reasonable—though conservative—point estimate is the minimum of the block maxima per time period. Lower endpoint

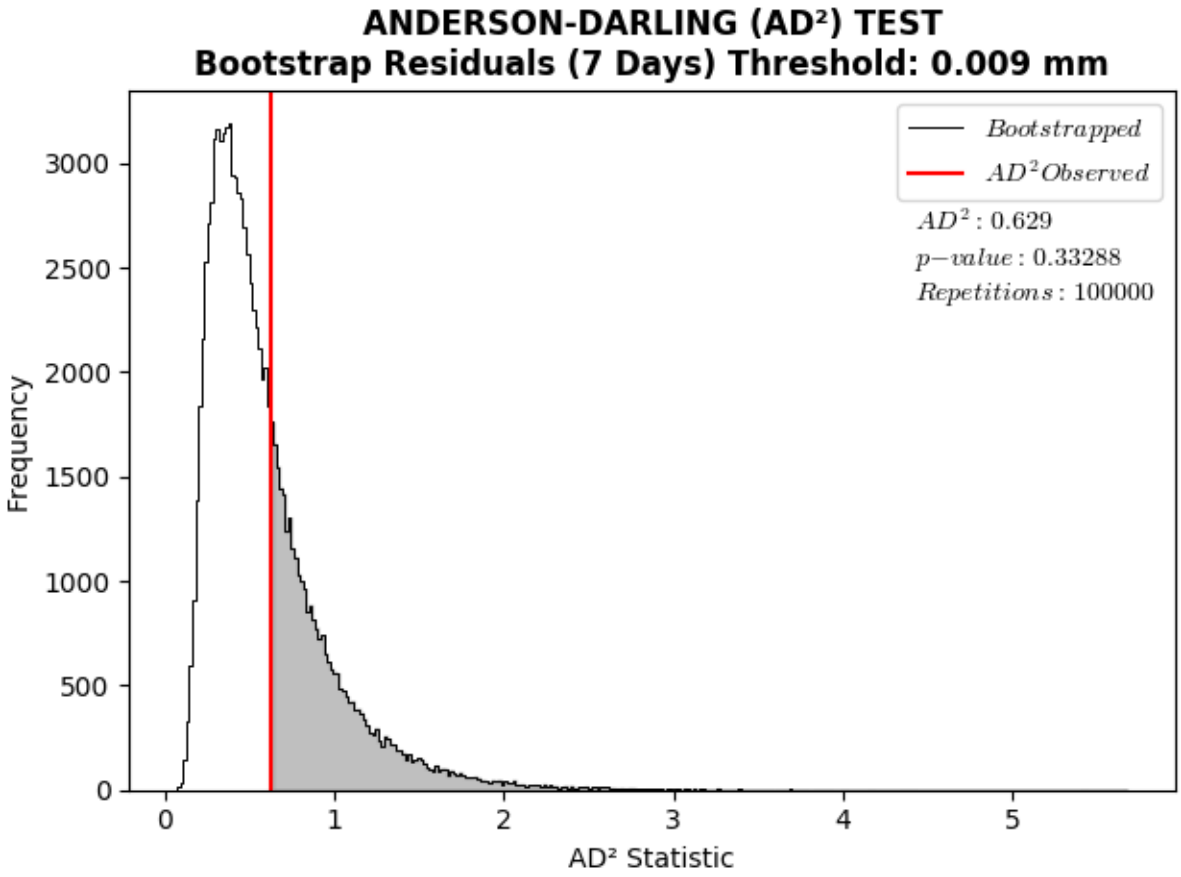

Figure C.4: Distribution of bootstrapped AD^2 statistic for the 7-day exposure period pit depths, with threshold $u = 0.009$ mm.

estimates are also included in Table C.2. Aside from a few exceptions, the lower end-point estimates are remarkably quite close to the MRL plot and goodness-of-fit threshold estimates.

The last constraint placed upon the selection of thresholds is that the intensity measure for the NHPPP must satisfy one of the fundamental properties of a non-stationary counting process, which is that the intensity measure must be finite-valued, non-negative, and a non-decreasing function of time (see Snyder and Miller, 1991, pg 42). To evaluate candidate thresholds against this constraint, the realisation x of the RV X, representing exceedances, is replaced by the proposed thresholds u in $\Lambda(x)$, Equation D.2. This substitution translates

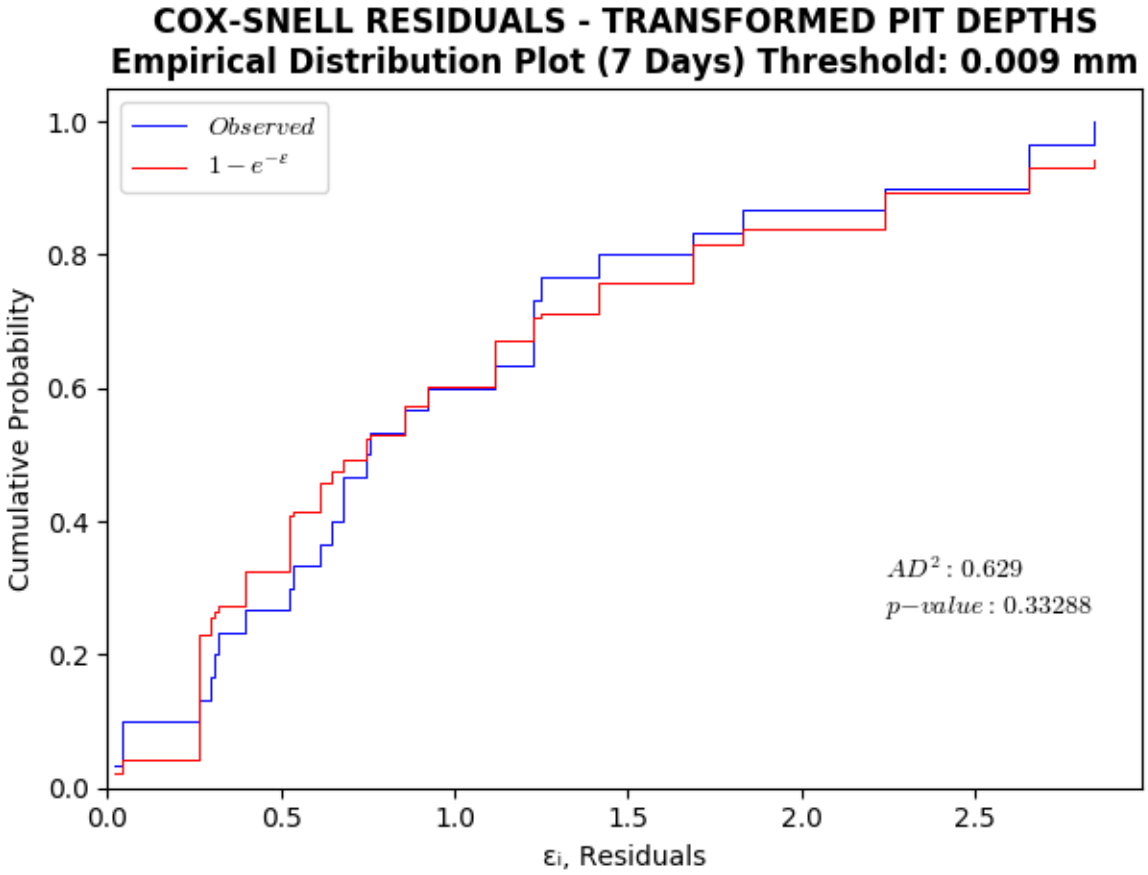

Figure C.5: Empirical distribution functions for the observed Cox-Snell residuals for the 7-day exposure period pit depths, with threshold $u = 0.009$ mm, and the Exp(1).

to estimating the expected number of exceedances at the four candidate levels (i.e., at thresholds $low1, low2, med$, and $high$), for each exposure period. However, because the GEV distribution is parametrised with time as covariate (see Equation B.8), it is necessary to assess the correct functional form of the thresholds with time as dependent variable—the very challenge presented at the beginning of section C.2. Since μ and α in the GEV distribution are modelled with a time power-law relationship, it seemed reasonable to assume the same for the thresholds. Figure C.7 provides a graphical perspective into the trend in thresholds with time for the $low1$ thresholds estimated by the MRL plot.

The trend is adequately captured by the power-law function fitted to the data. No-

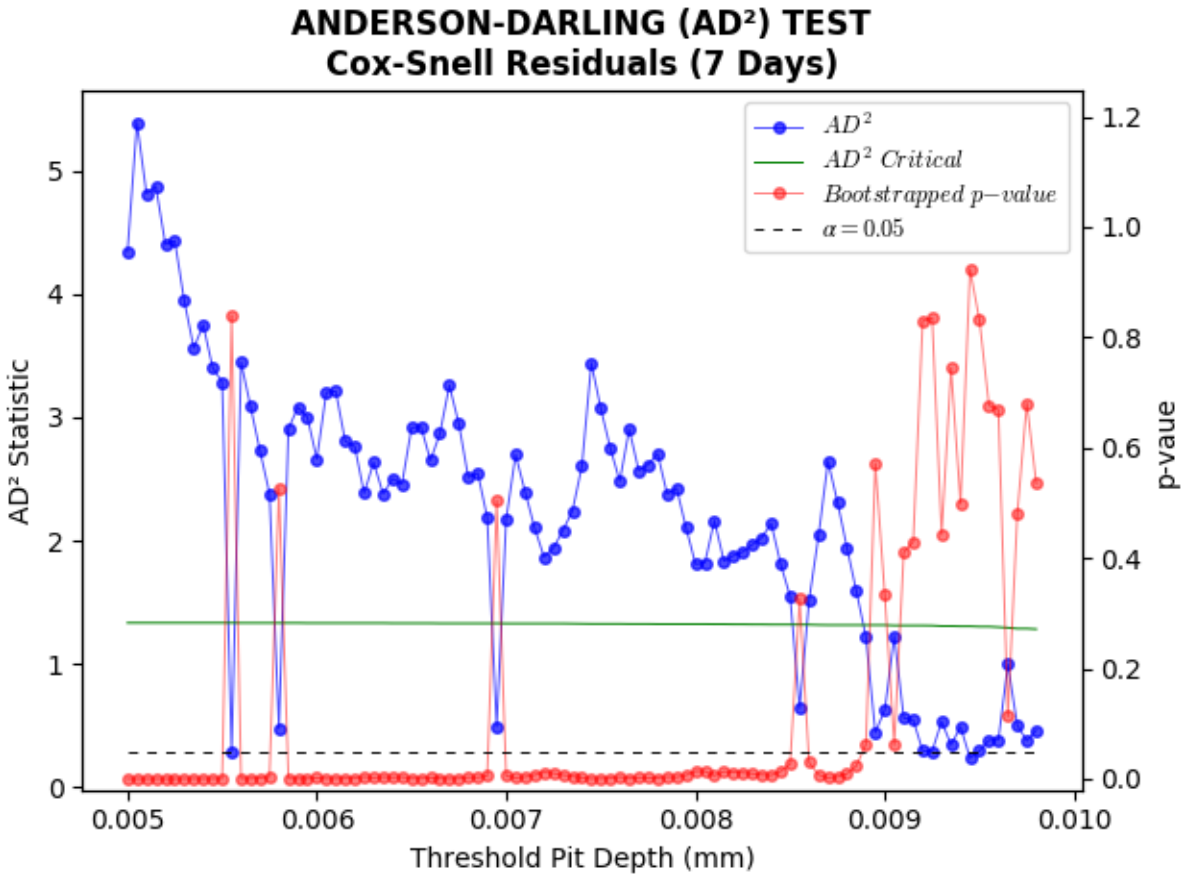

Figure C.6: Diagnostic plot of point-wise Anderson-Darling goodness-of-fit test for the 7-day exposure period pit depths.

ticeable in the figure are the thresholds at 30-, 120-, and 150-days, which are consistently lower than the trend line. A similar observation is made (though not plotted) for thresholds estimated by the goodness-of-fit tests and the GEV lower endpoints, suggesting this is a systemic effect for these three exposure periods. Power-law functions were subsequently fitted to the $low2, med$, and $high$ thresholds, resulting in overall adequate capture of trends. The corresponding coefficient and exponential terms of the power-law functions are found in Table C.3.

With the functional form of the thresholds established, $\Lambda(x)$ can be parametrised with time as shown in Equation C.7, using conveniently the coefficient and exponential terms

Table C.2: Mean Residual Life Plot, AD^2, and GEV Lower Endpoint Thresholds

Exposure Period (days)	$low1$[1]	$low2$	med	$high$	$AD^2 : u_{min}$	GEV:z_-
7	0.009	0.00901	0.0091	0.0092	0.0089	0.00962
14	0.0125	0.012505	0.0126	0.0127	0.01155	0.01186
21	0.0138	0.0141	0.0144	0.0148	0.01172	0.0141
28	0.0155	0.015503	0.0156	0.0157	0.01517	0.01592
30	0.0135	0.013505	0.0136	0.0137	0.01187	0.01391
60	0.021	0.02106	0.0212	0.0214	0.01751	0.02078
90	0.025	0.0255	0.026	0.027	0.02154	0.02446
120	0.026	0.0266	0.027	0.028	0.02567	0.02857
150	0.028	0.0286	0.029	0.030	0.02737	0.03088
180	0.034	0.0344	0.035	0.036	0.03321	0.03577

[1] All thresholds in mm

Table C.3: Thresholds Modelled with Power-law Functions

Level	k	u_k[1]	c_k
$low1$	1	0.04147	0.38854
$low2$	2	0.04240	0.39422
med	3	0.04312	0.39637
$high$	4	0.04481	0.40482

[1] Functional form is $u_k t^{c_k}$

derived for the GEV distribution parameters, and threshold levels defined in Table C.3. However, since the intent of this section is to demonstrate the use of the GPD in a POT framework for the analysis of pitting corrosion data, Equation C.1 is reformulated with time as covariate (Equation C.8 and Equation C.9) and parameters μ, α, κ and b estimated by maximising the corresponding likelihood function, Equation C.10.

$$\Lambda(t, \boldsymbol{\theta}) = \left[1 - \kappa \left(\frac{u_k t^{c_k} - \mu t^b}{\alpha t^b}\right)\right]^{\frac{1}{\kappa}} ; k = 1, 2, 3, 4 \tag{C.7}$$

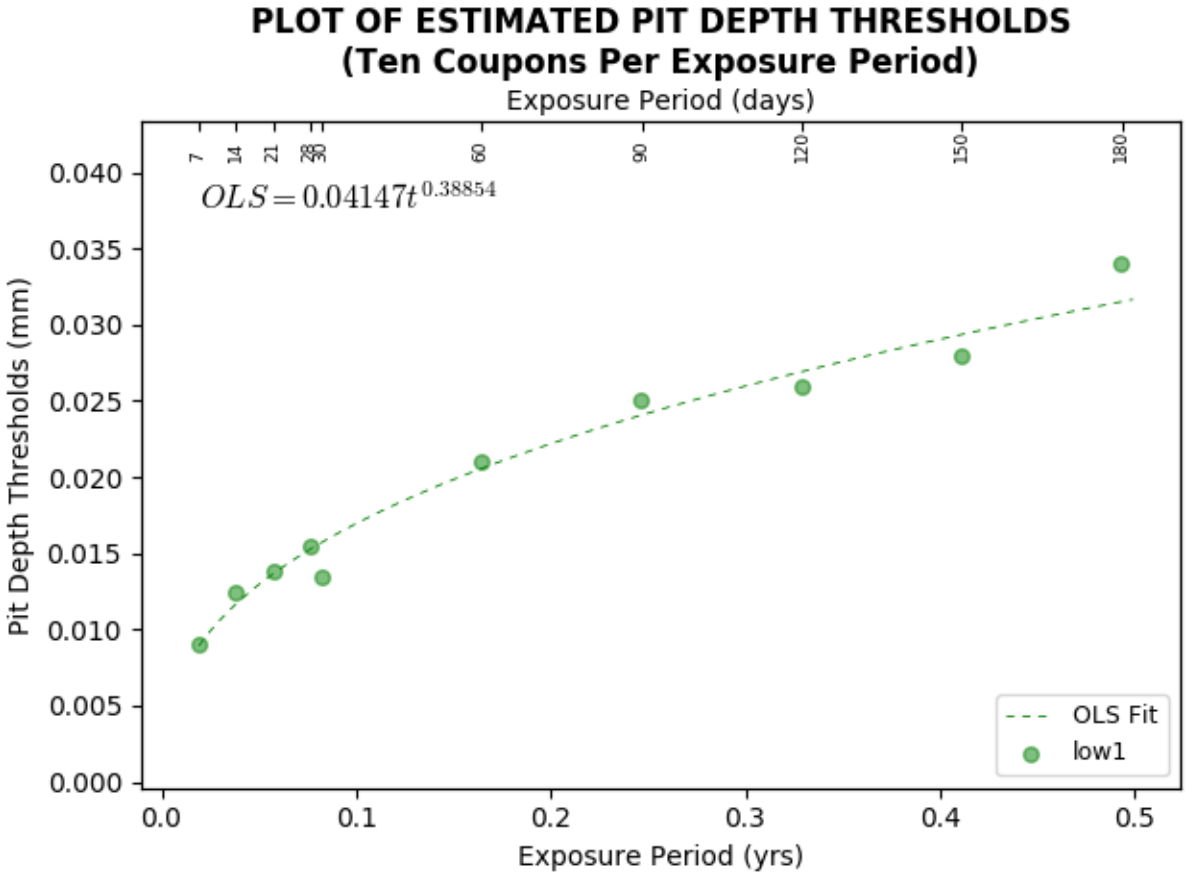

Figure C.7: The change in the *low*1 thresholds with time is captured by a power-law relationship, fitted by Ordinary Least Squares.

$$GPD(\boldsymbol{x}, \boldsymbol{t} \mid \boldsymbol{\theta}_2) = \left\{ 1 - \left[1 - \kappa \frac{(x - u_k t^{c_k})}{\alpha *} \right]^{1/\kappa} \right\}; \kappa \neq 0, \alpha * \geq 0, 1 - \kappa \frac{(x - u_k t^{c_k})}{\alpha *} \geq 0 \tag{C.8}$$

with $\alpha^* = \alpha t^b - \kappa(u_k t^{c_k} - \mu t^b)$.

$$f\left(\boldsymbol{x}, \boldsymbol{t} \mid \boldsymbol{\theta}_2\right) = \frac{1}{\alpha t^b - \kappa(u_i t^{c_k} - \mu t^b)} \left\{ \left[1 - \kappa \frac{(x - u_k t^{c_k})}{\alpha t^b - \kappa(u_k t^{c_k} - \mu t^b)} \right]^{\frac{1}{\kappa} - 1} \right\} \tag{C.9}$$

$$L(\boldsymbol{\theta}_2 \mid \boldsymbol{x}, \boldsymbol{t}) = \prod_{j=1}^{10} \left\{ \prod_{i=1}^{n_j} \frac{1}{\alpha t_j^b - \kappa(u_k t_j^{c_k} - \mu t_j^b)} \left[1 - \kappa \left(\frac{x_{i,j} - \mu t_j^b}{\alpha t_j^b - \kappa(u_k t_j^{c_k} - \mu t_j^b)} \right) \right]^{\frac{1}{\kappa}-1} \right\} \tag{C.10}$$

with $x_{i,j} > u_k t_j^{c_k}$ and the constraint that $1 - \kappa \left(\frac{x_{i,j} - \mu t_j^b}{\alpha t_j^b - \kappa(u_k t_j^{c_k} - \mu t_j^b)} \right) \geq 0$.

Numerical maximisation of the natural logarithm of the likelihood function $L(\boldsymbol{\theta}_2 \mid \boldsymbol{x}, \boldsymbol{t})$, with the noted constraints, for the different thresholds, resulted in the GPD parameter estimates presented in Table C.4. Included in this table are the estimates for the numerical value of the log-likelihood function of the GEV distribution (EquationB.23), with parameter set $\hat{\boldsymbol{\theta}}_2 \coloneqq \left\{ GPD : \hat{\mu}, \hat{\alpha}, \hat{\kappa}, \hat{b} \right\}$ substituted for $\hat{\boldsymbol{\theta}}_1$. This was added as a comparison to assess the quality of the fit and to gauge quantitatively the "merit" of the threshold levels. The results indicate that $low1$ thresholds lead to MLE-based parameters for the GPD that, when employed for the evaluation of $l(\hat{\boldsymbol{\theta}}_1 \,|\, \boldsymbol{x}, \boldsymbol{t})$, are in better in agreement with GEV distribution parameters than the other levels, though the first three levels ($low1, low2$, and med) lead to very similar results. An interesting outcome is that with increasing threshold levels, both $l(\hat{\boldsymbol{\theta}}_2 \,|\, \boldsymbol{x}, \boldsymbol{t})$ and $l(\hat{\boldsymbol{\theta}}_1 \,|\, \boldsymbol{x}, \boldsymbol{t})$ decrease. With higher thresholds, the absolute number of exceedances decrease, and this reduces the sum in the log-likelihood function. Consequently, the more relevant comparisons are the log-likelihood function values in the right most column of Table C.4. For completeness, a scatter plot of GPD exceedances for the various exposure periods, derived from the functional form of the $low1$ thresholds, is shown in Figure C.8.

The analysis is now in a good position to assess the last constraint on the thresholds, which is with respect to intensity measure $\Lambda(x)$ of the NHPPP. Figure C.9, which is a plot of $\Lambda(t:\theta)$ for the $low1$ thresholds (plotted for $\Lambda(t:\theta) > 1.25$), shows a finite-valued function, non-negative, and non-decreasing, thereby satisfying the last constraint. Similar plots were generated for the remaining three levels. All levels with the exception of the $high$ thresholds, satisfied the constraint. Threshold level $high$ exhibited a decreasing function with time. With increasing threshold levels (i.e., going from $low1$ to med), the maximum in $\Lambda(t:\theta)$ across the range of exposure period decreases. Table C.5 provides a summary of these findings.

Table C.4: Maximum Likelihood Parameter Estimates for the GPD with Time as Covariate

Threshold	$\hat{\mu}$	$\hat{\alpha}$	$\hat{\kappa}$	$\hat{b}$	$l(\hat{\boldsymbol{\theta}}_2 \mid \boldsymbol{x}, \boldsymbol{t})$	$l(\hat{\boldsymbol{\theta}}_1 \mid \boldsymbol{x}, \boldsymbol{t})$[1]
$low1$	0.04816	0.00410	0.35452	0.40634	1617.14	498.75
$low2$	0.04841	0.00397	0.34749	0.40635	1522.34	498.69
med	0.04765	0.00411	0.32456	0.40651	1431.40	497.87
$high$	0.04934	0.00332	0.30212	0.40238	1230.51	486.03
GEV[2]	0.04788	0.00400	0.34294	0.40294	—	498.96

[1] $l(\hat{\boldsymbol{\theta}}_1 \mid \boldsymbol{x}, \boldsymbol{t})$ is the log-likelihood for the GEV distribution, Equation B.23, determined by substituting parameter set $\hat{\boldsymbol{\theta}}_2$ for $\hat{\boldsymbol{\theta}}_1$ at each threshold level.
[2] GEV distribution parameters $\hat{\boldsymbol{\theta}}_1$, Table B.1

Table C.5: Non-homogeneous Poisson Process Intensity Characteristics

Level	$\Lambda(t:\theta)$	max(Range)[1]
$low1$	finite-valued, non-negative, non-decreasing	3.34
$low2$	finite-valued, non-negative, non-decreasing	3.18
med	finite-valued, non-negative, non-decreasing	2.43
$high$	finite-valued, non-negative, decreasing	—

[1] Maximum expected number of exceedances per corrosion coupon over the range of exposure periods.

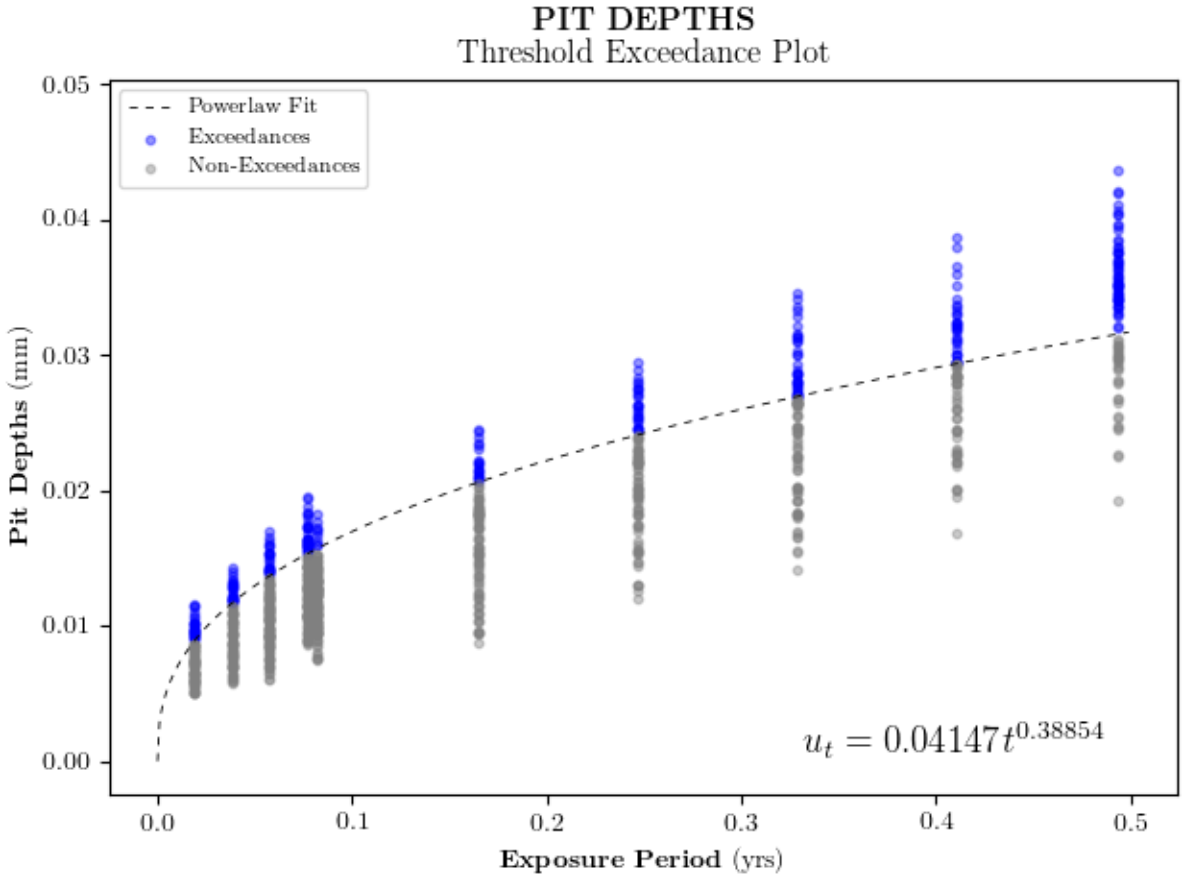

Figure C.8: Scatter plot of exceedances arising from the employment of the *low*1 thresholds.

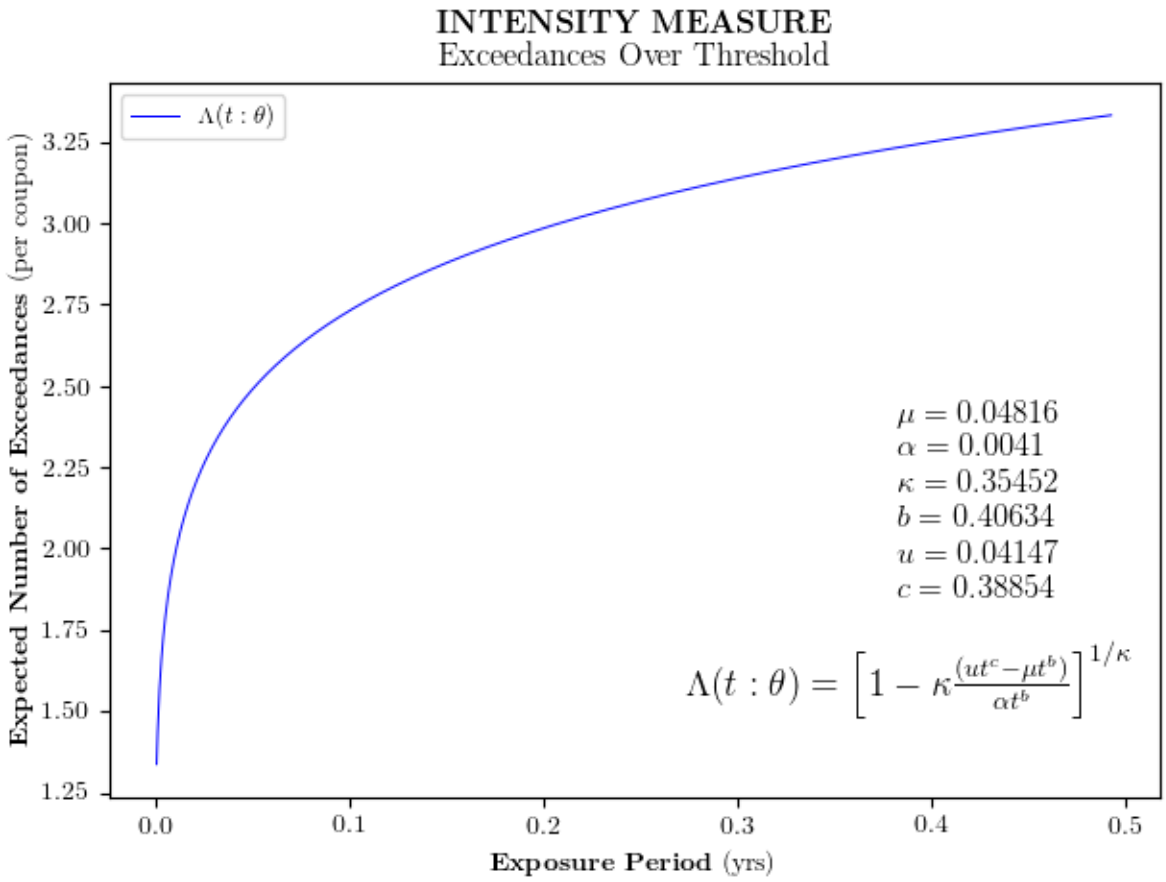

Figure C.9: Non-homogeneous Poisson process intensity measure for the *low*1 thresholds.

C.3.3 Algorithm to Assign Pit Depth Exceedances

Similar to the assignment of pit depths to a UFC from the GEV distribution, a fitted, time-extrapolated GPD (e.g., Equation C.9) may be sampled for pit depth exceedances. While size effect needs to be accounted for, as shown in the algorithm in section B.4.4, this is done simply by considering the fact that the total number of observed exceedances n_j over a time-specific threshold u_j ($u_j = u_k t_j^{c_k}$) is a function of the total number of blocks pooled for the specific exposure period. In the present case, ten blocks were pooled for each exposure period, and each block $\equiv$ coupon has already been determined to be approximately 1/251th the size of the surface area of the UFC quarter hemispherical end-cap. An unbiased, point-wise estimate of the total number of exceedances expected for the UFC quarter hemispherical end-cap n_j^{UFC} is $n_j \times 251/10$ or $n_j^{\text{UFC}} \approx 25.1 n_j$. Furthermore, since the assignment of pit depths occurs at the panel level, and there are $m = 255$ panels on the UFC quarter hemispherical end-cap, it follows that the number of pit depths to be sampled from the time-extrapolated GPD is $\text{int}(25.1 n_j)$ if $25.1 n_j < m$, else m otherwise. The limitation here is that when extrapolating outside of experimental conditions, which is the more likely case, one does not know n_j in advance. The GPD modelling framework, without a Point process perspective, does not afford estimation of the number of exceedances. Consequently, a conservative approach is to assign one pit per panel, or equivalently to sample m pit depth exceedances from the fitted GPD.

Note, it has been assumed that investigators seeking to apply a GPD to model corrosion pitting have no knowledge of Point processes and are unaware that $\Lambda(t : \theta)$ may be used to estimate the expected number of exceedance per coupon area. Additionally, it is assumed that the functional form of the thresholds has been identified and thresholds levels meeting requirements prescribed in the preceding sections have been selected—necessarily without satisfying the Point process constraints as these would be unknown to the investigator.

In words, the algorithm samples randomly m maximum pit depths from the GPD distribution extrapolated in time $T = \{t_{min}, t_{max}\}$, where t_{min}, t_{max} are the minimum and maximum timescales anticipated for the DGR during the dry, oxic period, respectively. The sampling generates two arrays of pit depth exceedances $(D_{tmin}, D_{t_{max}})$, one for each time segment. The algorithm also samples randomly m thicknesses from the initial copper coating thickness distribution ($f_{t_{\text{Cu}}} \sim$ Lognorm), creating an array of thicknesses. A new array is created by subtracting from the copper coating thickness array the pit depth exceedances. This is done twice, once for each time segment, to generate two modified initial copper coating thickness arrays, which would then be fed into the rest of the original UFC lifetime code for continued processing (not shown here). The algorithm is summarised below.

Algorithm 6 Pit Depth Exceedance Assignment—GPD

Require: $T, m, f(x, t; \mu, \alpha, \kappa, b, u_k, c_k), f_{t_{\mathrm{Cu}}} \sim Lognorm$

Initialise variables, arrays: $t, D_{t_{min}}, D_{t_{max}}, Cu, Cu_{t_{min}}, Cu_{t_{max}}$
$u_k, c_k \leftarrow$ select threshold level k
$Cu \leftarrow$ sample randomly m thicknesses from $f_{t_{\mathrm{Cu}}}$
for t_i in T **do**
    $f(x, t : \hat{\boldsymbol{\theta}}_2) \leftarrow f(x, t_i; \mu, \alpha, \kappa, b, u_k, c_k)$
    if $t_i == min(T)$ **then**
        $D_{t_{min}} \leftarrow$ sample randomly m pit depth exceedances from $f(x, t : \hat{\boldsymbol{\theta}}_2)$
        $Cu_{t_{min}} \leftarrow Cu - D_{t_{min}}$
    else
        $D_{t_{max}} \leftarrow$ sample randomly m pit depth exceedances from $f(x, t : \hat{\boldsymbol{\theta}}_2)$
        $Cu_{t_{max}} \leftarrow Cu - D_{t_{max}}$

Appendix D

Non-Homogeneous Poisson Point Process

The objective of this appendix is to provide the mathematical details covering the asymptotic arguments used to derive the intensity measure formulation in Chapter 5, Section 5.3.3, Equation 5.17. Two arguments are presented: Point process characterisation and the NHPP-GPD characterisation.

D.1 Point Process Characterisation

The convergence of the sequence of pit depth maxima M_n^*, Equation (B.3), occurs if and only if (Pickands, 1971; Smith, 1989)

$$n[1 - F(a_n x + b_n)] \to -\ln H(x) = \Lambda(x) \text{ as } n \to \infty, \tag{D.1}$$

and

$$\Lambda(x) = \left[1 - \kappa\left(\frac{x-\mu}{\alpha}\right)\right]^{\frac{1}{\kappa}}. \tag{D.2}$$

Equation (D.1) follows from the approximation $\lim_{y\to\infty}(1+t/y)^y = e^t$ and by re-arranging Equation (D.1) in the form $\lim_{n\to\infty}(1-\Lambda(x)/n)^n = e^{-\Lambda(x)}$ (see Leadbetter et al., 1983, pg 36; Resnick, 1987, pg 39). The normalising constants a_n and b_n are those introduced in Section B.1, and $\Lambda(x)$ is the argument of the negative exponential term in the GEV

distribution, Equation (B.5). Note, z in $H(z)$ (Equation (B.3)) has been replaced by x in Equation (D.1) without loss of generality.

To put the above equations into perspective, following the example in Smith (1994), define a Point process P_n on the closed interval $[0,1]\times\mathbb{R}$ by placing a point at each $\{i/(n+1), (X_i - b_n)/a_n\}$, $1 \leq i \leq n$, where n is the total number of points in the process. The $i/(n+1)$ scaling ensures that the process is always mapped to $[0,1]$, whereas the normalisation of X_i stabilises the behaviour of extremes as $n \to \infty$ (Coles, 2001, pg 129). The argument made by Smith (1989) is that the normalised X_i in the Point process P_n will tend to cluster near the lower endpoint of the (re-scaled) distribution. Away from the boundary, however, the process will look like a NHPP. Put in other words (Coles, 2001, pg 130), if x_- and x_+ are the respective lower and upper endpoints of the limiting GEV distribution (Equation (B.3) and Equation (B.5)), then as $n \to \infty$ the sequence of Point processes

$$P_n = \{(i/(n+1), (X_i - b_n)/a_n) : i = 1, \ldots, n\} \tag{D.3}$$

converges on regions of the form $[0,1]\times[y,\infty]$, for any $y > x_-$, to a NHPP P, with intensity measure on a region $A \coloneqq [t_1, t_2] \times [x, x_+]$, $0 \leq t_1 \leq t_2 \leq 1$, given by

$$\Lambda(A) = (t_2 - t_1)\Lambda(x). \tag{D.4}$$

The expected number of points in $[0,1]\times(y,\infty)$ for any fixed $y > x_-$ is $n[1-F(a_n y+b_n)]$ which, according to Equation (D.1), converges to $\Lambda(x)$. As explained by Smith (1994), in practice it is more practical to work directly with a NHPP applied to all observations over a threshold u. This in lieu of constructing a limiting Point process with the required renormalisation. Consequently, for any observation X_t, taken at time t, for which $X_t > u$, a point is placed at (t, X_t). This procedure is treated as part of a NHPPP on $\mathbb{R} \times (u, \infty)$ whose intensity measure (i.e., expected number of exceedances over u) satisfies

$$\Lambda\left\{(t_1, t_2), (x, \infty)\right\} = (t_2 - t_1)\left[1 - \kappa\left(\frac{x-\mu}{\alpha}\right)\right]^{\frac{1}{\kappa}}, t_1 \leq t_2, x \geq u. \tag{D.5}$$

Smith (1994, pg 231) proposed that if $\Lambda(x)$ is defined as per Equation D.2, and $v(x) \coloneqq -\partial\Lambda(x)/\partial x$, then if one observes a random number N of exceedances (T_j, X_j) with $X_j > u$

over a time period $(0, T)$, the approximate likelihood function is

$$\begin{aligned} L(\mu, \alpha, \kappa) &= \exp\{-T\Lambda(u)\} \cdot \prod_{j=1}^{N} v(X_j) \\ &= \exp\left\{-T\left[1-\kappa\left(\frac{u-\mu}{\alpha}\right)\right]^{\frac{1}{\kappa}}\right\} \cdot \prod_{j=1}^{N} \frac{1}{\alpha}\left[1-\kappa\left(\frac{X_j-\mu}{\alpha}\right)\right]^{\frac{1}{\kappa}-1}. \end{aligned} \tag{D.6}$$

The parameters $\mu, \alpha,$ and κ can be estimated by numerical maximisation of Equation (D.6). Subsequently, the intensity (density) function of the process is

$$v(x) \coloneqq -\partial\Lambda(x)/\partial x \equiv \lambda(x) = \frac{1}{\alpha}\left[1-\kappa\left(\frac{x-\mu}{\alpha}\right)\right]^{\frac{1}{\kappa}-1}. \tag{D.7}$$

Additionally, Smith (2003, pg 14) indicates that for "non-stationary processes", in which the parameters $\mu, \alpha,$ and κ are dependent on time, then the intensity function in Equation (D.7) is replaced by

$$\lambda(t, x) = \frac{1}{\alpha_t}\left[1-\kappa_t\left(\frac{x-\mu_t}{\alpha_t}\right)\right]^{\frac{1}{\kappa_t}-1}, \left[1-\kappa_t\left(\frac{x-\mu_t}{\alpha_t}\right)\right] > 0, \tag{D.8}$$

where $\mu_t, \alpha_t,$ and κ_t are functions of time.

The foregoing examples were concerned with environmental applications. To the best of this author's knowledge, the only application of a Poisson Point process for pit growth is presented in Scarf and Laycock (1996). Here, the authors refer to Smith (1989) and Smith (1994) to present a likelihood function for a NHPP. In particular, Scarf and Laycock (1996) state that if a random number N of exceedances $X_j > u$ over a unit area or time interval are observed, the likelihood function is

$$L = \exp\left\{-\left[1-\kappa(u-\mu)/\alpha\right]^{1/\kappa}\right\} \prod_{j=1}^{N}\left\{\frac{1}{\alpha}\left[1-\kappa(x_j-\mu)/\alpha\right]^{-1+1/\kappa}\right\}.$$

Scarf and Laycock (1996) further state that "the product of the likelihood over different time periods is considered in the usual way, when combining data;" and "if the time periods differ in length, then" Equation (B.35) (and its derivative, Equations B.37 and B.38) may be used to rescale μ and α accordingly.

Another example of modelling pitting corrosion by a stochastic process is found in the work by Datla et al. (2008), who modelled the number of pits in steam generator tubes of nuclear power reactors as a NHPP, with an intensity density function that assumed the form of a Weibull process or power-law function (i.e., $\lambda(t) = \alpha t^{\beta-1}$). Datla et al. (2008) ultimately derived the form of the GEV distribution whose argument $\Lambda_z(t)$, in the function $GEV = \exp(-\Lambda_z(t))$, expressed the expected number of pit depths exceeding a critical through-wall depth z. The intensity measure $\Lambda_z(t) \coloneqq \Lambda(t)(1 - F_X(z))$ was derived by fitting a GPD defined with time-invariant parameters (referred to as $F_X(z)$ in their work) to pit depth exceedance data, with $\Lambda(t) \coloneqq \int^{\tau} \alpha t^{\beta-1} dt$. The parameters α and β were estimated by maximising the likelihood function or joint density of the number of pits in discrete inspection intervals, which was simply the product of the non-homogeneous form of the Exponential distribution. Maximisation of the likelihood function was relatively straight forward to achieve. The closed-form solution from the method of moments was employed to estimate the GPD parameters. Ultimately the GEV distribution was used to estimate the probability of exceeding a critical pit depth. Assuming the Weibull for the number of pits generated with time and the time-invariant form for the GPD simplified greatly the computational effort. In the present work, neither the assumption of a Weibull process nor time-invariant exceedances apply.

D.2 NHPP-GPD Characterisation

The preceding section showed that, in the limit as $n \to \infty$, a Point process, whose points are normalised (i.e., $(X_i - b_n)/a_n$), converges to a NHPPP in a region of the form $[0,1] \times [y, \infty]$, for any $y > x_-$. Moreover, the expected number of points in $[0,1] \times (y, \infty)$, for any fixed $y > x_-$, is $n[1 - F(a_n y + b_n)]$, which, according to Equation (D.1), converges to $\Lambda(x)$. The intensity measure $\Lambda(x)$ and the intensity density function $\lambda(x) = -\partial\Lambda(x)/\partial x$ for a NHPPP, in the space $[0,1] \times [y, \infty]$, for any $y > x_-$, are thus defined.

Alternatively, one can arrive at the same expression for $\Lambda(x)$ by specifying the conditions that (i) the number of events N_u over some large enough threshold u are $\sim \text{Pois}(\Lambda(x))$, with parameter $\Lambda(x)$, and that (ii) the magnitude of events $X|X > u$ follow a GPD, with a POT framework. For example, assume

$$F_{X|X>u}(x) \coloneqq 1 - \left[1 - \kappa \frac{(x-u)}{\alpha - \kappa(u-\mu)}\right]^{1/\kappa}, x \geq y, \alpha - \kappa(y-\mu) > 0, \tag{D.9}$$

and

$$P(N_u = n) \coloneqq \frac{\Lambda(x)^n e^{-\Lambda(x)}}{n!}. \tag{D.10}$$

Then, the distribution F_{Y_n} of the largest exceedance $Y_n \coloneqq max(X_1, X_2, \ldots, X_n)$ for all n is

$$\begin{aligned} F_{Y_n}(x) &= \sum_{n=0}^{\infty} \left[F_{X|X>u}(x)\right]^n \frac{\Lambda(x)^n e^{-\Lambda(x)}}{n!} \\ &= e^{-\Lambda(x)} \sum_{n=0}^{\infty} \left[F_{X|X>u}(x)\right]^n \frac{1}{n!} \\ &= e^{-\Lambda(x)} e^{F_{X|X>u}(x)\Lambda(x)} \quad \text{(after invoking power series of } e^{F_{X|X>u}(x)\Lambda(x)}) \\ &= e^{\Lambda(x)\left[F_{X|X>u}(x)-1\right]} \\ &= e^{-\Lambda(x)\left[1-\kappa\frac{(x-u)}{\alpha-\kappa(u-\mu)}\right]^{1/\kappa}} \quad \text{(after substituting for } F_{X|X>u}(x), \text{Equation D.9).} \end{aligned} \tag{D.11}$$

However, as per Appendix B, for large n,

$$F_{Y_n}(x) \approx GEV(x) = e^{-\left[1-\kappa\frac{(x-\mu)}{\alpha}\right]^{1/\kappa}}.$$

Consequently,

$$e^{-\Lambda(x)\left[1-\kappa\frac{(x-u)}{\alpha-\kappa(u-\mu)}\right]^{1/\kappa}} \approx e^{-\left[1-\kappa\frac{(x-\mu)}{\alpha}\right]^{1/\kappa}},$$

which, after re-arranging and solving for $\Lambda(x)$, leads to

$$\Lambda(x) = \left[1-\kappa\left(\frac{x-\mu}{\alpha}\right)\right]^{\frac{1}{\kappa}}, \quad x \geq u.$$

D.3 Pitting Corrosion as a NHPPP

Pitting corrosion is a cumulative degradation process, where pit depth $X(t)$ at future time t is uncertain. From a stochastic process perspective, a natural approach to modelling pitting corrosion is to employ stochastic cumulative processes, such as the stationary Exponential or Gamma process, both of which sum or convolve iid pit depth increments per unit time (e.g., see Cheng and Pandey (2012); van Noortwijk (2009)). In this work, a cumulative degradation process is transformed into an "equivalent" Point process, specifically the NHPP, by interpreting an extreme pit depth $X(t)|X(t) > u(t)$ at time t, $u(t)$ a threshold pit depth, as an event, a point on a timeline, whose arrival is governed by a time-dependent process intensity.

By way of illustration, consider Figure D.1a where pitting corrosion, depicted as a cumulative degradation process, is simulated arbitrarily by 10 random trajectories or degradation paths observed (sliced) at an arbitrary moment in time t, with three extreme pit depths $X(t) > u(t)$ observed. At the time slice at t, the observer only records the pit depths; the progression of pit depths over the time interval $[0, t]$ is unobserved. In a Point process representation, extreme pit depths arrive on the surface of a corrosion coupon as discrete events at different times over the same time interval $[0, t]$. Because events occur at times less than t, their arrivals are unobserved at time slice t, Figure D.1b. Instead, at time t the total count of extreme events is recorded, Figure D.1c. As soon to be shown, re-interpreting a cumulative damage process as a non-homogeneous Point process is carried out simply enough by placing the points $(t, X(t))$, corresponding to observed extreme pit depths (e.g., see Figure 5.3), on a timeline. This is possible because the likelihood function formulation with time as co-variate shows that the intensity of the process, leading to the number of events occurring in a specified time interval, is dependent on the duration of the interval and the magnitude of the events (i.e., depth of extreme pits). Consequently, one only needs to know the count and magnitude of extreme pit depths at the time slice t, which occurs at the end of the time interval of interest, to apply the Point process representation.

From the foregoing sections, following the practical approach from Smith (1994) to place a point at $(t, X(t))$ for any observation $X(t) > u(t)$ at time t, the likelihood function for the pitting corrosion data, when formulated as a NHPPP with time-variant threshold $u(t)$, is expressed as per Equation D.6, with the modification suggested to account for the pooling of ten blocks (i.e., $C_p = 10$ corrosion coupons per exposure period). This formulation is expressed by Equation D.12. Here, the pooling of ten blocks (i.e., ten unit areas; a unit area $\equiv$ one coupon area) is interpreted to be equivalent to observing exceedances over ten unit time intervals, or $T = 10$ in Equation D.6. The intensity density function of the process $v(x_{i,j} \,|\, \boldsymbol{\theta}_3)$ (or $\lambda(x_{i,j} \,|\, \boldsymbol{\theta}_3)$) is invariant to the number of blocks pooled.

$$\begin{aligned} L(\boldsymbol{\theta}_3 \,|\, \mathbf{x}, \mathbf{t}) &= \prod_{j=1}^{N} \left\{ \exp\left\{ -C_p \cdot V(\theta_3) \right\} \cdot \prod_{i=1}^{n_j} v(x_{i,j} : \theta_3) \right\} \\ &= \prod_{j=1}^{N} \left\{ \exp\left\{ -C_p \cdot \left[1 - \kappa \left(\frac{u t_j^c - \mu t_j^b}{\alpha t_j^b} \right) \right]^{\frac{1}{\kappa}} \right\} \cdot \prod_{i=1}^{n_j} \frac{1}{\alpha t_j^b} \left[1 - \kappa \left(\frac{x_{i,j} - \mu t_j^b}{\alpha t_j^b} \right) \right]^{\frac{1}{\kappa} - 1} \right\} \end{aligned} \tag{D.12}$$

In Equation D.12, $N = 10$, $\boldsymbol{\theta}_3 \coloneqq \{\text{NHPPP} : \mu, \alpha, \kappa, b\}$, $x_{i,j}$, and n_j, represent respectively the number of exposure periods, the parameter vector for the NHPPP, the ith realisation of

the exceedance RV at the jth exposure period, and the number of exceedances for exposure period j. The constraints applied to the numerical maximisation of the natural logarithm of Equation (D.12), which was carried out in Python 3.6.9 with the optimisation algorithm SLSQP, were $1/\alpha t^b > 0$, $1 - \kappa(ut^c - \mu t^b)/\alpha t^b \geq 0$, and $1 - \kappa(x_{i,j} - \mu t^b)/\alpha t^b \geq 0$. Results are presented in Table D.1 for threshold levels $low1, low2$, and med.

Table D.1: Maximum Likelihood Parameter Estimates for the NHPP with Time as Covariate

Threshold	$\hat{\mu}$	$\hat{\alpha}$	$\hat{\kappa}$	$\hat{b}$	$l(\hat{\boldsymbol{\theta}}_3 \mid \mathbf{x}, \mathbf{t})$	$l(\hat{\boldsymbol{\theta}}_1 \mid \mathbf{x}, \mathbf{t})$[1]
$low1$	0.04876	0.00399	0.34450	0.40926	1660.94	498.20
$low2$	0.04875	0.00396	0.33940	0.40911	1540.89	498.21
med	0.04874	0.00385	0.31620	0.40933	1429.01	497.98
GEV[2]	0.04788	0.00400	0.34294	0.40294	—	498.96

[1] $l(\boldsymbol{\theta}_1 \mid \mathbf{x}, \mathbf{t})$ is the log-likelihood for the GEV distribution, Equation B.23, determined by substituting parameter set $\hat{\boldsymbol{\theta}}_3$ for $\hat{\boldsymbol{\theta}}_1$ at each threshold level.
[2] Estimated GEV distribution parameters, Table B.1

For the three threshold levels, the numerical values of the equivalent GEV log-likelihood function are essentially within a decimal place of each other, similar to the results for the GPD (Table C.4). However, the GPD parameters yield results that are marginally closer to the numerical value of the GEV log-likelihood function. Observed differences may simply be due to the sensitivity of the likelihood functions to the optimisation algorithm settings, though care was exercised to assess this sensitivity and maintain consistency. Overall, however, there is very good agreement within the GEV, GPD, and NHPPP maximum likelihood estimates for the extreme value parameters μ, α, κ, b.

Under a NHPPP representation of the pitting corrosion process, the expected number of pit depth exceedances $\Lambda(t; \boldsymbol{\theta}_3)$, observed in a single corrosion coupon (for the surrogate data), vary with time as depicted in Figure D.2.

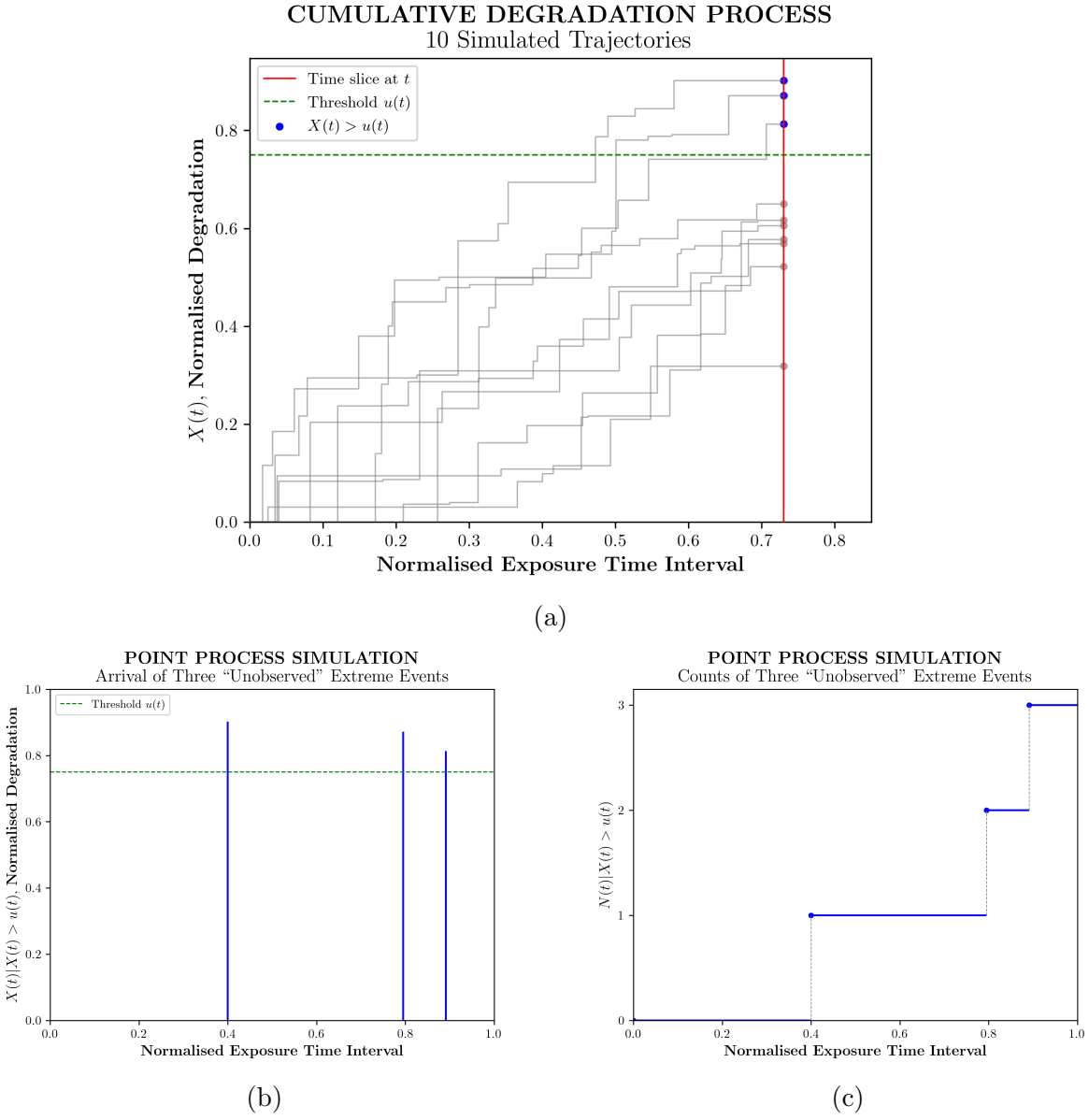

Figure D.1: Pitting corrosion as a cumulative degradation process is simulated by (a) 10 trajectories or degradation paths observed (sliced) at an arbitrary moment in time t, with three extreme pit depths $X(t) > u(t)$ observed. (b) In a Point process representation, the three extreme pit depths arrive unobserved at different times over the time interval $[0, t]$, according to some intensity measure $\Lambda(x, t)$, leading to (c) three counts by time t.

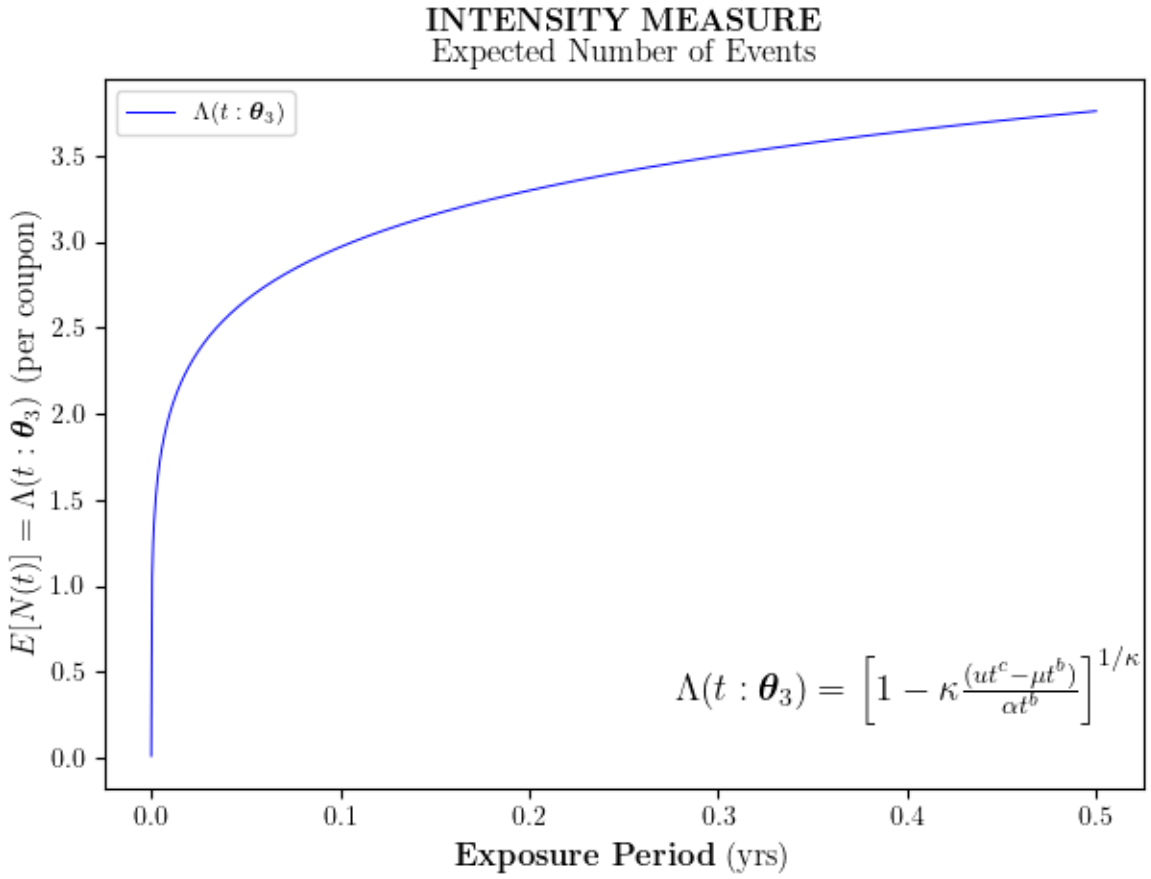

Figure D.2: Expected number of pit depth exceedances (events) per coupon by time t for the NHPPP, with parameter $\Lambda(t:\boldsymbol{\theta}_3)$.

D.4 Algorithm to Assign Pit Depth Exceedances—NHPPP

With the intensity measure $\Lambda(t;\boldsymbol{\theta}_3)$ defined, the number of pits n_j to be assigned at some future time j is estimated directly from $\text{int}(251\Lambda(t;\boldsymbol{\theta}_3))$, since $\Lambda(t;\boldsymbol{\theta}_3)$ is the expected number of exceedances over some threshold for unit area pertaining to a single corrosion coupon, whose area is approximately 1/251th of the surface area of the UFC quarter hemispherical end-cap. If this number exceeds $m = 225$—the number of panels on the UFC quarter hemispherical end-cap, then $n_j \coloneqq m$ pits are assigned. Note, for most times

j, $\Lambda(t;\boldsymbol{\theta}_3)) > 1$ (see Figure D.2) and thus $n_j = 225$, which translates to assigning one pit depth exceedance to every panel in the quarter hemispherical end-cap. Otherwise, the algorithm for pit depth assignment is very much that of the GPD approach (the simulation approach in the preceding section serves to validate the use of $\Lambda(t;\boldsymbol{\theta}_3)$ directly in lieu of the more computationally intense simulation). Note, sampling for pit depth exceedances is done from the GPD parametrised with $\boldsymbol{\theta}_3$. This process is summarised in Algorithm 7.

Algorithm 7 Pit Depth Exceedance Assignment—NHPPP

Require: $T, m, \Lambda(t;\hat{\boldsymbol{\theta}}_3), f(x,t\,|\,\mu,\alpha,\kappa,b,u_k,c_k), f_{t_{\text{Cu}}} \sim Lognorm$

Initialise variables, arrays: $t, D_{t_{min}}, D_{t_{max}}, Cu, Cu_{t_{min}}, Cu_{t_{max}}$
$u_k, c_k \leftarrow$ select threshold level k
for t_i in T **do**
    $n_j \leftarrow \text{int}(251\Lambda(t;\hat{\boldsymbol{\theta}}_3))$
    if $n_j > m$ **then**
        $n_j \coloneqq m$
    $Cu \leftarrow$ sample randomly n_j thicknesses from $f_{t_{\text{Cu}}}$
    $f(x,t\,|\,\hat{\boldsymbol{\theta}}_3) \leftarrow f(x,t_i\,|\,\mu,\alpha,\kappa,b,u_k,c_k)$
    if $t_i == min(T)$ **then**
        $D_{t_{min}} \leftarrow$ sample randomly n_j pit depth exceedances from $f(x,t\,|\,\hat{\boldsymbol{\theta}}_3)$
        $Cu_{t_{min}} \leftarrow Cu - D_{t_{min}}$
    else
        $D_{t_{max}} \leftarrow$ sample randomly n_j pit depth exceedances from $f(x,t\,|\,\hat{\boldsymbol{\theta}}_3)$
        $Cu_{t_{max}} \leftarrow Cu - D_{t_{max}}$